

**The Use of Converging
Biofabrication Techniques
to Address Nature's Complexity
in Joint Repair**

Paweena Diloksumpan

**THE USE OF CONVERGING
BIOFABRICATION
TECHNIQUES TO ADDRESS
NATURE'S COMPLEXITY IN
JOINT REPAIR**

Paweena Diloksumpan

2020

ISBN: 978-94-6380-852-1

Copyright © 2020 by Paweena Diloksumpan

All rights reserved. No part of this thesis may be reproduced, stored in a retrieval system, or transmitted in any form or by any means, without written consent of the author or the corresponding journals for previously published chapters.

Cover design and Layout by: Paweena Diloksumpan

Printed by: ProefschriftMaken || Proefschriftmaken.nl

Printing of this thesis was financially supported by the Department of Clinical Sciences, Faculty of Veterinary Medicine, Utrecht University and the Netherlands society for Biomaterials and Tissue Engineering (NBTE)

The use of converging biofabrication techniques to address nature's complexity in joint repair

**Hoe een slimme combinatie van biofabricage technieken de
natuurlijke complexiteit dicht benadert bij
gewrichtsreconstructie**

(met een samenvatting in het Nederlands)

Proefschrift

ter verkrijging van de graad van doctor aan de
Universiteit Utrecht
op gezag van de
rector magnificus, prof.dr. H.R.B.M. Kummeling,
ingevolge het besluit van het college voor promoties
in het openbaar te verdedigen op
dinsdag 7 juli 2020 des middags te 2.30 uur

door

Paweena Diloksumpan

geboren op 28 juli 1983
te Bangkok, Thailand

Promotoren:

Prof. dr. J. Malda

Prof. dr. P.R. Van Weeren

Copromotor:

Dr. R. Levato

Table of contents

Chapter 1	General introduction	1
Chapter 2	From intricate to integrated: Biofabrication of articulating joints	7
Chapter 3	Combining multi-scale 3D printing technologies to engineer reinforced hydrogel-ceramic interfaces	25
Chapter 4	Orthotopic bone regeneration within 3D printed Bioceramic scaffolds with region-dependent porosity gradients in an equine model	57
Chapter 5	The complexity of joint regeneration: How an Advanced implant could fail by its <i>in vivo</i> proven bone component	89
Chapter 6	Multi-scale, 3D bioprinted osteochondral implants demonstrate long-term mechanical stability in the equine model	117
Chapter 7	General discussion	151
Annex I.	Addressing the brittleness of printable calcium phosphate (pCaP) cements via supplementation with resilient silk fibroin	167
Appendices:	Nederlandse samenvatting	177
	English Summary	181
	List of abbreviations	185
	Acknowledgements	187
	List of publications	189
	Curriculum vitae	190



CHAPTER 1

General Introduction

INTRODUCTION

Among the many components that contribute to the locomotor function in animals, diarthrodial joints play a fundamental role, enabling the relative movement at the interface of two bones. The joint is a complex, multi-tissue organ (**Figure 1**), in which thin layers of hyaline cartilage, that cap the articulating ends of long bones, slide onto each other in an almost frictionless manner, while also protecting the underlying bone from wear and high mechanical loads¹. Other specialized tissues pertaining to joints include menisci, which are placed between two opposing sides of a joint. Here, they act as shock absorbers, but also improve congruency of the joint. Further elements include the fat pads, as well as the ligaments and tendons, respectively providing stability to the joint and transmitting forces generated by muscles to the bones to induce motion². The joint cavity is filled with synovial fluid, an ultra-filtrate of blood and the main source of lubrication and nutrients for the avascular cartilage. The joint is delimited by the synovial membrane, which serves as the interface between the synovium and the systemic vascular system³.

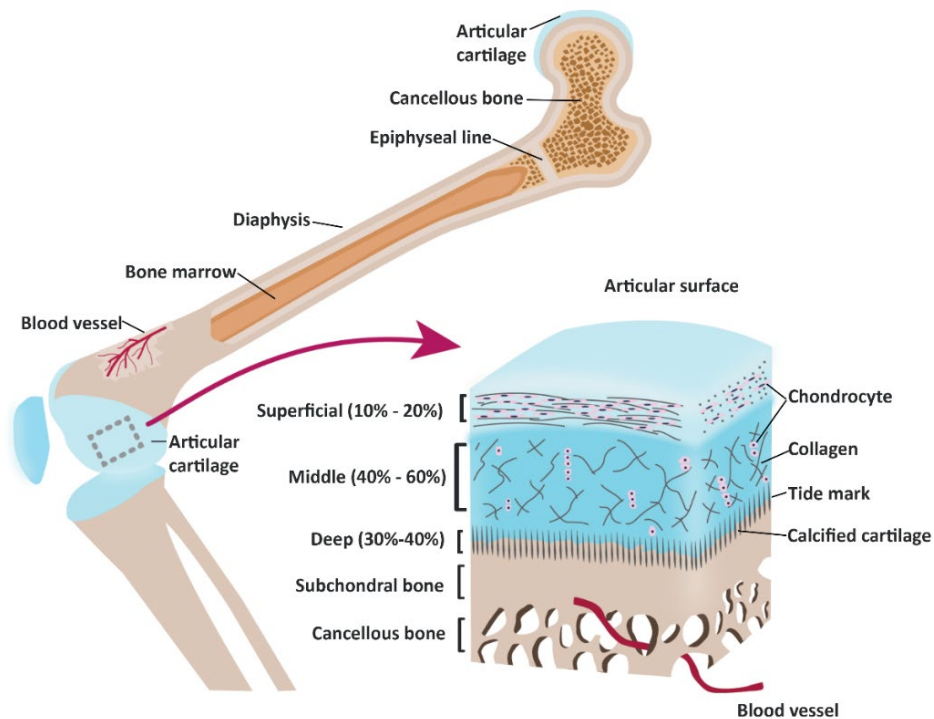


Figure 1. Schematic picture representing the osteochondral unit of a diarthrodial joint (modified from Ref⁴)

Joint trauma and pathology can originate from any of these tissues and, over time, typically results in the degradation of the cartilage layer, which eventually results in a compromised function of the whole joint, as the cartilage tissue has low self-reparative

capacity⁵. Such degeneration of the cartilage often results in osteoarthritis, a major cause of disability and reduced life quality for our aging population and for which to date no disease-modifying drug or definitive solution exists. In fact, the world has a significant medical and socio-economic challenge in restoring the function of injured joints. Metallic prostheses, albeit representing a functionally rather successful surgical intervention, have limited life spans as they are subject to wear and tear⁶. New regenerative therapies that restore the biological structure and function of the native joint and its cellular components, are thus sought as *Holy Grail* to treat both traumatic articular injuries and osteoarthritis⁷. With the advent of tissue engineering, in the past three decades, major efforts have been dedicated at combining biodegradable materials and stem cells to achieve this goal^{8, 9}. To date, regenerative, cell therapy-based approaches are clinically available and used with a certain degree of success¹⁰. However, they are limited to relatively small focal cartilage defects, apart from all of them being unable to create regenerated tissue with the same properties and quality of the original native tissue. Treating large portions of the joint remains an unsolved challenge, especially in cases where the delicate interplay between the multiple tissues that make up the joint is compromised.

A fundamental bottleneck for the successful clinical application of regenerative implants that can replace and heal partial or even whole-joint damage, is the restoration of the osteochondral boundary. Defects involving both bone and cartilage typically occur in young, active patients due to trauma, as well as during severe stages of osteoarthritis¹¹. In synovial joints, hyaline cartilage, the subchondral bone and the calcified cartilage layer that forms the interface between the previous two tissues, constitute a uniquely organized structure, which specifically evolved for transferring mechanical loads. Additionally, the calcified cartilage and the subchondral bone act as a diffusional barrier to modulate the exchange of solutes and bioactive signals to and from the cartilage layer^{12, 13}, and the preservation of such biochemical communication is paramount in joint homeostasis.

As such, when designing regenerative implants and developing new biomaterials for osteochondral repair, failure to establish a mechanically competent interconnection between bone and cartilage will always compromise the whole restorative process. Thus, new strategies and technologies need to be developed to overcome this challenge. In view of this, three-dimensional (3D) biofabrication holds great promise and provides new opportunities for osteochondral regeneration. Biofabrication entails the automated control over the spatial patterning of multiple cell types and biomaterials through layer-by-layer deposition methods, by means of 3D (bio-)printing and bio-assembly¹⁴. With this approach, gradient structures, as well as complex architectures that mimic the composition of native tissues, can be created. In particular, biofabrication and 3D-printing have been hailed for their promise to generate custom-made grafts in clinically relevant sizes, which could be designed to perfectly fit a patient-specific defect. Yet, the way how to integrate successfully the cartilage and the bone phase, remains elusive.

A main reason why this obstacle has not yet been cleared, is the intrinsic difficulty of integrating materials that display highly dissimilar mechanical properties. In the native

tissue, the osteochondral interface is a refined outcome of developmental processes occurring during the prenatal and postnatal period, in which the immature cartilage component is remodelled, invaded by vessels and replaced by mineralized type I collagen, which is later used as a template for bone formation¹⁵⁻¹⁷. In engineered structures, however, replicating such a process is a daunting task.

Tissue engineering and bioprinting have reached exciting results in the field of cartilage repair by loading cells into hydrogels, 3D structures rich in water, which can be designed to resemble the extracellular environment that is favourable for chondrocytes, or to guide the chondrogenic differentiation of stem cells¹⁸. Conversely, for bone regeneration, materials, such as calcium phosphate-based bioceramics, have a long history of success with specific formulations already translated to applications in bone repair and in orthopaedic and cranio-maxillofacial surgery¹⁹. Such materials, which can be designed to display mechanical properties and a mineral composition similar to native bone, have proven osteoconductive properties. By accurate engineering of their composition, they have been demonstrated to promote osteoinduction by stem and progenitor cells²⁰. Thus, hydrogels and bioceramics show independently promising properties for cartilage and bone regeneration, respectively. Unfortunately, most ceramics are processed with harsh chemical treatments (*i.e.* strongly acidic pH), or via sintering at high temperature, both conditions that impede the co-printing or the contextual processing with hydrogels, cells and in general even thermoplastic polymers^{19,21}. On the other hand, hydrogels typically display low mechanical properties and poor adhesive ability onto bioceramics, like the ones that compose bone, even when fabricated as composites with polymeric materials that can provide additional mechanical strength. New technologies are thus required to create strongly integrated osteochondral structures based on these classes of materials.

Hypothesis and aims of the thesis

The conceptual hypothesis of this thesis is that the use of a converged biofabrication approach, in which multiple printing technologies are combined that enable the fabrication of structures across different dimensional scales (from micro to macro), will permit the creation of an osteochondral construct featuring a functional integration of the bone phase with the structure-giving elements of the cartilage phase.

This conceptual hypothesis led to the following concrete aim: the development of an osteochondral implant with 1.) structurally integrated bone and cartilage phases that 2.) would allow for the firm fixation of the implant *in vivo* through the integration of the bone anchor with the native bone.

Scope of the thesis

In **Chapter 2**, we first review the hierarchical structure of the native osteochondral tissue and then present the current challenges to recapitulate the complexity of articulating joints and

how biofabrication could aid to overcome them. In this chapter, the state-of-the-art of 3D printing-based reinforcing strategies used to improve the mechanical performance of hydrogels for cartilage regeneration is presented and connected to the open challenge of integration with a bony and calcified substrate. A biofabrication-based approach to reinforce the bone-cartilage interface in regenerative implants is then introduced in **Chapter 3**. This approach is based on the development of a printable bioceramic material, based on alpha-tricalcium phosphate particles, which can set at physiological temperature and pH, thus even in the presence of cells and labile thermoplastic materials. Taking advantage of this feature, this chapter introduces a novel technology for the integration of extrusion printing of such bone-biomimetic ceramic ink and melt electrowriting (MEW) of spatially organized polymeric microfibres. **Chapter 4** subsequently confirms the bone forming capacity of the bone-biomimetic ceramic ink in a long-term *in vivo* equine tuber coxae bone defect model. In **Chapter 5**, integrated implants are generated, containing a fibrous cartilage phase inoculated with chondroprogenitor cells that were chondrogenically stimulated with growth differentiation factor-2 (GDF-2), that are tested *in vivo* in a large animal model. The approach for the integration of the cartilage and bone phases is then applied in another long-term large animal *in vivo* experiment in **Chapter 6** to a fully biofabricated osteochondral implant, which encompasses a zonally organized reinforced hydrogel cartilage phase. Further building onto these results, **Annex 1** introduces a new modification using silk as a reinforcing agent for the bioceramic printable paste presented in Chapter 3. The resilience of silk fibroin is studied with the aim to reduce the brittleness of the bioceramic composite and thus facilitate surgical implantation. The findings of this thesis are discussed in **Chapter 7**, along with novel avenues for future investigations.

REFERENCES

1. Lepage, S. I. M.; Robson, N.; Gilmore, H.; Davis, O.; Hooper, A.; St John, S.; Kamesan, V.; Gelis, P.; Carvajal, D.; Hurtig, M.; Koch, T. G., Beyond Cartilage Repair: The Role of the Osteochondral Unit in Joint Health and Disease. *Tissue Eng Part B Rev* **2019**, *25* (2), 114-125.
2. Piluso, S.; Li, Y.; Abinzano, F.; Levato, R.; Moreira Teixeira, L.; Karperien, M.; Leijten, J.; van Weeren, R.; Malda, J., Mimicking the Articular Joint with *In Vitro* Models. *Trends Biotechnol* **2019**, *37* (10), 1063-1077.
3. FitzGerald, O.; Bresnihan, B., Synovial membrane cellularity and vascularity. *Ann Rheum Dis* **1995**, *54* (6), 511-5.
4. Hu, X.; Xu, J.; Li, W.; Li, L.; Parungao, R.; Wang, Y.; Zheng, S.; Nie, Y.; Liu, T.; Song, K., Therapeutic "Tool" in Reconstruction and Regeneration of Tissue Engineering for Osteochondral Repair. *Appl Biochem Biotechnol* **2019**.
5. Zhang, W.; Ouyang, H.; Dass, C. R.; Xu, J., Current research on pharmacologic and regenerative therapies for osteoarthritis. *Bone Res* **2016**, *4*, 15040.
6. Gallo, J.; Goodman, S. B.; Kontinen, Y. T.; Wimmer, M. A.; Holinka, M., Osteolysis around total knee arthroplasty: a review of pathogenetic mechanisms. *Acta Biomater* **2013**, *9* (9), 8046-58.
7. Makris, E. A.; Gomoll, A. H.; Malizos, K. N.; Hu, J. C.; Athanasiou, K. A., Repair and tissue engineering techniques for articular cartilage. *Nat Rev Rheumatol* **2015**, *11* (1), 21-34.
8. Caldwell, K. L.; Wang, J., Cell-based articular cartilage repair: the link between development and regeneration. *Osteoarthritis and Cartilage* **2015**, *23* (3), 351-362.
9. Camarero-Espinosa, S.; Rothen-Rutishauser, B.; Foster, E. J.; Weder, C., Articular cartilage: from formation to tissue engineering. *Biomater Sci* **2016**, *4* (5), 734-67.
10. Huang, B. J.; Hu, J. C.; Athanasiou, K. A., Cell-based tissue engineering strategies used in the clinical repair of articular cartilage. *Biomaterials* **2016**, *98*, 1-22.
11. Lories, R. J.; Luyten, F. P., The bone–cartilage unit in osteoarthritis. *Nature Reviews Rheumatology* **2011**, *7* (1), 43-49.
12. Goldring, S. R.; Goldring, M. B., Changes in the osteochondral unit during osteoarthritis: structure, function and cartilage-bone crosstalk. *Nat Rev Rheumatol* **2016**, *12* (11), 632-644.
13. Pourn, B.; Arbabi, V.; Bleys, R. L.; Rene van Weeren, P.; Zadpoor, A. A.; Weinans, H., Solute transport at the interface of cartilage and subchondral bone plate: Effect of micro-architecture. *J Biomech* **2017**, *52*, 148-154.
14. Groll, J.; Boland, T.; Blunk, T.; Burdick, J. A.; Cho, D. W.; Dalton, P. D.; Derby, B.; Forgacs, G.; Li, Q.; Mironov, V. A.; Moroni, L.; Nakamura, M.; Shu, W.; Takeuchi, S.; Vozzi, G.; Woodfield, T. B.; Xu, T.; Yoo, J. J.; Malda, J., Biofabrication: reappraising the definition of an evolving field. *Biofabrication* **2016**, *8* (1), 013001.
15. Haleem, A. M.; Chu, C. R., Advances in Tissue Engineering Techniques for Articular Cartilage Repair. *Oper Tech Orthop* **2010**, *20* (2), 76-89.
16. Lofgren, M.; Ekman, S.; Svala, E.; Lindahl, A.; Ley, C.; Skioldebrand, E., Cell and matrix modulation in prenatal and postnatal equine growth cartilage, zones of Ranvier and articular cartilage. *J Anat* **2014**, *225* (5), 548-68.
17. Williams, G. M.; Klisch, S. M.; Sah, R. L., Bioengineering cartilage growth, maturation, and form. *Pediatr Res* **2008**, *63* (5), 527-34.
18. Balakrishnan, B.; Banerjee, R., Biopolymer-based hydrogels for cartilage tissue engineering. *Chem Rev* **2011**, *111* (8), 4453-74.
19. Habraken, W.; Habibovic, P.; Epple, M.; Bohner, M., Calcium phosphates in biomedical applications: materials for the future? *Materials Today* **2016**, *19* (2), 69-87.
20. Barba, A.; Maazouz, Y.; Diez-Escudero, A.; Rappe, K.; Espanol, M.; Montufar, E. B.; Öhman-Mägi, C.; Persson, C.; Fontecha, P.; Manzanera, M.-C.; Franch, J.; Ginebra, M.-P., Osteogenesis by foamed and 3D-printed nanostructured calcium phosphate scaffolds: Effect of pore architecture. *Acta Biomaterialia* **2018**, *79*, 135-147.
21. Fernandez, E.; Gil, F. J.; Ginebra, M. P.; Driessens, F. C.; Planell, J. A.; Best, S. M., Calcium phosphate bone cements for clinical applications. Part II: precipitate formation during setting reactions. *J Mater Sci Mater Med* **1999**, *10* (3), 177-83.

CHAPTER 2

From Intricate to Integrated: Biofabrication of Articulating Joints

Wilhelmina Margaretha Groen¹, Paweena Diloksumpan²,
Paul René van Weeren², Riccardo Levato¹, and Jos Malda^{1,2}

Published in the Journal of Orthopaedic Research (2017),
35(10): 2089-2097,
DOI 10.1002/jor.23602

¹Department of Orthopaedics, University Medical Centre Utrecht, PO Box 85500, 3508 GA, Utrecht, The Netherlands,

²Faculty of Veterinary Medicine, Department of Equine Sciences, Utrecht, The Netherlands

ABSTRACT

Articulating joints owe their function to the specialized architecture and the complex interplay between multiple tissues including cartilage, bone and synovium. Especially the cartilage component has limited self-healing capacity and damage often leads to the onset of osteoarthritis, eventually resulting in failure of the joint as an organ. Although in its infancy, biofabrication has emerged as a promising technology to reproduce the intricate organization of the joint, thus enabling the introduction of novel surgical treatments, regenerative therapies, and new sets of tools to enhance our understanding of joint physiology and pathology. Herein, we address the current challenges to recapitulate the complexity of articulating joints and how biofabrication could overcome them. The combination of multiple materials, biological cues and cells in a layer-by-layer fashion, can assist in reproducing both the zonal organization of cartilage and the gradual transition from resilient cartilage toward the subchondral bone in biofabricated osteochondral grafts. In this way, optimal integration of engineered constructs with the natural surrounding tissues can be obtained. Mechanical characteristics, including the smoothness and low friction that are hallmarks of the articular surface, can be tuned with multi-head or hybrid printers by controlling the spatial patterning of printed structures. Moreover, biofabrication can use digital medical images as blueprints for printing patient-specific implants. Finally, the current rapid advances in biofabrication hold significant potential for developing joint-on-a-chip models for personalized medicine and drug testing or even for the creation of implants that may be used to treat larger parts of the articulating joint.

Keywords: articular cartilage; osteochondral; bioprinting; additive manufacturing; regenerative medicine

Worldwide spending on three-dimensional (3D) printing is expected to surpass \$35 billion in 2020¹ and the technology holds promise for significant breakthroughs in medicine.² Like in other medical fields, also in orthopaedics additive manufacturing (AM) is driving a shift toward mass personalization, as personal scans can be converted into computer aided design (CAD) files, which are then used to design perfectly fitting surgical guides³ or other tools.⁴ The technology also allows for the generation of personalized external prostheses, which are, for example, mirrored from the healthy other limb.⁵ In addition, personalized implants can be designed and printed on demand for complex revisions of endoprostheses, in trauma cases⁶ or for reconstruction after tumor resection surgery.⁷ Although these developments will impact current treatment of joint damage, these approaches rely on synthetic and metallic materials that lack any biologically adaptive properties and cannot remodel with host tissues. The emerging field of biofabrication addresses this issue in tissue engineering and regenerative medicine, as it uses cells and bioactive materials in its fabrication process. Biofabrication is defined as “the automated generation of biologically functional products with structural organisation from living cells, bioactive molecules, biomaterials, cell aggregates such as microtissues, or hybrid cell-material constructs, through bioprinting or bioassembly and subsequent tissue maturation processes.”⁸ Biofabrication, therefore, potentially can deliver a biologically responsive implant that could address some important challenges that are currently faced in the treatment of articulating joints. Anatomically sized implants with a patient-specific shape could be provided by biofabrication following the same lines as AM. Such a personalized anatomical shape will secure smooth seamless transition between graft and host, contributing to an appropriate fit. This will avoid unnecessary wear and ensure mechanical stability of the joint. Nevertheless, there are more aspects to articular regeneration than just joint geometry. The layered structure of cartilage is essential to ensure proper physiologic and mechanical functioning, and assuring a firm integration between all these layers is crucial for producing an implant stable enough to withstand the mechanical forces that are generated in a joint. Implants should preferably come close to the mechanical characteristics of native tissue, especially in those situations where tissue engineered and original tissues sit close together.⁹ Clearly, proper fixation of an implant is a prerequisite for effective integration between both cartilage and bone from host and implant. Likewise, an implant would fail if the integration between the cartilage and bone compartment, which in native tissue is provided by the calcified cartilage, is not sufficient. Biofabrication can potentially deal with the abovementioned requirements using cells, multiple materials and biochemical compounds. As cells and bioactive molecules are key factors in the regenerative response, the ability of biofabrication techniques to orchestrate spatial concentrations of bioactive factors and/or cells, either through direct placement and/or by controlling the architecture of the implant¹⁰⁻¹² makes it a valuable tool in tissue engineering. This review discusses the current and future assets and opportunities of biofabrication to address challenges in treatment strategies for cartilage repair, particularly for replacing larger parts of the joint (**Figure 1**).

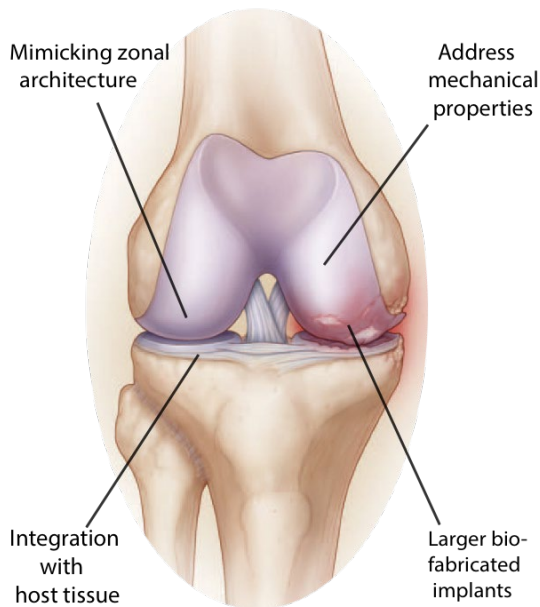


Figure 1. Challenges in biofabrication of articulating joints. Reproduced and adapted with permission from NEJM group.¹³

Mimicking the Layered Structure of Native Tissue

The relatively simple appearance of articular cartilage, which is avascular, aneural, and contains only one cell type,¹⁴ is deceptive and attempts at cartilage repair using implants with relatively homogenous structures have hitherto not succeeded in creating clinically successful products able to regenerate the articular surface. The intricate mechanical characteristics of articular cartilage are dictated by the complex zonal structure of the tissue,^{15–18} consisting of three layers with distinct composition and architecture: the shear and tension resistant superficial zone; the intermediate middle zone; and the deeper zone with its high compressive stiffness.^{16,19} From the articulating surface toward the bone, these layers show a decrease in cell density and water content combined with an increasing glycosaminoglycans (GAGs) and collagen content, while collagen fibril alignment gradually pivots^{15–18} according to the arcade model described by Benninghoff.²⁰ Together, these depth-dependent differences create a structure with unique gradually changing mechanical properties, dictating the variance in protein secretion and extracellular matrix (ECM) composition.^{15,21,22} A major challenge is to induce zone specific matrix production in engineered tissues. This can be done by orchestrating the spatial and temporal presentation of multiple growth factors and mechanical cues. For instance, the activity of transforming growth factor β 3 (TGF- β 3) acted synergistically with oscillatory application of hydrostatic pressure to enhance cartilage production in human adipose-derived stem cells.²³ This was

confirmed for human mesenchymal stem cells (MSCs) and multi axial loading even appeared to activate latent TGF- β 1 incorporated in the medium.²⁴ The combination of insulin-like growth factor-1 (IGF-1) with TGF- β 1, in the middle zone of a construct, promoted chondrogenic differentiation of human MSCs.^{21,25} Further, TGF- β 1 and BMP-7 enhanced expression of superficial zone markers and TGF- β 1 combined with hydroxyapatite led to expression of calcified zone markers.²⁵ Additionally, differences in zone-specific fiber or scaffold orientation, created by conventional techniques, influenced the expression of zonal markers^{26,27} and either osteogenic or cartilaginous differentiation of chondrocytes could be induced by variance in matrix stiffness.²¹ Such zonal complexity and combination of factors can be effectuated by biofabrication, which has the ability of tuning the micro architecture by depositing multiple materials to create gradients or reinforcing fibers in multiple directions, providing the possibility of steering local differences in the cartilage that will eventually be produced. It has further been demonstrated that direction of both cell alignment and collagen formation can follow the geometry of deposited polymer strands when subjected to an adequate strand spacing (<200 nm)²⁸ or to aligned nanofibers.²⁹ It remains challenging, however, to replicate the orientation of the collagen fibers, as the resolution of the available printing processes is still below the required resolution to mimic the Benninghoff arcades. Zonally organized constructs that were subsequently seeded with cells have been produced by AM.^{22,30,31} A gradient in pore-size of printed polymer scaffolds was shown to alter cell distribution, although no influence on tissue composition was observed.²² Seeding chondrocytes from specific zones on 3D printed zonal polymer scaffolds induced the formation of abundant cartilage-like tissue, yet chondrocytes lost their zone-specific characteristics.³¹

Biofabrication can incorporate cells in these fabrication processes and has already been used to create zonally organized composites (**Figure 2**).^{32–34} For example, a cell density gradient was bioprinted with a piston-driven depositional print head on a robotic arm. This promoted formation of a gradient distribution of ECM, which was correlated to the cell density.³² Also, a modified thermal inkjet printer was used in combination with simultaneous photopolymerization to deposit and crosslink a bioink. This produced an even cell distribution, however, modifying the time between photo-polymerization can create a zonal distribution of cells due their gravitation-driven movement.^{33,34}

Chondrocytes from specific zones have been used and were shown to respond differently to co-culture systems,³⁵ mechanical stimuli,³⁶ and biochemical compounds.³⁷ Nevertheless, dedifferentiation and loss of zone-specific characteristics are major challenges.^{17,31} Besides, zonal harvesting techniques have not been optimized, are time consuming and chondrocyte yield is generally low.^{15,38} Ultimately, the etiology of the zonal differences has not yet been sorted out. It could even be questioned if zone-specific or different types of chondrocytes exist at all, because chondrocytes could also express zone specific markers due to their spatial position and consequentially distinct mechanical stimuli they are subjected to.

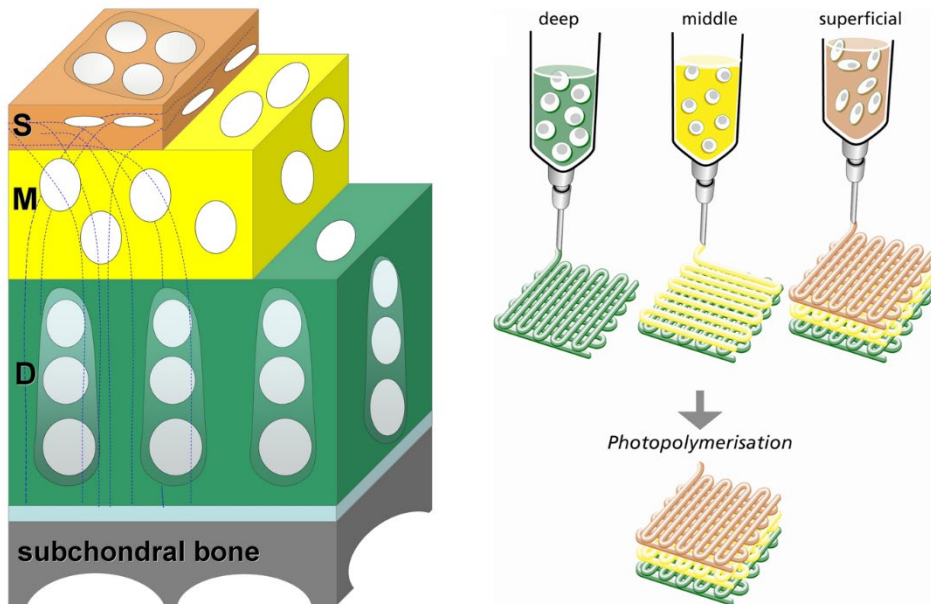


Figure 2. Schematic representation of the zonal organization of articular cartilage, showing how cell morphology and collagen fiber orientation vary across the thickness of the tissue. Multiple zone-specific bioinks could be used in a biofabrication set-up to replicate the zonal chondrocytes and ECM phenotype via printing in a layer-by-layer fashion. Reproduced with permission from John Wiley&Sons.¹⁶

In our opinion, the use of chondrocytes from a specific zone seems like an overcomplicated strategy that is probably of no added value in the clinic.¹⁵

While much knowledge has been gained regarding the response of chondrocytes to different stimuli, this knowledge is unfortunately not enough to generate a biologically functional graft for *in vivo* application that is able to create the desired organizational structure. To achieve this ambitious goal, multiple strategies will have to be combined.^{39,40} The layer-by-layer fashion in which biofabrication assembles its products, combined with the ability to incorporate different growth factors,^{41,42} vary cell densities and tailor fiber orientation, seems to meet all necessary requirements to create such complex biologically functional osteochondral implants.

Mechanical Properties of the Implant Approaching Those of Native Tissue

Articular cartilage is a biomechanical tissue par excellence, of which the properties and functions are largely dictated by its composition and structure.^{43,44} Basically, the role of intact hyaline cartilage is to function as a cushion between two opposing rigid bones in articulating joints, by distributing load and consequently decreasing stress at the contact point. In addition, cartilage ensures that movements occur under minimal friction and wear.⁴³ Restoration of biomechanical function is one of the crucial requirements of any attempt to

revive joint function for a long-term period, as an implant must withstand the substantial loading stresses associated with locomotion and sometimes even athletic activity.

Biofabrication generates cell-laden constructs by means of hydrogel-based bioinks. Hydrogels are very suitable for mimicking the native ECM as they provide a highly hydrated environment favorable for cells. For optimal printability, a hydrogel has to display shear thinning behavior, rapid gelation and little or no extrudate swell.⁴⁵ Several strategies have been used to improve rheological properties of hydrogels, such as the incorporation of additives tuning viscosity, yield stress and gelation kinetics, resulting in an improved printability and shape-fidelity after strand deposition.⁴⁶⁻⁴⁸ However, the design of hydrogels for bioprinting is challenging as the rheological properties also have to allow for biological activity of the cells.

Importantly, hydrogels are limited by low compressive stiffness,^{49,50} regardless of the crosslinking process they can be subjected to. Constructs simply composed of a hydrogel will not be appropriate for the treatment of load-bearing tissues. Nevertheless, hydrogels can be combined with other materials to yield reinforced composite structures with enhanced stability and overall mechanical properties. This approach has been explored with reinforcing structures based on thermoplastic polymers,^{51,52} on stiffer hydrogels printed by fused-deposition modeling,^{53,54} or on the incorporation of random microfibers, for example generated by electrospinning.⁵⁵ Importantly, these methods showed that approaching the compressive stiffness of native cartilage is feasible.^{51,53,54}

Although there are various strategies for the incorporation of multiple materials,⁵⁶ the evolution from AM toward biofabrication has shown an advantage over conventional and other AM techniques. This is thanks to the fact that biofabrication uses either multi-head or hybrid printing systems^{57,58} that allow both simultaneous and sequential printing, for building up highly organized cell-laden reinforced constructs.⁵⁸⁻⁶³ Moreover, convergence of multiple biofabrication technologies will further extend the possibilities, including the simultaneous deposition of hydrogels and ultra-thin reinforcing fibers produced by melt electrospinning writing (MEW). This technique allows precisely controlled deposition of these micro-fibers, which allows to generate structures with similar compressive behavior as native cartilage.⁶⁴ Additionally, biofabrication provides the opportunity to simultaneously control micro- and macro-architecture of an implant, as precise control can be exerted on spatial arrangement of the framework,⁶⁵ which inherently allows control over its mechanical properties. Actually, multiple parameters can be tuned to modulate porosity and compressive stiffness, such as fiber diameter through nozzle diameter or deposition speed, fiber spacing, layer thickness, layer configuration, and fiber orientation.⁶⁶⁻⁷⁰ In this way mechanical properties can, for example, be influenced by tailoring the local distribution of reinforcing fibers.⁶⁸

Furthermore, for the optimal performance of larger osteochondral implants, it is important that the geometry of an osteochondral implant can be controlled into detail. Consequently, it can provide a perfect fit and alignment with the surrounding tissues to ensure the stability and subsequent integration.⁷¹ Biofabrication can provide such perfectly fitting implants as it allows for the generation of patient-specific anatomical shapes based on digital

medical images.⁷² In addition, this control over precise geometry provides the ability to design shear resistant surfaces. Taken together, construct shape and mechanical properties can be highly controlled by the application of biofabrication techniques.

Improved Integration

The integration between both the cartilage and bone part of an implant, as well as with the host tissue, is a crucial prerequisite for correct functionality and prevention of graft failure, hence for long-term successful performance of the implant.^{39,73} Obviously, this requires a perfect fit and alignment of the construct with the surrounding tissues. Biofabrication technologies could also play a role in improving the integration between the cartilage and the bone, by recapitulating the subchondral bone-to-cartilage transition. This is particularly relevant, as composition, organization and anatomical structure of this interfacial region have important roles in force absorption and transmission.⁷⁴ In many conventional tissue engineering approaches, the “interface” is an unintentional by-product of combining the two main parts of the osteochondral construct, which were connected by just press-fitting, suturing, melting, or gluing prior to implantation.⁷⁵ However, further insights in the anatomy and function of the osteochondral interface have underscored the importance of proper integration between the bone and cartilage compartments.^{76–81} Incorporation of a calcified cartilage zone could improve interfacial shear strength of osteochondral constructs.⁸² This interfacial region can also fulfil an important role as a structural barrier to prevent vascular in growth from bone to cartilage.⁸³

Biofabrication technologies can pre-eminently yield integrated constructs with various compositions.⁸⁴ The simple introduction of gradients in structure (i.e., porosity),^{10,85} composition (i.e., minerals and growth factors)^{86–88} or mechanics (i.e., stiffness)²⁷ can influence the differentiation of cells toward bone and cartilage lineages.

Apart from building gradient structures, constructs comprising of a bone and cartilage region can be a simplified mimicry of the native osteochondral unit.^{39,89} One method would be depositing layers of the same material to ensure proper axial binding, supplementing it with biofunctional compounds to tune cell behavior in each region. For example, regional distribution of mineral components, such as calcium phosphate nanoparticles⁹⁰ and osteogenic micro particles,^{91,92} were used to facilitate the osteogenic differentiation in the bone region of bioprinted osteochondral constructs. Furthermore, brittle calcium phosphates can be combined with thermoplastic polymers, like polylactic acid (PLA) or polycaprolactone (PCL) to improve the elasticity of the constructs.⁹³ Also, composite scaffolds were generated based on layers of electrospun PCL and different concentrations of b-tricalcium phosphate nanoparticles. After 4-week culture, mouse pre-osteoblasts (MC3T3-E1) deposited matrix in a pattern resembling the bone-to-cartilage interface.⁹⁴ This approach was also employed to simultaneously fabricate nanofibrous PCL with gradients of insulin and beta-glycerophosphate (β -GP). Human adipose-derived stromal cells differentiated chondrogenically at the insulin-rich sites, while mineralization was predominantly observed

in regions where the β -GP concentration was higher.⁹⁵ Novel approaches involving the use of advanced biomaterials and the convergence of multiple AM technologies can allow firm integration between different layers even when using heterogeneous components. Recently, strategies to provide strong, covalent binding between hydrogels and polymeric, ceramic, and metallic surfaces have been developed, displaying adhesion forces in the range of the native bone-to-cartilage interface,⁹⁶ which could be adapted for tissue engineering.

Biofabricated osteochondral constructs have been already adopted in an *in vivo* study involving a MSC-laden collagen and hyaluronic acid hydrogel construct reinforced by PCL. This artificial osteochondral plug was implanted in a rabbit knee and appeared to be mechanically stable and to integrate well with the native cartilage and the underlying bone.⁹⁷ The success of this study was, at least in part, due to a perfectly fitting design of the prosthesis, as well as the good integration in both bone and cartilage region, achieved by stack crosslinking with the same cell-friendly chemistry. Although there is still major room for improvement, this example illustrates the potential of biofabrication for optimizing the performance and integration of tissue-engineered osteochondral grafts.

Stereolithographic techniques have been recently combined with extrusion-based AM techniques for application in osteochondral regeneration.^{86,98} For instance, an osteochondral unit with a gradual change of mineral composition and growth factors was fabricated using stereolithography. The constructs, composed of a hydrogel with TGF- β 1 in the cartilage part and a discrete gradient of hydroxyapatite nanoparticles in the bone part, revealed that differentiation of human MSCs toward the osteogenic and chondrogenic lineages corresponded to the compositional gradients.⁸⁶ An appealing approach would be that of combining extrusion of hydrogels, ceramics, and thermoplastics with melt electrospinning writing of nano- and microfibrinous meshes. In this way, such meshes could act as interlocking elements between the bioprinted bone and cartilage compartments, to produce a new generation of mechanically stable osteochondral grafts.

Toward Larger Implants and Miniaturized Models: A Future Outlook

Biofabrication has the potential to address the challenges mentioned above. It can recapitulate a zonal organization in a graft, it allows for the generation of constructs that approach mechanical properties of native cartilage, and it provides tools for improved integration, both of construct components and with surrounding host tissue. Moreover, it can produce complex shapes in a single fabrication process. Therefore, the technique poses an excellent opportunity to generate larger structures. A wide range of smaller osteochondral constructs have been successfully generated using AM alone^{34,75,99,100} or in combination with conventional techniques, including casting, freeze-drying and solvent casting/particle leaching.^{101–104} Even though the generation of a long-term functional solution in osteochondral tissue engineering remains challenging, *in vivo* approaches with 3D printed osteochondral plugs have already been reported.^{97,105–107}

There is now the opportunity to generate larger personal implants, as biofabrication can provide highly accurate anatomical structures^{62,108–110} using different materials, either with^{111,112} or without^{113,114} the aid of a sacrificial support. Feasibility of this concept has been successfully demonstrated in rabbit models, for example, the manufacturing of total knee⁷² and humeral head replacements.¹¹⁵ Nevertheless, there has been limited follow-up on this concept as it is associated with some significant challenges. Some of these are more general and related to the engineering of high quality tissue, while others are specifically related to biofabrication. Cell viability in bioprinting may be compromised, especially during longer printing processes¹² and the process of generating personalized implants in pre-clinical/translational studies is still labor intensive and expensive.^{116,117} Also, the establishment of appropriate *in vitro* pre-conditioning protocols is a time-consuming task^{36,118} and the need for post-implantation vascularization should also not be overlooked. While this latter challenge can well be addressed by biofabrication,^{119–122} the hollow structures still need to be populated with, for example, endothelial cells.

Biofabrication provides avenues for the generation of larger implants, however, it also offers opportunities for the organ-on-a-chip approach, a technology that aims to simulate specific organ functions and pathologies, and is rapidly advancing in medicine.¹²³ Models have been developed to mimic a range of different tissue conditions, including alveolar function,¹²⁴ intestinal disease,¹²⁵ the beating heart,¹²⁶ and the blood brain barrier.¹²⁷ In the spirit of the body-on-a-chip initiative,¹²⁸ the new concepts of “cartilage-on-a-chip” and “joint-on-a-chip” will be further matured.^{129,130} Since the resolution of AM has increased to micro- and nanoscale and progress is made in speeding up the printing process while maintaining its accuracy, biofabrication could definitely also prove itself a key technique in this new area. Ultimately, we envision that patients’ chondrocytes or synovial cells could be seeded on a chip, as has been shown in other fields using the organ-on-a-chip technology.¹³¹ The idea would be to determine the immunological profile and gain valuable insights on biomarkers of osteoarthritis, rheumatoid arthritis, and other joint diseases. Similarly, drug efficacy in balancing joint homeostasis could be evaluated.

CONCLUSION

For a successful approach to engineer osteochondral tissue, functional mimicking of this tissue in all its complexity is imperative. To achieve this, one has to address the zonal architecture with a firm connection between different zones and the adjacent host tissue, the biomechanical profile of the native tissue, which is of paramount importance, and a human-scaled personalized shape. For clinical applicability, standardization and possibilities for scaling up are important. Clearly, promising steps have been taken *in vitro* to create constructs featuring good integration between bone and cartilage and transition to (large) animal models should now be pursued. Despite being a relatively new field of technology, biofabrication potentially encompasses all tools and techniques to address these issues and

hence is opening promising avenues toward the generation of biologically active personalized osteochondral implants with the ability to regenerate tissue rather than replace it.

ACKNOWLEDGEMENTS

The authors have received funding from the European Community's Seventh Framework Programme (FP7/2007- 2013) under grant agreement n°309962 (HydroZONES), the European Research Council under grant agreement n° 647426 (3D-JOINT), and the Dutch Arthritis Foundation (LLP-12, LLP-22).

REFERENCES

1. Shirer, M.; Chute, C.; Kmetz, K. Worldwide Semiannual 3D Printing Spending Guide, 2016. <https://www.idc.com/getdoc.jsp?containerId=prUS41671116> (accessed January 31, 2017).
2. Hornick, J., 3D printing in Healthcare. *Journal of 3D Printing in Medicine* **2016**, *1* (1), 13-17.
3. Krishnan, S. P.; Dawood, A.; Richards, R.; Henckel, J.; Hart, A. J., A review of rapid prototyped surgical guides for patient-specific total knee replacement. *The Journal of Bone and Joint Surgery. British volume* **2012**, *94-B* (11), 1457-1461.
4. Liu, A.; Xue, G.-h.; Sun, M.; Shao, H.-f.; Ma, C.-y.; Gao, Q.; Gou, Z.-r.; Yan, S.-g.; Liu, Y.-m.; He, Y., 3D Printing Surgical Implants at the clinic: A Experimental Study on Anterior Cruciate Ligament Reconstruction. *Scientific Reports* **2016**, *6* (1), 21704.
5. Yoshikawa, M.; Sato, R.; Higashihara, T.; Ogasawara, T.; Kawashima, N. In *Rehand: Realistic electric prosthetic hand created with a 3D printer*, 2015 37th Annual International Conference of the IEEE Engineering in Medicine and Biology Society (EMBC), 25-29 Aug. 2015; 2015; pp 2470-2473.
6. Materialise Mobilife. <http://www.materialise.com/en/medical/mobilife>. (accessed January 31, 2017)
7. Liang, H.; Ji, T.; Zhang, Y.; Wang, Y.; Guo, W., Reconstruction with 3D-printed pelvic endoprosthesis after resection of a pelvic tumour. *The Bone & Joint Journal* **2017**, *99-B* (2), 267-275.
8. Groll, J.; Boland, T.; Blunk, T.; Burdick, J. A.; Cho, D.-W.; Dalton, P. D.; Derby, B.; Forgacs, G.; Li, Q.; Mironov, V. A.; Moroni, L.; Nakamura, M.; Shu, W.; Takeuchi, S.; Vozzi, G.; Woodfield, T. B. F.; Xu, T.; Yoo, J. J.; Malda, J., Biofabrication: reappraising the definition of an evolving field. *Biofabrication* **2016**, *8* (1), 013001.
9. Zhang, L.; Hu, J.; Athanasiou, K. A., The role of tissue engineering in articular cartilage repair and regeneration. *Crit Rev Biomed Eng* **2009**, *37* (1-2), 1-57.
10. Di Luca, A.; Lorenzo-Molero, I.; Mota, C.; Lepedda, A.; Auhl, D.; Van Blitterswijk, C.; Moroni, L., Tuning Cell Differentiation into a 3D Scaffold Presenting a Pore Shape Gradient for Osteochondral Regeneration. *Advanced Healthcare Materials* **2016**, *5* (14), 1753-1763.
11. Izadifar, Z.; Chang, T.; Kulyk, W.; Chen, X.; Eames, B. F., Analyzing Biological Performance of 3D-Printed, Cell-Impregnated Hybrid Constructs for Cartilage Tissue Engineering. *Tissue Engineering Part C: Methods* **2015**, *22* (3), 173-188.
12. Ferris, C. J.; Gilmore, K. G.; Wallace, G. G.; in het Panhuis, M., Biofabrication: an overview of the approaches used for printing of living cells. *Applied Microbiology and Biotechnology* **2013**, *97* (10), 4243-4258.
13. Felson, D. T., Osteoarthritis of the Knee. *New England Journal of Medicine* **2006**, *354* (8), 841-848.
14. Temenoff, J. S.; Mikos, A. G., Review: tissue engineering for regeneration of articular cartilage. *Biomaterials* **2000**, *21* (5), 431-440.
15. Schuurman, W.; Klein, T. J.; Dhert, W. J. A.; van Weeren, P. R.; Hutmacher, D. W.; Malda, J., Cartilage regeneration using zonal chondrocyte subpopulations: a promising approach or an overcomplicated strategy? *Journal of Tissue Engineering and Regenerative Medicine* **2015**, *9* (6), 669-678.
16. Klein, T. J.; Rizzi, S. C.; Reichert, J. C.; Georgi, N.; Malda, J.; Schuurman, W.; Crawford, R. W.; Hutmacher, D. W., Strategies for Zonal Cartilage Repair using Hydrogels. *Macromolecular Bioscience* **2009**, *9* (11), 1049-1058.
17. Hayes, A. J.; Hall, A.; Brown, L.; Tubo, R.; Caterson, B., Macromolecular Organization and *In Vitro* Growth Characteristics of Scaffold-free Neocartilage Grafts. *Journal of Histochemistry & Cytochemistry* **2007**, *55* (8), 853-866.
18. Silverberg, Jesse L.; Barrett, Aliyah R.; Das, M.; Petersen, Poul B.; Bonassar, Lawrence J.; Cohen, I., Structure-Function Relations and Rigidity Percolation in the Shear Properties of Articular Cartilage. *Biophysical Journal* **2014**, *107* (7), 1721-1730.
19. Little, C. J.; Bawolin, N. K.; Chen, X., Mechanical Properties of Natural Cartilage and Tissue-Engineered Constructs. *Tissue Engineering Part B: Reviews* **2011**, *17* (4), 213-227.
20. Benninghoff, A., Form und Bau der Gelenkknorpel in ihren Beziehungen zur Funktion. *Zeitschrift für Zellforschung und Mikroskopische Anatomie* **1925**, *2* (5), 783-862.

21. Moeinzadeh, S.; Pajoum Shariati, S. R.; Jabbari, E., Comparative effect of physicochemical and biomolecular cues on zone-specific chondrogenic differentiation of mesenchymal stem cells. *Biomaterials* **2016**, *92*, 57-70.
22. Woodfield, T. B. F.; Blitterswijk, C. A. V.; Wijn, J. D.; Sims, T. J.; Hollander, A. P.; Riesle, J., Polymer Scaffolds Fabricated with Pore-Size Gradients as a Model for Studying the Zonal Organization within Tissue-Engineered Cartilage Constructs. *Tissue Engineering* **2005**, *11* (9-10), 1297-1311.
23. Nazempour, A.; Quisenberry, C. R.; Van Wie, B. J.; Abu-Lail, N. I., Nanomechanics of Engineered Articular Cartilage: Synergistic Influences of Transforming Growth Factor- β 3 and Oscillating Pressure. *Journal of Nanoscience and Nanotechnology* **2016**, *16* (3), 3136-3145.
24. Gardner, O. F. W.; Fahy, N.; Alini, M.; Stoddart, M. J., Joint mimicking mechanical load activates TGF β 1 in fibrin-poly(ester-urethane) scaffolds seeded with mesenchymal stem cells. *Journal of Tissue Engineering and Regenerative Medicine* **2017**, *11* (9), 2663-2666.
25. Karimi, T.; Barati, D.; Karaman, O.; Moeinzadeh, S.; Jabbari, E., A developmentally inspired combined mechanical and biochemical signaling approach on zonal lineage commitment of mesenchymal stem cells in articular cartilage regeneration. *Integrative Biology* **2014**, *7* (1), 112-127.
26. Camarero-Espinosa, S.; Rothen-Rutishauser, B.; Weder, C.; Foster, E. J., Directed cell growth in multi-zonal scaffolds for cartilage tissue engineering. *Biomaterials* **2016**, *74*, 42-52.
27. Levingstone, T. J.; Matsiko, A.; Dickson, G. R.; O'Brien, F. J.; Gleeson, J. P., A biomimetic multi-layered collagen-based scaffold for osteochondral repair. *Acta Biomaterialia* **2014**, *10* (5), 1996-2004.
28. Warren, P. B.; Huebner, P.; Spang, J. T.; Shirwaiker, R. A.; Fisher, M. B., Engineering 3D-Bioplotting scaffolds to induce aligned extracellular matrix deposition for musculoskeletal soft tissue replacement. *Connective Tissue Research* **2017**, *58* (3-4), 342-354.
29. Baker, B. M.; Mauck, R. L., The effect of nanofiber alignment on the maturation of engineered meniscus constructs. *Biomaterials* **2007**, *28* (11), 1967-1977.
30. Di Luca, A.; Longoni, A.; Criscenti, G.; Mota, C.; van Blitterswijk, C.; Moroni, L., Toward mimicking the bone structure: design of novel hierarchical scaffolds with a tailored radial porosity gradient. *Biofabrication* **2016**, *8* (4), 045007.
31. Schuurman, W.; Harimulyo, E. B.; Gawlitta, D.; Woodfield, T. B. F.; Dhert, W. J. A.; van Weeren, P. R.; Malda, J., Three-dimensional assembly of tissue-engineered cartilage constructs results in cartilaginous tissue formation without retainment of zonal characteristics. *Journal of Tissue Engineering and Regenerative Medicine* **2016**, *10* (4), 315-324.
32. Ren, X.; Wang, F.; Chen, C.; Gong, X.; Yin, L.; Yang, L., Engineering zonal cartilage through bioprinting collagen type II hydrogel constructs with biomimetic chondrocyte density gradient. *BMC Musculoskeletal Disorders* **2016**, *17* (1), 301.
33. Au - Cui, X.; Au - Gao, G.; Au - Yonezawa, T.; Au - Dai, G., Human Cartilage Tissue Fabrication Using Three-dimensional Inkjet Printing Technology. *JoVE* **2014**, (88), e51294.
34. Cui, X.; Breitenkamp, K.; Finn, M. G.; Lotz, M.; D'Lima, D. D., Direct Human Cartilage Repair Using Three-Dimensional Bioprinting Technology. *Tissue Engineering Part A* **2012**, *18* (11-12), 1304-1312.
35. Sharma, B.; Williams, C. G.; Kim, T. K.; Sun, D.; Malik, A.; Khan, M.; Leong, K.; Elisseeff, J. H., Designing Zonal Organization into Tissue-Engineered Cartilage. *Tissue Engineering* **2007**, *13* (2), 405-414.
36. Grad, S.; Eglin, D.; Alini, M.; Stoddart, M. J., Physical Stimulation of Chondrogenic Cells *In Vitro*: A Review. *Clinical Orthopaedics and Related Research* **2011**, *469* (10), 2764-2772.
37. Darling, E. M.; Athanasiou, K. A., Growth factor impact on articular cartilage subpopulations. *Cell and Tissue Research* **2005**, *322* (3), 463-473.
38. Kim, T. K.; Sharma, B.; Williams, C. G.; Ruffner, M. A.; Malik, A.; McFarland, E. G.; Elisseeff, J. H., Experimental Model for Cartilage Tissue Engineering to Regenerate the Zonal Organization of Articular Cartilage. *Osteoarthritis and Cartilage* **2003**, *11* (9), 653-664.
39. Boushell, M. K.; Hung, C. T.; Hunziker, E. B.; Strauss, E. J.; Lu, H. H., Current strategies for integrative cartilage repair. *Connective Tissue Research* **2017**, *58* (5), 393-406.
40. Guo, T.; Lembong, J.; Zhang, L. G.; Fisher, J. P., Three-Dimensional Printing Articular Cartilage: Recapitulating the Complexity of Native Tissue. *Tissue Engineering Part B: Reviews* **2016**, *23* (3), 225-236.

41. Park, J. Y.; Shim, J.-H.; Choi, S.-A.; Jang, J.; Kim, M.; Lee, S. H.; Cho, D.-W., 3D printing technology to control BMP-2 and VEGF delivery spatially and temporally to promote large-volume bone regeneration. *Journal of Materials Chemistry B* **2015**, *3* (27), 5415-5425.
42. Tarafder, S.; Koch, A.; Jun, Y.; Chou, C.; Awadallah, M. R.; Lee, C. H., Micro-precise spatiotemporal delivery system embedded in 3D printing for complex tissue regeneration. *Biofabrication* **2016**, *8* (2), 025003.
43. Hung, C. T.; Mow, V. C., Biomechanics of Articular Cartilage. In *Basic Biomechanics of the Musculoskeletal System*, 4th ed.; Nordin, M.; Frankel, V. H., Eds. Lippincott Williams & Wilkins: Philadelphia, 2012; pp 60-101.
44. JM, M., Biomechanics of cartilage. In *Kinesiology The Mechanics and Pathomechanics of Human Movement*, 2nd ed.; Oatis, C. A., Ed. Lippincott Williams & Wilkins, a Wolter Kluwer Business: 2013; pp 69-83.
45. Jungst, T.; Smolan, W.; Schacht, K.; Scheibel, T.; Groll, J., Strategies and Molecular Design Criteria for 3D Printable Hydrogels. *Chemical Reviews* **2016**, *116* (3), 1496-1539.
46. Melchels, F. P. W.; Dhert, W. J. A.; Hutmacher, D. W.; Malda, J., Development and characterisation of a new bioink for additive tissue manufacturing. *Journal of Materials Chemistry B* **2014**, *2* (16), 2282-2289.
47. Kesti, M.; Müller, M.; Becher, J.; Schnabelrauch, M.; D'Este, M.; Eglin, D.; Zenobi-Wong, M., A versatile bioink for three-dimensional printing of cellular scaffolds based on thermally and photo-triggered tandem gelation. *Acta Biomaterialia* **2015**, *11*, 162-172.
48. Mouser, V. H. M.; Abbadessa, A.; Levato, R.; Hennink, W. E.; Vermonden, T.; Gawlitta, D.; Malda, J., Development of a thermosensitive HAMA-containing bio-ink for the fabrication of composite cartilage repair constructs. *Biofabrication* **2017**, *9* (1), 015026.
49. Rhee, S.; Puetzer, J. L.; Mason, B. N.; Reinhart-King, C. A.; Bonassar, L. J., 3D Bioprinting of Spatially Heterogeneous Collagen Constructs for Cartilage Tissue Engineering. *ACS Biomaterials Science & Engineering* **2016**, *2* (10), 1800-1805.
50. Hölzl, K.; Lin, S.; Tytgat, L.; Van Vlierbergh, S.; Gu, L.; Ovsianikov, A., Bioink properties before, during and after 3D bioprinting. *Biofabrication* **2016**, *8* (3), 032002.
51. Boere, K. W. M.; Blokzijl, M. M.; Visser, J.; Linszen, J. E. A.; Malda, J.; Hennink, W. E.; Vermonden, T., Biofabrication of reinforced 3D-scaffolds using two-component hydrogels. *Journal of Materials Chemistry B* **2015**, *3* (46), 9067-9078.
52. Kundu, J.; Shim, J.-H.; Jang, J.; Kim, S.-W.; Cho, D.-W., An additive manufacturing-based PCL-alginate-chondrocyte bioprinted scaffold for cartilage tissue engineering. *Journal of Tissue Engineering and Regenerative Medicine* **2015**, *9* (11), 1286-1297.
53. Melchels, F. P. W.; Blokzijl, M. M.; Levato, R.; Peiffer, Q. C.; Ruijter, M. d.; Hennink, W. E.; Vermonden, T.; Malda, J., Hydrogel-based reinforcement of 3D bioprinted constructs. *Biofabrication* **2016**, *8* (3), 035004.
54. Bakarich, S. E.; Gorkin, R.; in het Panhuis, M.; Spinks, G. M., Three-Dimensional Printing Fiber Reinforced Hydrogel Composites. *ACS Applied Materials & Interfaces* **2014**, *6* (18), 15998-16006.
55. Coburn, J.; Gibson, M.; Bandalini, P. A.; Laird, C.; Mao, H.-Q.; Moroni, L.; Seliktar, D.; Elisseeff, J., Biomimetics of the Extracellular Matrix: An Integrated Three-Dimensional Fiber-Hydrogel Composite for Cartilage Tissue Engineering. *Smart structures and systems* **2011**, *7* (3), 213-222.
56. Moutos, F. T.; Guilak, F., Composite scaffolds for cartilage tissue engineering. *Biorheology* **2008**, *45*, 501-512.
57. Xu, T.; Binder, K. W.; Albanna, M. Z.; Dice, D.; Zhao, W.; Yoo, J. J.; Atala, A., Hybrid printing of mechanically and biologically improved constructs for cartilage tissue engineering applications. *Biofabrication* **2012**, *5* (1), 015001.
58. Shanjani, Y.; Pan, C. C.; Elomaa, L.; Yang, Y., A novel bioprinting method and system for forming hybrid tissue engineering constructs. *Biofabrication* **2015**, *7* (4), 045008.
59. Schuurman, W.; Khristov, V.; Pot, M. W.; van Weeren, P. R.; Dhert, W. J. A.; Malda, J., Bioprinting of hybrid tissue constructs with tailorable mechanical properties. *Biofabrication* **2011**, *3* (2), 021001.
60. Lee, K.; Seo, C.-R.; Ku, J.-M.; Lee, H.; Yoon, H.; Lee, J.; Chun, W.; Park, K. W.; Kim, G., 3D-printed alginate/phenamil composite scaffolds constituted with microsized core-shell struts for hard tissue regeneration. *RSC Advances* **2015**, *5* (37), 29335-29345.

61. Kalsoom, U.; Nesterenko, P. N.; Paull, B., Recent developments in 3D printable composite materials. *RSC Advances* **2016**, *6* (65), 60355-60371.
62. Kang, H.-W.; Lee, S. J.; Ko, I. K.; Kengla, C.; Yoo, J. J.; Atala, A., A 3D bioprinting system to produce human-scale tissue constructs with structural integrity. *Nature Biotechnology* **2016**, *34* (3), 312-319.
63. Jakus, A. E.; Shah, R. N., Multi and mixed 3D-printing of graphene-hydroxyapatite hybrid materials for complex tissue engineering. *Journal of Biomedical Materials Research Part A* **2017**, *105* (1), 274-283.
64. Visser, J.; Melchels, F. P. W.; Jeon, J. E.; van Bussel, E. M.; Kimpton, L. S.; Byrne, H. M.; Dhert, W. J. A.; Dalton, P. D.; Hutmacher, D. W.; Malda, J., Reinforcement of hydrogels using three-dimensionally printed microfibrils. *Nature Communications* **2015**, *6* (1), 6933.
65. Lee, H.; Ahn, S.; Bonassar, L. J.; Kim, G., Cell(MC3T3-E1)-Printed Poly(ϵ -caprolactone)/Alginate Hybrid Scaffolds for Tissue Regeneration. *Macromolecular Rapid Communications* **2013**, *34* (2), 142-149.
66. Moroni, L.; de Wijn, J. R.; van Blitterswijk, C. A., 3D fiber-deposited scaffolds for tissue engineering: Influence of pores geometry and architecture on dynamic mechanical properties. *Biomaterials* **2006**, *27* (7), 974-985.
67. Wu, C.; Luo, Y.; Cuniberti, G.; Xiao, Y.; Gelinsky, M., Three-dimensional printing of hierarchical and tough mesoporous bioactive glass scaffolds with a controllable pore architecture, excellent mechanical strength and mineralization ability. *Acta Biomaterialia* **2011**, *7* (6), 2644-2650.
68. Sobral, J. M.; Caridade, S. G.; Sousa, R. A.; Mano, J. F.; Reis, R. L., Three-dimensional plotted scaffolds with controlled pore size gradients: Effect of scaffold geometry on mechanical performance and cell seeding efficiency. *Acta Biomaterialia* **2011**, *7* (3), 1009-1018.
69. Domingos, M.; Intranuovo, F.; Russo, T.; Santis, R. D.; Gloria, A.; Ambrosio, L.; Ciurana, J.; Bartolo, P., The first systematic analysis of 3D rapid prototyped poly(ϵ -caprolactone) scaffolds manufactured through BioCell printing: the effect of pore size and geometry on compressive mechanical behaviour and *in vitro* hMSC viability. *Biofabrication* **2013**, *5* (4), 045004.
70. Olubamiji, A. D.; Izadifar, Z.; Si, J. L.; Cooper, D. M. L.; Eames, B. F.; Chen, D. X. B., Modulating mechanical behaviour of 3D-printed cartilage-mimetic PCL scaffolds: influence of molecular weight and pore geometry. *Biofabrication* **2016**, *8* (2), 025020.
71. Bowland, P.; Ingham, E.; Jennings, L.; Fisher, J., Review of the biomechanics and biotribology of osteochondral grafts used for surgical interventions in the knee. *Proceedings of the Institution of Mechanical Engineers, Part H: Journal of Engineering in Medicine* **2015**, *229* (12), 879-888.
72. Woodfield, T. B. F.; Guggenheim, M.; Von Rechenberg, B.; Riesle, J.; Van Blitterswijk, C. A.; Wedler, V., Rapid prototyping of anatomically shaped, tissue-engineered implants for restoring congruent articulating surfaces in small joints. *Cell Proliferation* **2009**, *42* (4), 485-497.
73. Yang, P. J.; Temenoff, J. S., Engineering orthopedic tissue interfaces. *Tissue Engineering, Part B: Reviews* **2009**, *15*, 127+.
74. Oegema, T. R.; Carpenter, R. J.; Hofmeister, F.; Thompson, R. C., The interaction of the zone of calcified cartilage and subchondral bone in osteoarthritis. *Microscopy Research and Technique* **1997**, *37* (4), 324-332.
75. Lopa, S.; Madry, H., Bioinspired Scaffolds for Osteochondral Regeneration. *Tissue Engineering Part A* **2014**, *20* (15-16), 2052-2076.
76. Mollenhauer, J. A.; Burkhardt, C.; Nisch, W.; Bossert, J.; Hempel, H. J.; Jandt, K. D.; Muehleman, C., Definition of the Joint Cartilage-Bone Interface by Topological Scanning Technologies: Considerations for Optimized Material Interfaces in Implant Technology. *Advanced Engineering Materials* **2007**, *9* (12), 1097-1103.
77. Liu, Y.; Li, X.; Qu, X.; Zhu, L.; He, J.; Zhao, Q.; Wu, W.; Li, D., The fabrication and cell culture of three-dimensional rolled scaffolds with complex micro-architectures. *Biofabrication* **2012**, *4* (1), 015004.
78. Zhang, Y.; Wang, F.; Tan, H.; Chen, G.; Guo, L.; Yang, L., Analysis of the mineral composition of the human calcified cartilage zone. *International journal of medical sciences* **2012**, *9* (5), 353-360.
79. DeLise, A. M.; Fischer, L.; Tuan, R. S., Cellular interactions and signaling in cartilage development. *Osteoarthritis and Cartilage* **2000**, *8* (5), 309-334.

80. Yuan, X. L.; Meng, H. Y.; Wang, Y. C.; Peng, J.; Guo, Q. Y.; Wang, A. Y.; Lu, S. B., Bone–cartilage interface crosstalk in osteoarthritis: potential pathways and future therapeutic strategies. *Osteoarthritis and Cartilage* **2014**, *22* (8), 1077-1089.
81. Findlay, D. M.; Kuliwaba, J. S., Bone–cartilage crosstalk: a conversation for understanding osteoarthritis. *Bone Research* **2016**, *4* (1), 16028.
82. St-Pierre, J.-P.; Gan, L.; Wang, J.; Pilliar, R. M.; Grynblas, M. D.; Kandel, R. A., The incorporation of a zone of calcified cartilage improves the interfacial shear strength between *in vitro*-formed cartilage and the underlying substrate. *Acta Biomaterialia* **2012**, *8* (4), 1603-1615.
83. Hunziker, E. B.; Driesang, I. M. K.; Saager, C., Structural Barrier Principle for Growth Factor-Based Articular Cartilage Repair. *Clinical Orthopaedics and Related Research*® **2001**, 391.
84. Bian, W.; Lian, Q.; Li, D.; Wang, J.; Zhang, W.; Jin, Z.; Qiu, Y., Morphological characteristics of cartilage-bone transitional structures in the human knee joint and CAD design of an osteochondral scaffold. *BioMedical Engineering OnLine* **2016**, *15* (1), 82.
85. Sherwood, J. K.; Riley, S. L.; Palazzolo, R.; Brown, S. C.; Monkhouse, D. C.; Coates, M.; Griffith, L. G.; Landeen, L. K.; Ratcliffe, A., A three-dimensional osteochondral composite scaffold for articular cartilage repair. *Biomaterials* **2002**, *23* (24), 4739-4751.
86. Castro, N. J.; O'Brien, J.; Zhang, L. G., Integrating biologically inspired nanomaterials and table-top stereolithography for 3D printed biomimetic osteochondral scaffolds. *Nanoscale* **2015**, *7* (33), 14010-14022.
87. Singh, M.; Morris, C. P.; Ellis, R. J.; Detamore, M. S.; Berkland, C., Microsphere-Based Seamless Scaffolds Containing Macroscopic Gradients of Encapsulated Factors for Tissue Engineering. *Tissue Engineering Part C: Methods* **2008**, *14* (4), 299-309.
88. Dormer, N. H.; Singh, M.; Wang, L.; Berkland, C. J.; Detamore, M. S., Osteochondral Interface Tissue Engineering Using Macroscopic Gradients of Bioactive Signals. *Annals of Biomedical Engineering* **2010**, *38* (6), 2167-2182.
89. Knothe Tate, M. L.; Detamore, M.; Capadona, J. R.; Woolley, A.; Knothe, U., Engineering and commercialization of human-device interfaces, from bone to brain. *Biomaterials* **2016**, *95*, 35-46.
90. Lin, K.-F.; He, S.; Song, Y.; Wang, C.-M.; Gao, Y.; Li, J.-Q.; Tang, P.; Wang, Z.; Bi, L.; Pei, G.-X., Low-Temperature Additive Manufacturing of Biomimic Three-Dimensional Hydroxyapatite/Collagen Scaffolds for Bone Regeneration. *ACS Applied Materials & Interfaces* **2016**, *8* (11), 6905-6916.
91. Fedorovich, N. E.; Schuurman, W.; Wijnberg, H. M.; Prins, H.-J.; van Weeren, P. R.; Malda, J.; Alblas, J.; Dhert, W. J. A., Biofabrication of Osteochondral Tissue Equivalents by Printing Topologically Defined, Cell-Laden Hydrogel Scaffolds. *Tissue Engineering Part C: Methods* **2011**, *18* (1), 33-44.
92. Levato, R.; Visser, J.; Planell, J. A.; Engel, E.; Malda, J.; Mateos-Timoneda, M. A., Biofabrication of tissue constructs by 3D bioprinting of cell-laden microcarriers. *Biofabrication* **2014**, *6* (3), 035020.
93. Jakus, A. E.; Rutz, A. L.; Jordan, S. W.; Kannan, A.; Mitchell, S. M.; Yun, C.; Koube, K. D.; Yoo, S. C.; Whiteley, H. E.; Richter, C.-P.; Galiano, R. D.; Hsu, W. K.; Stock, S. R.; Hsu, E. L.; Shah, R. N., Hyperelastic “bone”: A highly versatile, growth factor–free, osteoregenerative, scalable, and surgically friendly biomaterial. *Science Translational Medicine* **2016**, *8* (358), 358ra127.
94. Erisken, C.; Kalyon, D. M.; Wang, H., Functionally graded electrospun polycaprolactone and β -tricalcium phosphate nanocomposites for tissue engineering applications. *Biomaterials* **2008**, *29* (30), 4065-4073.
95. Erisken, C.; Kalyon, D. M.; Wang, H.; Örnek-Ballanco, C.; Xu, J., Osteochondral Tissue Formation Through Adipose-Derived Stromal Cell Differentiation on Biomimetic Polycaprolactone Nanofibrous Scaffolds with Graded Insulin and Beta-Glycerophosphate Concentrations. *Tissue Engineering Part A* **2010**, *17* (9-10), 1239-1252.
96. Yuk, H.; Zhang, T.; Lin, S.; Parada, G. A.; Zhao, X., Tough bonding of hydrogels to diverse non-porous surfaces. *Nature Materials* **2016**, *15* (2), 190-196.
97. Shim, J.-H.; Jang, K.-M.; Hahn, S. K.; Park, J. Y.; Jung, H.; Oh, K.; Park, K. M.; Yeom, J.; Park, S. H.; Kim, S. W.; Wang, J. H.; Kim, K.; Cho, D.-W., Three-dimensional bioprinting of multilayered constructs containing human mesenchymal stromal cells for osteochondral tissue regeneration in the rabbit knee joint. *Biofabrication* **2016**, *8* (1), 014102.

98. De Santis, R.; D'Amora, U.; Russo, T.; Ronca, A.; Gloria, A.; Ambrosio, L., 3D fibre deposition and stereolithography techniques for the design of multifunctional nanocomposite magnetic scaffolds. *Journal of Materials Science: Materials in Medicine* **2015**, *26* (10), 250.
99. Holmes, B.; Zhu, W.; Li, J.; Lee, J. D.; Zhang, L. G., Development of Novel Three-Dimensional Printed Scaffolds for Osteochondral Regeneration. *Tissue Engineering Part A* **2014**, *21* (1-2), 403-415.
100. Ainola, M.; Tomaszewski, W.; Ostrowska, B.; Wesolowska, E.; Wagner, H. D.; Swieszkowski, W.; Sillat, T.; Peltola, E.; Konttinen, Y. T., A bioactive hybrid three-dimensional tissue-engineering construct for cartilage repair. *Journal of Biomaterials Applications* **2015**, *30* (6), 873-885.
101. Bian, W.; Li, D.; Lian, Q.; Li, X.; Zhang, W.; Wang, K.; Jin, Z., Fabrication of a bio-inspired beta-Tricalcium phosphate/collagen scaffold based on ceramic stereolithography and gel casting for osteochondral tissue engineering. *Rapid Prototyping Journal* **2012**, *18* (1), 68-80.
102. Nowicki, M. A.; Castro, N. J.; Plesniak, M. W.; Zhang, L. G., 3D printing of novel osteochondral scaffolds with graded microstructure. *Nanotechnology* **2016**, *27* (41), 414001.
103. Reed, S.; Lau, G.; Delattre, B.; Lopez, D. D.; Tomsia, A. P.; Wu, B. M., Macro- and micro-designed chitosan-alginate scaffold architecture by three-dimensional printing and directional freezing. *Biofabrication* **2016**, *8* (1), 015003.
104. Zhang, S.; Chen, L.; Jiang, Y.; Cai, Y.; Xu, G.; Tong, T.; Zhang, W.; Wang, L.; Ji, J.; Shi, P.; Ouyang, H. W., Bi-layer collagen/microporous electrospun nanofiber scaffold improves the osteochondral regeneration. *Acta Biomaterialia* **2013**, *9* (7), 7236-7247.
105. Mrosek, E. H.; Schagemann, J. C.; Chung, H.-W.; Fitzsimmons, J. S.; Yaszemski, M. J.; Mardones, R. M.; O'Driscoll, S. W.; Reinholz, G. G., Porous tantalum and poly-ε-caprolactone biocomposites for osteochondral defect repair: Preliminary studies in rabbits. *Journal of Orthopaedic Research* **2010**, *28* (2), 141-148.
106. Vindas Bolaños, R. A.; Cokelaere, S. M.; Estrada McDermott, J. M.; Benders, K. E. M.; Gbureck, U.; Plomp, S. G. M.; Weinans, H.; Groll, J.; van Weeren, P. R.; Malda, J., The use of a cartilage decellularized matrix scaffold for the repair of osteochondral defects: the importance of long-term studies in a large animal model. *Osteoarthritis and Cartilage* **2017**, *25* (3), 413-420.
107. Shao, X.; Goh, J. C. H.; Huttmacher, D. W.; Lee, E. H.; Zigang, G., Repair of Large Articular Osteochondral Defects Using Hybrid Scaffolds and Bone Marrow-Derived Mesenchymal Stem Cells in a Rabbit Model. *Tissue Engineering* **2006**, *12* (6), 1539-1551.
108. Martínez Ávila, H.; Schwarz, S.; Rotter, N.; Gatenholm, P., 3D bioprinting of human chondrocyte-laden nanocellulose hydrogels for patient-specific auricular cartilage regeneration. *Bioprinting* **2016**, *1-2*, 22-35.
109. Otto, I. A.; Melchels, F. P. W.; Zhao, X.; Randolph, M. A.; Kon, M.; Breugem, C. C.; Malda, J., Auricular reconstruction using biofabrication-based tissue engineering strategies. *Biofabrication* **2015**, *7* (3), 032001.
110. Farahani, R. D.; Chizari, K.; Therriault, D., Three-dimensional printing of freeform helical microstructures: a review. *Nanoscale* **2014**, *6* (18), 10470-10485.
111. Visser, J.; Peters, B.; Burger, T. J.; Boomstra, J.; Dhert, W. J. A.; Melchels, F. P. W.; Malda, J., Biofabrication of multi-material anatomically shaped tissue constructs. *Biofabrication* **2013**, *5* (3), 035007.
112. Hinton, T. J.; Jallerat, Q.; Palchesko, R. N.; Park, J. H.; Grodzicki, M. S.; Shue, H.-J.; Ramadan, M. H.; Hudson, A. R.; Feinberg, A. W., Three-dimensional printing of complex biological structures by freeform reversible embedding of suspended hydrogels. *Sci Adv* **2015**, *1* (9), e1500758-e1500758.
113. Hockaday, L. A.; Kang, K. H.; Colangelo, N. W.; Cheung, P. Y. C.; Duan, B.; Malone, E.; Wu, J.; Girardi, L. N.; Bonassar, L. J.; Lipson, H.; Chu, C. C.; Butcher, J. T., Rapid 3D printing of anatomically accurate and mechanically heterogeneous aortic valve hydrogel scaffolds. *Biofabrication* **2012**, *4* (3), 035005.
114. Moutos, F. T.; Glass, K. A.; Compton, S. A.; Ross, A. K.; Gersbach, C. A.; Guilak, F.; Estes, B. T., Anatomically shaped tissue-engineered cartilage with tunable and inducible anticytokine delivery for biological joint resurfacing. *Proceedings of the National Academy of Sciences* **2016**, *113* (31), E4513.
115. Lee, C. H.; Cook, J. L.; Mendelson, A.; Moiola, E. K.; Yao, H.; Mao, J. J., Regeneration of the articular surface of the rabbit synovial joint by cell homing: a proof of concept study. *The Lancet* **2010**, *376* (9739), 440-448.
116. Hollister, S. J., Scaffold engineering: a bridge to where? *Biofabrication* **2009**, *1* (1), 012001.

117. Meslin, E. M.; Blasimme, A.; Cambon-Thomsen, A., Mapping the translational science policy 'valley of death'. *Clinical and Translational Medicine* **2013**, *2* (1), 14.
118. McCoy, R. J.; O'Brien, F. J., Influence of Shear Stress in Perfusion Bioreactor Cultures for the Development of Three-Dimensional Bone Tissue Constructs: A Review. *Tissue Engineering Part B: Reviews* **2010**, *16* (6), 587-601.
119. Barabaschi, G. D. G.; Manoharan, V.; Li, Q.; Bertassoni, L. E., Engineering Pre-vascularized Scaffolds for Bone Regeneration. In *Engineering Mineralized and Load Bearing Tissues*, Bertassoni, L. E.; Coelho, P. G., Eds. Springer International Publishing: Cham, 2015; pp 79-94.
120. Miller, J. S.; Stevens, K. R.; Yang, M. T.; Baker, B. M.; Nguyen, D.-H. T.; Cohen, D. M.; Toro, E.; Chen, A. A.; Galie, P. A.; Yu, X.; Chaturvedi, R.; Bhatia, S. N.; Chen, C. S., Rapid casting of patterned vascular networks for perfusable engineered three-dimensional tissues. *Nature Materials* **2012**, *11* (9), 768-774.
121. Homan, K. A.; Kolesky, D. B.; Skylar-Scott, M. A.; Herrmann, J.; Obuobi, H.; Moisan, A.; Lewis, J. A., Bioprinting of 3D Convulated Renal Proximal Tubules on Perfusable Chips. *Scientific Reports* **2016**, *6* (1), 34845.
122. Kolesky, D. B.; Homan, K. A.; Skylar-Scott, M. A.; Lewis, J. A., Three-dimensional bioprinting of thick vascularized tissues. *Proceedings of the National Academy of Sciences* **2016**, *113* (12), 3179.
123. van der Meer, A. D.; van den Berg, A., Organs-on-chips: breaking the *in vitro* impasse. *Integrative Biology* **2012**, *4* (5), 461-470.
124. Huh, D.; Leslie, D. C.; Matthews, B. D.; Fraser, J. P.; Jurek, S.; Hamilton, G. A.; Thorneloe, K. S.; McAlexander, M. A.; Ingber, D. E., A Human Disease Model of Drug Toxicity-Induced Pulmonary Edema in a Lung-on-a-Chip Microdevice. *Science Translational Medicine* **2012**, *4* (159), 159ra147.
125. Kim, H. J.; Li, H.; Collins, J. J.; Ingber, D. E., Contributions of microbiome and mechanical deformation to intestinal bacterial overgrowth and inflammation in a human gut-on-a-chip. *Proceedings of the National Academy of Sciences* **2016**, *113* (1), E7.
126. Marsano, A.; Conficconi, C.; Lemme, M.; Occhetta, P.; Gaudiello, E.; Votta, E.; Cerino, G.; Redaelli, A.; Rasponi, M., Beating heart on a chip: a novel microfluidic platform to generate functional 3D cardiac microtissues. *Lab on a Chip* **2016**, *16* (3), 599-610.
127. van der Helm, M. W.; van der Meer, A. D.; Eijkel, J. C. T.; van den Berg, A.; Segerink, L. I., Microfluidic organ-on-chip technology for blood-brain barrier research. *Tissue Barriers* **2016**, *4* (1), e1142493-e1142493.
128. Williamson, A.; Singh, S.; Fernekorn, U.; Schober, A., The future of the patient-specific Body-on-a-chip. *Lab on a Chip* **2013**, *13* (18), 3471-3480.
129. Alexander, P. G.; Gottardi, R.; Lin, H.; Lozito, T. P.; Tuan, R. S., Three-dimensional osteogenic and chondrogenic systems to model osteochondral physiology and degenerative joint diseases. *Experimental Biology and Medicine* **2014**, *239* (9), 1080-1095.
130. Shi, X.; Zhou, J.; Zhao, Y.; Li, L.; Wu, H., Gradient-Regulated Hydrogel for Interface Tissue Engineering: Steering Simultaneous Osteo/Chondrogenesis of Stem Cells on a Chip. *Advanced Healthcare Materials* **2013**, *2* (6), 846-853.
131. Benam, K. H.; Novak, R.; Nawroth, J.; Hirano-Kobayashi, M.; Ferrante, T. C.; Choe, Y.; Prantil-Baun, R.; Weaver, J. C.; Bahinski, A.; Parker, K. K.; Ingber, D. E., Matched-Comparative Modeling of Normal and Diseased Human Airway Responses Using a Microengineered Breathing Lung Chip. *Cell Systems* **2016**, *3* (5), 456-466.e4.

CHAPTER 3

Combining multi-scale 3D printing technologies to engineer reinforced hydrogel-ceramic interfaces

Paweena Diloksumpan¹, Mylène de Ruijter², Miguel Castilho^{2,3,4},
Uwe Gbureck⁵, Tina Vermonden⁶, Paul René van Weeren¹,
Jos Malda^{1,2,3}, and Riccardo Levato^{1,2,3}

Published in *Biofabrication* (2020),
12(2): 025014,
DOI 10.1088/1758-5090/ab69d9

¹ Department of Clinical Sciences, Faculty of Veterinary Medicine, Utrecht University, The Netherlands

² Department of Orthopaedics, University Medical Center Utrecht, Utrecht University, Utrecht, The Netherlands

³ Regenerative Medicine Center, Utrecht, Utrecht University, Utrecht, The Netherlands

⁴ Department of Biomedical Engineering, Faculty of Engineering, Technical University of Eindhoven, The Netherlands

⁵ Department for Functional Materials in Medicine and Dentistry, University Hospital of Würzburg, Würzburg, Germany

⁶ Department of Pharmaceutics, Utrecht Institute for Pharmaceutical Sciences (UIPS), Faculty of Science, Utrecht University, The Netherlands

ABSTRACT

Multi-material 3D printing technologies that resolve features at different lengths down to the microscale open new avenues for regenerative medicine, particularly in the engineering of tissue interfaces. Herein, extrusion printing of a bone-biomimetic ceramic ink and melt electrowriting (MEW) of spatially organized polymeric microfibres are integrated for the biofabrication of an osteochondral plug, with a mechanically reinforced bone-to-cartilage interface. A printable physiological temperature-setting bioceramic, based on α -tricalcium phosphate, nanohydroxyapatite and a custom-synthesized biodegradable and crosslinkable poloxamer, was developed as bone support. The mild setting reaction of the bone ink enabled us to print directly within melt electrowritten polycaprolactone meshes, preserving their micro-architecture. Ceramic-integrated MEW meshes protruded into the cartilage region of the composite plug and were embedded with mechanically soft gelatin-based hydrogels, laden with articular cartilage chondroprogenitor cells. Such interlocking design enhanced the hydrogel-to-ceramic adhesion strength > 6.5 -fold, compared with non-interlocking fibre architectures, enabling structural stability during handling and surgical implantation in osteochondral defects *ex vivo*. Furthermore, the MEW meshes endowed the chondral compartment with compressive properties approaching those of native cartilage (20-fold reinforcement versus pristine hydrogel). The osteal and chondral compartment supported osteogenesis and cartilage matrix deposition *in vitro*, and the neo-synthesized cartilage matrix further contributed to the mechanical reinforcement at the ceramic-hydrogel interface. This multi-material, multi-scale 3Dprinting approach provides a promising strategy for engineering advanced composite constructs for the regeneration of musculoskeletal and connective tissue interfaces.

Keywords: biofabrication, melt electrowriting, bioinspired interface, bone and cartilage tissue engineering, microfibres, ceramics

INTRODUCTION

Establishing a secure integration between mechanically dissimilar materials is a major challenge in engineering interfaces between biological tissues. In musculoskeletal tissues, hard, mineralized materials are naturally integrated with soft tissues, for example, the cartilage-to-bone boundary. This interface plays a pivotal role in the regulation of inter-cellular communication, through the diffusion of bioactive molecules between the articular surface and the subchondral bone¹. Such filter function, together with the transmission of mechanical loads^{2,3}, contributes to maintaining homeostasis and hence functionality of the articulating joint. Traumatic injuries to the articular cartilage and degenerative processes can lead to osteoarthritis, which is a prevalent and debilitating condition in our aging population. This disorder may result in the disruption of the integrity of the subchondral bone, cartilage and their interface, urging the development of approaches that can functionally restore the affected tissue. Thus far, principally, the use of soft materials has been investigated for cartilage restoration, in particular those based on biocompatible hydrogels that can provide a highly hydrated environment aiding the encapsulation and differentiation of cells. However, these materials are difficult to integrate with stiff materials that constitute successful supports as regenerative scaffolds or prosthetic replacements for mineralized tissues, such as bone⁴. Nevertheless, specific classes of double-network hydrogel formulations have been designed to feature outstanding toughness and adhesion strength to ceramics and metals⁵. However, these gels are very stiff or composed of dense polymer networks that have not been proven as suitable to support homogenous neo-tissue matrix deposition from encapsulated cells^{6,7}. Several strategies for integrating soft hydrogels with stiff bone substitute have been developed^{4,8-11}, including binding with adhesive glues¹², coupling through covalent chemical bonds¹³, or forming compositional gradients using the same based material via casting¹⁴. A major drawback of these strategies is that the majority offer little to no control over the architecture of the engineered interface.

The recent advances in 3D printing and biofabrication technologies open new avenues for the creation of multi-material architectures that can mimic or replace biological interfaces. Medical imaging, such as computed tomography, can be used as blueprints to replicate anatomical features of the native osteochondral boundary¹⁵. The layer-by-layer fabrication approach, typical of additive manufacturing techniques, enables us to freely design different pore geometries across the depth of the bone and cartilage compartments¹⁶, as well as to introduce gradients of bioactive cues and inorganic particles¹⁷⁻²². Additionally, even low-viscosity hydrogels with low ability to retain their shape post-printing have been precisely deposited into biphasic structures reminiscent of osteochondral units, for instance with the aid of sacrificial supporting baths²³, extending the array of cell-friendly materials usable in bone and cartilage bioprinting. Importantly, cell-laden hydrogels can be mechanically reinforced when printed in coordination with thermoplastic polymers²⁴⁻²⁸ and even ceramics that set under cell-friendly conditions²⁹.

However, such co-printing methods result in the shielding of the soft hydrogels from mechanical loads and do not necessarily improve their binding ability to an osteal anchor. Moreover, most of these methods suffer from limited spatial resolution (typically $\sim 100\ \mu\text{m}$) and thus cannot mimic micro- and submicron- scale features of the osteochondral interfaces. A new solution for the generation of fully biofabricated osteochondral boundaries can come from combining printing technologies able to resolve details at different length-scales³⁰. MEW has recently emerged as a high-resolution 3D printing method to create highly-ordered, thermoplastic microfibre meshes³¹ in the micron and sub-micron range³², allowing for multimodal scaffold fabrication³³. These MEW meshes, when infused with cell-friendly hydrogels, create composite materials with improved shear properties and outstanding compressive properties approaching those of native cartilage³⁴. Despite this potential, the development of material-based strategies to create bioinspired, reinforced interfaces using such microfibre deposition methods has not been reported yet.

Biomaterials like α -tricalcium phosphate (α -TCP) have been used as injectable bone regenerative materials due to their biocompatibility and osteoconductivity^{35, 36}. The self-setting capacity of α -TCP through hydrolysis also results in products that have a structure comparable with the inorganic components of native bone³⁷. These properties allow us to process α -TCP for making customized scaffolds, for instance as recently shown for developing printable bone cements³⁸. However, there is a limitation to using α -TCP due to its high solubility which leads to fast degradation. Incorporation of other inorganic phases, for instance, nanohydroxyapatite, FDA approved in several biomedical products^{39, 40}, has been well-described to improve the osteogenic potential of the ceramic, both in terms of osteoinduction and osteoconduction⁴¹. Given these promising biological properties and the low-temperature setting reactivity, this system offers a unique opportunity for direct printing with low melting polymers, as explored in this work.

In this present study, we introduce a novel approach that combines different 3D printing technologies, with the aim to directly form a secure integration at the interface between two mechanically distinct materials, particularly between cell-laden hydrogels and biologically relevant ceramics and polymers. To achieve that, a bioceramic ink that sets at physiological conditions, was developed based on a calcium phosphate (CaP) formulation that mimics the mineral phase of bone and shaped as subchondral bone substitute using a pneumatic-driven extrusion-based printer. Next, microfibrinous polymeric meshes obtained by MEW were directly anchored into the ceramic ink and were embedded in a cell-laden soft hydrogel based on methacryloyl-modified gelatin (gelMA), to represent the cartilage component. Several microfibre structures were studied in their capacity as the interlocking agent to enhance the interfacial adhesion of the hydrogel-ceramic interface and as mechanical reinforcement to enhance the compressive properties of the hydrogel. This technology has been used to create fully biofabricated osteochondral plugs for the treatment of bone and cartilage defects.

MATERIALS AND METHODS

Preparation of the calcium phosphate-based paste

The printable calcium phosphate (pCaP)-based ink, consisting of a particle and a liquid phase, was prepared in-house (**Figure 1**). For 1 g of printable phase, 660 mg of milled alpha-tricalcium phosphate microparticles (α -TCP, average size 3.83 μm , Cambioceramics, Leiden, the Netherlands) were mixed with 40 mg of nanohydroxyapatite (nano-HA, particle size <200 nm, $\text{Ca}_5(\text{OH})(\text{PO}_4)_3$, Sigma Aldrich). The liquid phase was composed of a 40% $\text{w}\cdot\text{v}^{-1}$ hydrogel precursor solution, consisting of either unmodified poloxamer (Pluronic® F-127, Sigma-Aldrich) or a custom-synthesized hydrolysable, crosslinkable poloxamer, whose terminal hydroxyl groups were modified by grafting caprolactone oligomers and methacryloyl groups (P-CL-MA, with 1 repeating unit for CL), as reported previously⁴². The unmodified (non-crosslinkable) and modified (crosslinkable) poloxamer were dissolved in PBS and PBS supplemented with 25 mM ammonium persulphate (APS, Sigma Aldrich), respectively. Prior to mixing, the particle and the liquid phases were stored at 4 °C for 30 min in order to prevent thermal gelation of the poloxamer component. Subsequently, either the non-crosslinkable (NC) or crosslinkable (C) poloxamer was added to particles and mixed manually by stirring for 3 min at 4 °C to ensure homogenous distribution of the particles. Subsequently, the prepared non-crosslinkable pCaP inks (NC-pCaP) and crosslinkable pCaP inks (C-pCaP) were loaded into a dispensing cartridge, closed with a retainer cap, and stored at 4 °C until used.

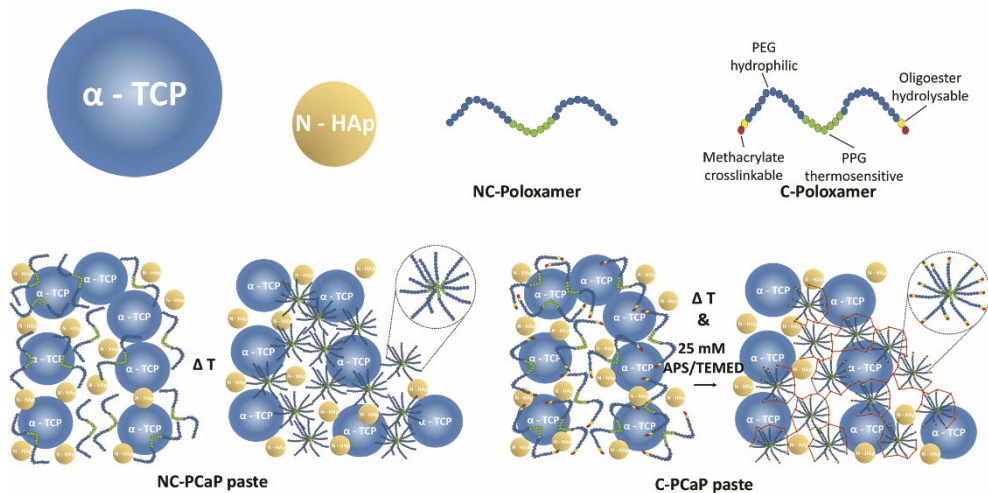


Figure 1. Material composition schematic pictures representing the compositions of the pCaP pastes.

Rheological characterization

Rheological characterization was performed on NC-pCaP, C-pCaP, NC-Poloxamer, C-Poloxamer and water-pCaP using a rheometer (Discovery Hybrid Rheometer (HR-2), TA instrument). The test was conducted on a Peltier plate with pre-set temperature of 20 °C. The test geometry was a 20 mm diameter parallel plate. All measurements were performed while covering each sample with a solvent trap to prevent water evaporation from the composite material. The geometry gap was set to 300 μm . Reactivity of the pCaP-based inks was assessed under oscillatory measurements at a frequency of 0.1 $\text{rad}\cdot\text{s}^{-1}$ and 0.1% strain, which is within the linear viscoelastic range (LVR) for all samples. Shear recovery measurements were carried out under oscillatory conditions by applying low and high strain cyclically. A low strain of 0.05% was applied for 300 s and then increased to 150% (outside LVR) for 300 s at the same frequency of 0.1 $\text{rad}\cdot\text{s}^{-1}$. These steps were repeated three times. Finally, steady-state flow measurements were performed in order to assess flow behaviour of the materials while applying shear rates from 0.001–1000 S^{-1} . Consistency was ensured by repeating all measurements three times.

Printing of the bioceramic scaffolds

Bioceramic scaffolds were fabricated with pneumatic driven, extrusion-based 3D (bio)printing equipment (3DDiscovery, regenHU, Villaz-St-Pierre, Switzerland). To optimize printing parameters, two layers of meander infill in a circle was designed as a printing path and eventually generated g-code by using BioCAD software (regenHU, Villaz-St-Pierre, Switzerland). The effects of extrusion pressure, translational speed of the collector plate and layer height on the diameter of printed strand were investigated, in order to optimize the printing resolution. The NC-pCaP ink was utilized initially for testing by extruding through a conical nozzle (inner diameter: 250 μm) at ambient temperature (while maintaining temperature between 20 and 25 °C). The average diameter of printed strands from each printing setting was measured from stereomicroscopy pictures by using ImageJ software⁴³. All printing settings for obtaining cylindrical filaments with precise alignment were selected. Additionally, the maximum designed strand-to-strand distance at which overhang filaments would retain their straightness without sagging to the lower layer was investigated. Based on the information, optimized porous cylindrical structures consisting of meandered infills in each layer were designed. After the printing process, the printed paste was allowed to set into a cement scaffold, through the hydrolytic conversion of the α -TCP microparticles into calcium deficient hydroxyapatite (CDHA)⁴⁴, via incubation in a saturated humidity environment at 37 °C for at least three days. Similar printing parameters and post-printing treatment was applied for the C-pCaP ink. Subsequently, C-pCaP scaffolds were immersed in 25 mM tetramethylethylenediamine (TEMED, Invitrogen) solution at 37 °C for one hour in order to polymerize the crosslinkable poloxamer. Finally, C-pCaP structures were rinsed in PBS twice, and air dried at ambient temperature. When required for cell culture, the

scaffolds were disinfected by immersion in 70% v·v⁻¹ ethanol, followed by exposure to UV light for 2 h.

Macroporosity of pCaP scaffolds

Porous cylindrical pCaP scaffolds (diameter: 5.0 mm, height: 5.0 mm) were produced from either NC-pCaP paste or C-pCaP paste. Scaffolds were obtained by stacking meander pattern layers in a double alternated pattern (0°-0°-90°-90°), to ensure a consistent lateral pore size of 500 μm. By varying the designed strand to-strand distance from 600 to 800 μm, NC and C scaffolds with four different macroporosity ranges were prepared: 20%–30%, 30%–40%, 40%–50%, and 50%–60% (N= 3–17). Porosity of printed pCaP scaffolds was determined by gravimetry analysis (equation (1))⁴⁵.

$$\text{Total porosity} = 1 - \frac{\rho_{\text{scaffold}}}{\rho_{\text{material}}} \quad (\text{equation (1)})$$

Relative density of the used material (ρ_{material}) was quantified as reported previously⁴⁶. Actual dry weight of dense scaffolds, regardless of micro-porosity, was measured using mass scales. Average diameter and height of the scaffolds were measured by using digital Vernier calipers. Relative density of fabricated scaffolds (ρ_{scaffold}) was calculated from actual dry weight and volume of porous scaffolds.

Mechanical characterization of the bioceramic scaffolds

Unconfined uniaxial compression tests were conducted on scaffolds with different ranges of macroporosity (20%–30%, 30%–40%, 40%–50%, and 50%–60% (N = 3-17)), using a system (MTS Criterion® Electromechanical universal Test Systems, Model 42) equipped with a 500 N load cell. Samples were measured after equilibration in PBS for at least 30 min and subjected to a displacement ramp (0.5 mm·min⁻¹) until failure. Raw data was used to calculate the compressive tangent modulus by measuring the slope of the linear region found in the range 0%-5% strain in the stress-strain curve, as well as ultimate strength and energy to failure using Matlab (R2018,MathWorks®).

Cell isolation and culture

Primary cells were obtained from healthy tissues (bone marrow and articular cartilage) of a deceased, skeletally mature equine donor (aged 6 years old; n = 1), donated for research by their owner, according to the guidelines of the Institutional Animal Ethical Committee of the veterinary clinic of Utrecht University. Mesenchymal stromal cells (MSCs) were harvested from bone marrow aspirated from the sternum, while articular cartilage-derived chondroprogenitor cells (ACPCs) were obtained from enzymatic digests of cartilage from the

metacarpophalangeal joint, following previously reported protocols and following the ethical regulations of the host institution⁴⁷. MSCs were expanded in minimum essential medium alpha (α -MEM, 22561 Gibco, The Netherlands) supplemented with 0.2 mM L-ascorbic acid 2-phosphate (ASAP, Sigma), 10% fetal calf serum (FCS, Lonza, The Netherlands), 100 U·ml⁻¹ penicillin with 100 mg·ml⁻¹ streptomycin (Life Technologies, The Netherlands) and 1 ng·ml⁻¹ basic fibroblast growth factor (bFGF, Peprotech, UK). ACPCs were expanded in Dulbecco's modified Eagle medium (DMEM, 31966, Gibco, The Netherlands), supplemented with 10% v/v FCS, 0.2 mM L-ascorbic acid-2-phosphate, 100 U·ml⁻¹ penicillin, 100 mg ml⁻¹ streptomycin and 5 ng·ml⁻¹ (bFGF, Peprotech, UK). Cells were used between passage 3 and 5.

***In vitro* cytocompatibility and osteogenic potential**

The indirect cytotoxicity of the bioceramic ink was determined to evaluate the potential release of harmful compounds from the CDHA and from the hydrogel component of the cement scaffolds. Four formulations of pCaP were prepared by mixing the particle phase with different liquid compositions: distilled water, NCpoloxamer, C-poloxamer and 10% gelatin-methacryloyl (gelMA). gelMA synthesis was performed as previously reported⁴⁸. Cast pCaP discs (diameter: 5.0 mm., height: 2.0 mm) were incubated in MSC expansion medium for 48 h before using. MSCs (10^4 cells/well) were seeded on tissue-culture treated polystyrene and cultured with eluates of the pCaP scaffolds. The pCaP-exposed medium was exchanged every two days. Cells exposed to MSCs expansion medium supplemented with 0.1% v·v⁻¹ Tween-20 were used as negative control. Cell metabolic activity was assessed with a resazurin assay (AlamarBlue™ Cell Viability, Invitrogen). Next, proliferation and osteogenic differentiation of cells that were in direct contact with the pCaP scaffold were assessed. To enhance the number of seeded cells on the scaffold, porous cylindrical C-pCaP scaffolds (diameter: 13.0 mm, height: 1.0 mm) were printed with single alternated pattern (0°-30°-60°-90°) and a designed strand-to-strand distance of 750 μ m.

Firstly, MSCs were seeded onto the scaffolds ($5 \cdot 10^4$ cells/scaffold, n = 4 per time point) and cultured in the expansion medium, supplemented with 10 mM N-2-hydroxyethylpiperazine-N-2-ethane sulfonic acid (HEPES, Gibco) to assess cell proliferation. At day 1, 3, 7 and 14 the cell-laden scaffolds were collected, and cell lysates were obtained by the addition of the protein extraction buffer M-PER (Thermo Scientific). The number of cells at each time point was quantified by measuring lactate dehydrogenase activity in the lysate (LDH- kit, Roche diagnostic GmbH). Additionally, cell-laden scaffolds at each time point were washed in PBS, fixed with phosphate buffered formalin (pH 7.2), and stained for actin with phalloidin conjugates FTIC (Sigma) for 30 min to observe cell morphology. Nuclei were counterstained with 4',6-diamidino-2-phenylindole (DAPI, 100 ng·ml⁻¹, Sigma) for 1 min. Secondly, MSCs were seeded on bioceramic constructs (10^5 cells/scaffold, n = 4 per analysis) and cultured in the expansion medium, supplemented with 20 mM β -glycerol phosphate, 100 nM dexamethasone and 10 mM HEPES to assess osteogenic

differentiation. The medium was refreshed every two days. At day 1, 7, 14, and 21 cell-laden scaffolds were lysated in M-PER and alkaline phosphate (ALP) activity was measured performing a p-nitrophenyl phosphate assay (SIGMAFAST™, Sigma Aldrich), together with DNA content, determined using the Quan-iT-Picogreen-dsDNA kit (Molecular Probes, Invitrogen, Carlsbad, USA). Formalin-fixed constructs were also labelled with DAPI and immunostained for the osteoblastic marker osteonectin (primary antibody, secondary antibody, Alexafluor 546 (goat anti-mouse, 1752107 Life technologies)). Fluorescently stained constructs were imaged with a confocal laser scanning microscope (TCS SP8, Leica, Netherlands).

Fabrication of multiphasic hydrogel thermoplastic-bioceramic composite scaffolds mimicking an osteochondral plug

Polycaprolactone (PCL) microfibre meshes were fabricated from medical-grade polycaprolactone (Purasorb® PC 12 Corbion PURAC, The Netherlands) using a custom-made melt electrowriting device as previously described⁴⁹. MEW printing parameters were: printing temperature of 90 °C, collector velocity of 50 mm s⁻¹, voltage of 10 kV, and pressure of 1.5 bar. Printing was performed at room temperature (22–24 °C) with a humidity between 30%–50%. By using these settings, microfibre meshes organized in orthogonal square box patterns (fibre diameter = 10 µm, fibre spacing = 300 µm, total height = 1.3 mm) were obtained, which were later cored to obtain 8 mm diameter cylinders using a biopsy punch. These cylindrical meshes were then fixed on a glass slide using a custom-made holder and placed onto the collecting platform of the extrusion-based printer. C-pCaP paste was directly printed over the MEW-printed microfibre mesh, to form a 6.3-mm diameter bioceramic scaffold. The initial height for depositing the C-pCaP paste was optimized thoroughly to ensure printing without damaging the architecture of the PCL microfibres. The first two layers were generated without macro-porosity to mimic the subchondral bone plate. The following layers were deposited with a designed strand-to-strand distance of 700 µm, forming a bone-mimetic osteal anchor. After letting the ceramic component set at 37 °C, the MEW mesh was infused with a 10% w/v gelMA solution⁵⁰ in PBS, supplemented with 25 mM APS/TEMED to allow chemical crosslinking of the hydrogel, thus completing the cartilage mimetic-region of the engineered osteochondral plug (**Figure 2**). Finally, the overall construct was removed from the mold and transferred into 25 mM APS/TEMED supplemented PBS at 37 °C for one hour to allow completion of crosslinking of both the C-poloxamer in C-pCaP and gelMA hydrogel.

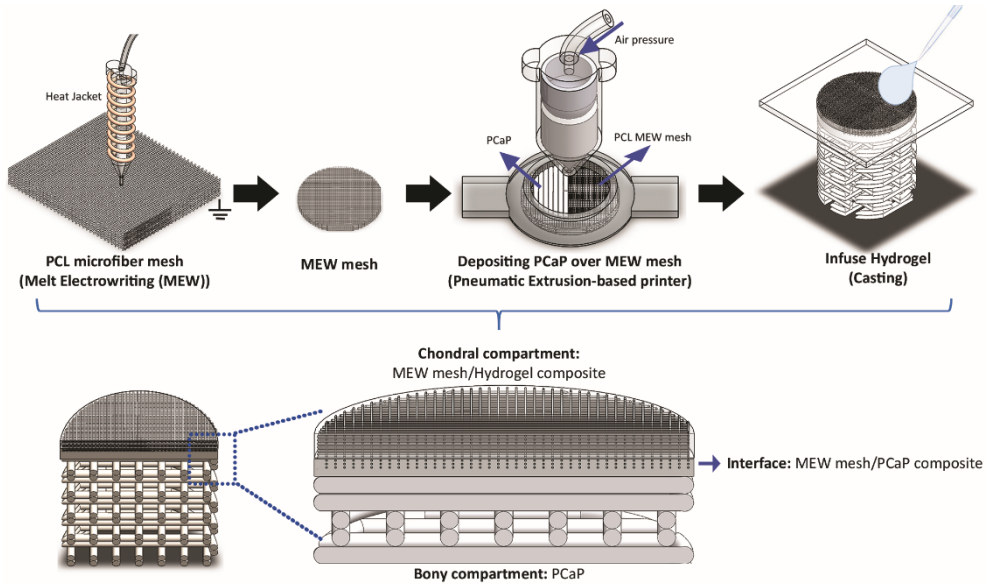


Figure 2. Fabrication process of the osteochondral construct by using a combination of different 3D printing techniques

Interfacial hydrogel-ceramic adhesion strength

The strength of the interconnection at the interface between microfibre-reinforced hydrogel and the bioceramic scaffold was determined using a Dynamic Mechanical Analyzer (DMA Q800, TA Instrument), modified with ring-shaped custom-made sample holders. Additively manufactured samples were mounted so that the C-pCaP and hydrogel compartments were lodged each into the circular cavity of a holder. These holders were then displaced in the direction parallel to the ceramic-hydrogel interface applying a force ramp, until the two parts were completely separated. Shear stress and energy at failure were calculated respectively. Experimental groups consisted of gelMA: (i) cast onto C-pCaP scaffolds with a flat surface, (ii) cast onto C-pCaP scaffolds with grooved surface, which were obtained by adding one layer of parallel C-pCaP struts (spacing = 1.4 mm.), (iii) a microfibre composite that was cast onto the C-pCaP bone-mimetic scaffold (un-anchored microfibres), (iv) a microfibre composite that was cast onto the C-pCaP bone-mimetic scaffold (anchored microfibres). The latter were obtained with the combined MEW and ceramic extrusion printing approach. As additional control, a cylinder made of only gelMA was also tested, to analyse the mechanical strength under shear of a monolithic hydrogel. For each experimental group $n = 3-9$ samples were analysed.

Scanning electron microscopy (SEM) imaging of the engineered ceramic-hydrogel interface

The morphology of the interface between the microfibre meshes and the C-pCaP, as established in the combined printing approach, was visualised via SEM (Phenom PRO SEM, Thermo Fisher scientific; accelerating voltage of 10 kV). All structures were kept at $-80\text{ }^{\circ}\text{C}$ overnight and freeze-dried to remove water from the cartilaginous compartment, and all samples were cut in half in liquid nitrogen, in order to visualize the longitudinal cross-section of the composite scaffold.

Mechanical characterization of reinforced gelMA (cartilaginous compartment) of osteochondral construct

The compressive properties of the microfibre-reinforced gelMA linked to the C-pCaP scaffold, were measured in unconfined uniaxial compression. A 0.1 N min^{-1} ramp force was applied with a DMA device with mounted compression clamps, until reaching a 50% deformation of the disk-shaped hydrogel-microfibre composite compartment (height 1 mm diameter 6 mm). Experimental groups consisted of gelMA: (i) pristine, (ii) a microfibre composite, (iii) cast onto a C-pCaP bone-mimetic scaffold, (iv) a microfibre composite cast onto a C-pCaP bone-mimetic scaffold (un-anchored microfibres), (v) a microfibre composite cast onto a C-pCaP bone-mimetic scaffold (anchored microfibres). For each group, $n = 5-10$ structures were tested. The compressive modulus was derived from curve fitting between 12%–17% strain rate.

Cartilage deposition *in vitro* in the engineered osteochondral plug

Engineered osteochondral plug preparation and culture:

In this part, osteochondral scaffolds consisted of a cellfree bone and an ACPC-laden cartilage compartment. The bone-mimetic region was composed of a porous C-pCaP structure, (designed strand-to-strand distance = 0.7 mm, diameter = 6.3 mm, height of C-pCaP = 3 mm), capped with a non-macroporous layer of C-pCaP struts, with an anchored microfibre mesh, prepared as described previously via combined printing. For the cartilage region, a 10% w/v gelMA hydrogel precursor solution in PBS was loaded with $2 \cdot 10^7$ ACPCs ml^{-1} and infused in the reinforcing microfibres linked to the C-pCaP structure. Cells were encapsulated at passage 4. To permit rapid crosslinking, the precursor solution was supplemented with a previously described visible-light responsive photoinitiator^{51, 52}, composed of 0.5 mM tris (2,2'- bipyridyl) dichloro-ruthenium (II) hexahydrate (Sigma - Aldrich) and 5 mM sodium persulfate (Sigma Aldrich), and exposed to a 1300 lumen white light lamp for 8 min. Samples were cultured in a chondrogenic medium, consisting of DMEM (Gibco, Life Technologies), supplemented with 1% v/v ITS + premix (BD biosciences), 0.2

mM ASAP (Sigma Aldrich), 0.1 μM dexamethasone (Sigma Aldrich), 1% v/v HEPES, 100 U ml^{-1} penicillin, 100 $\mu\text{g ml}^{-1}$ streptomycin (Gibco, Life Technologies) and 10 ng ml^{-1} of recombinant human transforming growth factor- β 1 (TGF- β 1, Peprotech). Samples were cultured for 6 weeks and harvested at two time points (day 1 and day 42) for subsequent analysis. Medium was refreshed every two days. Neo-cartilage formation in the cartilage-region of the engineered plugs, compared to the constructs composed of cell-laden reinforced gelMA only, was evaluated via immunohistochemistry and biochemical analysis. The effect of the neo-synthesized matrix over the culture time on the mechanical strength of the interface between the bone and cartilage compartment was also assessed.

Biochemical and histological evaluation of neocartilage formation:

For biochemical evaluation, samples at week 1 ($n = 3-6$) and 6 ($n = 5-14$) of culture were harvested, and the chondral compartment was removed and with a razor blade and digested in papain (Papain from papaya latex, Sigma Aldrich) at 60 °C overnight. Sulphated glycosaminoglycan and DNA contents of the constructs were quantified performing a dimethylmethylene blue (DMMB, Sigma-Aldrich, The Netherlands) colorimetric assay and with a Quan-iTPicogreen-dsDNA-kit assay (Molecular Probes, Invitrogen, Carlsbad, USA). For histological analysis, samples at day 42 ($n = 3$) were fixated in 4% buffered formalin. For paraffin embedding, samples were decalcified with 0.5 M EDTA disodium salt for 1 day. Dehydration was performed through a graded ethanol series, followed by clearing in xylene, embedding in paraffin, and slicing into 5 μm thin sections with a microtome. Sections were stained with safranin-O and Fast Green to visualize GAGs and collagens. Immunohistochemistry was performed to visualize type I collagen (primary antibody EPR7785, 0.0022 mg./ml., Abcam) and type II collagen (primary antibody Col2A1 II-II6313, 0.6 mg./ml., DSHB). Endogenous peroxidases were blocked via incubation with 0.3% v/v hydrogen peroxide. Antigen retrieval was performed with pronase and hyaluronidase for type II collagen and type I collagen, respectively, at 37 °C. Subsequently, sections were blocked with bovine serum albumin (BSA, 5% w·v⁻¹ in PBS) for 1 h at room temperature, and the primary antibody was incubated overnight at 4 °C. IgGs were used as negative controls. Horseradish peroxidase-labelled secondary antibodies were added for 1 h at room temperature, and the staining was developed using 3,3-diaminobenzidine. Nuclei were counterstained with haematoxylin and sections were mounted in DPX (Millipore). For the osteochondral constructs, in order to visualize structure without removing the pCaP scaffold due to de-calcification steps, one formalin-fixed sample was dehydrated through a graded ethanol series and embedded in a methyl methacrylate (MMA) resin. Sections (300 μm thick) were obtained with a saw microtome (Leica SP 1600). Thereafter, all sections were stained with basic fuchsin to assess scaffold morphology. Histological slides were imaged using a light microscope (Olympus BX51, Olympus Nederland B.V.) equipped with a digital camera (Olympus DP73, Olympus Nederland B.V.).

Interfacial adhesion strength at the engineered osteochondral interface after culture:

At day 1 (n = 3) and 42 (n = 9), osteochondral structures were harvested and kept in medium to ensure hydration. To determine the strength of the connection at the interface between the cartilaginous compartment and the pCaP-based bone compartment, the same settings that were performed for cell-free structures were applied.

Statistical analysis

Results were reported as mean \pm standard deviation. Statistical analyses were performed using Matlab (R2018a, The MathWorks, Inc.). Two-sample independent t-tests were performed to compare the diameter of strands that were printed from different pCaP formulations (NC-pCaP and C-pCaP), biochemical production of ACPCs from different structures (chondral and osteochondral constructs), and interfacial shear stress after cultivation with ACPCs for 1 and 42 days. The Wilcoxon rank sum test was performed to investigate the differences of the mechanical properties of pCaP scaffolds having different porosity and material composition (non-crosslinkable and crosslinkable). One-way ANOVA, with the Bonferroni post hoc test was performed to investigate the mechanical properties of produced osteochondral constructs in terms of interfacial shear stress and compressive modulus of the cartilaginous compartment. Additionally, this method was also applied to compare *in vitro* biological activity of cells with pCaP scaffolds (indirect and direct methods). Statistical significance was considered for $p < 0.05$.

RESULTS AND DISCUSSION**Optimization printing parameters of printable calcium phosphate (pCaP) paste**

First, a ceramic ink was developed to achieve high-resolution patterning and with a setting chemistry compatible with labile polymers and biological compounds. To reach this objective, α -TPC was selected as a main material, due to its mild setting reaction³⁸. Two formulations of pCaP that could be hardened at physiological temperature were evaluated: one containing a non-crosslinkable poloxamer component (NC-pCaP) and one containing a modified, crosslinkable poloxamer component (C-pCaP). The solid particle to liquid (P/L) ratio of both ink formulations ensured the extruded ink retained its shape and could bear weight after placement, allowing for the formation of multilayer constructs without additional support. These were assessed through rheological characterization, to analyze the flow behavior of the inks when shear forces are applied during printing (**Figure 3 and supplementary Figure S1**). When applying shear rates from 0.001 to 1000 S^{-1} , viscosity decreases over this range of shear rate. This flow profile shows a comparable shear-thinning behavior for both the NC-pCaP and C-pCaP (**Figure 3(A)**). Additionally, both NC-pCaP and C-pCaP could rapidly recover from applied shears, a condition beneficial to produce high

shape fidelity prints (**Figure 3(B)**). For printing, to ensure shape fidelity and uniformity of the printed filaments, printing parameters (extrusion pressure, translational speed) for deposition of the paste were established using the NC-pCaP formulation (**Figure 3(D)**). The optimal printing parameters: 0.2 MPa, 2 mm s⁻¹ and 250 μm were selected for the pneumatic pressure, translational speed and layer thickness, respectively. With these parameters, the average diameter of the obtained C-pCaP filaments (230.20 ± 31.24 μm) was close to the inner diameter of the used nozzle (250 μm.), indicating a higher printing resolution than was found for NC-pCaP filaments (349.22 ± 33.56 μm) (**Figure 3(E)**). Besides printing parameters, shape fidelity in the axial direction is also a pre-requisite for the formation of multi-layered constructs; this factor depends also on the ability of an ink not to undergo deformation when overhanging filaments are stacked without sacrificial supporting materials^[53]. Maximum designed strand-to-strand distance for overhanging 90-degree filaments on top of each other without sagging was 800 μm (**Figure 3(F)**). Overall, high shape fidelity was achieved post-printing and upon cement setting, with open and interconnected pores, as well exemplified via μCT (supplementary video SV1). Post-printing, the pCaP ink, which was composed of nanohydroxyapatite (N-HAp) and α-tricalcium phosphate microparticles (α-TCP), sets into a cement at physiological temperature, thanks to the hydrolytic conversion of α-TCP into calcium deficient hydroxyapatite (CDHA) (**supplementary Figure S2 and supplementary Table 2**), and by further crosslinking of the methacryloyl groups in the C-pCaP formulation. While this stabilizes the fabricated construct, the α-TCP reactivity and setting initiation could influence the rheology and printability of the ink over time (**Figure 3(C)**). This potential risk can be overcome through tight control of the temperature during the printing process.

Mechanical properties of the biomimetic pCaP scaffolds

After obtaining optimal parameters for printing, mechanical properties of the printed structure (**Figure 4(A)**) are crucial especially for using it as a bone replacement. First of all, the presence of nanohydroxyapatite in the bioprintable paste was not found to significantly alter the mechanical properties of the cement after setting (**supplementary Figure S3**). Next, scaffolds with different ranges of porosity were obtained after printing NC-pCaP and C-pCaP biomaterial inks following hardening and hardening-crosslinking, respectively. Tangent modulus, ultimate strength and energy to failure were characterized by performing unconfined compression tests and calculated from the stress-strain curves (**Figure 4(B)**, **supplementary Figures S4(A) and (B)**). Importantly, all formulations and pore designs exhibited compressive properties in the range of cancellous bone^{54, 55}. Tangent modulus, ultimate strength and energy to failure of scaffolds made from both NC-pCaP and C-pCaP gradually decreased with increasing porosity, as expected (**Figures 4(B), (D) and supplementary Figure S4(C)**). Interestingly, there were no obvious differences in the compressive modulus of scaffolds produced from NC-pCaP and C-pCaP inks, with the only exception of the samples displaying 30%–40% designed porosity.

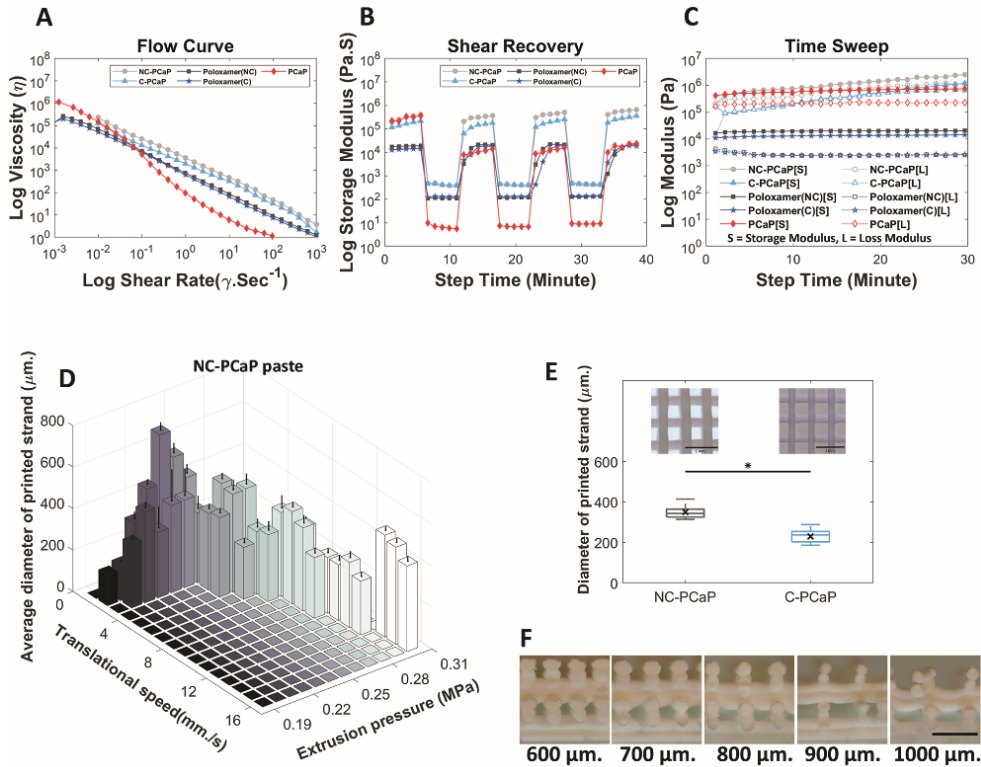


Figure 3. Rheometry and optimization of printing parameters. Rheological analysis highlighting (A) the shear-thinning and (B) shear recovery behaviour of all the inks, and (C) the storage modulus over the printing time, showing no distinctly different behavior between cements based on the C or NC polymeric carriers. (D) Average diameter of printed strands obtained from two main setting parameters (translational speed and extrusion pressure), (E) comparison between diameter of printed strands fabricated from NC-pCaP paste and C-pCaP paste at the same settings and, (F) the strand-to-strand distance of printable calcium phosphate paste (pCaP). (Scale bar = 1 mm).

It has been mentioned in the literature that mechanical properties of self-setting ceramics are lower than high-temperature sintering ceramics [56]. Nevertheless, the scaffolds from this study still showed values in the physiological range reported for trabecular bone [54, 55]. While sintering may further improve the mechanical strength of the constructs, this would prevent the direct incorporation and anchoring of low-melting point thermoplastic polymers as presented in this study as a strategy to improve bone-to-soft tissue interfaces. As such, the high ratio selected for this study (70% w/w of particle content), while giving optimal shape fidelity post-printing, may hinder the formation of a densely crosslinked polymer network, hampering an increase in fracture toughness of the constituent ceramics that could come from the hydrogel covalent crosslink. Nevertheless, considering the overall promising compressive properties and the higher printed filament resolution, C-pCaP was used for the remaining part of this study.

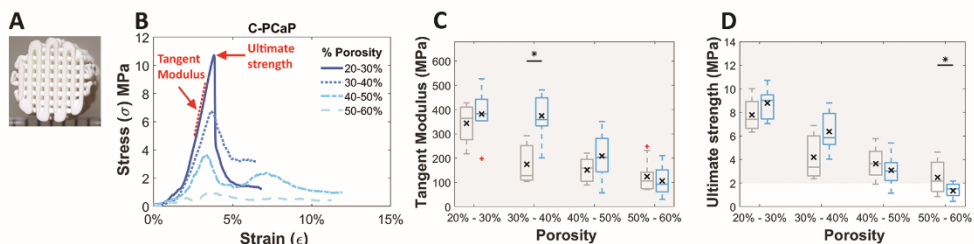


Figure 4. Mechanical properties: (A) representative pCaP scaffold, (B) representative engineered stress-strain curves of C-pCaP scaffolds, (C) tangent modulus, (D) ultimate strength of NC-pCaP paste (grey) and C-pCaP paste (blue) scaffolds with different porosities. (Greyish-filled area showing range of tangent modulus of cancellous bone [10–5000 MPa^[54]] (B) and ultimate strength [2–45 MPa^[55]] (C)).

In vitro evaluation of bioactivity using mesenchymal stromal cells (MSCs)

Cytocompatibility and osteogenic potential of the bone constructs (**Figure 5**) was assessed *in vitro*, using equine bone marrow-derived cells, which were selected in the perspective of future *in vivo* analysis, as the horse is a well-accepted-respected model for evaluating cartilage and osteochondral repair therapies^{57–59}. The effects of the release of potentially harmful components was investigated through the culture of MSCs in pCaP conditioned medium, using formulations of the cements that feature different polymeric carriers in the liquid phase. Although free poloxamer above a certain concentration can be harmful⁶⁰, our data indicates no negative effect, suggesting no release of detrimental degradation products from the crosslinked poloxamer network or uncontrolled pH changes due to ions released by an incomplete setting reaction of the α -TCP microparticles. There was an increase in number of viable cells from day 1 to day 7 in all experimental groups (**Figure 5(A)**) and there were no statistically significant differences after 7 days between the poloxamer-CaP conditioned medium, the positive control (fresh culture medium), and a CaP control with an embedded well-known biocompatible polymer (gelMA). Importantly, MSCs were able to proliferate when seeded directly onto the C-pCaP scaffolds, as indicated by lactate dehydrogenase (LDH) activity (**supplementary table 1**). Moreover, osteogenic differentiation of equine MSCs cultured on C-pCaP scaffolds was observed after 21 days of culture. The expression of alkaline phosphatase (ALP), an early marker of osteogenic differentiation⁶¹, increased upon MSC culture directly on scaffolds, with higher values and characteristic early peak detection at 7 days in medium supplemented with osteogenic factors (**Figure 5(B)**). Cell proliferation was confirmed via immunofluorescence, observing confluent cell layers on the printed struts that displayed an elongated morphology and developed actin stress filaments after 14 days of culture (**Figure 5(C)**). This is in line with previous studies involving scaffolds using comparable ceramic base components³⁸. Importantly, upregulation of osteonectin, a marker of maturing osteoblasts and a hallmark of bone deposition, was detected starting from day 14 in samples with osteogenic medium (**Figure 5(D)**, see **supplementary Figures S4(D), (E)**). Overall, the data confirms that the selected pCaP

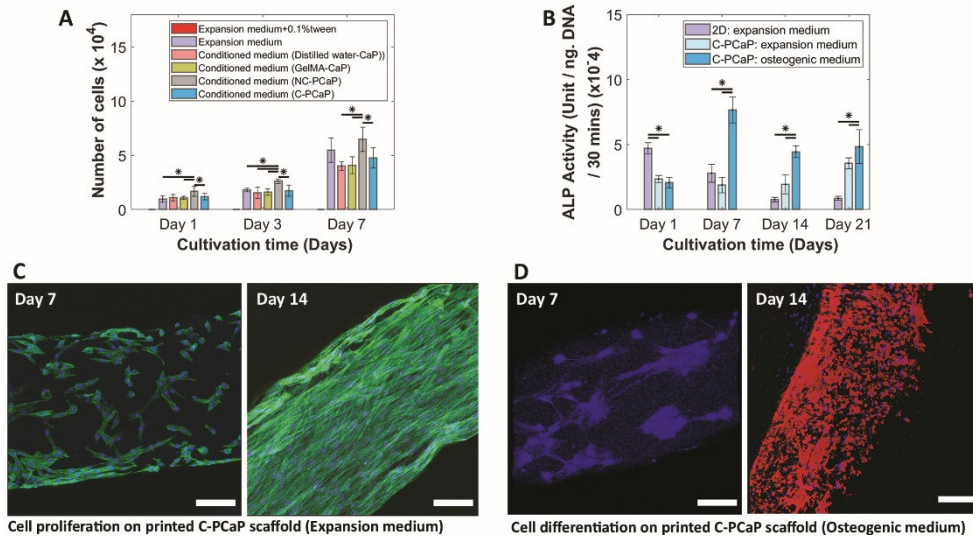


Figure 5. *In vitro* evaluation of bioactivity of the pCaP scaffold. (A) The effect of possible harmful release from composite CaP-based material contained different polymeric carriers on the number of viable cells, (B) the potential of osteogenic differentiation of equine MSCs was investigated through ALP activity, (C) cell proliferation on the C-pCaP filament after cultivation for 7 and 14 days (nucleus (dapi: blue) and F-actin (phalloidin: green)), and (D) cell differentiation on the C-pCaP filament toward an osteogenic lineage after cultivation for 7 and 14 days in an osteogenic medium (nucleus (dapi: blue) and osteonectin protein (osteonectin: red)) (scale bar = 100 μ m.)

formulation and scaffold have the potential for osteo-regeneration, in line with results reported on other bioceramic materials with similar chemical composition.

Fabrication and mechanical properties of the engineered cartilage-bone interface

For proper integration, it is crucial that the deposition of C-pCaP ink does not alter the organized structure of PCL-microfibre mesh (**Figure 6**). Additionally, preservation of the MEW-printed architecture and microfibre alignment is fundamental to control the mechanical reinforcing effect against compression provided by the PCL mesh when soft hydrogels are embedded in it⁶². Therefore, the initial height for the deposition of the first layer of C-pCaP was set to 80% of total mesh height. Thanks to the fluid paste-like rheological behavior of the ceramic ink before setting, the material is able to form an interpenetrated structure with the PCL mesh, without altering the microfibre organization and with no detectable effect on the shape fidelity of the extruded ceramic filaments. After the setting of the C-pCaP, the PCL-ceramic ordered composite is formed, with the microfibrils anchored into the cement phase and protruding in an ordered fashion into the cartilage region of the osteochondral plug, in which the gelMA hydrogel is lodged by a simple injection (**Figure 7(A)**). The strength of the interconnection (**Figure 7(B)**) at the engineered ceramic-hydrogel interface and the compressive modulus of the chondral compartment (**Figure 7(C)**) were evaluated by using the systems in **Figure 7(D)**, and analysing the yield point under

interfacial shear stress (**Figure 7(E)**) and the compressive modulus (**Figure 7(F)**), respectively. The interfacial strength of the structures was significantly improved compared to conditions in which the hydrogel was either cast on a smooth or grooved pristine pCaP osteal part, or when the reinforcing microfibrils were laid on top of but not anchored into the pCaP (**Figure 7(E)**). The embedding of the MEW reinforcing microfibrils within the bioceramic resulted in an approximately 6.5-fold increase, from 2.7 ± 0.5 kPa for the gelMA casted on top of the ceramic, without microfibril interlocked within ceramic, to 17.7 ± 2.0 kPa for the condition in which the fibres were embedded within the ceramic scaffold. Evaluation of the interfacial toughness showed a similar trend as the interfacial strength (**supplementary Figure S5**). Interestingly, upon mechanical failure of the interface, the microfibrils remained well organized and anchored within the bioceramic material, as found by microstructural observation via scanning electron microscopy (SEM) (**Figures 7(G) and (H)**). Collapse upon shear occurred due to loss of adhesion integrity and delamination of the sole hydrogel component.

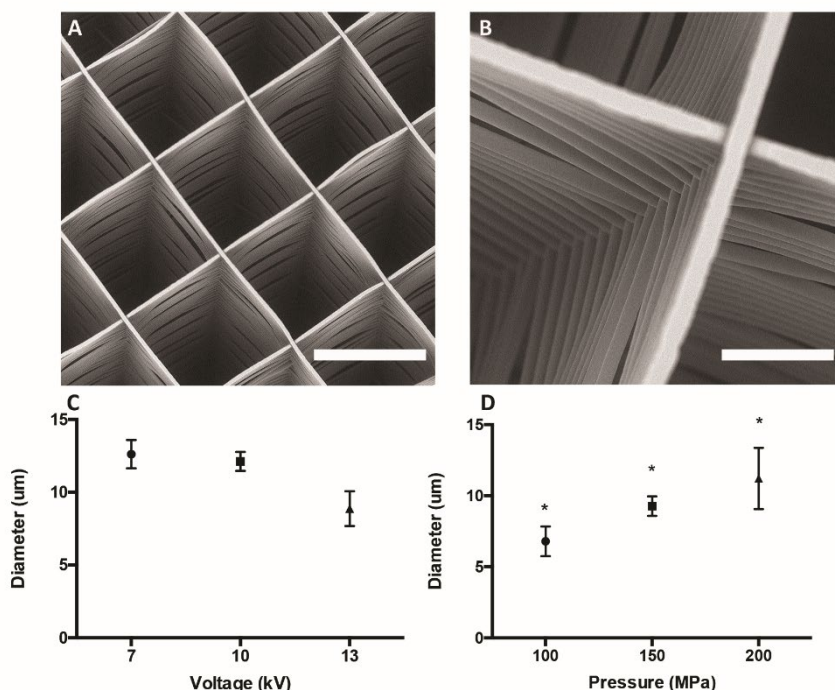


Figure 6. Micro-structure and printing parameters of the MEW fibrous scaffold. (A) and (B) SEM micrographs showing the architecture of the microfibril mesh produced by MEW (A: scale bar = $300 \mu\text{m}$., B: scale bar = $50 \mu\text{m}$), (C) Relationship between voltage and diameter of PCL microfibril for printing the MEW microfibril mesh. (D) Relationship between pressure and diameter of PCL microfibril for printing MEW microfibril mesh

The observed yield shear stresses were slightly above that of gelMA itself (15.6 ± 2.4 kPa), as measured by submitting a monolithic gelMA hydrogel to the shear test. In contrast, for the biphasic hydrogel-bioceramic the fracture was propagated along the interface between hydrogel and bioceramic. Taken together, these results suggest that the MEW microfibrinous mesh acts as a bridge between the bony and cartilage compartment in the engineered plug, and that the stability of the interconnection could be further improved employing hydrogels with higher shear strength than gelMA, as well as with strategies to covalently graft the hydrogel component to the thermoplastic microfibrines⁶³. An important implication of using MEW-microfibrines is their ability as reinforcing elements, to remarkably improve the mechanical properties of otherwise soft hydrogels. Previous work demonstrated the ability to enhance the stiffness of gelMA-based constructs, reaching compressive properties mimicking those of native cartilage³¹, while computational modelling unravels the mechanisms beyond this behavior⁶². In line, in the present study, an increment in compressive modulus was observed for the microfibre-reinforced gelMA structures (**Figure 7(F)**), with the orthogonal boxes structure architecture selected for the MEW-printed meshes. Importantly, properties were even further improved when the microfibrines were embedded within the bioceramic scaffold (3.2-fold versus reinforced hydrogels alone) (**Figure 7(F)**), approaching the values of healthy human knee cartilage⁶⁴. This was likely achieved through the stabilisation of the base of the MEW-printed structure and facilitated load transfer to the pCaP scaffold. Such stabilization could prevent early bucking of the stacked layers of microfibrines, which has been identified as the main cause of failure of MEW box-shaped meshes under compressive loads⁶². Also, the stabilization of the MEW fibres within the ceramic scaffold allows a more effective lateral confinement of the gelMA hydrogel upon axial compression, thus resulting in a stiffer response. Although interfacial strength is still lower than those found in the native, mature bone-cartilage boundary⁶⁵, this mechanical stabilization and reinforcing effect greatly facilitates the surgical handling of the engineered cartilage construct, as well as its implantation in situ by press-fitting into an osteochondral defect in a tissue explant model (**Figure 8(A)**).

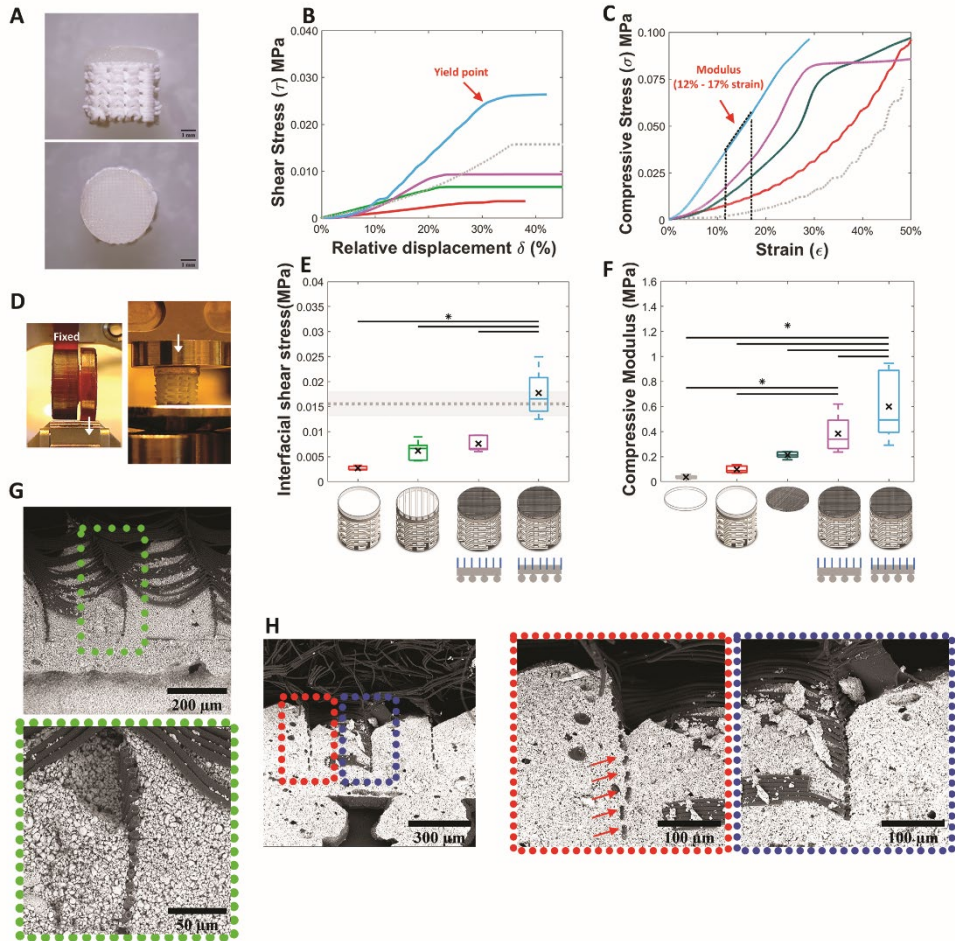


Figure 7. Mechanical properties of the osteochondral unit. (A) Osteochondral unit (scale bar = 1 mm.), (B) representative stress-displacement curves from interfacial shear stress assessment at the interface between the chondral and bone compartment, (C) representative stress-strain curves from compression assessment of chondral compartment, (D) mechanical testing (interfacial shear stress: left, and compressive modulus (right)), (E) interfacial shear stress of an engineered osteochondral unit showing alterations due to differences in either interfacial architecture or compositions (gelMA on ceramic (unmodified surface; red), gelMA on ceramic (modified surface; bright green), microfibre reinforced gelMA on ceramic (non-anchor fibre; pink), microfibre reinforced gelMA on ceramic (anchor fibre; blue) and monolithic gelMA hydrogel (mean (grey dotted line) \pm SD (grey filled area))), (F) compressive modulus of chondral compartment showing alterations due to difference in composition (gelMA alone (grey), gelMA over flat interfacial surface of pCaP (red), microfibre reinforced gelMA alone (dark green), microfibre reinforced gelMA on ceramic (non-anchor fibre; pink), microfibre-reinforced gelMA on ceramic (anchor fibre; blue)), (G) SEM micrographs of cross sections of an osteochondral unit revealing embedded microfibrils within non-macro porous layer of the bone compartment of newly fabricated structure and (H) after interfacial shear stress assessment

To further investigate the potential of the multiscale composite osteochondral plugs for the formation of cartilage-like matrix *in vitro*, the chondral reinforcing meshes were infused with articular cartilage derived progenitor cells (ACPC)-containing gelMA and constructs were cultured for 6 weeks. Constructs with **(Figure 8(B))** and without the osteal C-pCaP anchor were tested, to evaluate the possibility to obtain neo-cartilage in the presence of a bone-supporting material. ACPCs remained viable within the microfibre reinforced gelMA and the deposition of the cartilage-like extracellular matrix was observed in both structures after 6 weeks of culture **(Figure 8(C))**.

Additionally, the neo-synthesized matrix influenced the strength of the interconnection at the bone-cartilage interface of the cell-laden grafts, which improved approximately 3.7-fold from 6.6 ± 1.7 kPa at day 1 to 24.4 ± 6.5 kPa at day 42 **(Figure 8(D))**. Interfacial toughness showed a similar trend **(Figure 8(E))**. Histological evaluation by means of safranin-O staining revealed sGAG deposition **(Figures 8(F1), (G1))**. Type II collagen (Col II) production was also detected in both chondral **(Figure 8(F2))** and osteochondral constructs **(Figure 8(G2))**, respectively. Type I collagen (Col I) deposition was also detected via histological analysis **(Figures 8(F3), (G3))**. Col I is often present as an immature marker in gelMA-based constructs^{37, 66} and can be reduced by incorporation of hyaluronan into the hydrogel matrix⁶⁷. These results underscore that the differentiation of ACPCs towards the chondrogenic lineage is not hampered by the calcium phosphate-based scaffold, suggesting that the construct can be safely used for testing of osteochondral repair techniques.

Overall, a dual reinforcing effect (compression stiffness and interfacial shear strength) was achieved using the combination of ceramic extrusion printing and microfibre electrowriting. Moreover, the coordinated fabrication of such organized, multi-scale composite structures offers new possibilities for functional restoration of damaged osteochondral units. This approach can be further refined by tuning both biological and mechanical properties of the constructs, taking advantage of the physiological setting kinetics of the pCaP ink. Besides facilitating the formation of a tight engineered cartilage-to-subchondral bone connection and supporting osteogenesis *in vitro*, low-temperature setting cements hold the potential to incorporate growth factors (i.e. to enhance osteoinductive and angiogenic properties⁶⁸, or even the simultaneous printing of ceramic and hydrogel embedded living cells²⁶). With this in mind, the co-printing in a single biofabrication process of cell-friendly ceramics, cell-laden hydrogels and electrowritten microfibres, can be envisioned to comprehensively capture the architecture of native tissue interfaces. In fact, although in this study gelMA was infused in the chondral compartment of the construct, MEW and extrusion-based bioprinting can already be converged in a single biofabrication process, for instance to mimic phenotypic gradients within tissues, such as the zonal cell distribution in articular cartilage²⁷. Likewise, as more convoluted microfibre reinforcement geometries can be produced in the hydrogel compartment, specifically designed microfibre motifs could be incorporated to further enhance shear resistance⁶⁹, or even to improve tensile behavior⁷⁰, the latter with potential application towards the regeneration of tendon and ligament-to-bone interfaces.

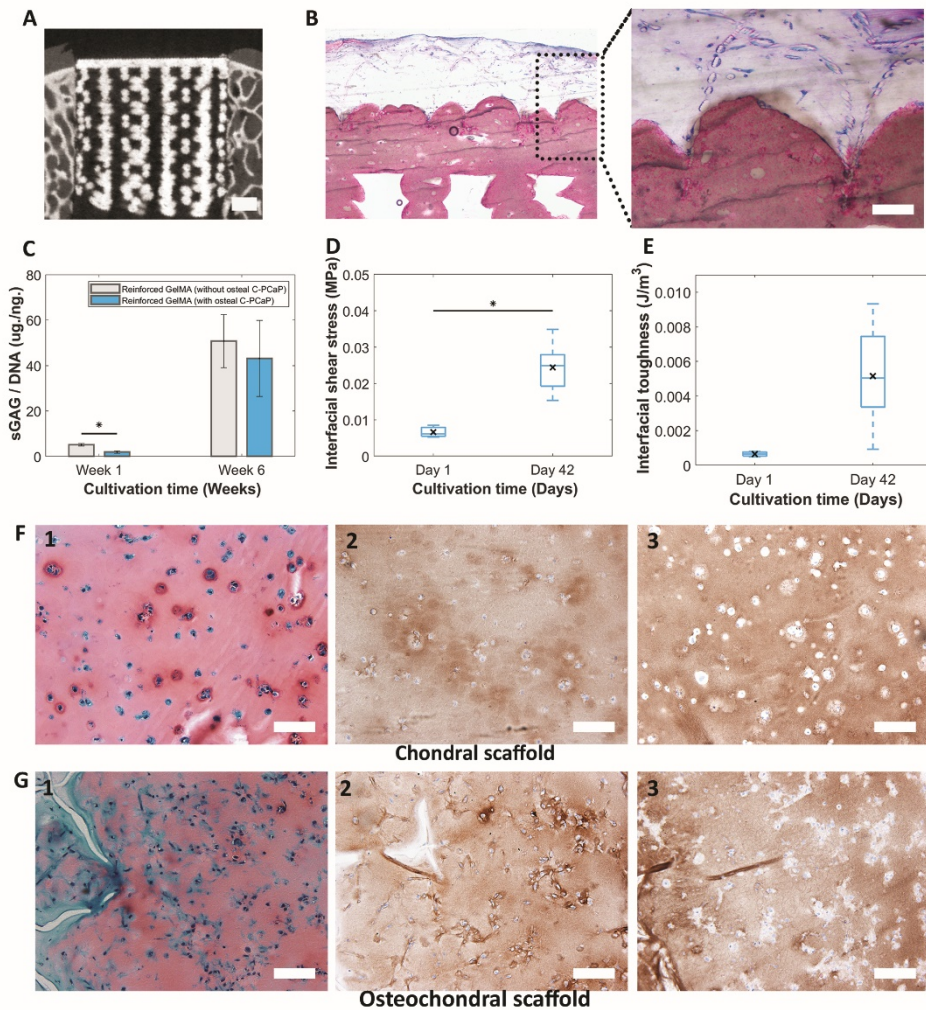


Figure 8. Cartilage deposition *in vitro* in the engineered osteochondral plug. (A) Micrograph obtained from micro-CT scanning showing a biomimetic pCaP scaffold that could be placed press-fit inside an *ex vivo* osteochondral defect. (Scale Bar = 1 mm.), (B) basic fuchsin and methylene blue staining reveal pattern of embedded PCL microfibres inside the non-porous layer of the C-pCaP scaffold of the constructs with osteal C-pCaP anchor. (Scale Bar = 100 μ m.), (C) quantification of sGAG in hydrogel per DNA content. (D) Interfacial adhesion strength and (E) interfacial toughness (day 1 and day 42) while applying shear force at the interface between equine ACPCs encapsulated in gelMA and C-pCaP-based bone compartment. (F1), (G1) Safranin-O staining, (F2), (G2) type II collagen immunostaining and (F3), (G3) type I collagen immunostaining of paraffin embedded microfibre reinforced gelMA without osteal C-pCaP (F) and with osteal C-pCaP (G), respectively, after cultivation for 42 days. (Scale Bar = 100 μ m.).

CONCLUSIONS

In this study, we demonstrate a novel approach to mechanically integrate hydrogel-based soft tissues to a stiff, bone-like material with potential application for the regeneration hard-to-soft tissue interfaces, in particular in case of osteochondral plugs. To achieve this, a multiscale printing approach, combining ceramic extrusion 3D plotting and the electrowriting of thermoplastic microfibrils, was developed. Importantly, the mechanical properties of each compartment (bone, cartilage, interface) can be controlled through the internal architecture of both the reinforcing microfibre mesh and porous bioceramic by means of printing. Additionally, such an approach relying on low stiffness, electrowritten meshes, provides hydrogel strengthening and compressive properties comparable to native cartilage, without shielding cells from beneficial mechanical loads. Owing to the compatibility of the operating physiological temperatures and environmental conditions used for the printing and setting of the pCaP ink, direct anchoring of electrowritten PCL structures in the cement material could be achieved. All materials used, as well as the composite structure, had no impact on cell survival and hence permitted bone and cartilage engineering *in vitro*. This approach offers a promising opportunity for designing interfaces and composite materials with multiple applications in connective tissue regenerative medicine. Overall, these results provide important cues for the biofabrication of a next generation of multi-material, composite tissues and interfaces, which could integrate 3D printed elements mimicking living tissues down to the micron range.

ACKNOWLEDGEMENTS

The authors would like to thank Anneloes Mensinga and Mattie van Rijen for the assistance with cell culture and the histological analysis. The authors also wish to acknowledge the funding support from the Royal Thai government scholarship (Thailand, PD), the Dutch Arthritis Association (LLP-12 and LLP22) and the European Research Council under grant agreement 647426 (3D-JOINT). The primary antibodies against type II collagen (II-II6B3) developed by T F Linsenmayer and E S Engvall, respectively, were obtained from the DSHB developed under the auspices of the NICHD and maintained by the University of Iowa, Department of Biology, Iowa City, IA, USA.

REFERENCES

1. Pouran, B.; Arbabi, V.; Bleys, R. L. A. W.; René van Weeren, P.; Zadpoor, A. A.; Weinans, H., Solute transport at the interface of cartilage and subchondral bone plate: Effect of micro-architecture. *Journal of Biomechanics* **2017**, *52*, 148-154.
2. Groen, W. M.; Diloksumpan, P.; van Weeren, P. R.; Levato, R.; Malda, J., From intricate to integrated: Biofabrication of articulating joints. *Journal of Orthopaedic Research* **2017**, *35* (10), 2089-2097.
3. Deymier, A. C.; An, Y.; Boyle, J. J.; Schwartz, A. G.; Birman, V.; Genin, G. M.; Thomopoulos, S.; Barber, A. H., Micro-mechanical properties of the tendon-to-bone attachment. *Acta Biomaterialia* **2017**, *56*, 25-35.
4. Nover, A. B.; Lee, S. L.; Georgescu, M. S.; Howard, D. R.; Saunders, R. A.; Yu, W. T.; Klein, R. W.; Napolitano, A. P.; Ateshian, G. A.; Hung, C. T., Porous titanium bases for osteochondral tissue engineering. *Acta Biomaterialia* **2015**, *27*, 286-293.
5. Yuk, H.; Zhang, T.; Lin, S.; Parada, G. A.; Zhao, X., Tough bonding of hydrogels to diverse non-porous surfaces. *Nature Materials* **2016**, *15* (2), 190-196.
6. Zhao, Y.; Li, M.; Liu, B.; Xiang, J.; Cui, Z.; Qu, X.; Qiu, D.; Tian, Y.; Yang, Z., Ultra-tough injectable cytocompatible hydrogel for 3D cell culture and cartilage repair. *Journal of Materials Chemistry B* **2018**, *6* (9), 1351-1358.
7. Means, A. K.; Shrode, C. S.; Whitney, L. V.; Ehrhardt, D. A.; Grunlan, M. A., Double Network Hydrogels that Mimic the Modulus, Strength, and Lubricity of Cartilage. *Biomacromolecules* **2019**, *20* (5), 2034-2042.
8. Lima, E. G.; Grace Chao, P.-h.; Ateshian, G. A.; Bal, B. S.; Cook, J. L.; Vunjak-Novakovic, G.; Hung, C. T., The effect of devitalized trabecular bone on the formation of osteochondral tissue-engineered constructs. *Biomaterials* **2008**, *29* (32), 4292-4299.
9. Jiang, J.; Tang, A.; Ateshian, G. A.; Guo, X. E.; Hung, C. T.; Lu, H. H., Bioactive Stratified Polymer Ceramic-Hydrogel Scaffold for Integrative Osteochondral Repair. *Annals of Biomedical Engineering* **2010**, *38* (6), 2183-2196.
10. Jeon, J. E.; Vaquette, C.; Theodoropoulos, C.; Klein, T. J.; Huttmacher, D. W., Multiphasic construct studied in an ectopic osteochondral defect model. *Journal of The Royal Society Interface* **2014**, *11* (95), 20140184.
11. Seol, Y.-J.; Park, J. Y.; Jeong, W.; Kim, T.-H.; Kim, S.-Y.; Cho, D.-W., Development of hybrid scaffolds using ceramic and hydrogel for articular cartilage tissue regeneration. *Journal of Biomedical Materials Research Part A* **2015**, *103* (4), 1404-1413.
12. Scotti, C.; Wirz, D.; Wolf, F.; Schaefer, D. J.; Bürgin, V.; Daniels, A. U.; Valderrabano, V.; Candrian, C.; Jakob, M.; Martin, I.; Barbero, A., Engineering human cell-based, functionally integrated osteochondral grafts by biological bonding of engineered cartilage tissues to bony scaffolds. *Biomaterials* **2010**, *31* (8), 2252-2259.
13. Levingstone, T. J.; Matsiko, A.; Dickson, G. R.; O'Brien, F. J.; Gleeson, J. P., A biomimetic multi-layered collagen-based scaffold for osteochondral repair. *Acta Biomaterialia* **2014**, *10* (5), 1996-2004.
14. Li, C.; Ouyang, L.; Pence, I. J.; Moore, A. C.; Lin, Y.; Winter, C. W.; Armstrong, J. P. K.; Stevens, M. M., Buoyancy-Driven Gradients for Biomaterial Fabrication and Tissue Engineering. *Advanced Materials* **2019**, *31* (17), 1900291.
15. Bian, W.; Lian, Q.; Li, D.; Wang, J.; Zhang, W.; Jin, Z.; Qiu, Y., Morphological characteristics of cartilage-bone transitional structures in the human knee joint and CAD design of an osteochondral scaffold. *BioMedical Engineering OnLine* **2016**, *15* (1), 82.
16. Holmes, B.; Zhu, W.; Li, J.; Lee, J. D.; Zhang, L. G., Development of Novel Three-Dimensional Printed Scaffolds for Osteochondral Regeneration. *Tissue Engineering Part A* **2014**, *21* (1-2), 403-415.
17. Erisken, C.; Kalyon, D. M.; Wang, H., Functionally graded electrospun polycaprolactone and β -tricalcium phosphate nanocomposites for tissue engineering applications. *Biomaterials* **2008**, *29* (30), 4065-4073.
18. Erisken, C.; Kalyon, D. M.; Wang, H.; Örnek-Ballanco, C.; Xu, J., Osteochondral Tissue Formation Through Adipose-Derived Stromal Cell Differentiation on Biomimetic Polycaprolactone Nanofibrous Scaffolds with Graded Insulin and Beta-Glycerophosphate Concentrations. *Tissue Engineering Part A* **2010**, *17* (9-10), 1239-1252.

19. Shim, J.-H.; Jang, K.-M.; Hahn, S. K.; Park, J. Y.; Jung, H.; Oh, K.; Park, K. M.; Yeom, J.; Park, S. H.; Kim, S. W.; Wang, J. H.; Kim, K.; Cho, D.-W., Three-dimensional bioprinting of multilayered constructs containing human mesenchymal stromal cells for osteochondral tissue regeneration in the rabbit knee joint. *Biofabrication* **2016**, *8* (1), 014102.
20. Levato, R.; Visser, J.; Planell, J. A.; Engel, E.; Malda, J.; Mateos-Timoneda, M. A., Biofabrication of tissue constructs by 3D bioprinting of cell-laden microcarriers. *Biofabrication* **2014**, *6* (3), 035020.
21. Castro, N. J.; O'Brien, J.; Zhang, L. G., Integrating biologically inspired nanomaterials and table-top stereolithography for 3D printed biomimetic osteochondral scaffolds. *Nanoscale* **2015**, *7* (33), 14010-14022.
22. Aydogdu, M. O.; Oner, E. T.; Ekren, N.; Erdemir, G.; Kuruca, S. E.; Yuca, E.; Bostan, M. S.; Eroglu, M. S.; Ikram, F.; Uzun, M.; Gunduz, O., Comparative characterization of the hydrogel added PLA/ β -TCP scaffolds produced by 3D bioprinting. *Bioprinting* **2019**, *13*, e00046.
23. Moxon, S. R.; Cooke, M. E.; Cox, S. C.; Snow, M.; Jeys, L.; Jones, S. W.; Smith, A. M.; Grover, L. M., Suspended Manufacture of Biological Structures. *Advanced Materials* **2017**, *29* (13), 1605594.
24. Schuurman, W.; Khristov, V.; Pot, M. W.; van Weeren, P. R.; Dhert, W. J. A.; Malda, J., Bioprinting of hybrid tissue constructs with tailorable mechanical properties. *Biofabrication* **2011**, *3* (2), 021001.
25. Pati, F.; Jang, J.; Ha, D.-H.; Won Kim, S.; Rhie, J.-W.; Shim, J.-H.; Kim, D.-H.; Cho, D.-W., Printing three-dimensional tissue analogues with decellularized extracellular matrix bioink. *Nature Communications* **2014**, *5* (1), 3935.
26. Kang, H.-W.; Lee, S. J.; Ko, I. K.; Kengla, C.; Yoo, J. J.; Atala, A., A 3D bioprinting system to produce human-scale tissue constructs with structural integrity. *Nature Biotechnology* **2016**, *34* (3), 312-319.
27. Kim, B. S.; Jang, J.; Chae, S.; Gao, G.; Kong, J.-S.; Ahn, M.; Cho, D.-W., Three-dimensional bioprinting of cell-laden constructs with polycaprolactone protective layers for using various thermoplastic polymers. *Biofabrication* **2016**, *8* (3), 035013.
28. Mouser, V. H. M.; Levato, R.; Bonassar, L. J.; D'Lima, D. D.; Grande, D. A.; Klein, T. J.; Saris, D. B. F.; Zenobi-Wong, M.; Gawlitta, D.; Malda, J., Three-Dimensional Bioprinting and Its Potential in the Field of Articular Cartilage Regeneration. *CARTILAGE* **2016**, *8* (4), 327-340.
29. Ahlfeld, T.; Doberenz, F.; Kilian, D.; Vater, C.; Korn, P.; Lauer, G.; Lode, A.; Gelinsky, M., Bioprinting of mineralized constructs utilizing multichannel plotting of a self-setting calcium phosphate cement and a cell-laden bioink. *Biofabrication* **2018**, *10* (4), 045002.
30. de Ruijter, M.; Ribeiro, A.; Dokter, I.; Castilho, M.; Malda, J., Simultaneous Micropatterning of Fibrous Meshes and Bioinks for the Fabrication of Living Tissue Constructs. *Advanced Healthcare Materials* **2019**, *8* (7), 1800418.
31. Brown, T. D.; Dalton, P. D.; Huttmacher, D. W., Direct Writing By Way of Melt Electrospinning. *Advanced Materials* **2011**, *23* (47), 5651-5657.
32. Hochleitner, G.; Jüngst, T.; Brown, T. D.; Hahn, K.; Moseke, C.; Jakob, F.; Dalton, P. D.; Groll, J., Additive manufacturing of scaffolds with sub-micron filaments via melt electrospinning writing. *Biofabrication* **2015**, *7* (3), 035002.
33. Hrynevich, A.; Elçi, B. Ş.; Haigh, J. N.; McMaster, R.; Youssef, A.; Blum, C.; Blunk, T.; Hochleitner, G.; Groll, J.; Dalton, P. D., Dimension-Based Design of Melt Electrowritten Scaffolds. *Small* **2018**, *14* (22), 1800232.
34. Visser, J.; Melchels, F. P. W.; Jeon, J. E.; van Bussel, E. M.; Kimpton, L. S.; Byrne, H. M.; Dhert, W. J. A.; Dalton, P. D.; Huttmacher, D. W.; Malda, J., Reinforcement of hydrogels using three-dimensionally printed microfibrils. *Nature Communications* **2015**, *6* (1), 6933.
35. Carrodeguas, R. G.; De Aza, S., α -Tricalcium phosphate: Synthesis, properties and biomedical applications. *Acta Biomaterialia* **2011**, *7* (10), 3536-3546.
36. Dziadek, M.; Kudlackova, R.; Zima, A.; Slosarczyk, A.; Ziabka, M.; Jelen, P.; Shkarina, S.; Cecilia, A.; Zuber, M.; Baumbach, T.; Surmeneva, M. A.; Surmenev, R. A.; Bacakova, L.; Cholewa-Kowalska, K.; Douglas, T. E. L., Novel multicomponent organic-inorganic WPI/gelatin/CaP hydrogel composites for bone tissue engineering. *Journal of Biomedical Materials Research Part A* **2019**, *107* (11), 2479-2491.

37. Sadowska, J.-M.; Guillem-Marti, J.; Montufar, E. B.; Espanol, M.; Ginebra, M.-P., Biomimetic Versus Sintered Calcium Phosphates: The *In Vitro* Behavior of Osteoblasts and Mesenchymal Stem Cells. *Tissue Engineering Part A* **2017**, *23* (23-24), 1297-1309.
38. Lode, A.; Meissner, K.; Luo, Y.; Sonntag, F.; Glorius, S.; Nies, B.; Vater, C.; Despang, F.; Hanke, T.; Gelinsky, M., Fabrication of porous scaffolds by three-dimensional plotting of a pasty calcium phosphate bone cement under mild conditions. *Journal of Tissue Engineering and Regenerative Medicine* **2014**, *8* (9), 682-693.
39. Epple, M., Review of potential health risks associated with nanoscopic calcium phosphate. *Acta Biomaterialia* **2018**, *77*, 1-14.
40. Bobo, D.; Robinson, K. J.; Islam, J.; Thurecht, K. J.; Corrie, S. R., Nanoparticle-Based Medicines: A Review of FDA-Approved Materials and Clinical Trials to Date. *Pharmaceutical Research* **2016**, *33* (10), 2373-2387.
41. Zhou, H.; Lee, J., Nanoscale hydroxyapatite particles for bone tissue engineering. *Acta Biomaterialia* **2011**, *7* (7), 2769-2781.
42. Melchels, F. P. W.; Blokzijl, M. M.; Levato, R.; Peiffer, Q. C.; Ruijter, M. d.; Hennink, W. E.; Vermonden, T.; Malda, J., Hydrogel-based reinforcement of 3D bioprinted constructs. *Biofabrication* **2016**, *8* (3), 035004.
43. Schindelin, J.; Arganda-Carreras, I.; Frise, E.; Kaynig, V.; Longair, M.; Pietzsch, T.; Preibisch, S.; Rueden, C.; Saalfeld, S.; Schmid, B.; Tinevez, J.-Y.; White, D. J.; Hartenstein, V.; Eliceiri, K.; Tomancak, P.; Cardona, A., Fiji: an open-source platform for biological-image analysis. *Nature Methods* **2012**, *9* (7), 676-682.
44. Ginebra, M. P.; Fernández, E.; De Maeyer, E. A. P.; Verbeeck, R. M. H.; Boltong, M. G.; Ginebra, J.; Driessens, F. C. M.; Planell, J. A., Setting Reaction and Hardening of an Apatitic Calcium Phosphate Cement. *Journal of Dental Research* **1997**, *76* (4), 905-912.
45. Karageorgiou, V.; Kaplan, D., Porosity of 3D biomaterial scaffolds and osteogenesis. *Biomaterials* **2005**, *26* (27), 5474-5491.
46. Gleeson, J. P.; Plunkett, N. A.; O'Brien, F. J., Addition of hydroxyapatite improves stiffness, interconnectivity and osteogenic potential of a highly porous collagen-based scaffold for bone tissue regeneration. *Eur Cell Mater* **2010**, *20*, 218-30.
47. Levato, R.; Webb, W. R.; Otto, I. A.; Mensinga, A.; Zhang, Y.; van Rijen, M.; van Weeren, R.; Khan, I. M.; Malda, J., The bio in the ink: cartilage regeneration with bioprintable hydrogels and articular cartilage-derived progenitor cells. *Acta Biomaterialia* **2017**, *61*, 41-53.
48. Van Den Bulcke, A. I.; Bogdanov, B.; De Rooze, N.; Schacht, E. H.; Cornelissen, M.; Berghmans, H., Structural and Rheological Properties of Methacrylamide Modified Gelatin Hydrogels. *Biomacromolecules* **2000**, *1* (1), 31-38.
49. Castilho, M.; Feyen, D.; Flandes-Iparraguirre, M.; Hochleitner, G.; Groll, J.; Doevendans, P. A. F.; Vermonden, T.; Ito, K.; Sluijter, J. P. G.; Malda, J., Melt Electrospinning Writing of Poly-Hydroxymethylglycolide-co-ε-Caprolactone-Based Scaffolds for Cardiac Tissue Engineering. *Advanced Healthcare Materials* **2017**, *6* (18), 1700311.
50. Schuurman, W.; Levett, P. A.; Pot, M. W.; van Weeren, P. R.; Dhert, W. J. A.; Hutmacher, D. W.; Melchels, F. P. W.; Klein, T. J.; Malda, J., Gelatin-Methacrylamide Hydrogels as Potential Biomaterials for Fabrication of Tissue-Engineered Cartilage Constructs. *Macromolecular Bioscience* **2013**, *13* (5), 551-561.
51. Lim, K. S.; Schon, B. S.; Mekhileri, N. V.; Brown, G. C. J.; Chia, C. M.; Prabakar, S.; Hooper, G. J.; Woodfield, T. B. F., New Visible-Light Photoinitiating System for Improved Print Fidelity in Gelatin-Based Bioinks. *ACS Biomaterials Science & Engineering* **2016**, *2* (10), 1752-1762.
52. Lim, K. S.; Levato, R.; Costa, P. F.; Castilho, M. D.; Alcalá-Orozco, C. R.; van Dorenmalen, K. M. A.; Melchels, F. P. W.; Gawlitta, D.; Hooper, G. J.; Malda, J.; Woodfield, T. B. F., Bio-resin for high resolution lithography-based biofabrication of complex cell-laden constructs. *Biofabrication* **2018**, *10* (3), 034101.
53. Ribeiro, A.; Blokzijl, M. M.; Levato, R.; Visser, C. W.; Castilho, M.; Hennink, W. E.; Vermonden, T.; Malda, J., Assessing bioink shape fidelity to aid material development in 3D bioprinting. *Biofabrication* **2017**, *10* (1), 014102.

54. Ajaxon, I.; Acciaioli, A.; Lionello, G.; Ginebra, M.-P.; Öhman-Mägi, C.; Baleani, M.; Persson, C., Elastic properties and strain-to-crack-initiation of calcium phosphate bone cements: Revelations of a high-resolution measurement technique. *Journal of the Mechanical Behavior of Biomedical Materials* **2017**, *74*, 428-437.
55. Hannink, G.; Arts, J. J. C., Bioresorbability, porosity and mechanical strength of bone substitutes: What is optimal for bone regeneration? *Injury* **2011**, *42*, S22-S25.
56. Dorozhkin, S. V., Self-setting calcium orthophosphate formulations. *Journal of functional biomaterials* **2013**, *4* (4), 209-311.
57. Malda, J.; Benders, K. E. M.; Klein, T. J.; de Grauw, J. C.; Kik, M. J. L.; Hutmacher, D. W.; Saris, D. B. F.; van Weeren, P. R.; Dhert, W. J. A., Comparative study of depth-dependent characteristics of equine and human osteochondral tissue from the medial and lateral femoral condyles. *Osteoarthritis and Cartilage* **2012**, *20* (10), 1147-1151.
58. Hurtig, M. B.; Buschmann, M. D.; Fortier, L. A.; Hoemann, C. D.; Hunziker, E. B.; Jurvelin, J. S.; Mainil-Varlet, P.; McIlwraith, C. W.; Sah, R. L.; Whiteside, R. A., Preclinical Studies for Cartilage Repair: Recommendations from the International Cartilage Repair Society. *CARTILAGE* **2011**, *2* (2), 137-152.
59. McGowan, K. B.; Stieglman, G., Regulatory Challenges for Cartilage Repair Technologies. *CARTILAGE* **2012**, *4* (1), 4-11.
60. Khattak, S. F.; Bhatia, S. R.; Roberts, S. C., Pluronic F127 as a Cell Encapsulation Material: Utilization of Membrane-Stabilizing Agents. *Tissue Engineering* **2005**, *11* (5-6), 974-983.
61. Golub, E. E.; Boesze-Battaglia, K., The role of alkaline phosphatase in mineralization. *Current Opinion in Orthopaedics* **2007**, *18* (5).
62. Castilho, M.; Hochleitner, G.; Wilson, W.; van Rietbergen, B.; Dalton, P. D.; Groll, J.; Malda, J.; Ito, K., Mechanical behavior of a soft hydrogel reinforced with three-dimensional printed microfibre scaffolds. *Scientific Reports* **2018**, *8* (1), 1245.
63. Boere, K. W. M.; Visser, J.; Seyednejad, H.; Rahimian, S.; Gawlitta, D.; van Steenberghe, M. J.; Dhert, W. J. A.; Hennink, W. E.; Vermonden, T.; Malda, J., Covalent attachment of a three-dimensionally printed thermoplastic to a gelatin hydrogel for mechanically enhanced cartilage constructs. *Acta Biomaterialia* **2014**, *10* (6), 2602-2611.
64. Shepherd, D. E.; Seedhom, B. B., The 'instantaneous' compressive modulus of human articular cartilage in joints of the lower limb. *Rheumatology* **1999**, *38* (2), 124-132.
65. St-Pierre, J.-P.; Gan, L.; Wang, J.; Pilliar, R. M.; Grynblas, M. D.; Kandel, R. A., The incorporation of a zone of calcified cartilage improves the interfacial shear strength between *in vitro*-formed cartilage and the underlying substrate. *Acta Biomaterialia* **2012**, *8* (4), 1603-1615.
66. Daly, A. C.; Critchley, S. E.; Rencsok, E. M.; Kelly, D. J., A comparison of different bioinks for 3D bioprinting of fibrocartilage and hyaline cartilage. *Biofabrication* **2016**, *8* (4), 045002.
67. Levett, P. A.; Melchels, F. P. W.; Schrobback, K.; Hutmacher, D. W.; Malda, J.; Klein, T. J., Chondrocyte redifferentiation and construct mechanical property development in single-component photocrosslinkable hydrogels. *Journal of Biomedical Materials Research Part A* **2014**, *102* (8), 2544-2553.
68. Akkineni, A. R.; Luo, Y.; Schumacher, M.; Nies, B.; Lode, A.; Gelinsky, M., 3D plotting of growth factor loaded calcium phosphate cement scaffolds. *Acta Biomaterialia* **2015**, *27*, 264-274.
69. de Ruijter, M.; Hrynevich, A.; Haigh, J. N.; Hochleitner, G.; Castilho, M.; Groll, J.; Malda, J.; Dalton, P. D., Out-of-Plane 3D-Printed Microfibers Improve the Shear Properties of Hydrogel Composites. *Small* **2018**, *14* (8), 1702773.
70. Bas, O.; De-Juan-Pardo, E. M.; Meinert, C.; D'Angella, D.; Baldwin, J. G.; Bray, L. J.; Wellard, R. M.; Kollmannsberger, S.; Rank, E.; Werner, C.; Klein, T. J.; Catelas, I.; Hutmacher, D. W., Biofabricated soft network composites for cartilage tissue engineering. *Biofabrication* **2017**, *9* (2), 025014.

SUPPLEMENTARY INFORMATION

Supplementary methods

X-ray diffraction pattern

X-ray diffraction patterns were recorded with a Bruker D8 Advance system (Bruker, Karlsruhe, Germany) in a 2Theta range from 20–40° with Cu K α radiation (40 KV/ 40 mA) with a step size of 0.02° and a total measurement time of 1 s/step. Quantification was performed by Rietveld refinement analysis using Topas software (Bruker, Germany). The amorphous content of the samples was calculated using the G-factor method with a crystalline corundum reference according to Hurle et al [S1].

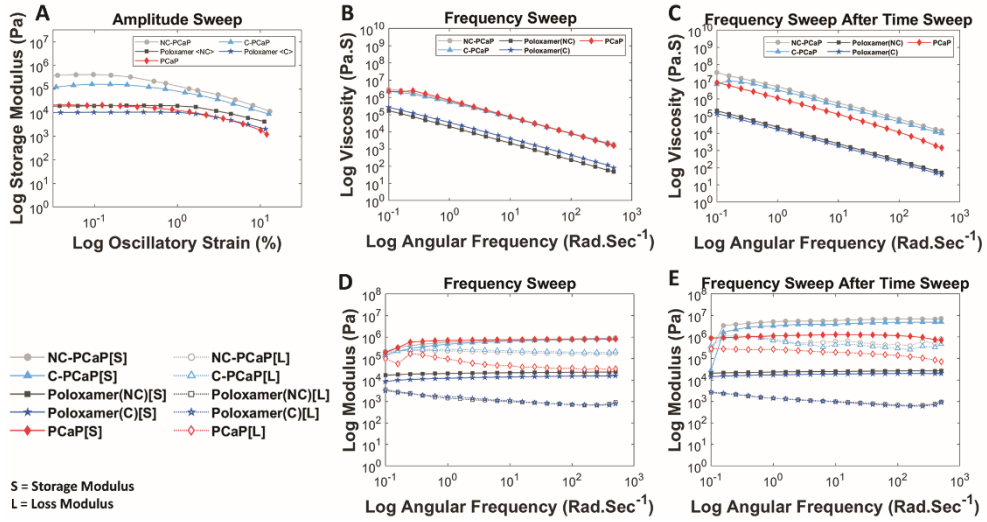
Supplementary data

Amount of cells	Day 3	Day 7	Day 14
Mean	1602.62	6568.07	10201.17
Standard Deviation	± 570.00	± 3256.64	± 5992.86

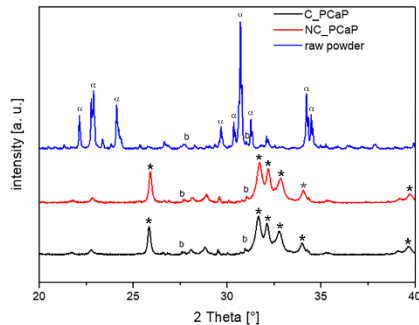
Supplementary Table 1. Equine MSCs proliferation on C-pCaP scaffolds during cultivation for 14 days.

Sample	Hydroxyapatite [%]	α -TCP [%]	β -TCP [%]
Powder	1.5	94.2	4.3
C-pCaP	95.8	2.1	2.1
NC-pCaP	95.2	1.8	3.0

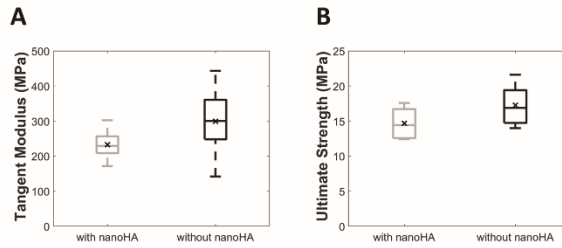
Supplementary Table 2: Quantification of the XRD patterns by Rietveld refinement (TOPAS software, Bruker, USA), showing the conversion of α -TCP to an apatitic phase. No relevant difference was found between the NC and C cement after the setting of the ceramic powder.



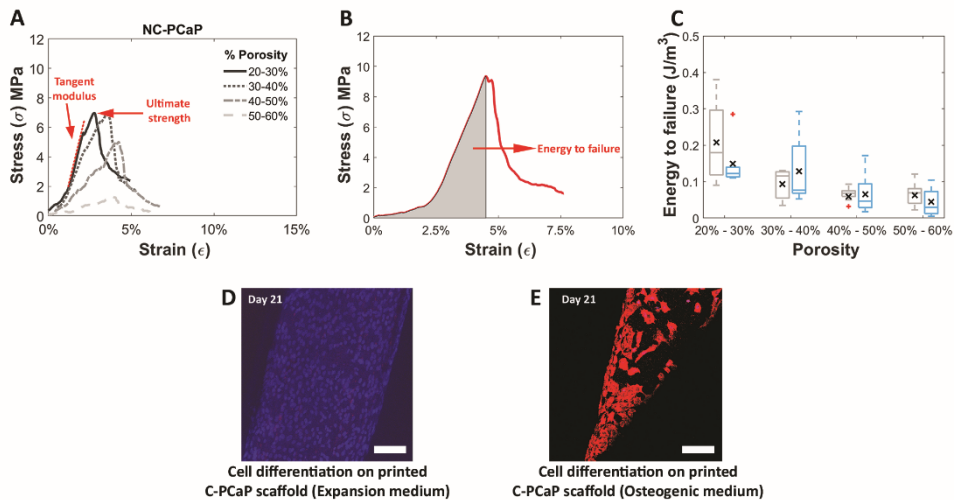
Supplementary Figure S1. A; Amplitude sweep representing LVR, B; Frequency sweep (relationship between angular frequency and modulus), C; Frequency sweep (relationship between angular frequency and complex viscosity), D ; Frequency sweep (relationship between angular frequency and modulus)(same material after performing time sweep test), E; Frequency sweep (relationship between angular frequency and complex viscosity) (same material after performing time sweep test). S = Storage modulus, L = Loss Modulus



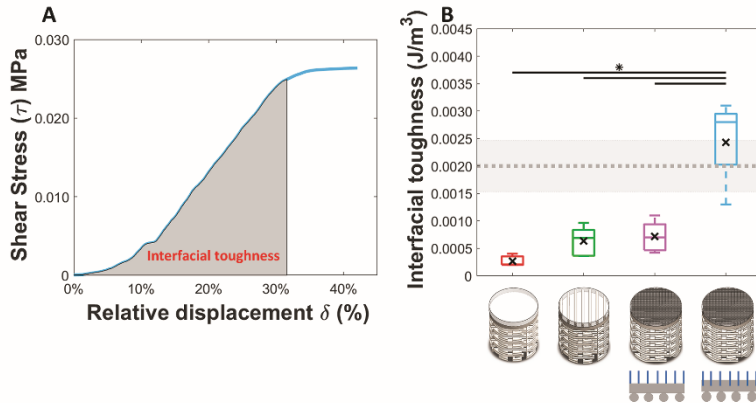
Supplementary Figure S2. X-ray diffraction patterns of raw powder and scaffolds. Diffraction peaks in the raw powder can be assigned to crystalline α -tricalcium phosphate (PDF-No.: 09-0438) with a minor fraction of β -tricalcium phosphate (PDF-No.: 09-0169, marked with “b”), possibly present as minor impurity in the α -TCP particle formulation. The fabricated scaffolds consisted of low crystalline hydroxyapatite (PDF-No.: 09-0432) from hydrolysis of α -TCP, as shown by the typical broad peaks peculiar of CDHA formation [S2], while the β -TCP fraction remained unreacted. (α = α -TCP, b = β -TCP, * = CDHA)



Supplementary Figure S3. A; Tangent Modulus of hardened structure produced from composition of α -TCP with and without nano-hydroxyapatite, B; Ultimate strength of hardened structure produced from composition of α -TCP with and without nano-hydroxyapatite. No significant difference were found between the two groups, suggesting that the added nanoHA does not have a relevant impact on the compressive properties of the produced cement. (n = 6 for each group)



Supplementary Figure S4. A; Representative stress-strain curves of NC-pCaP scaffolds at different porosities showing how to calculate tangent modulus and ultimate strength. B; Representative stress-strain curves showing how to calculate energy to failure. C; Energy to failure of NC-pCaP paste (grey) and C-pCaP (blue) scaffolds with different porosities. D; Merged image between fluorescence staining of nucleus (dapi: blue) and osteonectin protein (osteonectin: red) of equine MSCs that were cultured on a C-pCaP scaffold for 21 days in an expansion medium showed no sign of osteogenic upregulation. (Scale Bar = 100 μ m.) E; Merged image between fluorescence staining of nucleus (dapi: blue) and osteonectin protein (osteonectin: red) of equine MSCs that were cultured on a C-pCaP scaffold for 21 days in an osteogenic supplement medium showed sign of osteogenic upregulation. (Scale Bar = 100 μ m.)



Supplementary Figure S5. A; Representative area under stress-displacement curve for calculation energy to failure. B; Interfacial toughness at the interface between chondral and bony compartment of an engineered osteochondral unit showing alterations due to differences in either interfacial architecture or compositions. The different construct types: gelMA on ceramic (un-modified surface; red), gelMA on ceramic (modified surface; bright green), microfibre reinforced gelMA on ceramic (non-anchor fiber; pink), microfibre reinforced gelMA on ceramic (anchor fiber; blue) and only gelMA hydrogel (mean (grey dotted line) \pm SD (grey filled area))

SUPPLEMENTARY VIDEO SV1.

Video showing the open and interconnected porosity within the inner structure of the porous 3D printed scaffolds, as shown through a series of μ -CT sections of the constructs.

(This could be access through: <https://iopscience.iop.org/article/10.1088/1758-5090/ab69d9#supplementarydata>)

SUPPLEMENTARY REFERENCES

[S1] Hurle, K.; Neubauer, J.; Bohner, M.; Doebelin, N.; Goetz-Neunhoeffler, F, Effect of amorphous phases during the hydraulic conversion of alpha-TCP into calcium-deficient hydroxyapatite, *Acta Biomaterialia*, 2014, 10, 3931-3941

[S2] Barba A, Diez-Escudero A, Maazouz Y, Rappe K, Espanol M, Montufar EB, Bonany M, Sadowska JM, Guillem-Marti J, Öhman-Mägi C, Persson C, Manzanares MC, Franch J, Ginebra MP. Osteoinduction by Foamed and 3D-Printed Calcium Phosphate Scaffolds: Effect of Nanostructure and Pore Architecture. *ACS Appl Mater Interfaces*. 9(48) (2017) 41722-36.

CHAPTER 4

Orthotopic bone regeneration within 3D printed bioceramic scaffolds with region-dependent porosity gradients in an equine model

Paweena Diloksumpan^{1*}, Rafael Vindas Bolaños^{2*}, Stefan Cokelaere¹,
Behdad Pouran³, Janny de Grauw¹, Mattie van Rijen³,
Paul René van Weeren¹, Riccardo Levato^{1,3}, and Jos Malda^{1,3}

Published in *Advanced Healthcare Materials* (2020)

April :1901807,

DOI 10.1002/adhm.201901807

* These authors contributed equally to this work

¹ Department of Clinical Sciences, Faculty of Veterinary Medicine, Utrecht University, Yalelaan 1, 3584 CL, Utrecht, The Netherlands

² Escuela de Medicina Veterinaria, Universidad Nacional Costa Rica, Heredia, Lagunilla, Barreal de Heredia, 86-3000, Costa Rica

³ Department of Orthopaedics and Regenerative Medicine Center, University Medical Center Utrecht, Utrecht University, Heidelberglaan 100, 3584CX, Utrecht, The Netherlands

ABSTRACT

The clinical translation of three-dimensional printed bioceramic scaffolds with tailored architectures hold great promises towards the regeneration of bone to heal critical-size defects. Herein, the long-term *in vivo* performance of printed hydrogel-ceramic composites made of methacrylated-oligocaprolactone-poloxamer and low-temperature self-setting calcium-phosphates is assessed in a large animal model. Scaffolds printed with different internal architectures, displaying either a designed porosity gradient or a constant pore distribution, were implanted in equine tuber coxae critical size defects. Bone ingrowth was challenged and facilitated only from one direction via encasing the bioceramic in a polycaprolactone shell. After 7 months, total new bone volume and scaffold degradation were significantly greater in structures with constant porosity. Interestingly, gradient scaffolds showed lower extent of remodeling and regeneration even in areas having the same porosity as the constant scaffolds. Low regeneration in distal regions from the interface with native bone impaired ossification in proximal regions of the construct, suggesting that anisotropic architectures modulate the crosstalk between distant cells within critical-size defects. The study provides key information on how engineered architectural patterns impact osteoregeneration *in vivo*, and also indicates the equine tuber coxae as promising orthotopic model for studying materials stimulating bone formation.

Keywords: low-temperature setting calcium phosphate, biofabrication, porous architecture, bone regeneration, equine model

INTRODUCTION

In the quest for methods to heal large bone defects, bioceramic-based scaffolds can overcome current key challenges, such as limited donor material availability or donor site morbidity that are associated with the use of allografts and autografts. Due to their composition mimics that of the inorganic phase of the native bone and because of their proven osteoconductivity, bioceramics based on calcium phosphates (CaP) have been extensively evaluated as conduits to guide bone regeneration¹. Focus during the last decades has been on how properties, like solubility, particle size, crystallinity, surface roughness and surface charge of CaP-based implants, may affect their bioactivity and interaction with host tissue. Clearly, both chemical and physical properties of these implants may, by themselves or through their interactions, affect the rate and quality of new tissue formation².

The influence of scaffold porosity on the regenerative process has also been a major topic of investigation^{3,4}. Recent studies have highlighted how the pore size, shape and interconnections are essential in driving the exchange of nutrients and bone remodeling, cellular and vascular infiltration, progenitor cell differentiation, material degradation, and immunological response^{5, 6}. Although specific pore features, such as size, geometry, and directionality, can to a certain extent be controlled with conventional scaffold fabrication techniques, recent developments in additive manufacturing (AM) technologies have greatly enhanced the capacity of designing and fine-tuning the specific scaffold architecture.

An anisotropic pore distribution can, for example, be introduced in printed structures to mimic the native gradient from highly porous cancellous bone to less porous cortical bone in the subchondral bone layer in implants for osteochondral repair in articulating joints^{7, 8}. However, even though a pore size of over 300 μm has often been recommended for facilitating bone and vascular ingrowth within porous scaffolds⁹, the *in vivo* performance of anisotropic yet geometrically defined porous printed ceramic implants has not been fully explored.

Recently, low-temperature self-setting CaP cements based on alpha-tricalcium phosphate (α -TCP) microparticles, which are also used as injectable bone cements¹⁰, have emerged as promising materials for printable ceramic formulations. In fact, by accurately controlling the rheology of the cement precursor paste, these cements can be utilized as a biomaterial ink¹¹ for extrusion-based three-dimensional (3D) printing. After printing, the printed structure is exposed to a humidified environment at physiological temperature to initiate the setting reaction by converting the α -TCP paste into calcium deficient hydroxyapatite cement (CDHA). This is a mild reaction that permits co-printing of such CaP cements with cell-laden bioinks to generate composite constructs¹². This class of materials have already been successfully exploited to obtain printed CaP cements with osteoinductive properties, either by encapsulation of growth factors in the paste precursor¹³ or by tuning printable CaP nano-topography¹⁴. As new three-dimensionally (3D) -printed CDHA-based scaffolds with controllable macro- and microscale architectures are becoming available, it

becomes increasingly important to investigate their relative regenerative potential not only *in vitro*, but also in reliable animal models^{15, 16}.

In orthopedic regenerative medicine, the evaluation of novel interventions in large animal models is a pre-requisite for their eventual human clinical application. However, at the same time, such human pre-clinical studies constitute end-stage testing for veterinary application in the animal species involved¹⁷⁻¹⁹. Much like humans and unlike other more common large animal models like goats or sheep, horses participate as athletes in competitions, in which bone and osteochondral injuries regularly lead to both great economic losses and serious animal welfare concerns²⁰⁻²². This makes studies addressing bone regenerative capacity in the horse not only of great interest for human medicine, but also for the equestrian industry and equine health care^{18, 19}.

This study aimed at the evaluation of the *in vivo* bone regenerative potential of a novel CaP-based scaffold with a variation in pore distribution in an equine model. Low temperature setting CaP-based bioceramic-hydrogel composite scaffolds, consisting of α -TCP, hydroxyapatite nanoparticles (nano-HA) and a biodegradable, crosslinkable poloxamer derivative were fabricated via 3D printing, to create scaffolds with either an isotropic pore distribution or a anisotropic gradient of porosity. Finally, to better assess the ability of bone to grow within large constructs, the regenerative process was challenged by encasing the CaP scaffold within a polycaprolactone (PCL) cage, which prevented infiltration of progenitor cells from the periosteum and allowed preferentially unidirectional tissue ingrowth. The scaffolds were implanted orthotopically in the tuber coxae of horses and bone regeneration was studied over a 7-months period.

RESULTS AND BONE REGENERATION WITHIN 3D PRINTED BIOCERAMIC

Implants and postoperative clinical data

The implants consisted of printable hydrogel-calcium phosphate ceramic composite scaffolds (pCaP) encased within a non-porous PCL chamber, as detailed in the experimental section. Scaffolds were produced to obtain constructs characterized either by a discrete gradient or constant pore distribution in the direction of layer-by-layer deposition of the printable material (z-direction) (**Figure 1**). The gradient scaffolds were characterized by four regions with decreasing distances between the pCaP strands (500 μm , 400 μm , 300 μm and 200 μm), whereas the constant scaffolds displayed consistently a 500 μm fiber spacing. Total porosities of the fabricated scaffolds were $40.03 \pm 1.78 \%$ and $51.14 \pm 0.78 \%$ for the gradient and constant architectures, respectively.

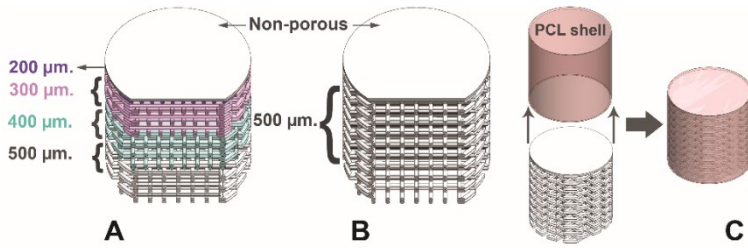


Figure 1. Schematic representation of the cross-section of the pCaP scaffolds with (A) gradient and (B) constant pore architecture. (C) Representation of the PCL-encased pCaP scaffolds.

Both types of scaffolds were implanted at the tuber coxae of each horse by randomly transplanting each type of scaffold in each side (1 defect/side) (**Figure 2**). After 7 months, the surgical incisions healed without complications, and no local inflammatory reactions (heat, swelling, tenderness) or signs of pain or discomfort were observed at any time. Likewise, the animals did not experience any detectable pain or lameness during the post-operative period, the rehabilitation period, or other parts during the course of the experiment. Clinical and blood parameters remained within the normal physiologic limits (**Supplementary Table ST1**). Only in one case, partial wound dehiscence occurred during the recovery period, and after re-suturing, the wound healed without further complications and the correct positioning of the implant at the defect site was confirmed by radiography. At the time of euthanasia, surgical sites were easily identified, both visually and by palpation. In some cases, a slight depression was observed at the site of the defects; in others there was some thickening because of scar tissue formation. After removal of the overlying soft tissues, the implants appeared all well attached to the surrounding osseous tissue. There were no signs of any inflammation or otherwise adverse reactions.

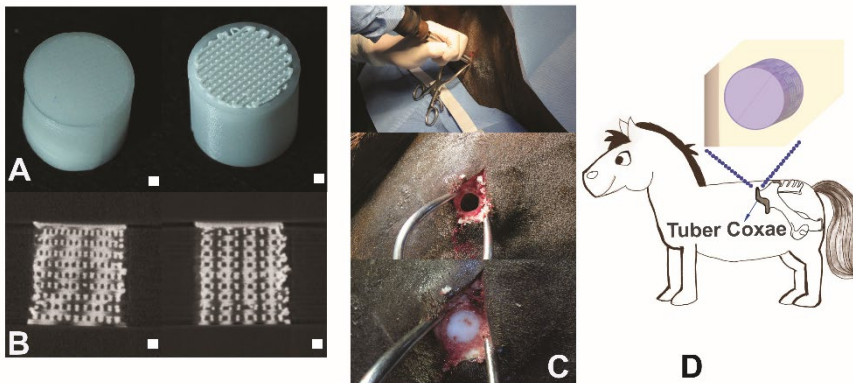


Figure 2. Visualization of the implant and surgical implantation procedure. (A) Top (left) and bottom (right) view of the pCaP implants embedded into the PCL shell. (B) Representative μ -CT images of an implant with gradient pore size (left) and constant pore size (right) before implantation. (C) Sequence of implantation of the scaffolds in the tuber coxae, including drilling and exposure of the defect, followed by scaffold implantation. (D) Schematic representation of the implant location in the tuber coxae. Scale bar = 1 mm.

Quantitative analyses

Upon retrieval of the implants at the end point of the experiment, four scaffolds per group could be safely used for the analysis of the effect of the porous architecture on osteo-regeneration and displayed a structurally integer PCL cage, as observed via micro computed tomography (μ -CT) (**Supplementary Figure S1**). First of all, our data confirms that the material and the printed scaffolds produced with it have high potential to guide bone regeneration. Among the structures in which the integrity of the PCL cage was compromised, new bone could readily invade the constructs, even resulting in a complete bridging of the defect (**Figure 3**).

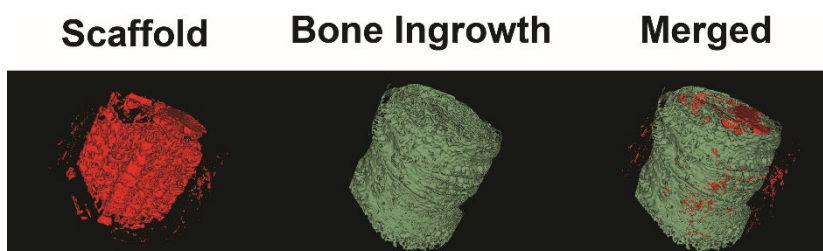


Figure 3. Formation of new bone throughout the whole volume of a constant porosity scaffold, as observed via μ -CT, in a sample in which the PCL cage was damaged and had permitted bone ingrowth from the side.

For the quantitative determination of neo-bone formation, the scaffolds were divided into three zones: zone 1 (basal part of pCaP scaffold); zone 2 (middle part of pCaP scaffold); and zone 3 (uppermost part of pCaP scaffold) (**Figure 4A**). The amount of new bone ingrowth in the constant porosity scaffold group ($85.13 \pm 34.62 \text{ mm}^3$) was significantly larger than for the gradient scaffold group ($25.03 \pm 8.96 \text{ mm}^3$) (**Figure 4B**). This difference was also evident in zones 1 (constant: $39.87 \pm 22.95 \text{ mm}^3$; gradient: $13.68 \pm 1.18 \text{ mm}^3$), 2 (constant: $26.16 \pm 8.19 \text{ mm}^3$; gradient: $9.54 \pm 3.13 \text{ mm}^3$), and zone 3 (constant: $19.13 \pm 7.36 \text{ mm}^3$; gradient: $7.81 \pm 4.90 \text{ mm}^3$) (**Figure 4C**). Additionally, the bone distribution in each printed layer varied, as a function of the distance to the scaffold-native bone interface (basal side of the scaffold). In terms of ratio over the Volume of Interest (VOI), constant porosity scaffolds showed more bone volume (constant: $22.05 \pm 6.18\%$; gradient: $10.67 \pm 2.65\%$), as well as non-mineralized repair tissue (constant: $48.90 \pm 8.20\%$; gradient: $38.90 \pm 4.79\%$) (**Figure 4D**). The percentage of remaining ceramic material was significantly lower in the constant porosity group ($29.05 \pm 3.98\%$) than in the gradient group ($50.43 \pm 3.62\%$) (**Figures 4D-E**), suggesting a faster resorption of the material. Quantitative analysis of the total volume of ceramic before and after implantation (**Figures 4E-F**) from microcomputed tomography (μ -CT) data revealed an estimated percentage of scaffold degradation of $57.92 \pm 11.32\%$ for the constant scaffold group and of $33.47 \pm 8.67\%$ for the gradient scaffold.

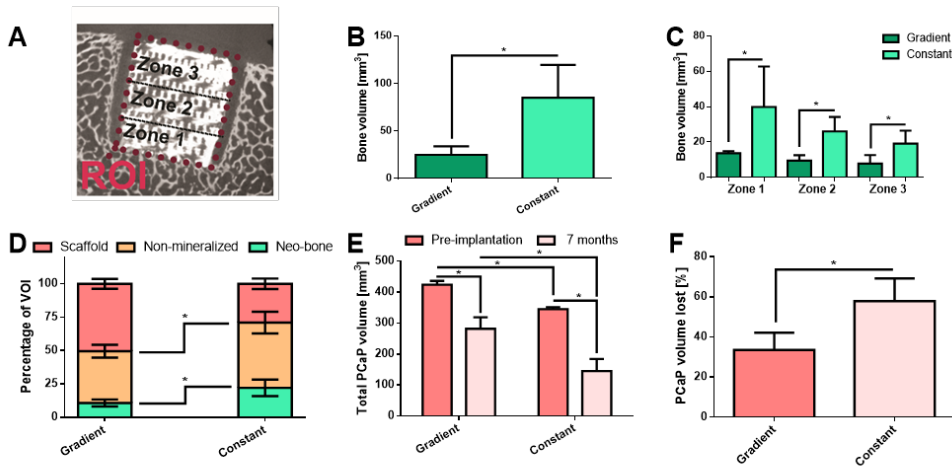


Figure 4. Quantitative analysis of bone regeneration, showing (A) the three zones that were analyzed inside the scaffold; the quantification of new bone volume (B) within the defect and (C) within each zone, and (D) ratio of the VOI occupied by new bone, non-mineralized tissue and remnants of pCaP scaffold after 7 months *in vivo*. (E, F) Degradation of both types of scaffolds was highlighted by the quantification of the pCaP volume prior to implantation and at the end of the experiment. Asterisks indicate $p < 0.05$.

Three-dimensional (3D) reconstruction images from μ -CT data (**Figure 5**) showed the distribution of new bone formation in all scaffolds. The spatial distribution of the neo-tissue in the planes perpendicular to the longitudinal axis of the scaffold was analyzed in correspondence with the 3 main zones. Notably, new bone formation between the basal periphery and the transitional zone between zone 2 and zone 3 of the scaffold was more homogeneous in the constant scaffold than in the gradient scaffold. Bone formation appeared less uniform in zone 3 for both scaffold types, with the constant pore group having an overall considerably higher amount of neo-bone tissue.

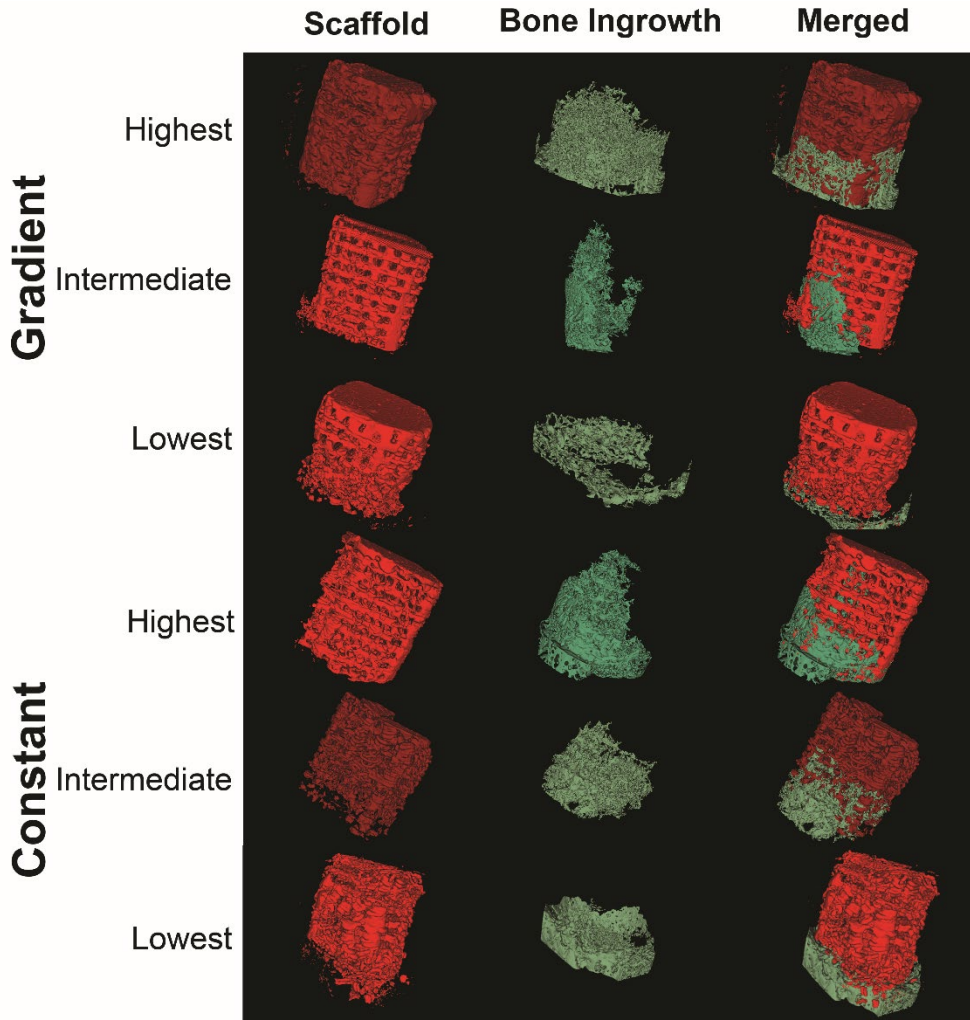


Figure 5. Representative μ -CT 3D reconstruction of the samples with highest, average, and lowest new bone formation in scaffolds with gradient and constant porosity in which the structural integrity of the PCL cage was preserved over the course of the experiment.

Histological analysis of cell infiltration and new bone and vasculature regeneration

Macroscopic assessment

Once formalin-fixed samples were cut transversely, the positions of the implant were easily visible. From cross-sectional surface, the PCL shells were visible in all samples as opaque white colored struts surrounding the area of the ceramic scaffold (**Figure 6**).

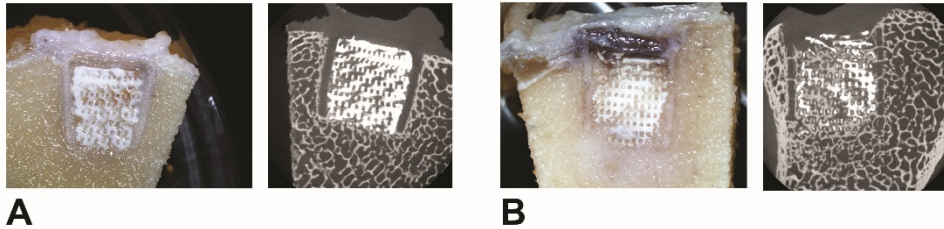


Figure 6. Representative cross-sections and μ -CT sectioned graphs of formalin-fixed samples showing appearance of both gradient (A) and constant (B) porous implants with surrounding tissue.

Microscopic assessment: extent of bone healing

Microscopic analysis of the basic fuchsin and methylene blue stains of methyl methacrylate (MMA) embedded sections showed areas of new bone ingrowth within the macro-pores of the ceramic scaffolds in both gradient and constant scaffolds, displaying good attachment and integration between the neo-bone and the ceramic material (**Figure 7A**, **Supplementary Figure S2**). Histological analysis together with μ -CT images revealed the continuous connection between the host bone and the new bone ingrowth that penetrated into the scaffold from the host bone at the basal periphery of all scaffolds, regardless of the type of porosity, as well as the presence of non-calcified tissue, which was predominantly located in the regions of the scaffold further away from the interface with the native bone. The extent of new bone ingrowth varied per scaffold type. On the constant porosity scaffolds, new bone extended from the basal periphery of the scaffold, throughout the entire zone 2 to zone 3 (close to one side of the cylindrical wall) and towards the non-porous layer. In the gradient scaffolds, new bone extended to the middle region of zone 2 but not or hardly observed in zone 3. The newly formed bone inside the gradient porous scaffold was predominantly woven (immature) bone with some lamellar (mature) bone in zone 1 (**Supplementary Figure S3**). In the constant pore scaffolds both woven bone and lamellar bone were found, with a preponderance of lamellar bone, and found in higher amounts in all zones. Lamellar bone structures were found organized concentrically in a Haversian pattern around blood vessels, typical of native osteons (**Figure 7B**).

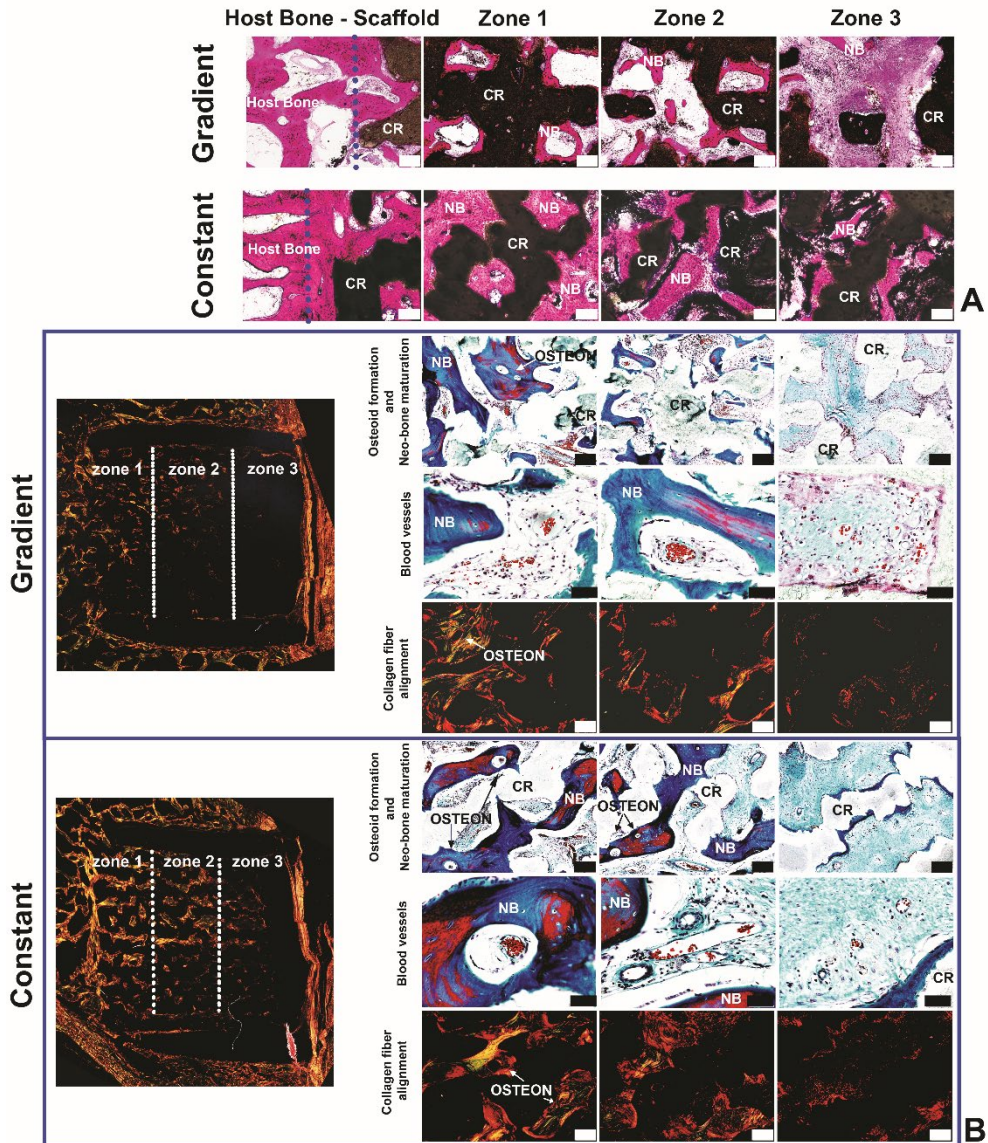


Figure 7. Histological assessment of neo-bone formation. (A) Basic fuchsin and methylene blue stainings of undecalcified sections of both gradient and constant porous structures after 7 months of implantation showed connection between the original host bone and newly formed bone, as well as the presence of neo-bone ingrowth in a zone-dependent fashion, with the lowest amount of bone present in the third zone of the gradient scaffolds. (B; 1st row) Goldner's trichrome staining of decalcified sections of both gradient and constant porous structures after 7 months of implantation displayed mineralized newly formed bone (bluish-green color), and non-mineralized newly formed bone (red color). Newly formed bone with a lamellar pattern surrounding haversian canals could be observed (black/white arrows (osteon)) (Scale bar = 200 μ m). (B; 2nd row) Goldner's trichrome staining showing blood vessel formation in each zone (Scale bar = 50 μ m). (B; 3rd row) Picrosirius staining of decalcified sections when observed using polarized light microscopy showing birefringence of collagen fibers (Scale bar = 200 μ m). CR = Ceramic Remnant, NB = New Bone.

New blood vessels from zone 1 to zone 3 in both constant and gradient scaffolds were prevalently located in newly formed lamellar bone and between the macro-pores of the ceramic printed structures. The number of blood vessels showed a (non-significant) decreasing trend from zone 1 to zone 3 in both architectures (**Figure 8A**). Regarding the dimension of the lumen, estimated by the length of the major axis, larger vessels were detected in the scaffolds with constant porosity (**Figure 8B**), across all zones. For gradient architectures, the sizes of blood vessels (mean \pm SD) were: 46.60 \pm 63.20 μm (zone 1), 27.95 \pm 23.29 μm (zone 2) and 23.91 \pm 21.74 μm (zone 3). For constant architectures, vessel sizes were: 77.53 \pm 66.12 μm (zone 1), 65.39 \pm 77.23 μm (zone 2) and 38.65 \pm 26.58 μm (zone 3).

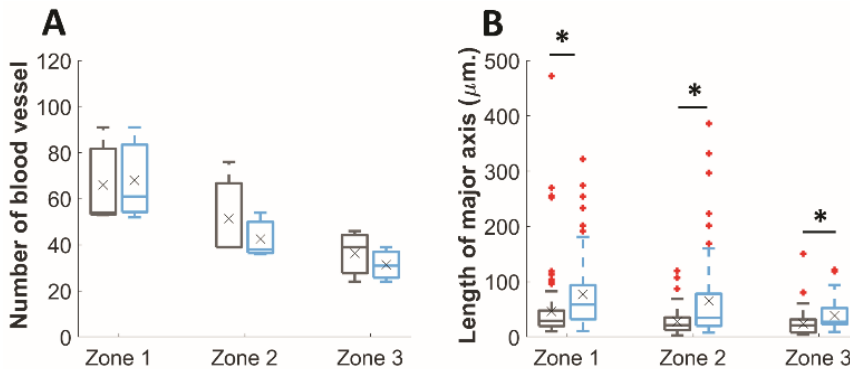


Figure 8. Vascularization of neo-bone. (A) Amount of blood vessels in each zone as observed from representative histological sections from both gradient and constant structure. (B) Dimension of blood vessels in each zone based on length of the major axis. Central lines in each box of the boxplot indicate median, whereas the black X indicates average, and the red + indicate outliers. All data point, including the outliers were included in the statistical analysis, and * indicate $p < 0.05$. (grey box = gradient, blue box = constant)

Microscopic assessment: cellular and molecular indicators of bone healing and remodeling

All types of scaffold showed areas of non-calcified tissue infiltration with different volumes in each zone. At the site of new bone formation, there were areas with positive staining for osteonectin, a marker of osteocytes, and a fundamental component of the extracellular matrix, which is able to bind collagen and known to facilitate bone mineralization²³, in indicating osteoblastic activity. Osteonectin-positive osteocytes were found embedded in lacunae inside newly-formed mineralized bone osteons, and Tartrate-resistant acid phosphatase (TRAP) - positive multinucleated cells were found in contact and in the proximity of the ceramic remnants, indicating osteoclastic activity that can mediate pCaP resorption (**Figure 9, Figures S4-S6**).

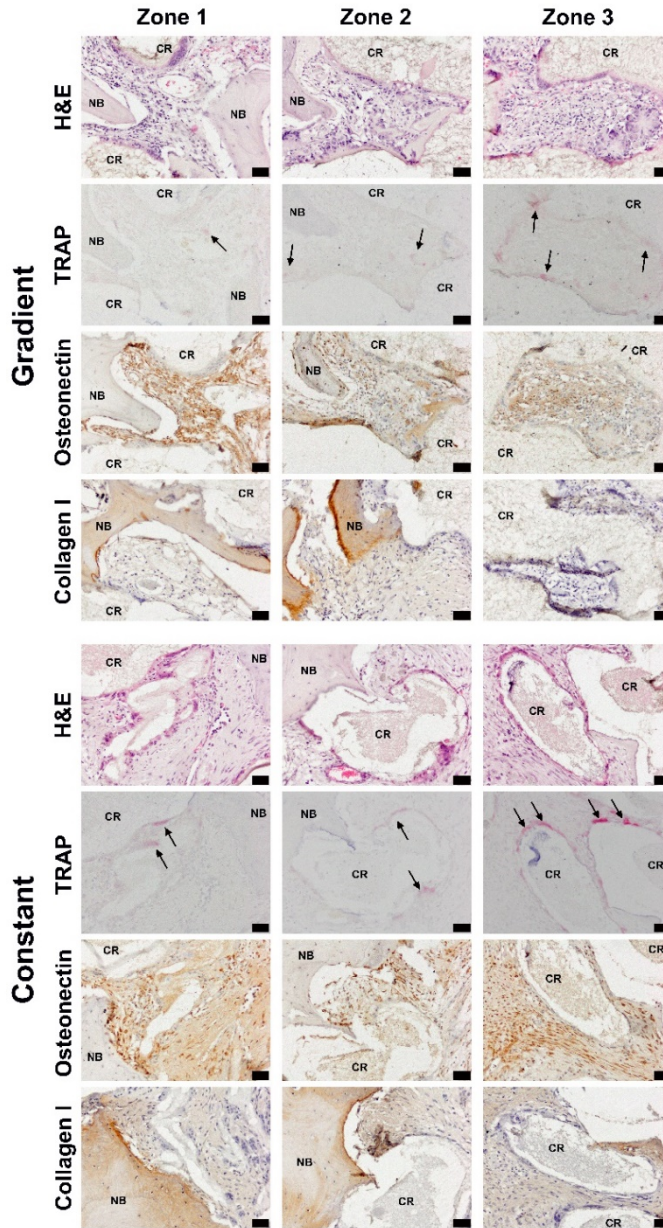


Figure 9. Hematoxylin and eosin (H&E), TRAP, osteonectin and type I collagen staining of decalcified sections of both gradient and constant porous structures after 7 months of implantation. Positions of cells involved in new bone ingrowth were identified. TRAP-positive multinucleated cells were found lying against the surface of the ceramic material. Osteonectin-positive cells were present at the sites of apposition of newly- formed bone and on the lining of newly-formed bone. Osteocytes were embedded in the lacunae of the bone (Scale bar = 100 μ m, CR = Ceramic Remnant, NB = New Bone).

In gradient structures, TRAP-positive multinucleated cells could be found throughout the scaffold from the basal periphery until zone 3, where they were found to be relatively higher in number than in the constant pore structure (**Supplementary Figure S6A**). For both type I collagen and osteonectin (**Figures S6B and S6C**), no significant difference could be detected between the gradient and constant porosity scaffolds, although areas with positive staining could be found mostly on the newly-formed bone, which in the gradient structure was situated mostly in zone 1 and declined from there to zones 2 and 3.

DISCUSSION

Native bone possesses a remarkable spontaneous regenerative ability, which is, however, not unlimited. Large bone defects caused by trauma, degenerative diseases or tumor resection, as well as non-healing fractures, are common problems in musculoskeletal medicine and require new strategies and biomaterials to help unlock, restore and guide bone repair. In this study, we investigated the long-term pro-regenerative performance of a new formulation of 3D-printed CaP-based bioceramic scaffolds in an *in vivo* equine model, as a function of the printed pore distribution.

All scaffolds showed the ability to promote neo-bone formation. Importantly, the incorporation and covalent crosslinking of the biodegradable poloxamer hydrogel, of which biocompatibility was previously demonstrated *in vitro*²⁴ and that ensured the printability and shape fidelity of the cement paste precursors, did not impede the healing process *in vivo*, and did not appear to provoke any detrimental inflammatory response. In both scaffold types, common features of the regenerative process can be identified. The volume within the pores of the scaffolds is filled with new bone and collagenous, non-calcified tissue. The latter is rich in osteonectin-positive cells, a marker of osteoblasts and a key matrix molecule for the initiation of the mineralization process²⁵. This osteonectin abundance suggests the formation of an osteoid-like tissue, which is a preliminary step for the maturation towards neo-bone²⁶. The amount of neo-bone and non-mineralized tissue differed between the gradient and the constant porosity scaffolds, with the latter displaying a significantly higher amount of both tissue types. This consistent difference in the degradation rate of the two architectures, albeit produced with the same materials, as well as its association with a difference in neo-bone deposition, suggests an active, cell-driven resorption. Indeed, there was ample osteoclast activity, as evidenced by the histological data (**Figure S3**). Osteoclast activity was higher in the more remote zones of both scaffold types (zones 2 and 3), possibly indicating an ongoing more intense remodeling activity in those areas that are still in an early stage of neo-bone development.

Previous studies on CDHA and nano-HA, the main components of the pCaP scaffolds tested in this study, have convincingly shown their osteoconductive capacity¹⁴. Also, our work shows an osteoconductive component of the regenerative process, as neo-bone is progressing through the scaffold from the host tissue, and integrates tightly with the ceramic remnants, but our analysis at a single time point provides no clear evidence for

intrinsic osteoinduction. In other studies, osteoinductive properties in the absence of exogenously added growth factors have already been demonstrated, first for nano-HA²⁷, but also for CDHA, depending on the nanostructure of the biomimetic apatite particles resulting from the hardening process of the cement²⁸. The superior performance of the constant porosity scaffolds as compared to the gradient group may not be intuitive. The gradient scaffolds do indeed present a lower degree of porosity, but all pores are well interconnected, with minimum size and geometry compatible with what is reported in the literature as necessary to permit bone ingrowth^{3, 4, 29}.

In this study, the bone restorative process promoted by the 3D printed scaffolds was challenged by encasing the pCaP scaffolds in a PCL shell, to prevent infiltration of progenitor cells from the periosteum, and to facilitate only unidirectional bone ingrowth. However, in some occurrences (2/7 for both groups), the integrity of the PCL cage was lost over time, resulting in bone ingrowth also from the sides of the scaffolds. While these samples are still useful to estimate the osteoconductive potential of the material, this led to the a net reduction of the sample size available to assess the effect of the porous architecture, although it did not compromise the overall analysis. To improve the consistency across donors, non-degradable materials may should be recommended for future studies. Interestingly, this approach could possibly simulate features of large bone defects, as given the fact that bone growth can be conducted only from one side, distal regions on the defect have impaired interaction with the front of bone repair. While bone possess a remarkable ability to self-heal, especially concerning small defects, as new bone can infiltrate neighboring defects, large defects, areas towards the center of the scaffold and further away from the native bone have more difficulties in receiving all cells and signals necessary to trigger the regenerative process. In a previous study on the degradation and osteoconductive properties of α - and β -Tricalcium phosphate, an 8mm-diameter titanium chamber was used to ensure equal space and prevent soft tissue interference³⁰.

In the specific environment of this study, the overall design and architecture of the macro-pores greatly influenced the extent, quality, homogeneity and spatial distribution of the new bone and of the repair tissue, in an anisotropic, region-dependent fashion. While for both the gradient and the constant architecture neo-bone was consistently well integrated with the native bone at the interface at the open side of the PCL cage, the constant pore diameter scaffolds exhibited significantly higher bone formation, as well as the presence of more mature lamellar bone over woven bone. This was seen already from zone 1, even though the macro-pore architecture in this region was the same for both gradient and constant constructs. Furthermore, in the constant group, the neo-bone was more homogeneously distributed throughout the section of the scaffold in the plane parallel to the open face of the PCL shell, and these differences were also evident further away inside the scaffold, in zone 2. A similar trend could be observed for zone 3, although differences were not statistically significant for this zone. Overall, when also considering the bone forming potential of the constructs including also the samples in which bone could infiltrate from the side of the scaffolds, the best extent of healing, *i.e.* full bridging of the defect with bone present throughout the whole

scaffold, was found only in the constant porosity group, possibly due to the larger pore size in all zones.

Vascularization is a critical step for bone regeneration³¹. Blood vessels, associated with bone (either lamellar, as Haversian canals, or woven) and non-mineralized tissue were present throughout all zones, regardless of the architecture. The size of these vessels, which is an indicator of vessel stability and vascularization potential of the scaffolds³², showed a decreasing trend from zone 1 to zone 3 for both architectures, albeit this difference was not statistically significant. However, there was a significant difference in size, with larger average lumen size for the vessels in the constant porosity group, when comparing the effect of the pore architecture within a given zone. Vascular infiltration is a necessary element for bone tissue remodeling and the degree of maturation and amount of blood vessels (**Figure 8**) can affect the influx of nutrients, biochemical cues, and cells (*i.e.* osteoclasts, progenitor cells and osteoblasts) that accelerate neo-bone deposition and development^{33, 34}. The decrease in the maturity and size of blood vessels from the constant to the gradient scaffolds seems correlated with our findings for neo-bone formation, which was consistently better for the constant group regardless of the zone.

Importantly, our results suggest that areas further away from the front of mineralization may influence other regions. This is particularly relevant, as areas with poor regeneration may limit osteoconductive repair also in regions close to the native bone. In the constant group, vascularization and repair tissue can progress with relative more ease from zone 1 to 2 (and finally to 3), compared to the gradient group, leading to faster degradation and remodeling of the scaffold, accompanied by a satisfactory regeneration of bone in zones 1 and 2. Conversely, in gradient scaffolds, the hindrance of neo-bone progression in the deeper zones also negatively affects the quality and kinetics of the remodeling of the repair tissue in the first zone. Although such phenomena might not be experienced in a relatively small scaffold in which the porous architecture is accessible from all sides, this would be relevant for large scaffolds and the observation may hence be important for bone scaffold design and especially scaling-up of these scaffolds.

Finally, in the perspective of scaling up bone regenerative scaffolds, the selection of appropriate animal models is fundamental. Most biomaterials for bone regeneration are tested in small animal models, which possess superior regenerative ability compared to humans and larger animals³⁵. While these models provide important information on the osteoconductive and osteoinductive properties of a material, they poorly represent the human musculoskeletal milieu and the associated mechanical loads. Therefore, they are insufficient to translate new biomaterials towards human and veterinary clinical practice. The model proposed in this study may aid significantly towards this objective. A previous study on osteoinductive gelatin/ β -TCP sponges demonstrated favorable bone regeneration in third metacarpal bone defects in horses³⁶. This location of defect is, however, challenging in terms of surgical approach and interventions at this site easily lead to severe discomfort of the animals, which will manifest as lameness. The equine tuber coxae has not previously been used as a site for bone regeneration studies thus far, but presents several advantages: it is

easily accessible, contains compact and trabecular bone, is hardly affected by skin displacement and surgery can be performed in the standing horse. The little impact of surgical interventions at this site also allows the simultaneous investigation of novel regenerative approaches at different sites (*e.g.*, stifle joints for cartilage repair); thus, contributing to the refinement and reduction of experimental animal use, in compliance with the 3R principle³⁷. Apart from all practical advantages that have been discussed earlier and different to most other large animals, such as sheep and goats³⁸, horses are often also orthopedic patients, and thus may profit from the outcome of this type of experiments.

CONCLUSION

In this work, the long-term *in vivo* performance of 3D-printed porous pCaP based scaffolds with different pore distributions (vertical gradient and constant porosity) was tested in an equine orthotopic bone defect model. The challenging environment created by PCL capping provided valuable insights in the influence of scaffold pore architecture on bone neo-formation, although replacing PCL for non-degradable materials is recommended. In this setting, the macro-pore patterns of the scaffolds, which were produced from compositionally equivalent material, were shown to both influence new bone ingrowth and material degradation. This is important information for scaffold manufacturing, especially with regard to the possible upscaling of scaffolds for healing of larger bone defects. This study has further shown that the –porosity-influenced- bone ingrowth and vascular characteristics in turn have an effect on bone formation and/or scaffold degradation at places at a relatively large distance from the interfaces of the scaffold with the native bone. Additionally, the study highlights the value of the equine tuber coxae model for orthotopic testing of bone scaffolds. The tuber coxae is situated at the end of the wing of the ileum and hence is part of the pelvis. It is a place where muscles attach, such as the tensor fasciae latae muscle. It contains mainly trabecular bone, which is surrounded, however, by a rather thin layer of cortical bone. This is not unlike the situation in a joint where the subchondral bone is made up of trabecular bone that is shielded from the articular cartilage by the subchondral bone plate. Apart from many advantages including ease of surgery, maximum size of implants, and limited experimental animal welfare impact, there is the important ethical consideration that for orthopedic regenerative medicine studies, the horse is not merely an experimental animal, but a target species in its own right that may benefit from possible positive outcomes of experimental studies.

MATERIALS AND METHODS

Experimental Section

pCaP Paste preparation:

As ceramic precursor, pCaP paste was prepared by mixing a powder particle phase and a liquid phase. Briefly, the optimal distribution of the particles and liquid phases that allowed the paste to be printable was 70% and 30% w/w, respectively. The powder consisted of microparticles of milled α -TCP (average size 3.37 μm , Cambioceramics, The Netherlands) mixed with 4% w/w nano-HA (average size 200 nm, Sigma-Aldrich). The liquid phase consisted of a shear-thinning hydrogel precursor solution dissolved in phosphate-buffered saline (PBS), supplemented with ammonium persulphate (APS, Sigma Aldrich, 25 mM), to form a 40% (w/v) solution. The dissolved polymer, forming this hydrogel precursor, consisted of a biodegradable and crosslinkable poloxamer derivative (P-CL-MA), which was custom synthesized by grafting a biodegradable ϵ -caprolactone ester block and a methacrylate group onto both terminal hydroxyl groups of poloxamer 407 (Sigma-Aldrich), as previously described²⁴. Before mixing, the powder and liquid phases were stored separately at 4°C for 30 minutes and finally the P-CL-MA solution was added to a composite solid particle at 4°C and manually mixed with a spatula. To ensure homogeneous distribution of solid particles, the mixing process was performed for 3 minutes at 4°C. Finally, the pCaP paste was loaded into a 5 ml dispensing cartridge, closed with retainer caps, and stored at 4°C until using.

Porous pCaP scaffold preparation:

Cylindrical pCaP scaffolds (diameter: 9.8 mm. height: 9.5 mm) were designed and produced using a pneumatic extrusion printer (RegenHU, Villaz-St-Pierre, Switzerland). Scaffold architecture was designed and converted to printing path and eventually g-code with the BioCAD software (RegenHU, Villaz-St-Pierre, Switzerland). The pCaP paste was extruded through a conical nozzle (inner diameter = 250 μm , pressure = 0.21 MPa, translation speed 2 $\text{mm}\cdot\text{s}^{-1}$ and layer height of 250 μm) at ambient temperature (20 - 25°C). All scaffolds were printed with a 0-0-90-90° laydown pattern, stacking two contiguous layers in the same direction in order to ensure a constant lateral porosity of 500 μm . Two types of axial pore structures (**Figure 1**) were formed: i) a gradient of porosity with a discrete 4-steps reduction of the strand-to-strand distance (500 μm , 400 μm , 300 μm and 200 μm), and ii) a constant pore pattern, created by printing within each layer pCaP filaments with a strand-to-strand distance of 500 μm . For both types of scaffolds, a non-porous last layer was printed on top. After finishing the printing process, pCaP scaffolds were set by leaving them in a humidified environment, saturated with water vapor at 37°C for three days. Subsequently, the scaffolds were immersed in tetramethylethylenediamine (TEMED, Life Technologies, 25 mM)

solution in PBS at 37°C for one hour, to allow the polymerization of the P-MA component of the pCaP cement, initiated by TEMED diffusing into the APS-enriched cement formulation. As observed with x-ray diffraction (XRD) analysis, about 95.8% of the cement precursor was converted to poorly crystalline CDHA after setting and polymer crosslinking as demonstrated in **Chapter 3**³⁹. Crosslinked scaffolds were rinsed and washed with PBS twice, dried in air at ambient temperature, and stored until further use. The overall range of porosity as measured via μ -CT was found to be $40.03 \pm 1.78\%$ and $51.14 \pm 0.78\%$ for the constant and gradient structure respectively. The mechanical properties were characterized by performing an unconfined compression tests (MTS criterion® Electromechanical Universal Test Systems, model 42, 500 N load cell). Samples were kept in PBS for at least 30 minutes before performing the test. The testing system was set to apply displacement ramp (0.5 mm/min) until failure of the structure. The tangent modulus, calculated in the elastic regime and the ultimate strength were found to be 105.80 ± 55.74 MPa and 1.36 ± 0.59 MPa, respectively for the constant scaffold, and of 208.37 ± 84.90 MPa and 3.09 ± 1.17 MPa for the gradient structures, in line with what previously observed as demonstrated in **Chapter 3**³⁹.

PCL cylindrical shell, implant assembly and sterilization:

To allow tissue growth into the construct from a single direction, the entire scaffold, except for the side that was positioned towards the bottom of the osteal defect, was insulated with a 3D-printed bucket-shaped medical-grade PCL (Purasorb® PC 12 Corbion PURAC, The Netherlands, with printing temperature of 80°C, translation speed $1 \text{ mm}\cdot\text{sec}^{-1}$, and layer thickness of 200 μm) shell (height: 10 mm, inner diameter: 10 mm, outer diameter: 10.47 mm) by using the same pneumatic-driven printer as described for the pCaP paste. Hardened and crosslinked pCaP scaffolds were pressed-fit inside the PCL shell, with the non-porous pCaP layer at the closed side of the shell (**Figure 1**). All assembled scaffolds were sterilized by gamma irradiation (8kGy) and kept separately in sterile falcon tubes until implantation.

In vivo study design and surgical procedure:

Cylindrical defects were drilled into the tuber coxae of the ilium in 8 horses (one defect per side) (**Figure 2**). Each horse received both one gradient and one constant porous scaffold (with random left/right distribution). Scaffolds were placed by letting the open circular side of the PCL cylindrical shell in contact with native bone at the bottom of the defect while the closed circular side was covered with periosteum. The protocols and studies described were approved by the ethical and animal welfare committees of the National University of Costa Rica. Eight healthy adult Criollo breed horses (mean age 7.1 years, range 5-9 years; mean weight 319 kg, range 275-375 kg) were used. The study was performed on a cohort of horses which was already involved in another study, in which engineered constructs were implanted in osteochondral defects in the stifle joint. As there is no cross-talk between the two

anatomical locations (stifle and tuber coxae), the tuber coxae bone defect is a suitable model to perform multiple parallel assays, minimizing the need of experimental animals, in accordance to the 3Rs principle (reduce, refine, replace). Horses were clinically sound on lameness examination and did not have clinical or radiographic evidence of joint pathology. They were housed in individual box stalls and fed a standard maintenance ration of concentrate with hay *ad libitum* and had free access to water during the first three months of the study, in order to avoid excessive loads on the stifle joint, in relation to the scaffolds implantation in the osteochondral defect. After this period, they had free exercise at pasture at the University farm, with unlimited access to hay and water. After premedication with xylazine ((Pisa, Mexico), $1.1 \text{ mg}\cdot\text{kg}^{-1}$, intravenous (IV)), anesthesia was induced with midazolam ((Holliday, Argentina), $0.05 \text{ mg}\cdot\text{kg}^{-1}$, IV) and ketamine ((Holliday, Argentina), $2.2 \text{ mg}\cdot\text{kg}^{-1}$, IV). Afterward, the horse was positioned in lateral recumbency. General anesthesia was maintained with isoflurane in oxygen. An incision was made in the skin and subcutaneous tissue 10 cm above the tuber coxae to expose the underlying bone. Once the tuber coxae was exposed, a cylindrical microdefect of 11 mm wide x 10 mm deep was created using a power drill. Defect sites were flushed with saline (Baxter, USA) and the experimental scaffolds were implanted using a press-fit approach. Subcutaneous tissue and skin were sutured, and the horses were allowed to recover without wound dressings.

Post-operative care and monitoring:

Horses received antibiotics for 5 days (procaine penicillin (Phenix, Belgium), $15000 \text{ IU}\cdot\text{kg}^{-1}$, intramuscular (IM), once daily (SID) and gentamicin (KEPRO BV, the Netherlands), $6.6 \text{ mg}\cdot\text{kg}^{-1}$, IV, SID), and non-steroidal anti-inflammatory drugs (phenylbutazone (Lisan, Costa Rica), $2.2 \text{ mg}\cdot\text{kg}^{-1}$, oral administration (PO), twice daily (BID)) during the first 10 days. Horses were clinically monitored daily for rectal temperature, heart rate and respiratory rate, as well as stance, demeanor and general appearance. The surgical wounds were inspected, and the area gently palpated for local heat, swelling and tenderness. Locomotion was daily evaluated at walk and horses were occasionally trotted up to check for eventual subtle lameness. Routine blood analysis (complete blood count (CBC), chemistry panel) was performed at months 1, 3 and 6 post-operatively. From 3 months post-operation, horses were turned out onto pasture, allowing free exercise until the end of the experiment.

Euthanasia and sample harvesting:

One horse was euthanized because of an accident at pasture unrelated to the study at 4 months post-operatively and was excluded from the study. The remaining 7 horses were euthanized 7 months post-operatively. Deep anesthesia was induced with a combination of xylazine ((Pisa, Mexico), $1 \text{ mg}\cdot\text{kg}^{-1}$, IV) followed by ketamine and midazolam ((Holliday, Argentina), $3 \text{ mg}\cdot\text{kg}^{-1}$, IV and $0.05 \text{ mg}\cdot\text{kg}^{-1}$, IV, respectively), after which a bolus of oversaturated magnesium sulphate ($200 \text{ g}\cdot\text{L}^{-1}$) and chloral hydrate ($200 \text{ g}\cdot\text{L}^{-1}$) solution was

administered IV to effect. Death was confirmed by absence of breathing, ictus and corneal reflex. After dissection of the skin and subcutaneous tissues, the tuber coxae was exposed and the surgical sites were readily recognizable. Macroscopic pictures were taken and blocks of tissue containing the defects were excised. Pieces containing the defects were fixed and stored in formalin in individual plastic containers.

μ-CT evaluation:

Three assembled implants of either constant or gradient porous pCaP scaffolds were randomly selected for scanning in a μ-CT scanner (Quantum FX-Perkin Elmer) before implantation. All formalin-fixed tissue explants, containing the implant and the surrounding native tissue that were harvested postmortem at the endpoint of an experiment, were also scanned (voltage = 90 kV, current = 200 μA, voxel size = 20 μm³ and total scanning time = 3 minutes). Subsequently, the 3D reconstructed images were processed and analyzed using image J⁴⁰ and Bone J⁴¹ software, respectively. First, a two-dimensional (2D) region of interest (ROI) was selected in a transverse plane (parallel to the surface of the scaffold) at the boundary between the ceramic scaffold and the inner wall of the PCL chamber. For the analysis of the whole construct, similar ROIs were created every two stacks (512 stacks/each μ-CT file), then a 3D VOI was obtained by automatically interpolating these ROIs in ImageJ. For the quantification by separating into three zones, a similar process was followed, except that 3 VOIs were identified. Subsequently, thresholding was performed in order to select either the signal derived from the ceramic scaffold only, or from the newly formed bone. Finally, the volume fraction within a given VOI was analyzed using the Bone J plugin in ImageJ. Seven main parameters were quantified including total volume of newly-formed bone in the overall VOI, volume of newly-formed bone in each zonal VOI, percentage of new bone ingrowth ((new bone volume/VOI) * 100), percentage of remaining pCaP ((volume of ceramic/ VOI)*100), estimated percentage of other, non-mineralized tissue infiltration (100 – (percentage of new bone ingrowth + percentage of remaining ceramic)), total volume of ceramic material of scaffolds before and after implantation, and percentage of pCaP volume loss. μ-CT 3D reconstructions of new bone formation and remaining ceramic were generated using the 3D Slicer software (4.10.0, BWH and 3D Slicer contributors)

Histological assessment:

After retrieval, all formalin-fixed samples were kept in formalin (4%) and cut through the defect area and, therefore, longitudinally through the scaffold to obtain two rectangular cross sections for embedding in either paraffin or MMA resin. For paraffin embedding, tissue explants were decalcified with ethylenediaminetetraacetic acid (EDTA) disodium salt (0.5 M) for 6 weeks. Dehydration was performed through a graded ethanol series, followed by clearing in xylene and embedding in paraffin. Embedded samples were sectioned into 5 μm thin slices. To observe the morphology of cells that had infiltrated in the porous constructs,

H&E staining was performed (nuclei: blue, other parts: pink). Subsequently, to understand the identity of specific cell populations found within the scaffolds, different stainings to detect cells involved in bone remodeling were performed. TRAP stain was performed to reveal TRAP-positive osteoclasts (showing in red). Stainings for osteonectin, a major non-collagenous protein in bone, (Osteonectin AB SPARC AON-1, DSHB; nuclei: blue, positive osteonectin: brown) and for type I collagen, (Anti-collagen I antibody EPR7785, Abcam; nuclei: blue, positive type I collagen: brown) were performed to reveal the activity of osteoblasts. To assess the presence of collagen fibers within the newly formed bone and to differentiate between non-mineralized (osteoid) and mineralized bone, Goldner's trichrome stain was performed (nuclei: blue, immature bone: red orange, mineralized mature bone: blue green). To observe the spatial arrangement of collagen fibers in the repair tissue, a picosirius red stain was performed and imaged under polarized light which revealed collagen birefringence (collagen: birefringent patterns against a black background). For MMA embedding, formalin-fixed tissue sections were dehydrated through a graded ethanol series, embedded in MMA resin and allowed to harden at 37°C in a water bath overnight. Embedded samples were sectioned into 330 µm-thick slices. Thereafter, all sections were stained with basic fuchsin and methylene blue to visualize new bone ingrowth and soft tissue infiltration (nuclei: blue, pink: bone). Stained histological slides were imaged using a light microscope (Olympus BX51, Olympus Nederland B.V.) equipped with a digital camera (Olympus DP73, Olympus Nederland B.V.). Also, for the analysis of the histological data, the implant region was divided into three zones that were dependent on the distance across the depth of the scaffold, starting from the native bone-scaffold interface. Relative amounts of TRAP-positive stain, osteonectin-positive stain and type I collagen -positive stain were quantified, converting the acquired microscopy images to binary files, applying a threshold to select the stained area and quantifying the area coverage of the staining (ratio between the stained area and the total area of new tissue formation (excluding the ceramic)). The size and number of blood vessels penetrating into the scaffolds were also quantified by selecting 3 random pictures from each zone of the scaffolds and counting the number of vessels and measuring the length of their main axis with ImageJ software.

Statistical analysis:

Measurements at the endpoint of the *in vivo* experiment were performed on seven horses (N=7). Regarding the analysis of the effect of the printed pore structure, three samples from each group were withdrawn from the evaluation, either because the structural integrity of the PCL cage was found to be compromised, with neo-bone infiltrating from the sides of the structure, or due to failure to retrieve the entirety of the scaffold (final sample size N=4 for both groups). Calculated values for the constant and gradient porosity scaffolds were reported as mean ± standard deviation. Statistical analysis was performed using Matlab (R2018a, The MathWorks, Inc.). A Mann-Whitney U-test was performed to investigate the differences between the groups in terms of total bone volume, zonal bone volume, percentage of pCaP

volume loss, including size and number of blood vessels. Likewise, the same test was used for evaluating the bone volume fraction, remaining material volume fraction and non-mineralized tissue volume fraction in the VOI. Two-way ANOVA was performed for analyzing the total pCaP volume before and after implantation. Statistical significance was considered for $p < 0.05$.

ACKNOWLEDGEMENTS

PD and RVB contributed equally to this work. PD acknowledges the funding from the Royal Thai Government scholarship (Thailand). PD, SC, MvR, JdG, RvW, RL, JM acknowledge the Dutch Arthritis Society (CO-14-1-001, LLP-12 and LLP-22), and the European Research Council (grant agreement #647426, 3DJOINT). The primary antibodies against type II collagen (II-II6B3) developed by T. F. Linsenmayer and E. S. Engvall, respectively, were obtained from the DSHB developed under the auspices of the NICHD and maintained by the University of Iowa, Department of Biology, Iowa City, IA, USA.

REFERENCES

1. Li, J. J.; Ebied, M.; Xu, J.; Zreiqat, H., Current Approaches to Bone Tissue Engineering: The Interface between Biology and Engineering. *Advanced Healthcare Materials* **2018**, *7* (6), 1701061.
2. Samavedi, S.; Whittington, A. R.; Goldstein, A. S., Calcium phosphate ceramics in bone tissue engineering: A review of properties and their influence on cell behavior. *Acta Biomaterialia* **2013**, *9* (9), 8037-8045.
3. Karageorgiou, V.; Kaplan, D., Porosity of 3D biomaterial scaffolds and osteogenesis. *Biomaterials* **2005**, *26* (27), 5474-5491.
4. Loh, Q. L.; Choong, C., Three-Dimensional Scaffolds for Tissue Engineering Applications: Role of Porosity and Pore Size. *Tissue Engineering Part B: Reviews* **2013**, *19* (6), 485-502.
5. Ratner, B. D., A pore way to heal and regenerate: 21st century thinking on biocompatibility. *Regenerative Biomaterials* **2016**, *3* (2), 107-110.
6. Serra, I. R.; Fradique, R.; Vallejo, M. C. S.; Correia, T. R.; Miguel, S. P.; Correia, I. J., Production and characterization of chitosan/gelatin/ β -TCP scaffolds for improved bone tissue regeneration. *Materials Science and Engineering: C* **2015**, *55*, 592-604.
7. Di Luca, A.; Lorenzo-Molero, I.; Mota, C.; Lepedda, A.; Auhl, D.; Van Blitterswijk, C.; Moroni, L., Tuning Cell Differentiation into a 3D Scaffold Presenting a Pore Shape Gradient for Osteochondral Regeneration. *Advanced Healthcare Materials* **2016**, *5* (14), 1753-1763.
8. Cai, S.; Xi, J.; Chua, C. K., A Novel Bone Scaffold Design Approach Based on Shape Function and All-Hexahedral Mesh Refinement. In *Computer-Aided Tissue Engineering*, Liebschner, M. A. K., Ed. Humana Press: Totowa, NJ, 2012; pp 45-55.
9. Yin, S.; Zhang, W.; Zhang, Z.; Jiang, X., Recent Advances in Scaffold Design and Material for Vascularized Tissue-Engineered Bone Regeneration. *Advanced Healthcare Materials* **2019**, *8* (10), 1801433.
10. Perez, R. A.; Ginebra, M.-P., Injectable collagen/ α -tricalcium phosphate cement: collagen-mineral phase interactions and cell response. *Journal of Materials Science: Materials in Medicine* **2013**, *24* (2), 381-393.
11. Groll, J.; Burdick, J. A.; Cho, D. W.; Derby, B.; Gelinsky, M.; Heilshorn, S. C.; Jüngst, T.; Malda, J.; Mironov, V. A.; Nakayama, K.; Ovsianikov, A.; Sun, W.; Takeuchi, S.; Yoo, J. J.; Woodfield, T. B. F., A definition of bioinks and their distinction from biomaterial inks. *Biofabrication* **2018**, *11* (1), 013001.
12. Ahlfeld, T.; Doberenz, F.; Kilian, D.; Vater, C.; Korn, P.; Lauer, G.; Lode, A.; Gelinsky, M., Bioprinting of mineralized constructs utilizing multichannel plotting of a self-setting calcium phosphate cement and a cell-laden bioink. *Biofabrication* **2018**, *10* (4), 045002.
13. Akkineni, A. R.; Luo, Y.; Schumacher, M.; Nies, B.; Lode, A.; Gelinsky, M., 3D plotting of growth factor loaded calcium phosphate cement scaffolds. *Acta Biomaterialia* **2015**, *27*, 264-274.
14. Barba, A.; Maazouz, Y.; Diez-Escudero, A.; Rappe, K.; Espanol, M.; Montufar, E. B.; Öhman-Mägi, C.; Persson, C.; Fontecha, P.; Manzanares, M.-C.; Franch, J.; Ginebra, M.-P., Osteogenesis by foamed and 3D-printed nanostructured calcium phosphate scaffolds: Effect of pore architecture. *Acta Biomaterialia* **2018**, *79*, 135-147.
15. Pearce, A. I.; Richards Rg Fau - Milz, S.; Milz S Fau - Schneider, E.; Schneider E Fau - Pearce, S. G.; Pearce, S. G., Animal models for implant biomaterial research in bone: a review. (1473-2262 (Electronic)).
16. Moran, C. J.; Ramesh, A.; Brama, P. A. J.; O'Byrne, J. M.; O'Brien, F. J.; Levingstone, T. J., The benefits and limitations of animal models for translational research in cartilage repair. *Journal of Experimental Orthopaedics* **2016**, *3* (1), 1.
17. Gyles, C., One Medicine, One Health, One World. *Can Vet J* **2016**, *57* (4), 345-346.
18. Cope, P. J.; Ourradi, K.; Li, Y.; Sharif, M., Models of osteoarthritis: the good, the bad and the promising. *Osteoarthritis and Cartilage* **2019**, *27* (2), 230-239.
19. Kuyinu, E. L.; Narayanan, G.; Nair, L. S.; Laurencin, C. T., Animal models of osteoarthritis: classification, update, and measurement of outcomes. (1749-799X (Electronic)).
20. Williams, R. B.; Harkins, L. S.; Hammond, C. J.; Wood, J. L. N., Racehorse injuries, clinical problems and fatalities recorded on British racecourses from flat racing and National Hunt racing during 1996, 1997 and 1998. *Equine Veterinary Journal* **2001**, *33* (5), 478-486.

21. Bigam-Sadegh, A.; Oryan, A., Selection of animal models for pre-clinical strategies in evaluating the fracture healing, bone graft substitutes and bone tissue regeneration and engineering. *Connective Tissue Research* **2015**, *56* (3), 175-194.
22. Wright, I. M., Racecourse fracture management. Part 1: Incidence and principles. *Equine Veterinary Education* **2017**, *29* (7), 391-400.
23. Termine Jd Fau - Kleinman, H. K.; Kleinman Hk Fau - Whitson, S. W.; Whitson Sw Fau - Conn, K. M.; Conn Km Fau - McGarvey, M. L.; McGarvey Mi Fau - Martin, G. R.; Martin, G. R., Osteonectin, a bone-specific protein linking mineral to collagen. (0092-8674 (Print)).
24. Melchels, F. P. W.; Blokzijl, M. M.; Levato, R.; Peiffer, Q. C.; Ruijter, M. d.; Hennink, W. E.; Vermonden, T.; Malda, J., Hydrogel-based reinforcement of 3D bioprinted constructs. *Biofabrication* **2016**, *8* (3), 035004.
25. Rosset, E. M.; Bradshaw, A. D., SPARC/osteonectin in mineralized tissue. (1569-1802 (Electronic)).
26. Gheron Robey, P., Chapter 17 - Noncollagenous Bone Matrix Proteins. In *Principles of Bone Biology (Third Edition)*, Bilezikian, J. P.; Raisz, L. G.; Martin, T. J., Eds. Academic Press: San Diego, 2008; pp 335-349.
27. Hu, J.; Zhou, Y.; Huang, L.; Liu, J.; Lu, H., Effect of nano-hydroxyapatite coating on the osteoinductivity of porous biphasic calcium phosphate ceramics. *BMC Musculoskeletal Disorders* **2014**, *15* (1), 114.
28. Barba, A.; Diez-Escudero, A.; Maazouz, Y.; Rappe, K.; Espanol, M.; Montufar, E. B.; Bonany, M.; Sadowska, J. M.; Guillem-Marti, J.; Öhman-Mägi, C.; Persson, C.; Manzanares, M.-C.; Franch, J.; Ginebra, M.-P., Osteoinduction by Foamed and 3D-Printed Calcium Phosphate Scaffolds: Effect of Nanostructure and Pore Architecture. *ACS Applied Materials & Interfaces* **2017**, *9* (48), 41722-41736.
29. Marrella, A.; Lee, T. Y.; Lee, D. H.; Karuthedom, S.; Syla, D.; Chawla, A.; Khademhosseini, A.; Jang, H. L., Engineering vascularized and innervated bone biomaterials for improved skeletal tissue regeneration. *Materials Today* **2018**, *21* (4), 362-376.
30. Yamada, M.; Shiota, M.; Yamashita, Y.; Kasugai, S., Histological and histomorphometrical comparative study of the degradation and osteoconductive characteristics of α - and β -tricalcium phosphate in block grafts. *Journal of Biomedical Materials Research Part B: Applied Biomaterials* **2007**, *82B* (1), 139-148.
31. García, J. R.; García, A. J., Biomaterial-mediated strategies targeting vascularization for bone repair. *Drug Delivery and Translational Research* **2016**, *6* (2), 77-95.
32. Scaglione, S.; Ilengo, C.; Fato, M.; Quarto, R., Hydroxyapatite-Coated Polycaprolacton Wide Mesh as a Model of Open Structure for Bone Regeneration. *Tissue Engineering Part A* **2008**, *15* (1), 155-163.
33. Filipowska, J.; Tomaszewski, K. A.; Niedźwiedzki, Ł.; Walocha, J. A.; Niedźwiedzki, T., The role of vasculature in bone development, regeneration and proper systemic functioning. *Angiogenesis* **2017**, *20* (3), 291-302.
34. Malhotra, A.; Habibovic, P., Calcium Phosphates and Angiogenesis: Implications and Advances for Bone Regeneration. *Trends in Biotechnology* **2016**, *34* (12), 983-992.
35. Muschler, G. F.; Raut, V. P.; Patterson, T. E.; Wenke, J. C.; Hollinger, J. O., The Design and Use of Animal Models for Translational Research in Bone Tissue Engineering and Regenerative Medicine. *Tissue Engineering Part B: Reviews* **2009**, *16* (1), 123-145.
36. Tsuzuki, N.; Otsuka, K.; Seo, J.; Yamada, K.; Haneda, S.; Furuoka, H.; Tabata, Y.; Sasaki, N., *In vivo* osteoinductivity of gelatin β -tri-calcium phosphate sponge and bone morphogenetic protein-2 on an equine third metacarpal bone defect. *Research in Veterinary Science* **2012**, *93* (2), 1021-1025.
37. Guhad, F., Introduction to the 3Rs (Refinement, Reduction and Replacement). *Journal of the American Association for Laboratory Animal Science* **2005**, *44* (2), 58-59.
38. Loozen, L. D.; van der Helm, Y. J. M.; Öner, F. C.; Dhert, W. J. A.; Kruyt, M. C.; Alblas, J., Bone Morphogenetic Protein-2 Nonviral Gene Therapy in a Goat Iliac Crest Model for Bone Formation. *Tissue Engineering Part A* **2015**, *21* (9-10), 1672-1679.
39. Diloksumpan, P.; de Ruijter, M.; Castilho, M.; Gbureck, U.; Vermonden, T.; van Weeren, P. R.; Malda, J.; Levato, R., Combining multi-scale 3D printing technologies to engineer reinforced hydrogel-ceramic interfaces. *Biofabrication* **2020**, *12* (2), 025014.

40. Schindelin, J.; Arganda-Carreras, I.; Frise, E.; Kaynig, V.; Longair, M.; Pietzsch, T.; Preibisch, S.; Rueden, C.; Saalfeld, S.; Schmid, B.; Tinevez, J.-Y.; White, D. J.; Hartenstein, V.; Eliceiri, K.; Tomancak, P.; Cardona, A., Fiji: an open-source platform for biological-image analysis. *Nature Methods* **2012**, *9* (7), 676-682.
41. Doube, M.; Klosowski, M. M.; Arganda-Carreras, I.; Cordelières, F. P.; Dougherty, R. P.; Jackson, J. S.; Schmid, B.; Hutchinson, J. R.; Shefelbine, S. J., BoneJ: Free and extensible bone image analysis in ImageJ. *Bone* **2010**, *47* (6), 1076-1079.

SUPPLEMENTARY INFORMATION

Supplementary table ST1. Full sets of hematologic data from all individual horses. PCV=packed cell volume; Hb=hemoglobin content; MCHC= mean corpuscular hemoglobin concentration; Leuko=leukocyte count, followed by differential cell count (in percentages) of the various cell types making up the number of leukocytes (neut=neutrophils; eosi=eosinophils; baso=basophils; lymp=lymphocytes; mono=monophils); To.prot=total protein; alb=albumin; Glob=globulin. None of the ponies had aberrant blood values.

Horse # 1. Male, 375 kg., 9 years old.

Horse 1	PCV %	Hb g/dl	MCHC g/dl	Leuko ul	Neut %	Eosi %	Baso %	Lymp %	Mono %	To.Prot g/dl	Alb g/dl	Glob g/dl
Day 0	35	12	33	7400	53	2	0	35	0	6	3	3
Month 1	33	11.8	35	8300	59	1	0	40	0	5.9	3.5	2.4
Month 3	37	12.9	35	9900	56	2	0	44	0	5.7	3.2	2.5
Month 6	34	11.9	36	9600	59	2	0	39	0	5.9	3	2.9

Horse # 2. Female, 350 kg., 5 years old.

Horse 2	PCV %	Hb g/dl	MCHC g/dl	Leuko ul	Neut %	Eosi %	baso %	Lymp %	Mono %	To.Prot g/dl	Alb g/dl	Glob g/dl
Day 0	30	12	35	5800	57	2	0	41	0	6.1	3.1	3
Month 1	32	12	36	7450	55	1	0	43	1	5.4	2.7	2.7
Month 3	35	12.8	34	7500	68	2	0	30	0	5.9	3	2.9
Month 6	32	12.1	37	8100	60	0	0	39	1	5.5	2.5	3

Horse #3. Male, 325 kg., 9 years old.

Horse 3	PCV %	Hb g/dl	MCHC g/dl	Leuko ul	Neut %	Eosi %	Baso %	Lymp %	Mono %	To.Prot g/dl	Alb g/dl	Glob g/dl
Day 0	33	11.9	35	6900	69	1	0	30	0	6.2	3	3.2
Month 1	31	12	36	7300	67	3	0	29	1	6.4	2.7	3.7
Month 3	38	12.1	35	6300	53	2	0	45	0	5.7	2.4	3.3
Month 6	30	12	37	6850	58	2	0	40	0	6.2	3.1	3.1

Horse # 4*. Female, 325 kg., 7 years old.

Horse 4	PCV %	Hb g/dl	MCHC g/dl	Leuko ul	Neut %	Eosi %	Baso %	Lymp %	Mono %	To.Prot g/dl	Alb g/dl	Glob g/dl
Day 0	32	11.5	35	10800	59	3	0	38	0	6	3	3
Month 1	33	11	33	9600	61	3	0	36	0	6.1	3	3.1

*Horse # 4 died during the course of the experiment due to an accident at pasture, as reported in the body of the main manuscript.

Horse # 5. Male, 300 kg., 7 years old.

Horse 5	PCV %	Hb g/dl	MCHC g/dl	Leuko ul	Neut %	Eosi %	Baso %	Lymp %	Mono %	To.Prot g/dl	Alb g/dl	Glob g/dl
Day 0	34	11	35	9000	63	2	0	35	0	6	2.6	3.4
Month 1	33	11.7	36	12000	45	0	0	45	0	5.9	3.1	2.8
Month 3	30	12.6	37	7700	55	4	0	40	1	6.1	3.1	3
Month 6	34	12.4	36	11900	63	3	0	34	0	6.7	3.4	3.3

Horse # 6. Male, 300 kg., 6 years old.

Horse 6	PCV %	Hb g/dl	MCHC g/dl	Leuko ul	Neut %	Eosi %	baso %	Lymp %	Mono %	To.Prot g/dl	Alb g/dl	Glob g/dl
Day 0	34	12	36	7450	65	0	0	35	0	5.6	2.6	3
Month 1	33	12	37	10500	58	0	0	42	0	5.9	3.2	2.7
Month 3	33	12.1	36	9500	57	2	0	43	0	5.7	2.9	2.8
Month 6	35	13	38	8100	60	1	0	39	0	6	2.9	3.1

Horse # 7. Female, 275 kg., 5 years old.

Horse 7	PCV %	Hb g/dl	MCHC g/dl	Leuko ul	Neut %	Eosi %	Baso %	Lymp %	Mono %	To.Prot g/dl	Alb g/dl	Glob g/dl
Day 0	34	12.1	33	13100	64	1	0	35	0	6.1	3.1	3
Month 1	34	12.4	34	8100	62	4	0	34	0	6	2.6	3.4
Month 3	35	12.9	32	7800	67	0	0	33	0	5.9	2.4	3.5
Month 6	33	12.7	35	11200	75	0	0	25	0	6	3	3

Horse # 8. Female, 300 kg., 9 years old.

Horse 8	PCV %	Hb g/dl	MCHC g/dl	Leuko ul	Neut %	Eosi %	Baso %	Lymp %	Mono %	To.Prot g/dl	Alb g/dl	Glob g/dl
Day 0	33	12	32	7000	69	1	0	30	0	6	3.3	2.7
Month 1	31	11	33	9200	61	2	0	32	0	5.9	2.8	3.1
Month 3	35	11.1	35	7300	58	2	0	40	0	5.9	2.9	3
Month 6	32	12.1	34	7100	65	4	0	31	0	5.8	2.9	2.9

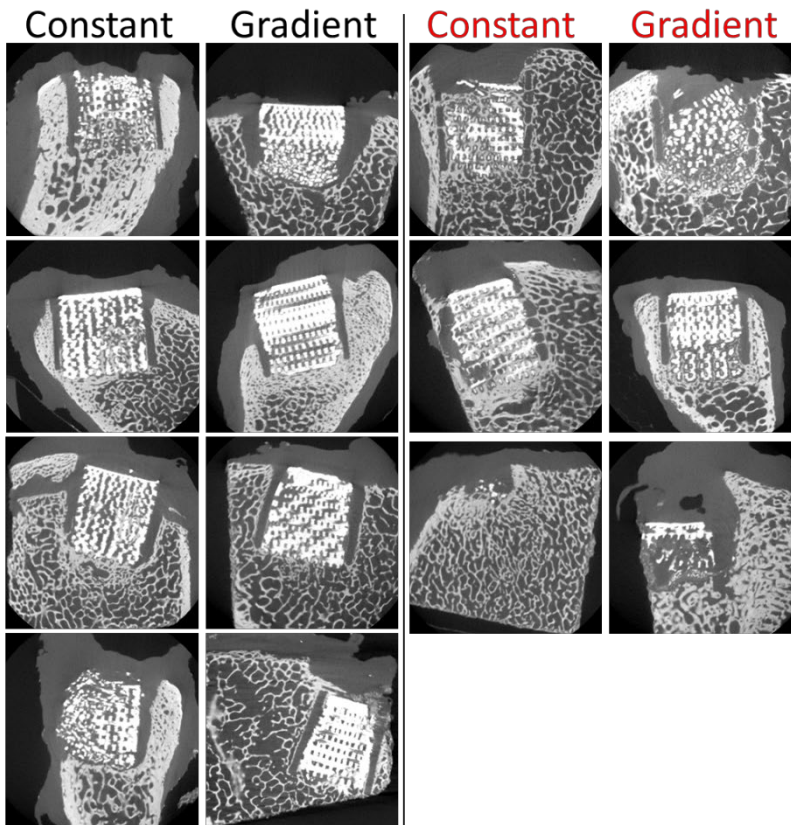


Figure S1. Representative tomographic sections of the scaffolds as obtained 7 months post-implantation, each picture representing one implant. These sections were used to identify in which cases the PCL cages had not succeeded in preventing bone ingrowth from the sides and in which cases insufficient material had been harvested. Those samples were excluded from certain analyses (columns in red, see also explanation in the Experimental Section).

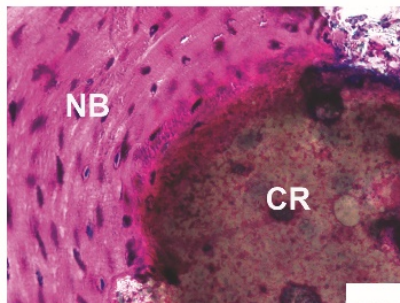


Figure S2. Integration of the newly formed and matured lamellar bone with the ceramic scaffold, showing adhesion of the neo-tissue onto the scaffolds, as indicated by the basic fuchsin staining of MMA sections (NB= New Bone, CR= Ceramic Remnants) (Scale bar = 50 μ m).

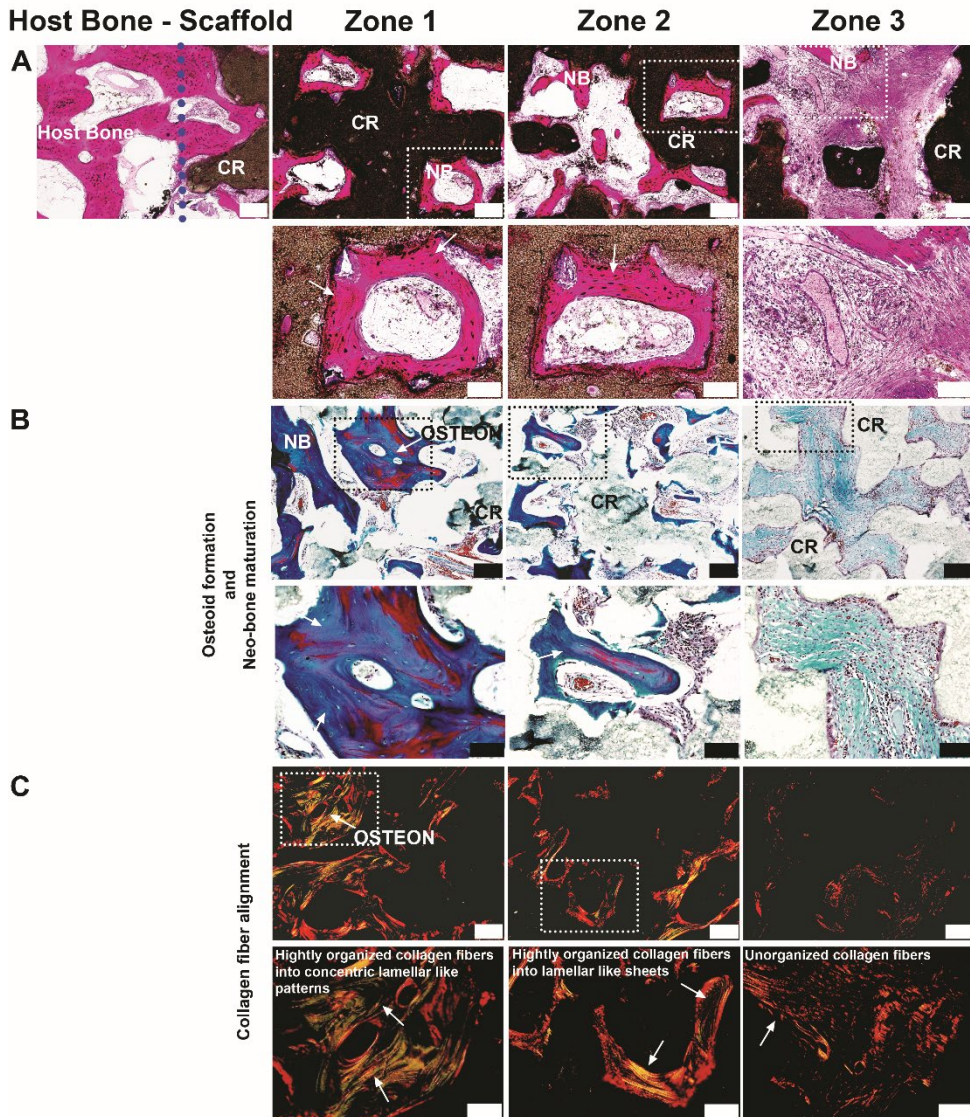


Figure S3: Representative histological staining from the gradient structure Panels from Figure 7 are reported here, in addition to higher magnification images to better visualize the nature of the neo-deposited bone. Basic fuchsin/methylene blue staining revealed the structure of bone ingrowth into the scaffolds in each zone (A) (Scale bar = 200 μm for 1st row, Scale bar = 100 μm for 2nd row), Goldner trichrome staining revealed the formation of newly mineralized bone (blue-green color) and non-mineralized newly formed bone (red color) (B) (Scale bar = 200 μm for 1st row, Scale bar = 100 μm for 2nd row), Picrosirius red staining revealed the highly organized collagen fibers, featuring as concentric lamella-like structures, when observed under polarized light (C) (Scale bar = 200 μm for 1st row, Scale bar = 100 μm for 2nd row).

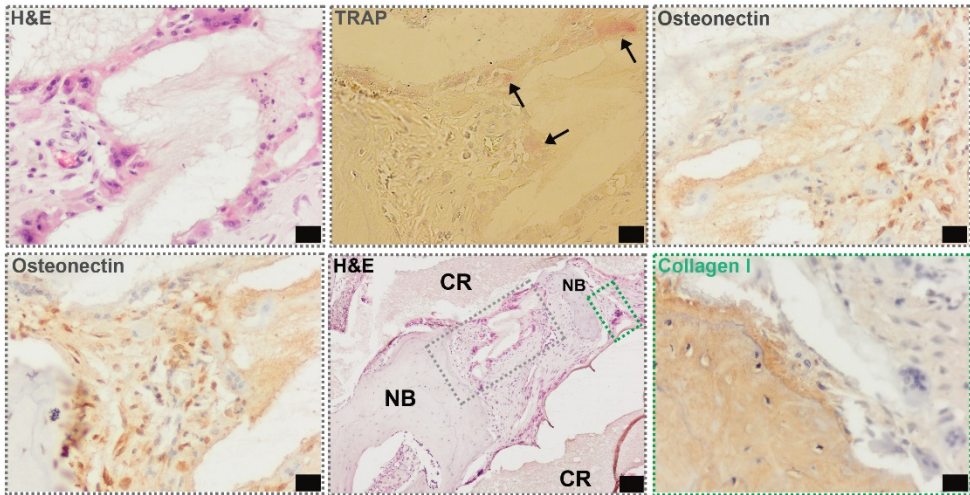


Figure S4. Representative high magnification of H&E, TRAP, Osteonectin, and Collagen type I staining of zone I from the constant structure, Scale bar = 20 μm ., Scale bar = 100 μm (H&E on the 2nd row)).

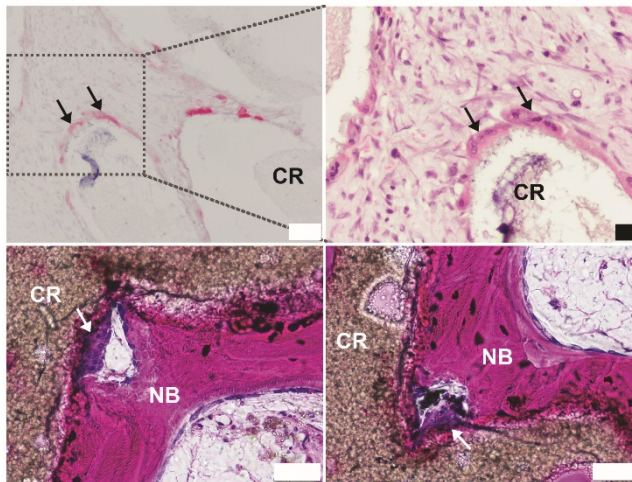


Figure S5. Osteoclastic resorption paired with bone apposition: (Top left) TRAP staining section displaying positive area (black arrow) (Scale bar = 50 μm), (Top right) Comparative H&E staining at the same position (Scale bar = 20 μm), (Bottom left and right) Basic fuchsin & Methylene blue staining section displaying multinucleated osteoclast aligned against the ceramic (white arrow) (Scale bar = 50 μm). (CR = Ceramic Remnant, NB = New Bone Ingrowth)

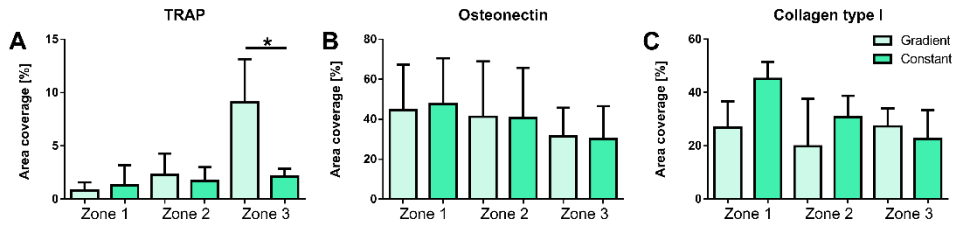


Figure S6. Quantitative analysis of histological staining of the repair bone tissue, showing the area of the histological slide covered by the staining of interest. Osteoclastic activity as indicated by TRAP-positive staining (A); Osteonectin-positive staining, indicative of the presence of osteoblastic cells (B); and type I collagen (C). Statistically significant differences are marked by a *, indicating $p < 0.05$

CHAPTER 5

The Complexity of Joint Regeneration: How an Advanced Implant could Fail by Its *In Vivo* Proven Bone Component

Paweena Diloksumpan^{1*}, Florencia Abinzano^{2*}, Mylène de Ruijter²,
Anneloes Mensinga^{1,2}, Saskia Plomp¹, Ilyas Khan³, Harold Brommer¹,
Ineke Smit¹, Miguel Dias Castilho², Paul René van Weeren¹, Jos Malda^{1,2},
and Riccardo Levato^{1,2}

Submitted

* These authors contributed equally to this work

¹Department of Clinical Sciences, Faculty of Veterinary Medicine, Utrecht University, 3584 CM, Utrecht, the Netherlands

²Department of Orthopaedics, University Medical Center Utrecht, Utrecht University, 3584 CX, Utrecht, the Netherlands

³Center for Nanohealth, Institute of Life Science, College of Medicine, Swansea University, SA2 8PP, Swansea, UK

ABSTRACT

Focal cartilage defects are a major clinical problem and often result in the development of osteoarthritis. There are several promising regenerative implant-based approaches for the treatment of joint damage, but the fixation of the implant remains a significant challenge. This study aimed to evaluate a novel integrated osteochondral scaffold, with and without regenerative cells, in a large animal model. Implants consisted of a melt electro-written polycaprolactone structure for the cartilage phase, which was firmly integrated with a bone anchor produced by extrusion-based printing of a low-temperature setting bioceramic material that had been proven to be effective for osteoregeneration in an orthotopic, non-articular site in the target species in an earlier *in vivo* study. Articular cartilage-derived progenitor cells were seeded on the scaffolds and cultured for 28 days *in vitro* in the presence of growth differentiation factor-2 (GDF-2), resulting in the formation of abundant extracellular matrix rich in glycosaminoglycans (GAGs) and type II collagen. The constructs were implanted in the stifle joints of Shetland ponies with cell-free scaffolds as controls. Clinical signs were monitored, and progression of healing was observed non-invasively through radiographic examinations and quantitative gait analysis. Biochemical and histological analyses 6 months after implantation revealed minimal deposition of GAGs and type II collagen in the chondral region of the defect site for both types of the implants. Quantitative micro-computed tomography (μ -CT) showed collapse of the bone anchor with low volume of mineralized neo-bone formation in both groups. Histology confirmed that the reinforced microfiber meshes within the cartilage phase were still present. It was concluded that the collapse of the osteal anchor, resulting in loss of the mechanical support of the cartilage phase, strongly affected overall outcome, precluding evaluation of the influence of GDF-2-stimulated cells on *in vivo* cartilage regeneration.

Keywords: cartilage, 3D printing, equine model, osteochondral, chondroprogenitor cells

INTRODUCTION

Focal cartilage damage and ensuing osteoarthritis is a major challenge in human healthcare.¹ Most of the available therapeutic approaches are palliative with limited alleviation time² and there are thus far no treatments that have been proven to be successful in fully restoring damage to articular cartilage, neither in an anatomical nor in a functional sense. This unmet clinical need drives the ongoing quest for regenerative approaches for articular cartilage.³

Many new promising technologies^{4,5} that are currently being developed give hope of finding an implant that is effective in facilitating regeneration of cartilage. Given the great difficulties associated with the fixation of a chondral construct^{6,7}, a promising approach is to use a composite construct with an osteal and a chondral phase that can surgically be press-fit implanted, avoiding the risk of dislodgement.⁸ However, also this approach still faces many challenges, including determination of the best osteal part of the scaffold, design of a firm and durable connection of the osteal and chondral phase⁹, and the nature of the composition and/or structure of the chondral phase.^{10,11}

Recently, a very promising technique of anchoring the chondral phase in the osteal phase using melt-electro writing (MEW) has been developed, as introduced in **Chapter 3**.¹² Also, 3D printed brushite-based scaffolds have been shown to be effective in promoting new bone growth after 6 months in an equine model that used the tuber coxae as implantation site¹³, making the material a potential candidate for the osteal phase. These materials are usually fabricated involving aggressive acidic treatments, precluding the direct incorporation of cells and/or polymers during the fabrication phase, and therefore are not directly applicable to anchor MEW-based cartilage scaffolds. To address such limitation, a printable bioceramic that sets under physiological conditions into a calcium-deficient hydroxyapatite (CDHA) scaffold was developed. Such material was shown to be effective in an 7-month long *in vivo* study, upon implantation in a critical size defect in the tuber coxae of warmblood horses, as described in **Chapter 4**. In that study that compared two sophisticated architectures with constant pore size versus a gradient in pore size, the material was shown to facilitate excellent new bone formation, particularly when using the scaffold with constant pore size, as demonstrated in **Chapter 4**.¹⁴

Articular cartilage derived chondroprogenitor cells (ACPCs) were relatively recently identified and characterized in both humans and horses as a distinct cell population that has the potential for cartilage repair.^{15,16} This potential was retained in combination with biomaterials^{17,18}, making the cell type a promising candidate for a comprehensive regenerative approach.

The current study aimed at evaluating an osteochondral composite scaffold for cartilage repair that combines the proven osteogenic CDHA scaffold for the osteal part with the novel interface for the connection of the chondral and osteal parts. For the chondral part, an experimental group in which the MEW structure was seeded with articular cartilage derived progenitor cells (ACPCs) that had been stimulated for 28 days with GDF-2 before implantation¹⁹, was compared with an implant featuring a non-filled, cell-free MEW cartilage

scaffold as control. It was hypothesized that 1.) the CDHA scaffold would show comparable performance in the horse when implanted in the subchondral bone as in the tuber coxae; 2.) the novel interface would provide a lasting connection between the bone and cartilage phase and 3.) the engineered cartilage phase containing the stimulated ACPCs would outperform the cell-free structures in terms of *in vivo* cartilage regeneration.

MATERIALS AND METHODS

Experimental design

To assess the performance of integrated 3D-printed osteochondral grafts that contained a cell-laden or a cell-free chondral compartment, the constructs were orthotopically implanted using a large animal model. Eight Shetland ponies (female, age 4–12 years, weight 149 - 217 kg (165.75 ± 29.47 kg)) were used and samples were implanted in the stifle joints. Healing was monitored for 6 months, after which the animals were humanely euthanized. The ethical and animal welfare body of the Utrecht University had approved the study (Approval nr. AVD108002015307 WP23).

Ponies were housed in individual boxes and fed a limited ration of concentrates together with hay for maintenance and free access to water. Quantitative gait analysis and radiographic examination of the stifles were performed before surgery for baseline values. Post-operatively, the animals were kept stabled for 6 weeks with daily monitoring of vital signs, lameness checks at walk and examination of the operated joints for swelling or other signs of inflammation. In week 5 and 6, they were hand-walked for 10 minutes twice daily and from week 7 they were kept at pasture. Quantitative gait analysis and radiographic exams were performed at 3 weeks, 3 months and 6 months post-operatively. After 6 months, ponies were humanely euthanized for harvesting samples for both quantitative and qualitative analyses. The timeline of the experiment is represented in **Figure 1**.

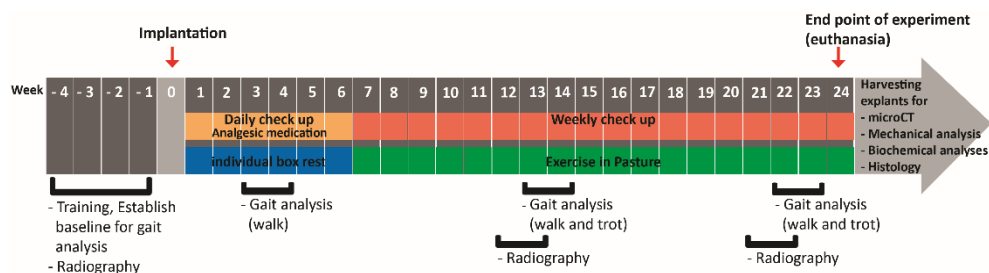


Figure 1. Flow chart representing timeline of the experiment including health monitoring at each phase of the experiment.

Fabrication of construct

Microfiber meshes were produced from medical-graded polycaprolactone (PCL, Purasorb® PC 12 Corbion PURAC, The Netherlands) by using a melt electrowriting (MEW) technology as previously described.²⁰ The meshes were produced by horizontally patterning the microfiber (diameter = 10 μm) to form continuously uniform square spacing (400x400 μm) and vertically stacking the same pattern until reaching 1300 μm in total thickness. This structure was achieved by printing with a temperature of 90°C, a pressure of 1.25 bar, voltage of 10 kV, and collector velocity of 15 $\text{mm}\cdot\text{sec}^{-1}$. Additionally, printing was performed at ambient temperature (22 – 24 °C) with a humidity between 30 – 50%. Subsequently, PCL microfiber meshes were hydrolyzed by soaking them in sodium hydroxide (1M NaOH) for 15 minutes and washed in Milli Q water for 10 minutes 4 times. Finally, sterilization was carried out by immersion of the mesh in 70% ethanol for 15 minutes, followed by air-drying in a sterile cabinet until use.

The printable calcium phosphate (pCaP) paste was prepared as described in **Chapter 3**.¹² In short, 2.2 $\text{g}\cdot\text{ml}^{-1}$ of alpha-tri calcium phosphate (α -TCP, average particle size = 3.83 μm , Cambioceramics, Leiden, the Netherlands) and 0.13 $\text{g}\cdot\text{ml}^{-1}$ of nano-hydroxyapatite (nano-HA, particle size < 200 nm, $\text{Ca}_5(\text{OH})(\text{PO}_4)_3$, Sigma-Aldrich) were mixed with 40% $\text{w}\cdot\text{v}^{-1}$ poloxamer solution (Pluronic® F-127, Sigma-Aldrich). α -TCP and nano-HA powder were disinfected with UV-light for 1 hour before mixing. The poloxamer solution was disinfected by filtration through a 0.22 μm sterile filter (Millex®-GS). This paste was loaded into a cartridge and kept at 4°C until use.

Osteochondral constructs were produced by combining the PCL microfiber mesh and the pCaP paste to form the reinforcement of the chondral compartment and the biomimetic bone compartment, respectively. Fabrication was performed by directly depositing the pCaP paste (approximated strand diameter = 250 μm) on the hydrolyzed MEW mesh (**Figure 2**). Eighty percent of the mesh thickness was set as the initial height for depositing the pCaP paste, as this proved to be the height that did not damage the mesh structure and ensured an optimal integration between the bone compartment and the chondral compartment. The first two layers of pCaP were deposited without macro-spacing, to mimic the subchondral bone plate, and followed by layers with designed macro-spacing of 700 μm to mimic the cancellous section with same stacking pattern as described in **Chapter 4** (diameter = 6 mm, height = 6 mm)

After finishing the fabrication process, the osteochondral constructs were allowed to set at 37°C under saturated relative humidity to form a solid, biomimetic bone compartment through conversion of the pCaP composite to calcium deficient hydroxyapatite (CDHA). Finally, the osteochondral constructs were disinfected in 70% ethanol and exposed to UV-light for 1 hour, prior to seeding of cells.

In vitro pre-culture

Allogeneic articular cartilage progenitor cells (ACPCs) were obtained as previously described^{16, 18} from animals that were euthanized at the Utrecht University Veterinary Hospital for causes unrelated to diseases or impairment of the musculoskeletal system and whose remains were donated for research purposes. Briefly, hyaline cartilage was collected in a sterile fashion, minced, and digested at 37°C with 0.2% w·v⁻¹ pronase solution for 2 hours, followed by 12 hours in 0.075% w·v⁻¹ collagenase solution. ACPCs were then selected using a fibronectin adhesion assay.¹⁸ Cells were expanded in culture and stored in liquid nitrogen. After thawing, cells were expanded until passage 3 prior to their use for these experiments.

The constructs made of the combined printed CaP and MEW meshes were sterilized in ethanol and by exposure to UV-light for 1 hour. To avoid any pH changes that might affect the cells, the constructs were washed 3 times for 10 minutes with PBS and then immersed for 1 week in cell culture medium consisting of Dulbecco's Modified Eagle Medium/Nutrient Mixture F-12 (DMEM/F-12, 11320033, Gibco, The Netherlands) supplemented with 10% v·v⁻¹ heat-inactivated foetal calf serum (FCS, Gibco, The Netherlands), 0.2 mM L-ascorbic acid 2-phosphate (Sigma), 1% MEM Non-Essential Amino Acids Solution (11140035, Gibco, The Netherlands) and 100 U/mL penicillin with 100 µg·mL⁻¹ streptomycin (Life Technologies, The Netherlands). Media were refreshed every 2-3 days.

On the day of seeding, the medium was refreshed 2 hours before seeding, then scaffolds were placed inside a custom-made polydimethylsiloxane (PDMS) ring (**Figure 2**) that prevented overflow of the cell suspension from the cartilage compartment to the bone scaffold. Ten million cells were suspended in 100 µl of medium and seeded on top of the constructs. The cell suspension was left to settle at the bottom of the cartilage part for 30 minutes. Afterwards, 2 ml of cartilage medium supplemented with 100 ng·ml⁻¹ of GDF-2 (PeproTech, The Netherlands) were carefully added to the well. The seeded constructs were cultured for 4 weeks prior to implantation, refreshing the medium 3 times a week.

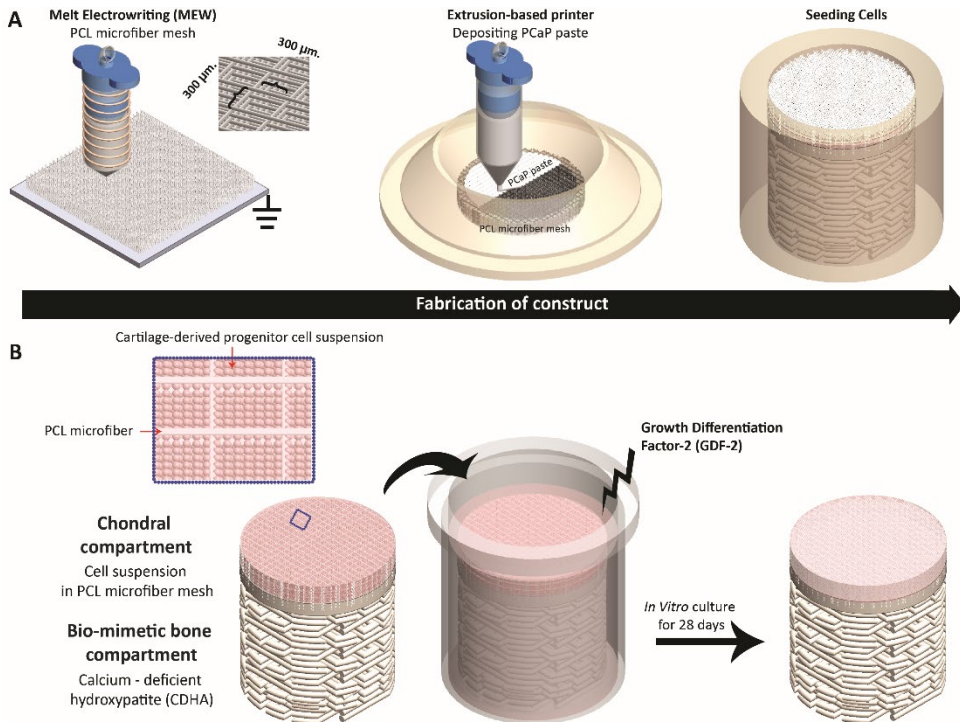


Figure 2. Schematic picture representing the fabrication process of the tissue engineered osteochondral constructs.

Surgical procedure

Ponies were premedicated with detomidine (intravenous (IV), $10 \mu\text{g}\cdot\text{kg}^{-1}$) and morphine (IV, $0.1 \text{ mg}\cdot\text{kg}^{-1}$) and anesthesia was induced with midazolam (IV, $0.06 \text{ mg}\cdot\text{kg}^{-1}$) and ketamine (IV, $2.2 \text{ mg}\cdot\text{kg}^{-1}$). Anesthesia was maintained with isoflurane in oxygen together with continuous rate infusion of detomidine (IV, $10 \mu\text{g}\cdot\text{kg}^{-1}/\text{h}$) and ketamine (IV, $0.5 \text{ mg}\cdot\text{kg}^{-1}/\text{h}$). Meloxicam (IV, $0.6 \text{ mg}\cdot\text{kg}^{-1}$), morphine (epidural injection, $0.1 - 0.2 \text{ mg}\cdot\text{kg}^{-1}$) and ampicillin (IV, $10 - 15 \text{ mg}\cdot\text{kg}^{-1}$) were administered pre-operatively as analgesic medication and antibacterial preventative therapy, respectively.

The medial femoral ridge of the stifle joint was exposed by arthrotomy and an osteochondral lesion (diameter = 6 mm, depth = 6 mm) was surgically created using a power drill. The surgical area was flushed by saline for cooling and removal of debris. Cell-laden constructs were implanted press-fit in a randomly chosen hind limb, with the cell-free control being implanted in the contralateral limb. After closing the arthrotomy wound in 3 layers in routine fashion, procaine penicillin was administered (Procopen, intramuscular (IM), $20 \text{ mg}\cdot\text{kg}^{-1}$). Post-operatively, nonsteroidal anti-inflammatory medication (metacam, per os (PO), SID, $0.6 \text{ mg}\cdot\text{kg}^{-1}$) was administered for 5 days and opioids (tramadol, PO, BID, $5 \text{ mg}\cdot\text{kg}^{-1}$) were administered for 2 days.

Gait analysis

The ponies were trained on a treadmill prior to the study using a standard protocol for treadmill habituation. Twenty-eight spherical reflective markers with a diameter of 24 mm (topline) and 19 mm (elsewhere) were attached with double-sided tape and second glue to anatomical landmarks (**Figure 3**). Kinematic data were collected on a treadmill (Mustang, Fahrwangen, Switzerland) at trot using six infrared optical motion capture cameras (ProReflex, Qualisys, Gothenburg, Sweden) recording at a frame rate of 200 Hz for 30 seconds at each session to obtain a sufficient number of strides.

To process the data, the reconstruction of three-dimensional coordinates of each marker was automatically calculated by Q-Track software (Qtrack, Qualisys, Gothenburg, Sweden). Each marker was identified and labelled using an automated model (AIM model) and manual tracking. Raw data of the designated markers were exported to Matlab (version 2018a, Niantics, California) for further analysis, using custom written scripts. For each stride, two symmetry parameters were calculated using the vertical displacement of the head and pelvis (tubera sacrale) markers. For each stride the differences between the two vertical displacement minima of the head (MinDiffhead) and pelvis (MinDiffpelvis) were calculated. Using the markers, limb-segments were formed and angles between these limb-segments were calculated. The difference between the maximal and minimal angle was defined as the range of motion (ROM) of a joint. For each timepoint, the mean value of all strides for each parameter was calculated.

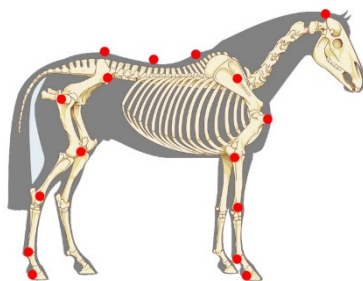


Figure 3. Schematic picture representing location of the markers for gait analysis.

Radiographic examination

Stifles were radiographed in 3 projections: lateromedial, craniolateral-caudomedial oblique and caudo-cranial projection using standard machine settings before surgery (baseline), at 3 weeks postoperatively and at 6 months, just before euthanasia.

Euthanasia and sample harvest

After 6 months, animals were euthanized by induction with Midazolam (IV, 0.06 mg·kg⁻¹ body weight) with ketamine IV, (2.2 mg·kg⁻¹ body weight) and subsequent administration of sodium pentobarbital (IV, 1400 mg·kg⁻¹ body weight). Next, the stifle joint was exposed and gross assessment of the medial trochlear ridge was performed, focusing at the degree of filling of the defect, the integration of repair tissue with the surrounding native tissue and the surface quality of the repair tissue. Subsequently, the entire osteochondral area containing the constructs was harvested for further analyses with the aid of a surgical bone saw. Harvested tissues were initially kept in sterilized PBS for μ -CT scanning, biomechanical analyses and for collecting tissue from the chondral compartment of the implant for biochemical analyses. After this, all tissues were fixed in 4% formaldehyde for subsequent histological processing.

Biomechanical evaluation

The compressive properties of the chondral compartment of the defect site, the adjacent surrounding native cartilage and the more distant surrounding native cartilage (5-10 mm from the boundary of the defect) (N=7 for cell-laden constructs and N=7 for cell-free constructs) were evaluated with a dynamic mechanical analyzer (DMA, DMA Q800, TA instrument) equipped with a custom-size compressing probe (diameter = 2 mm). A ramp force of 0.250 N/min was applied until reaching 2.0 N, to limit the deformation of the sample to values below 200 μ m. Young's modulus was calculated as the slope of the stress-strain curve in the range between 10-12 % strain.

Biochemical evaluation

Firstly, biochemical analyses were performed on supplemental pre-implantation constructs (N=3) that had been prepared in the same batch as the constructs that were later implanted. The chondral compartments of 28-day cultured constructs were removed and freeze-dried. Next, dry samples were digested in papain (Sigma Aldrich) at 60°C overnight. DNA, sulphated glycosaminoglycan (sGAG), and alkaline phosphatase (ALP) content were quantified by performing the Quan-iT-Picogreen-dsDNA-kit assay (Molecular Probes, Invitrogen, Carlsbad, USA), the dimethylmethylene blue assay (DMMB, Sigma-Aldrich, The Netherlands) and the p-nitrophenyl phosphate assay (SIGMAFAST™, Sigma-Aldrich), respectively.

Secondly, tissue fractions that were collected from the chondral compartments of harvested implants (N=6 for cell-laden constructs, N=7 for cell-free constructs) were kept at -80°C, followed by lyophilization. Collagen content was quantified using an hydroxyproline assay (L-Hydroxyproline, Merck KGaA), and the sGAG and DNA quantification was performed as described above.

Microcomputed tomography

Microcomputed tomography (μ -CT) was employed for the quantitative analysis of the bone compartments from the harvested osteochondral lesions (N=7 for cell-laden constructs, N=7 for cell-free constructs). Six freshly made osteochondral grafts were scanned in a μ -CT scanner (Quantum FX-Perkin Elmer) to quantify the initial volume of pCaP material, pre-operatively. The post-mortem harvested tissue containing the defect area and the surrounding native tissue were similarly scanned (voltage = 90 kV, current = 200 μ A, voxel size = 30 μ m³ and total scanning time = 3 minutes). Subsequently, the 3D-reconstructed images were processed and analyzed using the ImageJ²¹ software and the BoneJ²² plugin. Two-dimensional regions of interest (ROIs) were selected in an axial plane at the boundary between the defect and the surrounding native tissue and interpolated to form 3D-volumes of interest (VOI). Thresholding was performed to separately selected area of ceramics and newly formed bone for further calculation. Then, the percentages of mineralized newly formed bone, of non-mineralized tissue and of remaining ceramics, including the percentage of ceramics volume loss, were quantified.

Histological evaluation

Firstly, supplemental pre-implantation constructs (N=3) that had been prepared in the same batch as the ones that later were implanted were fixed in 4% formaldehyde. After decalcification in 0.5M EDTA disodium salt (pH = 8) for 1 day, tissues were dehydrated with graded ethanol series, cleared in xylene and embedded in paraffin. Paraffin embedded tissues were sliced to 5 μ m sections. Histochemical evaluation of glycosaminoglycans (GAGs) was done by safranin-O/ fast green staining. Type I collagen (primary antibody: monoclonal antibody EPR7785, 1.083 mg.ml⁻¹, Abcam) and type II (primary antibody: monoclonal antibody II-II6B3, 0.06 mg.ml⁻¹, DSHB) were visualized by immunohistochemistry.

The tissues that were harvested after 6 months (N=7 for cell-laden constructs, N=7 for cell-free constructs) were kept in 4% formaldehyde and then decalcified in 0.5M EDTA disodium salt (pH = 8) for 24 weeks. Decalcified tissues were cut into two halves before processing to enable visual inspection of the center of the lesion. Tissues were dehydrated with graded ethanol series, cleared in xylene and finally embedded in paraffin. Paraffin embedded tissues were sliced to 5 μ m sections. For assessment of morphology and cell distribution, hematoxylin-eosin staining (Mayer's haematoxylin, Merck 109249 and eosin, Merck 115935) was performed. Glycosaminoglycans and collagen alignment were assessed after safranin-O / fast green and picrosirius red staining, respectively. Type I and type II collagen were visualized by immunohistochemistry, as described above. For immunohistochemistry, all samples were treated according to previously published protocols.¹⁸ Stained histological slides were imaged using a light microscope (Olympus BX51, Olympus Nederland B.V.) equipped with a digital camera (Olympus DP73, Olympus

Nederland B.V.). To observed picosirius red stained slides, polarizer was also equipped to the light microscope.

Statistical analysis

Normal distribution of data was assessed from skewness, kurtosis and Q-Q plots. Results were reported as mean \pm standard deviation. Wilcoxon signed rank tests were used to analyze the biochemical, biomechanical and μ -CT data. Statistical significance was set at $p < 0.05$. All tests were performed using Matlab (R2018b, The MathWorks, Inc.).

To evaluate the gait parameters, stride-level data were analyzed with R software (version 3.6.0, R Core Team, 2019), using package NLME (version 3.1-137) for mixed modelling. Dependent variables were investigated for normality using normal probability plotting and examining for skewness and kurtosis. If not normally distributed, data were transformed to permit linear mixed modeling. The random effect was subject and timepoint was the fixed effect. Significance was set at $p < 0.05$ and p values were corrected using the false discovery rate method. Residual plots were checked for heteroscedasticity versus the outcome, as well as for normality in Q-Q plots.

RESULTS

In vitro pre-culture and cartilage tissue engineering

Growth differentiation factor two (GDF-2) stimulated ACPCs to colonize the MEW scaffolds and the neo-tissue grew into a disc shape after 3 weeks of culture. During the 4th week of culture, outgrowth from the MEW meshes was observed (**Figure 4A**). Cell-free constructs did not change after immersion in growth factor-free medium for 4 weeks (**Figure 4B**). Biochemical analyses of the chondral compartment of the cell-laden constructs revealed the presence of GAGs (GAG/DNA was $199.7 \pm 67.7 \mu\text{g} \cdot \mu\text{g}^{-1}$). Moreover, ALP activity was also observed (ALP/DNA was $3702 \pm 2111 \text{ U} \cdot \mu\text{g}^{-1}$). Safranin-O staining and type II collagen immunohistochemistry revealed abundant deposition of GAGs and type II collagen within the constructs after 3 weeks of *in vitro* culture (**Figure 4C**), showing that the chondral regions of the constructs (meant for subsequent implantation) were filled with a hyaline cartilage-like tissue. However, a preferential alignment of the collagen fibers could not be observed.

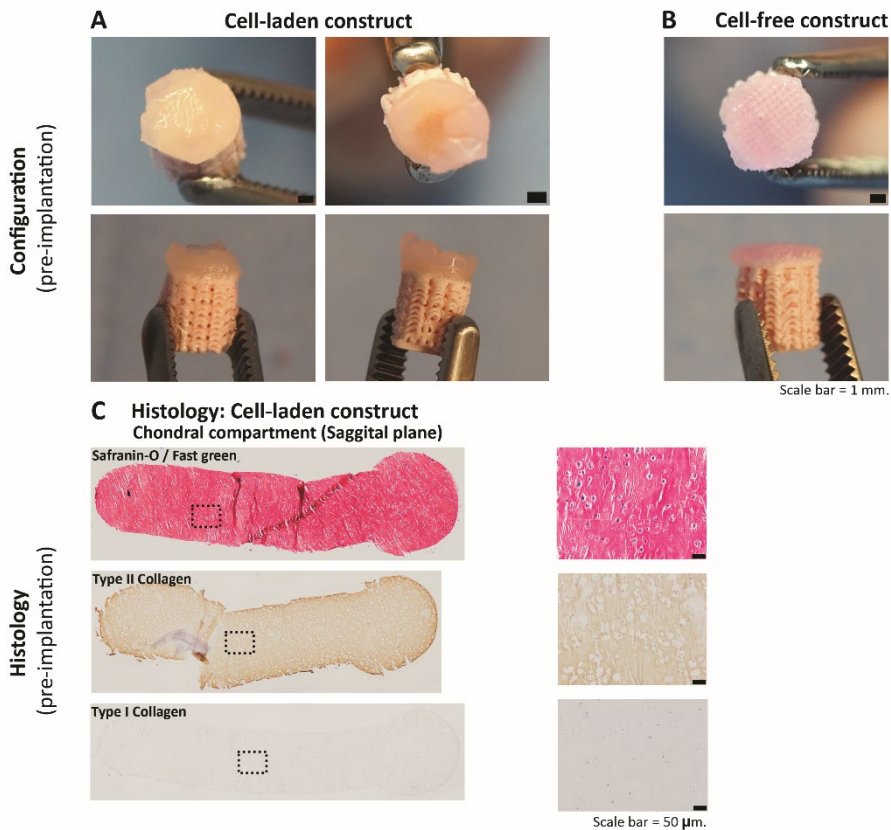


Figure 4. Cell-laden (A) and cell-free constructs (B) at the time of implantation. (C) Positive safranin-O staining, positive type II collagen and negative type I collagen immunohistochemistry were observed in the chondral compartments of the cell-laden constructs before implantation.

Surgical procedure

Both cell-laden and cell-free constructs were press-fit implanted into the surgically created defect sites. During this procedure, the slightly irregular outside surface of the osteal part of the construct hampered easy sliding of the construct down into the defect and some fragmentation of the edges of the pCaP was observed during the procedure. This was similar for the cell-seeded and cell-free constructs, which had identical osteal parts (**Figure 5**).

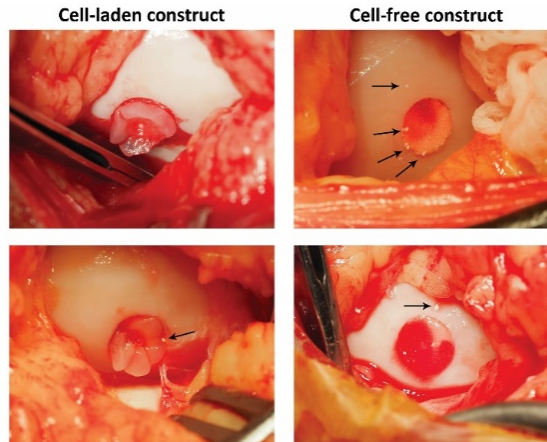


Figure 5. White fragments (arrows) from the ceramic, biomimetic bone compartment of the osteochondral construct that broke off during the implantation procedure.

Clinical monitoring

All ponies recovered well from anesthesia after surgery and passed uneventfully through the rehabilitation period without any abnormalities in body temperature or behavior, with good weight-bearing on all operated limbs and no clinical signs of lameness during the entire period, with the exception of a single pony that developed severe lameness at 10 weeks after surgery. This pony was treated with anti-inflammatory medication and examined radiographically, which revealed extensive osteolysis around the created lesion. Because of persistent discomfort, the pony was euthanized.

Gait analysis

Symmetry parameters:

Front and hind limb lameness were analyzed through evaluation of the symmetry parameters of the head (MinDiff Head (**Figure 6A**)) and of the pelvis (MinDiff Pelvis (**Figure 6B**)). These values reflect the differences in minimal vertical displacement with a negative MinDiff indicating a left-sided asymmetry and a positive MinDiff a right-sided asymmetry. In the treated ponies (except for the case referred to above that was euthanized), for both the head and the pelvis, there was no clear pattern in the direction of the asymmetries between baseline and endpoint and those differences between baseline and endpoint were minimal and statistically not significant. Therefore, symmetry measures could not discriminate between cell-laden and cell-free constructs. Further, there was also no clear effect of timepoint on pelvis roll and pelvis yaw range of motion (**Supplementary Figure 1**), however, pelvis pitch

range of motion (ROM) (**Figure 6C**) decreased for all subjects with almost 20% over time (**Supplementary Table 1**).

Limb parameters, effects of time:

There was a significant effect of time for the height the toe was lifted from the surface during the swing phase of the limb that decreased significantly in the cell-free treated limbs, but not in the limbs treated with cell-laden constructs (**Supplementary Table 1**). The only other significant effect of time was a decrease in the extension of the metacarpophalangeal joint of the forelimb ipsilateral to the hind limb that had been treated with cell-laden constructs, indicating unloading of that forelimb (**Supplementary Table 1**).

Limb parameters, differences between cell-laden and cell-free at endpoint:

There were no significant differences between any of the cell-laden and cell-free limb parameters. Results from the linear mixed model are shown in **Supplementary table 2**.

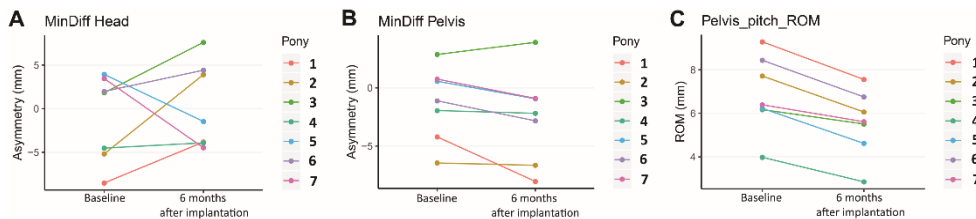


Figure 6. Symmetry data of the head (A) and pelvis (B) show no consistent differences over time. However, pelvis pitch decreased consistently in all individuals (C).

Radiographic examination

On the radiographs taken at baseline, 3 and 6 months no abnormalities were seen other than the defects that had been created, except for the pony that developed severe lameness. In that animal, severe osteolysis was noted at the implantation site (**Supplementary Figure 2**).

Macroscopic evaluation

After 6 months, macroscopic evaluation revealed that the defects were filled with repair tissue that in all cases did not fill the entire defect and remained lower than the level of the surrounding native cartilage in both cell-laden and cell-free treatments (**Figure 7A**). The color of the repair tissue was variable (from reddish, to yellow and translucent) within the different treatments (**Figure 7B**). In some cases, ceramic fragments could be observed within the repair tissue of the chondral compartment.

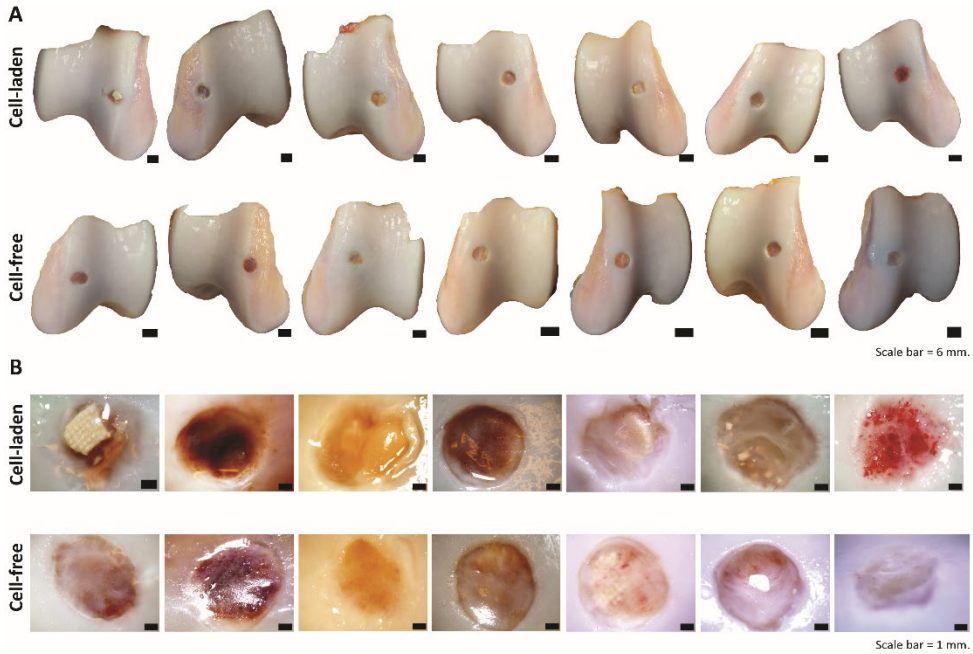


Figure 7. Macroscopic appearance of the repair tissue and surrounding native tissue in all individual animals at euthanasia.

Biochemical analyses

There were no significant differences in either glycosaminoglycans (GAGs) (cell-laden: $30.46 \pm 15.95 \mu\text{g} \cdot \mu\text{g}^{-1}$, cell-free: $24.44 \pm 15.31 \mu\text{g} \cdot \mu\text{g}^{-1}$) or collagen expressed per DNA (cell-laden: $79.66 \pm 91.21 \mu\text{g} \cdot \mu\text{g}^{-1}$, cell-free: $134.21 \pm 153.73 \mu\text{g} \cdot \mu\text{g}^{-1}$) between the chondral compartments of the cell-laden and cell-free constructs (**Figures 8A, 8B and Supplementary Figure 3**). However, all values were substantially lower than those from native cartilage (**Figure 8**, grey dotted line) that was harvested distantly from the defect site.

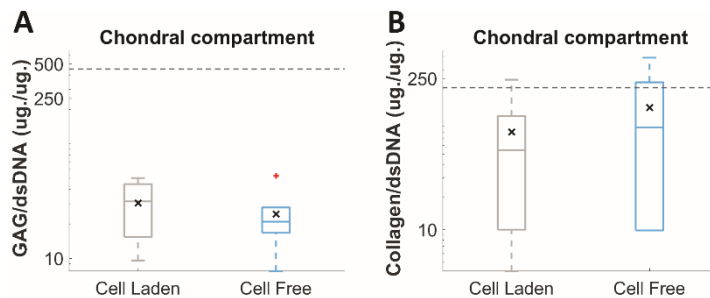


Figure 8. Quantitative analysis of GAG/DNA between cell-laden and cell-free treatments (A). Quantitative analysis of collagen/DNA between cell-laden and cell-free treatments (B) (x = mean). Grey dotted line indicates level in native cartilage.

Biomechanical properties

There were no significant differences in Young's modulus of the chondral compartments between cell-laden (0.31 ± 0.13 MPa) and cell-free (0.42 ± 0.19 MPa) constructs (**Figure 9A**). This was also true for two sites of the native cartilage, one close to the border of the defect (cell-laden: 1.75 ± 0.80 MPa, cell-free: 2.22 ± 0.48 MPa) and one at 5 - 10 mm from the defect boundary (cell-laden: 1.86 ± 0.78 MPa, cell-free: 2.19 ± 0.77 MPa) (**Figure 9B, 9C**). However, Young's modulus of the native tissue was substantially higher than of the chondral compartment.

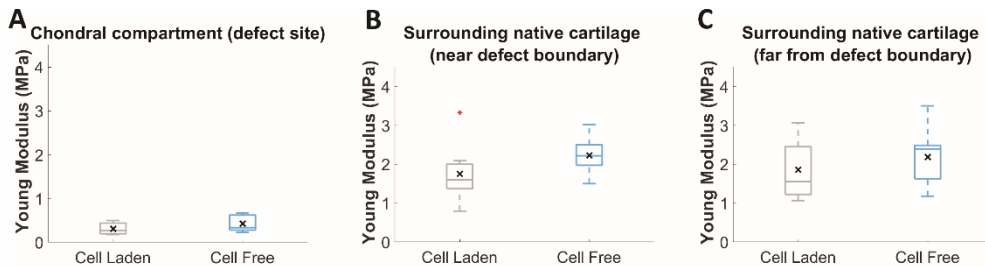


Figure 9. Young's moduli of the chondral compartments of cell-laden and cell-free constructs at 6 months (A) and at two sites of the native cartilage, close to the border of the defect (B) and further away (C). (x = mean)

Micro-CT (Quantification within the bone compartment)

Micro-CT images showed significant bone loss surrounding the implant in both the cell-laden and the cell-free groups. However, mineralized bone formation could be visualized in some scaffolds from both groups with an integration to neighboring native bone (**Figure 10A**). Statistically, there were no significant differences in mineralized bone formation (cell-laden: $6.14\% \pm 10.09\%$, cell-free: $4.73\% \pm 4.93\%$) and non-mineralized tissue (cell-laden: $81.38\% \pm 15.37\%$, cell-free: $74.71\% \pm 12.44\%$). However, there was a significant difference in the amount of remaining ceramics between the two groups (cell-laden: $12.48\% \pm 9.75\%$, cell-free: $20.56\% \pm 10.54\%$ ($p = 0.0313$)) (**Figure 10B**). In line with this, there was a difference in the degradation of ceramics in the cell-laden construct versus the cell-free constructs (cell-laden: $79.02 \pm 16.18\%$, cell-free: $63.20 \pm 13.90\%$ ($p = 0.0313$)) (**Figure 10C**)

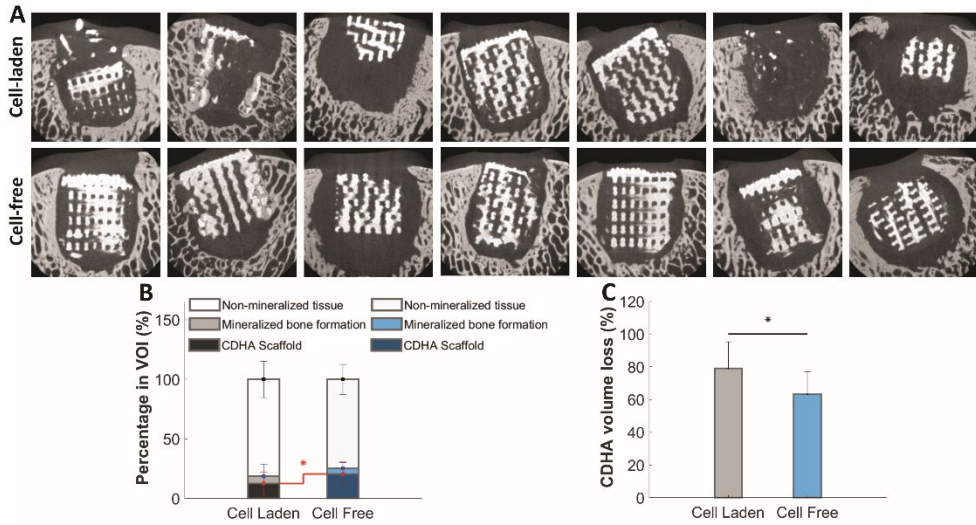


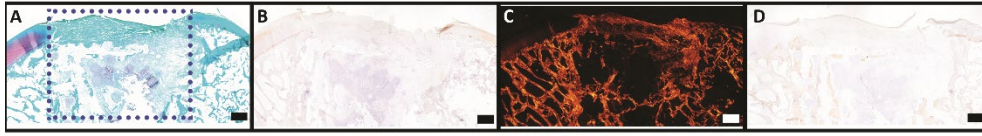
Figure 10. Representative μ -CT images from the middle of the sagittal plane of the constructs (A). Quantitative analysis from μ -CT reconstruction showing percentage of mineralized bone formation, non-mineralized tissue and remaining ceramics (B). The volume loss of ceramics was slightly higher in the cell-seeded constructs compared to the cell-free ones (C).

Histology

In the chondral region, the defect sites of both cell-laden and cell-free structures were filled with fibrous repair tissue, as revealed by H&E and safranin-O staining (**Figure 11, Supplementary Figure 4**). Integration at the boundary of the defect between chondral repair tissue and surrounding native cartilage was observed in both groups. Production of GAGs, type II collagen and type I collagen was very limited in the repair tissue in both groups (**Figure 11**). The organization of the collagen fibrils in both groups seemed random, without any hierarchical pattern that could be identified by polarized light imaging of picrosirius red staining. Additionally, the special distribution of PCL-microfibers, which had disappeared because of the xylene treatment during sample preparation, was still visible within the chondral region of from both groups (1 out of 7 for cell-laden and 5 out of 7 for cell-free structure).

In the bone region, there was positive staining for type I collagen in some scaffolds from both groups at places where there were islands of new mineralized bone formation.

Cell-laden



Cell-free

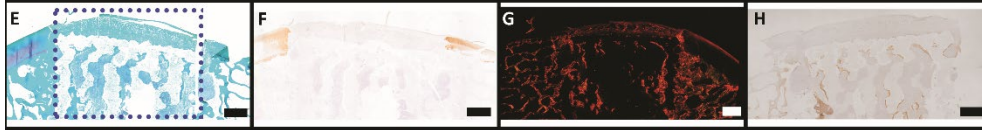


Figure 11. Representative histological images from the middle of cell-laden and cell-free structures after implantation for 6 months. (A,E) Safranin-O/fast green (red color = positive); (B,F) Type II collagen (brown color = positive); (C,G) Picosirius-red; (D,H) type I collagen (brown color = positive) of cell-laden (A-D) and cell-free structures (E-H). (Scale bar = 1mm.).

DISCUSSION

There are many factors that need to be taken into account when developing tissue-engineered osteochondral implants, including the nature of the osteal anchor, the design of a strong and durable connection at the bone-cartilage scaffold interface and the composition and structure of the chondral compartment. These are all crucial elements, as they all will influence the eventual efficacy of the implant. Much work has been done on the development of several types of bone grafts and many of these are routinely used in clinical settings²³, so of these elements the osteal part is seemingly the least difficult one. However, the relationship between the osteal anchor and the quantity and quality of the repair tissue in the chondral region has been subject of debate²⁴ and it is still unclear what osteal scaffold would form the best base for facilitating cartilage repair. In earlier studies^{25, 26}, fibrous repair tissue in the chondral region was observed together with osteolysis surrounding an osteal anchor when tissue-engineered osteochondral grafts were implanted in a load-bearing area for a long-term study. It was hypothesized in those studies that insufficient support of an osteal anchor leading to instability might be one of the causes for deficient chondral regeneration. In this context, stiffness, and position/alignment of an osteal anchor are some of the parameters that have been considered²⁷⁻³⁰, as all of these might affect stability of the chondral compartment.

In the current study, the chondral region performed poorly, remodeling into fibrous tissue with low content of GAGs and type II collagen. The cell-laden engineered tissue at the time of implantation showed a high presence of neo-cartilage ECM components, yet the average GAGs content decreased approximately 6.5-fold during the *in vivo* residency period. Some of the osteal anchors showed misalignment and even collapse, with bone loss surrounding the implant in both cell-laden and cell-free treatments after the 6-month implantation period, which is strongly suggestive of instability of the implant. This instability could be related to the difficulties encountered during the surgical placement of the implants, resulting in fragments breaking off from the bioceramic osteal anchor. This in itself may be

related to the less than perfect cylindrical shape of the implant due to slight variations in the consecutively deposited layers during the printing process, combined with the brittleness of the CaP-based material. These circumstances may have resulted in failure to place the implant in a real press-fit fashion and, hence, in the creation of (micro-) movement, leading to increasing instability under repetitive loading and ensuing osteolysis, as observed previously.³¹ Additionally, the gap between the implant and surrounding native cartilage due to the imperfect fit might have allowed for the intrusion of synovial fluid. Contact of synovial fluid with subchondral bone has been shown to induce osteolysis.³² The misalignment and partial collapse of the osteal part of the construct will also be at the basis of the protrusion of the chondral compartment of some cell-laden constructs and the inconsistent position of the chondral graft with respect to the surrounding native tissue in both groups. These conditions may have led to an abnormal load distribution, possibly inducing inferior biomechanical properties.³³

The exact same bioceramic material that was used for the osteal anchor in this study, had performed very well in an earlier study¹⁴ in the same species. However, there are two major differences with the use of the material in the current study. First, in the previous study, the material was implanted in the tuber coxae of the horses, which is an orthotopic area, but unloaded and not located intra-articularly. Second, in the former study the implant was surrounded by a cylindrical case made of PCL that served to prevent bone ingrowth from the side. Therefore, although in fact inadvertently and as a side-effect, the problem of fragment formation due to the combination of the imperfect perimeter of the construct and the brittleness of the material was avoided. In fact, PCL is a deformable material and the used encasing could have accommodate the shape of the ceramic implant to fit into the defect. Whereas the duration of both studies was not identical (7 months in the earlier study, 6 months in the current study) and direct comparison is therefore not possible, there were clear histological differences with many more eosinophilic and plasma cells in the current study compared to the earlier study in which there were very few inflammatory cells visible. This difference is likely due to the chronic irritation caused by the instability in the current study.

In the few scaffolds that remained in place, the volume of mineralized bone formation was lower than in the earlier study, in both cell-laden and cell-free treatments. This may have to do with the site used in the current study, which was a repetitively loaded intra-articular site. It is therefore not unlikely that the failure of the osteal part of the implant was not only due to the factors described above, but also to loading. Nevertheless, it is clear that the imperfect implantation had severe repercussions and can be considered a major factor that affected the chondral compartment and hence the outcome of the study. This to the extent that drawing any conclusions about the effect of GDF-2 seeded ACPCs, which was the principal variable that was to be tested in the study, is not possible. Also, no conclusion could be reached about the interface between the osteal and chondral parts that was used. Delocalized MEW-mesh structures could be recognized in some scaffolds from both groups. This might be due to misalignments of the osteal regions as discussed above, or to shear forces during loading.

During the *in vivo* post-operative monitoring of the animals, the clinical signs were very mild and far from alarming, except for the single pony that developed severe lameness. The gait analysis data did not show many differences with respect to baseline. This may to a certain extent have been related to methodological factors. During the assessment, ponies were put on a treadmill and they were imposed the same belt velocity during both measurements. Therefore, the subjects were forced to trot at the same velocity, making that stride length needed to be maintained. This might be the reason why there were no differences between timepoints for maximal protraction and retraction (the limb parameters). However, pelvis pitch range of motion (ROM) decreased for all subjects with almost 20% over time. This pattern is often seen in case of dysfunction of the back and may possibly indicate that bilateral hindlimb lameness may induce back problems in horses.³⁴⁻³⁶ Toe dragging, in which the hoof is lifted less high off the ground, of the lame limb is another sign of pain.³⁷ Overall, the impact of the bilateral lesions in the stifle joints was low, as evidenced by the fact that there was no sign of load redistribution from the hind to the front limbs. If that had been the case, the subjects would have compensated by displacing their center of mass more to the front, resulting in more negative angles for forelimb fetlock extension, as fetlock hyper extension correlates with peak ground reaction force (GRFpeak)³⁸, where less negative angles indicate a lowered GRFpeak. In fact, only the fetlock angles of the forelimb ipsilateral to cell-laden construct changed, becoming less negative, hence indicating unloading rather than additional loading (lower GRFpeak). The reason for this is not clear.

It can be concluded that even seemingly minor modifications of a successful implant may have grave consequences and extrapolation is dangerous in the complex *in vivo* situation. In this case, the failure of the osteal part of the construct, the use of which seemed well-backed by solid *in vivo* data, did not permit drawing of any conclusions about the original hypotheses. Given the relatively frequently occurring rather disappointing results of *in vivo* orthotopic testing of promising techniques for joint repair, it may be wise to put more emphasis on performing pilot experiments before embarking on a full-scale *in vivo* study in a large animal experiment.³⁹ Functional joint repair remains a huge challenge that has not been addressed to some satisfying extent during the last decades, despite many promising approaches. It is likely that the quest for a real solution will go on for some time by trial and error with more errors to come. Those errors are inevitable and need to be made but should take the least possible toll on experimental animals.

ACKNOWLEDGEMENTS

The authors would like to thank Dr. S. (Stefanie) Veraa for the assistance with radiographic examination and Dr. J.P.A.M. (Thijs) van Loon and Dr. Janny de Grauw for the assistance with anesthesia. The authors also wish to acknowledge the funding support from Royal Thai government scholarship (Thailand, PD), the Dutch Arthritis Foundation (LLP-12 and LLP-22) and the European Research Council under grant agreement N0. 647426 (3D-JOINT). The primary antibodies against type II collagen (II-II6B3) developed by T. F. Linsenmayer and

E. S. Engvall, respectively, were obtained from the DSHB developed under the auspices of the NICHD and maintained by the University of Iowa, Department of Biology, Iowa City, IA, USA.

REFERENCES

1. Kloppenburg, M.; Berenbaum, F., Osteoarthritis year in review 2019: epidemiology and therapy. *Osteoarthritis Cartilage* **2020**.
2. Kwon, H.; Brown, W. E.; Lee, C. A.; Wang, D.; Paschos, N.; Hu, J. C.; Athanasiou, K. A., Surgical and tissue engineering strategies for articular cartilage and meniscus repair. *Nat Rev Rheumatol* **2019**, *15* (9), 550-570.
3. Malda, J.; Groll, J.; van Weeren, P. R., Rethinking articular cartilage regeneration based on a 250-year-old statement. *Nat Rev Rheumatol* **2019**, *15* (10), 571-572.
4. Johnstone, B.; Stoddart, M. J.; Im, G. I., Multi-Disciplinary Approaches for Cell-Based Cartilage Regeneration. *J Orthop Res* **2019**.
5. Patel, J. M.; Saleh, K. S.; Burdick, J. A.; Mauck, R. L., Bioactive factors for cartilage repair and regeneration: Improving delivery, retention, and activity. *Acta Biomater* **2019**, *93*, 222-238.
6. Gotterbarm, T.; Breusch, S. J.; Schneider, U.; Jung, M., The minipig model for experimental chondral and osteochondral defect repair in tissue engineering: retrospective analysis of 180 defects. *Lab Anim* **2008**, *42* (1), 71-82.
7. Mancini, I. A. D.; Vindas Bolanos, R. A.; Brommer, H.; Castilho, M.; Ribeiro, A.; van Loon, J.; Mensinga, A.; van Rijen, M. H. P.; Malda, J.; van Weeren, R., Fixation of Hydrogel Constructs for Cartilage Repair in the Equine Model: A Challenging Issue. *Tissue Eng Part C Methods* **2017**, *23* (11), 804-814.
8. Martin, I.; Miot, S.; Barbero, A.; Jakob, M.; Wendt, D., Osteochondral tissue engineering. *J Biomech* **2007**, *40* (4), 750-65.
9. Boushell, M. K.; Hung, C. T.; Hunziker, E. B.; Strauss, E. J.; Lu, H. H., Current strategies for integrative cartilage repair. *Connect Tissue Res* **2017**, *58* (5), 393-406.
10. Diekman, B. O.; Guilak, F., Stem cell-based therapies for osteoarthritis: challenges and opportunities. *Curr Opin Rheumatol* **2013**, *25* (1), 119-26.
11. Lee, J. K.; Responde, D. J.; Cissell, D. D.; Hu, J. C.; Nolte, J. A.; Athanasiou, K. A., Clinical translation of stem cells: insight for cartilage therapies. *Crit Rev Biotechnol* **2014**, *34* (1), 89-100.
12. Diloksumpan, P.; de Ruijter, M.; Castilho, M.; Gbureck, U.; Vermonden, T.; van Weeren, P. R.; Malda, J.; Levato, R., Combining multi-scale 3D printing technologies to engineer reinforced hydrogel-ceramic interfaces. *Biofabrication* **2020**.
13. Bolaños, R. V.; Castilho, M.; de Grauw, J.; Cokelaere, S.; Plomp, S.; Groll, J.; van Weeren, P. R.; Gbureck, U.; Malda, J., Long-Term *in Vivo* Performance of Low-Temperature 3D-Printed Bioceramics in an Equine Model. *ACS Biomaterials Science & Engineering* **2020**.
14. Diloksumpan, P.; Bolaños, R.V.; Cokelaere, S.; Pouran, B.; de Grauw, J.; van Rijen, M.; van Weeren, R.; Levato, R.; Malda, J.; Orthotopic bone regeneration within 3D printed bioceramic scaffolds with region-dependent porosity gradients in an equine model **submitted**.
15. McCarthy, H. E.; Bara, J. J.; Brakspear, K.; Singhrao, S. K.; Archer, C. W., The comparison of equine articular cartilage progenitor cells and bone marrow-derived stromal cells as potential cell sources for cartilage repair in the horse. *Vet J* **2012**, *192* (3), 345-51.
16. Williams, R.; Khan, I. M.; Richardson, K.; Nelson, L.; McCarthy, H. E.; Anabelsi, T.; Singhrao, S. K.; Dowthwaite, G. P.; Jones, R. E.; Baird, D. M.; Lewis, H.; Roberts, S.; Shaw, H. M.; Dudhia, J.; Fairclough, J.; Briggs, T.; Archer, C. W., Identification and clonal characterisation of a progenitor cell sub-population in normal human articular cartilage. *PLoS One* **2010**, *5* (10), e13246.
17. Frisbie, D. D.; McCarthy, H. E.; Archer, C. W.; Barrett, M. F.; McIlwraith, C. W., Evaluation of articular cartilage progenitor cells for the repair of articular defects in an equine model. *J Bone Joint Surg Am* **2015**, *97* (6), 484-93.
18. Levato, R.; Webb, W. R.; Otto, I. A.; Mensinga, A.; Zhang, Y.; van Rijen, M.; van Weeren, R.; Khan, I. M.; Malda, J., The bio in the ink: cartilage regeneration with bioprintable hydrogels and articular cartilage-derived progenitor cells. *Acta Biomater* **2017**, *61*, 41-53.
19. Abinzano, F.; de Ruijter, M.; Mensinga, A.; Castilho, M.; Khan, I.; Levato, R.; Malda, J. Combining melt electrowriting of microfiber meshes with aggregated chondroprogenitor cells stimulated with GDF-2 to

- enhance cartilage tissue engineering. In: Annual Meeting of the European Society for Biomaterials; 2018 September 9-13; Maastricht, the Netherlands. Abstract nr 557
20. de Ruijter, M.; Ribeiro, A.; Dokter, I.; Castilho, M.; Malda, J., Simultaneous Micropatterning of Fibrous Meshes and Bioinks for the Fabrication of Living Tissue Constructs. *Adv Healthc Mater* **2019**, *8* (7), e1800418.
 21. Schindelin, J.; Arganda-Carreras, I.; Frise, E.; Kaynig, V.; Longair, M.; Pietzsch, T.; Preibisch, S.; Rueden, C.; Saalfeld, S.; Schmid, B.; Tinevez, J. Y.; White, D. J.; Hartenstein, V.; Eliceiri, K.; Tomancak, P.; Cardona, A., Fiji: an open-source platform for biological-image analysis. *Nat Methods* **2012**, *9* (7), 676-82.
 22. Doube, M.; Klosowski, M. M.; Arganda-Carreras, I.; Cordelieres, F. P.; Dougherty, R. P.; Jackson, J. S.; Schmid, B.; Hutchinson, J. R.; Shefelbine, S. J., BoneJ: Free and extensible bone image analysis in ImageJ. *Bone* **2010**, *47* (6), 1076-9.
 23. Oryan, A.; Alidadi, S.; Moshiri, A.; Maffulli, N., Bone regenerative medicine: classic options, novel strategies, and future directions. *J Orthop Surg Res* **2014**, *9* (1), 18.
 24. Bal, B. S.; Rahaman, M. N.; Jayabalan, P.; Kuroki, K.; Cockrell, M. K.; Yao, J. Q.; Cook, J. L., *In vivo* outcomes of tissue-engineered osteochondral grafts. *J Biomed Mater Res B Appl Biomater* **2010**, *93* (1), 164-74.
 25. Bothe, F.; Deubel, A. K.; Hesse, E.; Lotz, B.; Groll, J.; Werner, C.; Richter, W.; Hagmann, S., Treatment of Focal Cartilage Defects in Minipigs with Zonal Chondrocyte/Mesenchymal Progenitor Cell Constructs. *Int J Mol Sci* **2019**, *20* (3).
 26. van Susante, J. L.; Buma, P.; Homminga, G. N.; van den Berg, W. B.; Veth, R. P., Chondrocyte-seeded hydroxyapatite for repair of large articular cartilage defects. A pilot study in the goat. *Biomaterials* **1998**, *19* (24), 2367-74.
 27. Heuijers, A.; Wilson, W.; Ito, K.; van Donkelaar, C. C., Osteochondral resurfacing implantation angle is more important than implant material stiffness. *J Orthop Res* **2018**, *36* (11), 2911-2922.
 28. Nosewicz, T. L.; Reilingh, M. L.; Wolny, M.; van Dijk, C. N.; Duda, G. N.; Schell, H., Influence of basal support and early loading on bone cartilage healing in press-fitted osteochondral autografts. *Knee Surg Sports Traumatol Arthrosc* **2014**, *22* (6), 1445-51.
 29. Schlichting, K.; Schell, H.; Kleemann, R. U.; Schill, A.; Weiler, A.; Duda, G. N.; Epari, D. R., Influence of scaffold stiffness on subchondral bone and subsequent cartilage regeneration in an ovine model of osteochondral defect healing. *Am J Sports Med* **2008**, *36* (12), 2379-91.
 30. von Rechenberg, B.; Akens, M. K.; Nadler, D.; Bittmann, P.; Zlinszky, K.; Kutter, A.; Poole, A. R.; Auer, J. A., Changes in subchondral bone in cartilage resurfacing—an experimental study in sheep using different types of osteochondral grafts. *Osteoarthritis and Cartilage* **2003**, *11* (4), 265-277.
 31. Albrektsson, T.; Becker, W.; Coli, P.; Jemt, T.; Molne, J.; Sennerby, L., Bone loss around oral and orthopedic implants: An immunologically based condition. *Clin Implant Dent Relat Res* **2019**, *21* (4), 786-795.
 32. Kold, S. E.; Hickman, J.; Melsen, F., An experimental study of the healing process of equine chondral and osteochondral defects. *Equine Veterinary Journal* **1986**, *18* (1), 18-24.
 33. Bowland, P.; Ingham, E.; Jennings, L.; Fisher, J., Review of the biomechanics and biotribology of osteochondral grafts used for surgical interventions in the knee. *Proceedings of the Institution of Mechanical Engineers, Part H: Journal of Engineering in Medicine* **2015**, *229* (12), 879-888.
 34. Alvarez, C. B. G.; Bobbert, M. F.; Lamers, L.; Johnston, C.; Back, W.; van Weeren, P. R., The effect of induced hindlimb lameness on thoracolumbar kinematics during treadmill locomotion. *Equine Veterinary Journal* **2008**, *40* (2), 147-152.
 35. Alvarez, C. B. G.; Wennerstrand, J.; Bobbert, M. F.; Lamers, L.; Johnston, C.; Back, W.; Weeren, P. R., The effect of induced forelimb lameness on thoracolumbar kinematics during treadmill locomotion. *Equine Veterinary Journal* **2007**, *39* (3), 197-201.
 36. Greve, L.; Dyson, S.; Pfau, T., Alterations in thoracolumbosacral movement when pain causing lameness has been improved by diagnostic analgesia. *The Veterinary Journal* **2017**, *224*, 55-63.
 37. Buchner, H. H. F.; Savelberg, H. H. C. M.; Schamhardt, H. C.; Barneveld, A., Bilateral lameness in horses a kinematic study. *Veterinary Quarterly* **1995**, *17* (3), 103-105.
 38. Crevier-Denoix, N.; Robin, D.; Pourcelot, P.; Falala, S.; Holden, L.; Estoup, P.; Desquilbet, L.; Denoix, J. M.; Chateau, H., Ground reaction force and kinematic analysis of limb loading on two different beach sand tracks in harness trotters. *Equine Veterinary Journal* **2010**, *42* (s38), 544-551.

39. Vindas Bolaños, R. A.; Cokelaere, S. M.; Estrada McDermott, J. M.; Benders, K. E. M.; Gbureck, U.; Plomp, S. G. M.; Weinans, H.; Groll, J.; van Weeren, P. R.; Malda, J., The use of a cartilage decellularized matrix scaffold for the repair of osteochondral defects: the importance of long-term studies in a large animal model. *Osteoarthritis and Cartilage* **2017**, *25* (3), 413-420.

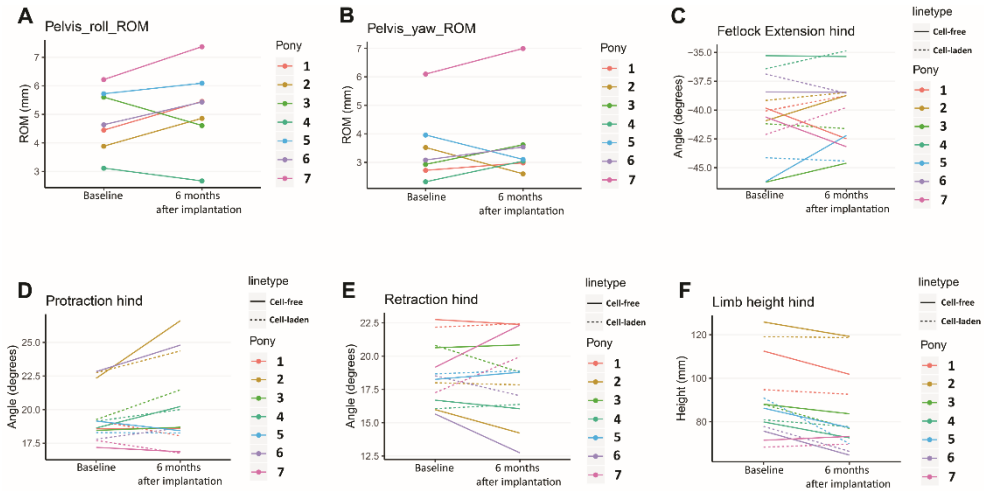
SUPPLEMENTARY INFORMATION

Variable	Baseline	endpoint	p-value	% Difference
MinDiff Poll	-1.00 (-5.08 - 3.08)	0.33 (-3.75 - 4.41)	0.59	
Pelvis roll ROM	4.81 (3.67 - 5.94)	5.21 (4.08- 6.35)	0.24	8.50
Pelvis pitch ROM	6.89 (5.38 - 8.39)	5.57 (4.06 - 7.07)	0.00	-19.16
Pelvis yaw ROM	3.52 (2.29 - 4.75)	3.70 (2.46 - 4.93)	0.56	5.07
MinDiff Pelvis	-1.36 (-4.61 - 1.89)	-2.52 (-5.77 - 0.73)	0.10	
MaxDiff Pelvis	0.98 (-2.08 - 4.04)	1.68 (-1.39 -4.74)	0.54	
Fetlock Extension (cell-laden) Ipsilateral Front	-36.11 (-37.96 - -34.25)	-33.58 (-35.43 - -31.72)	0.00	-7.01
Fetlock Extension (cell-free) Ipsilateral Front	-36.41 (-39.02 - -33.80)	-34.61 (-37.22 - -32.00)	0.19	-4.93
Fetlock Extension (cell-laden)	-40.00 (-42.59 - -37.41)	-39.49 (-42.08 --36.90)	0.37	-1.27
Fetlock Extension (cell-free)	-41.08 (-44.30 - -37.86)	-40.72 (-43.94 - -37.50)	0.71	-0.87
Limb Height (cell-laden)	88.55 (72.90 - 104.19)	81.70 (66.06 - 97.35)	0.06	-7.73
Limb Height (cell-free)	91.39 (73.26 - 109.51)	84.64 (66.51 - 102.76)	0.01	-7.39
max Protraction (cell-laden)	19.16 (17.22 - 21.11)	19.65 (17.71 - 21.59)	0.34	2.55
max Protraction (cell-free)	19.59 (16.93 - 22.26)	20.60 (17.94 - 23.27)	0.18	5.16
max Retraction (cell-laden)	18.78 (16.99 - 20.58)	18.76 (16.97 - 20.56)	0.97	-0.11
Max Retraction (cell-free)	18.45 (15.48 - 21.42)	18.19 (15.22 - 21.16)	0.74	-1.39

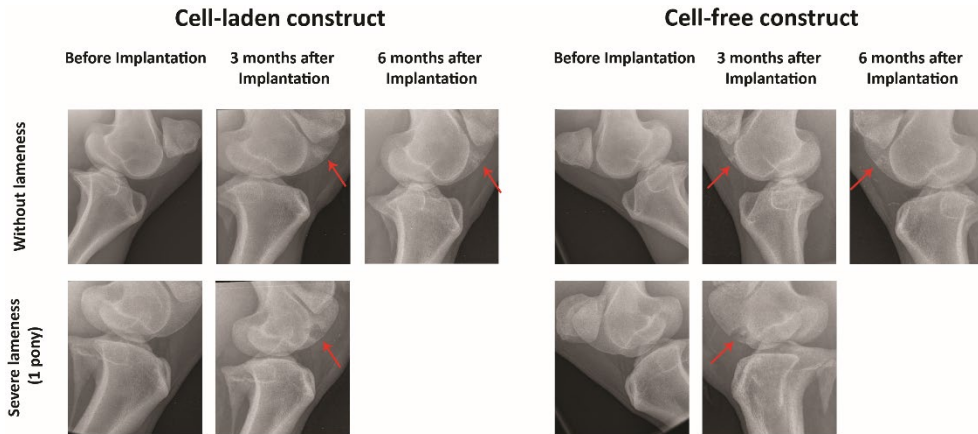
Supplementary Table 1. Symmetry parameters (differences between baseline and endpoint of the study for all ponies). Values are given in estimated means (CI), significant results are **bold**.

Variable	cell-free	cell-laden	% difference	p-value
Fetlock hyperextension (ROM)	-40.7 (-43.5 - -37.9)	-39.5 (-42.2 - -36.7)	3.12	0.19098
Maximal protraction (ROM)	20.6 (17.8 - 23.3)	19.7 (16.9 - 22.4)	4.85	0.39042
Maximal retraction (ROM)	18.2 (15.5 - 20.9)	18.8 (16.1 - 21.5)	-3.04	0.57655
Limb height (mm)	84.6 (67.4 - 101.9)	81.7 (64.4 - 98.9)	3.59	0.18918

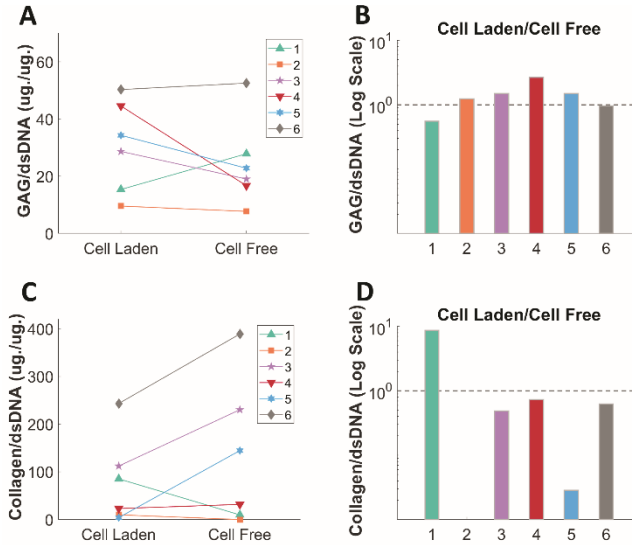
Supplementary Table 2. Differences between hind limb parameters at endpoint that was implanted with cell-laden and cell-free constructs. Values are given in estimated means (CI)



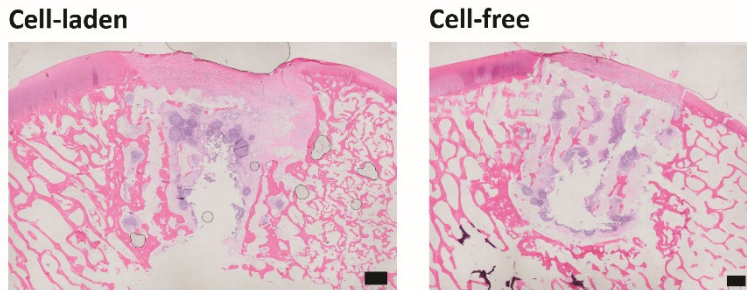
Supplementary Figure 1. Pelvis roll and yaw joint angles (A, B) showed no significant differences between baseline and 6 months after implementation. Kinematic hind limb parameters showed no significant differences for joint angles (C, D, E) between baseline and 6 months after induction. Limb height of the hind limbs (F) decreased for both hindlimbs, but only significantly for the cell free group, though there was no difference in limb height between cell-laden and cell-free groups at 6 months after implementation.



Supplementary Figure 2. Representative radiographic images (latero-medial and craniolateral-caudomedial oblique projections) of the stifle of ponies before implantation, 3 months after implantation and 6 months after implantation. Red arrows indicate the implantation sites. No radiographic abnormalities were noted in any of the ponies (1st row), except for the pony that became severely lame at 10 weeks. In this animal extensive osteolysis was observed (2nd row).



Supplementary Figure 3. Amount of GAG/DNA as absolute value (A) and as a ratio (B) in the individual animals. Amount of collagen/DNA as absolute value (C) and as a ratio (D) in the individual animals.



Supplementary Figure 4. Representative Hematoxylin-Eosin (H&E) staining showing repair tissue from both cell-laden and cell-free structures (Scale bar = 1 mm.)

CHAPTER 6

Multi-scale, 3D bioprinted osteocondral implants demonstrate long-term mechanical stability in the equine model

Mylène de Ruijter¹, Paweena Diloksumpan², Inge Dokter¹,
Harold Brommer², Filipe M. Braganca², Riccardo Levato¹,
Paul René van Weeren², Miguel Castilho^{1,3}, and Jos Malda^{1,2}

Manuscript in preparation

¹Department of Orthopaedics, RMCU Utrecht, UMC Utrecht, University of Utrecht, The Netherlands.

²Department of Clinical Sciences, Faculty of Veterinary Medicine, Utrecht University, The Netherlands.

³Department of Biomedical Engineering, Eindhoven University of Technology, The Netherlands

ABSTRACT

The aim of this study was to evaluate a cell-free and a cell-laden version of multi-scale osteochondral implants with hierarchy in the cartilage compartment in both cell density and fibre orientation in a long-term, large animal model. The implant was fabricated by converging additive manufacturing techniques, pre-cultured *in vitro*, and orthotopically implanted in ponies for 6 months. The bi-layered cartilage design increased both the compressive and shear properties of the implants. Prior to implantation, the constructs showed *in vitro* cartilage-like tissue formation, as evidenced by deposition of glycosaminoglycan and type II collagen. *In vivo* data showed that, where no differences between cell-free and cell-laden groups were shown, while both implant types did survive the mechanically challenging environment of the knee joint. To our knowledge, this study reports the first mechanically stable, biofabricated, osteochondral implant, thus highlighting the aptness of biofabrication for functional tissue restoration in the harsh articular environment and the potential for clinical translation.

INTRODUCTION

Articular cartilage (AC) defects significantly affect the quality of life of patients as they generally result in progressive deterioration of the joint, provoking pain and reducing mobility.^{1,2} The shift towards a more active lifestyle in current society, combined with the aging population and the increased prevalence of obesity^{3,4}, all risk factors for cartilage damage and/or the development of chronic joint diseases such as osteoarthritis (OA), make the issue into a growing socioeconomic challenge. The problem is aggravated by the fact that chondral defects are difficult to heal, as cartilage tissue has limited regenerative capacity.^{5,6} Current surgical approaches to repair focal defects show sub-optimal long-term outcomes and will typically result in the formation of fibrous tissue with inferior mechanical properties compared to native hyaline cartilage. Allograft transplantation may result in the formation of qualitatively better tissue, yet the application is restricted due to logistical constraints.⁷

For the reasons mentioned above, there is a great clinical and societal need to improve the (early) treatment of articular cartilage damage. Biofabrication⁸ seems a natural approach to realize this, as the technique aims at restoring tissue function by combining the regenerative capacity of the patient's own cells with biomaterials and/or bioactive cues using additive manufacturing techniques. Biofabrication strategies are very versatile as they can be tailored to the individual patient's specific defect, have the potential to repair damage ranging from partial thickness chondral defects up to full osteochondral defects and can even be expanded to full joint resurfacing.

Native articular cartilage exhibits a highly organized, zonal structure and can be considered multi-scale with different cell densities and contents of a variety of matrix components at different depths of the tissue.⁶⁻¹⁰ The tissue is characterized by a specific collagen architecture, known as "Benninghoff arcades"¹¹, which is the main structure-giving element of the tissue and increasingly seen as a key element in the design of regenerative approaches, as they provide the strength and resilience to the articular cartilage.¹¹ Combining further insights into the development of these arcades with multiscale biofabrication technologies, of which many exist, has been proposed as a strategy to improve the fabrication of cartilage equivalents with long-lasting properties.¹² A functional structural framework is required for regenerative biofabrication strategies, as in these strategies cell-laden hydrogels are generally used to stimulate tissue specific matrix formation. These intrinsically soft hydrogels need to be mechanically reinforced to attain (biomechanical) tissue properties coming close to those of native tissue.

Among the numerous fibre reinforcing strategies that have been explored, such as the use of interpenetrating networks¹³, addition of nano-fibres¹⁴, and randomly oriented solution electrospinning scaffolds¹⁵, one of the most promising technologies that can generate fibre structures that may fulfil this reinforcing role is melt electrowriting (MEW).¹⁶⁻¹⁸ MEW fabricates (sub)micrometer-scale fibres in a controlled manner, and can be used to increase the compressive and shear properties of hydrogel-thermoplastic composites.¹⁹⁻²³ Computational models have revealed the mechanisms behind this reinforcing effect, and can

be used to further improve reinforcing designs.²⁴ Recently, fibres generated by MEW have been anchored in a 3D-printable calcium phosphate-based (pCaP) material to create a strong interface between the osteal and cartilage phases of biofabricated osteochondral implants, as introduced in **Chapter 3**.²⁵ In this way, converging MEW with an extrusion-based 3D bioprinting process allows for control over both fibre and cell deposition in a single step approach, with preservation of the reinforcing effect of the fibres and the chondrogenic differentiation capacity of mesenchymal stromal cells (MSCs).²⁶

In vitro studies with these composite and multi-phasic scaffolds show promising results with regard to the deposition of cartilage-like matrix.²³ However, these constructs have not yet been extensively tested in orthotopic *in vivo* models. In fact, *in vivo* evaluation of cartilage constructs is often done in ectopic locations to assess biocompatibility of the materials used²⁷⁻³¹, which does not provide insights in the performance of the implant under the complex loading conditions in the actual joint. Those that have been implanted orthotopically often show poor mechanical stability resulting in dislocation of the implant upon movement.^{32, 33} This poor mechanical stability is thought to be related to insufficient adhesion between the construct and the recipient tissues and between the cartilage and osteal phases of the implant. Recently, it was shown that including an osteal anchor that permits press-fit surgical placing of the implant is more effective in an equine model for the repair of chondral defects than fixation of a chondral segment using fibrin glue.³³

The current study focuses on the long-term orthotopic *in vivo* evaluation of an osteochondral implant designed along the lines indicated above, using converging (bio)fabrication technologies. The chondral region of this implant features a hierarchical organization in both cell density and fibre orientation. These osteochondral implants show *in vitro* cartilage-like tissue formation, as well as sufficient mechanical properties. *In vivo* data show that, where no differences between cell-free and cell-laden groups were shown, the implants survived the mechanically challenging environment of the equine knee joint over an extensive period of time. To our knowledge, this study reports the first mechanically stable, biofabricated, osteochondral implant, thus highlighting the aptness of biofabrication for functional tissue restoration and the potential for clinical translation.

MATERIALS AND METHODS

Cell isolation, expansion, and differentiation

Equine Articular Cartilage-resident Chondroprogenitor Cells (ACPCs) were isolated from healthy metacarpophalangeal joints of skeletally mature equine donors, as previously described.^{34, 35} These donors were donated to science by their owners and procedures were followed according to the guidelines of the Institutional Animal Ethical Committee of the Faculty of Veterinary Medicine of Utrecht University.

ACPCs were cultured in expansion medium until passage 5, after which they were cultured in chondrogenic differentiation medium (1mL per implant) for 28 days. Expansion

medium consisted of Dulbecco's Modified Eagle Medium (31966, Thermo Fisher Scientific, USA) supplemented with 10% fetal bovine serum (Gibco, Thermo Fisher Scientific, USA), 1% penicillin-streptomycin (Gibco, Thermo Fisher Scientific, USA), 1% l-ascorbic acid-2-phosphate (0.2×10^3 M, Sigma Aldrich, USA), 1% non-essential amino acids (100X, Gibco, Thermo Fisher Scientific, USA), and $5 \text{ ng} \cdot \text{mL}^{-1}$ bFGF (Preprotech, UK), and medium was refreshed twice per week. Chondrogenic differentiation medium consisted of Dulbecco's Modified Eagle Medium (31966, Thermo Fisher Scientific, USA) supplemented with 1% penicillin/streptomycin, 1% l-ascorbic acid-2-phosphate, 1% ITS + Premix Universal culture supplement (Corning, USA), 2.5% HEPES (1M, Gibco, Thermo Fisher Scientific, USA), 0.4% dexamethasone (0.1×10^{-6} M, Sigma Aldrich, USA) and 0.1% recombinant human transforming growth factor- $\beta 1$ (TGF- $\beta 1$) (10 ng/mL , Preprotech, UK). Medium was refreshed three times per week. All cultures were performed under sterile and normoxic culture conditions at a temperature of 37°C and 5% CO_2 .

Materials

Bioink:

Gelatin methacryloyl (gelMA, degree of functionalization = 80%) was synthesized from low endotoxin gelatin (beMatrix gelatin LS-H, type B, porcine skin, 300 Bloom, Nitta Gelatin, USA) as previously described.³⁶ Dialysis was performed for 4 days at 4°C , after which gelMA was lyophilized, and stored at -20°C until further use. Upon use, freeze-dried gelMA was dissolved in PBS at 8% w/v. 2-hydroxy-1-[4-(2-hydroxyethoxy)phenyl]-2-methyl-1-propanone (Irgacure 2959, BASF, Germany) was used as a crosslinking agent at 0.1 % w/v and UV-crosslinked for 15 minutes (UVP CL-1000 Ultraviolet Crosslinker, 120 000 microjoules per cm^2). Gels were prepared at 8% w/v to match the same compressive properties observed in previous studies when using gelatin from different sources [Groen *et al.* submitted].

Printable calcium phosphate (pCaP):

The paste was prepared as a mixture of 2.2 g/mL of alpha-tricalcium phosphate (α -TCP) (average particle size = $3.83 \mu\text{m}$, Cambioceramics, The Netherlands), 0.13 g/mL of nano-hydroxyapatite (nano-HA, particle size $< 200 \text{ nm}$, $\text{Ca}_5(\text{OH})(\text{PO}_4)_3$, Sigma-Aldrich, USA) in a 40% w/v poloxamer-solution (Pluronic® F-127, Sigma-Aldrich, USA). After scaffold fabrication, pCaP-scaffolds were allowed to set for 4 days at 37°C under saturated humidity as described in **Chapter 3**.

Polycaprolactone (PCL):

Medical-grade PCL (PURASORB PC 12, Corbion, The Netherlands) was used as received for the MEW process.

Scaffold design and fabrication

An osteochondral implant (**Figure 1A**, total height = 7.7 mm, diameter = 6 mm), consisting of three different layers, was fabricated by combining extrusion-based printing with MEW and 3D bioprinting (3DDiscovery Evolution, regenHU, Switzerland). The bone compartment (height = 6.5 mm) of the implant consisted of printable calcium phosphate. This biomimetic bone compartment was fabricated from pCaP paste by using pneumatic extrusion-based 3D printing (3DDiscovery, regenHU, Switzerland). pCaP was printed on top of 50 layers (total height = 400 μm) of PCL MEW fibres to increase the interfacial strength between the bone and cartilage layer. Cylindrical structures (diameter = 6 mm) were printed consisting of 2 solid layers where pCaP integrated with PCL micro-fibres. Subsequently, macro-pored layers were added by depositing pCaP strands (diameter = 250 μm) with a designed strand-to-strand distance of 700 μm in a double alternating pattern (orientation = 0°- 0°- 90°- 90°). pCaP scaffold fabrication was performed at room temperature (20 – 25°C) with an extrusion pressure of 0.2 MPa and a translational speed of 2 $\text{mm}\cdot\text{s}^{-1}$. The cartilage compartment of the implant was bi-layered with a distinction between the deep/middle zone and the superficial zone. The deep/middle zone (height = 1 mm) consisted of box-like (orientation = 0°- 90°- 0°- 90°) MEW PCL fibres (interfibre spacing = 300 μm), infused with 8% gelMA and ACPCs ($20 * 10^6 / \text{ml}$). The superficial zone (height = 200 μm) consisted of MEW fibres (interfibre spacing = 100 μm) that were deposited in 0°-45°-90°-135° orientation, with a slight offset to induce a higher density of horizontally aligned fibres. The 100 μm interfibre spacing for the superficial layer was selected after an optimization process that selected for an interfibre spacing that allowed for cell entrapment into the mesh, combined with reproducible and accurate distribution of the fibres, as the smoothness of the superficial layer is imperative. These fibre-meshes were infused with 8% gelMA and ACPCs ($80 * 10^6 \text{ ml}^{-1}$).

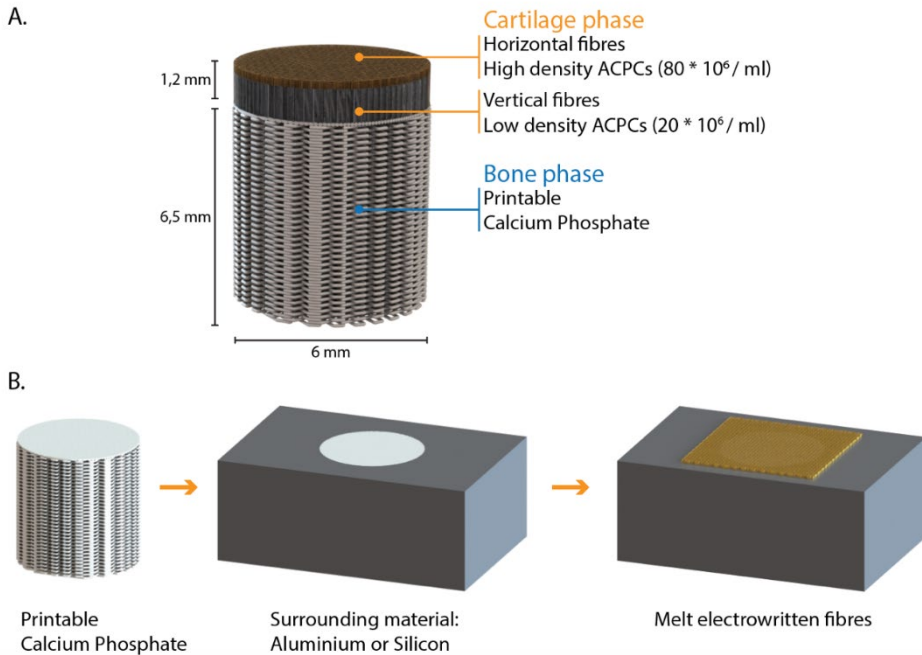


Figure 1. Design and fabrication process of the osteochondral implant. A) Design details of the bi-layered cartilage phase and osteoinductive pCaP bone phase. B) Schematic representation of the printing process, involving surrounding materials (silicon, aluminium) to ensure accurate deposition of MEW fibres. ACPCs = Articular Cartilage-resident Chondroprogenitor Cells.

MEW fibre deposition optimization

The driving force behind MEW fibre deposition is the strong electrical field between the spinneret and the collector plate. By introducing a structure into this field, the electrical field is altered and therewith the fibre deposition is different. To decrease alteration of the fibre deposition on the implant due to this effect, a more stable electrical field around the edges of the implants was established by using aluminium (conductive) or silicon (isolating) as surrounding materials (**Figure 1B**). To optimize MEW printing parameters, the measured line spacing was compared with the programmed line spacing, while using voltages ranging from 5-10 kV and relative collector distances ranging from 5 – 9 mm. Additionally, the line spacing on top of the pCaP implant was compared with the line spacing onto the surrounding material, as a substantial deviation between these two outcomes would suggest irregular or accumulating fibre deposition at the edges of the implant. Pressure and collector velocity remained at 1.25 bar and $15 \text{ mm} \cdot \text{s}^{-1}$, respectively. After optimization, aluminium was selected as the final surrounding material for the fabrication of the implants. Light microscopy (Olympus BX51, Olympus Nederland B.V., The Netherlands) was used to assess the fibre

deposition quality, images were taken (Olympus DP73, Olympus Nederland B.V., The Netherlands) and measurements were performed with ImageJ (version 2.0.0-rc-54/1.51h).

SEM imaging

Scanning electron microscopy (SEM) (Phenom Pro Desktop SEM, Thermo Fischer Scientific, USA) was performed with an accelerating voltage of 10 kV to image the MEW fibres on top of the pCaP implant. Prior to imaging, samples were coated with 2 nm of gold to improve imaging quality.

***In vitro* evaluation of 3D fabricated implants**

After culture, chondrogenic matrix distribution was assessed by means of biochemistry and (immuno)histology.

Biochemical evaluation:

To quantify the amount of sulphated glycosaminoglycans (GAGs) and correct them for DNA content, colorimetric dimethylmethylene blue (DMMB, Sigma Aldrich, USA) and fluorometric Picogreen (Quant-iT-Picogreen-dsDNA-kit, Invitrogen, USA) assays were performed, respectively. Prior to these assays, implants were enzymatically digested overnight at 60°C using a papain digestion solution.

(Immuno) histological evaluation:

Histological evaluation of the implants was performed to assess the distribution of cartilage-like matrix components. The constructs were formalin-fixed and embedded in paraffin. The *in vivo* explants were decalcified with EDTA for 6 months, prior to embedding in paraffin. EDTA was refreshed weekly and the decalcification progress was checked weekly with micro-CT imaging. Tissue sections (thickness = 5 µm) were deparaffinized with xylene and were rehydrated by gradual ethanol steps (100% - 70%) prior to staining. Safranin-O staining was used to visualize GAGs distribution, combined with fast green (Sigma Aldrich, USA) to stain fibrous tissue, and haematoxylin (Sigma Aldrich, USA) to stain cell nuclei. Picrosirius red staining was performed to assess collagen alignment with polarized light microscopy. A haematoxylin/eosin (H&E) staining was performed to provide an overview of matrix formation and implant stability.

Immunohistochemistry was performed to visualize type I, type II, type VI, and type X collagen deposition. First, pronase (1 mg·mL⁻¹, Roche, USA) and hyaluronidase (10 mg·mL⁻¹, H2126, Sigma Aldrich, USA) were used for antigen retrieval, and sections were blocked with bovine serum albumin prior to primary antibody incubation (EPR7785 (ab138492, 1:400 dilution, Abcam), II-II6B3 (DSHB, USA), 5C6 (1:100 dilution, DSHB,

USA), and X53 monoclonal antibody (1:30 dilution, ThermoFischer Scientific, USA) for type I, II, VI, and X collagen, respectively). IgG was used as negative control staining. Incubation was performed overnight at 4°C after which the sections were thoroughly washed and incubated for 30 minutes to 1 hour at room temperature or at 4°C (1:100 dilution, EnVision+ K4010, DAKO), Goat Anti Mouse IgG HRP (DAKO P0447), iotinylated Anti Mouse igG (1:200 dilution, RPN1001V, GE healthcare) and subsequently Streptavidin/HRP (1:1000 dilution, P0397, DAKO), Biotinylated Anti Mouse IgG (1:200 dilution, RPN1001V, GE Healthcare) and subsequent Streptavidin – Peroxidase (1: 1000 dilution, P0397, DAKO) as secondary antibodies for type I, II, VI, and X collagen, respectively at room temperature. Subsequently, 3,3-diaminobenzidine-horseradish peroxidase (DAB, Sigma Aldrich, USA) was used to visualize the staining. After staining the cell nuclei with haematoxylin, pictures of histologically stained sections were made with a light microscope (Olympus BX51, The Netherlands).

Mechanical analysis

The compressive Young's modulus and complex shear modulus of gel only constructs were compared with constructs that contained boxed reinforcement and with constructs that contained bi-layered reinforcement. The compressive Young's modulus was evaluated at $t = 0$ days, after 14 days, and after 28 days. Dynamical mechanical analysis (DMA, Q800, TA instruments, USA) was performed with an unconfined compression protocol that induced 20% strain $\cdot \text{min}^{-1}$ until 30% strain with a preload of 0.001N. After explantation, compressive mechanical testing was performed on the implant and adjacent native cartilage tissue. A ramp force of 0.250 N $\cdot \text{min}^{-1}$ up to 2.0 N was induced with a preload of 0.001 N. During compression, the cartilage was kept hydrated by adding PBS. Stress was calculated based on the force and implant surface area, and strain was based on displacement and height of the cartilage compartment. The compressive Young's modulus was calculated from the linear part of the stress-strain curve.

The complex shear modulus was evaluated after 28 days of culture and measured with a rheometer (Discovery HR-2, TA instruments, USA). An oscillatory rheometric protocol with plate-plate (diameter = 25 mm) configuration was employed. After determining the viscoelastic (LVE) range with an amplitude sweep, a frequency sweep within this LVE range (0.05 – 500 $\text{rad} \cdot \text{s}^{-1}$, 0.01% strain) was performed under a 5% strain preload to prevent sliding of the sample. The complex shear modulus was calculated at 10 $\text{rad} \cdot \text{s}^{-1}$.

***In vivo* evaluation of implants: the animal model**

Equus caballus (Shetland ponies, female, weight = 150 - 200 kg, $n = 8$, **Table 1**) was used as an animal model to evaluate the mechanical stability and regenerative capacity of the hierarchically structured osteochondral implants. As an internal control, a cell-free osteochondral scaffold was used with the same architecture as the cell-laden implants.

Implants were inserted in defects in the trochlea of the equine knee or stifle joint, under randomization of implant placement in the left or right joint.

Table 1. Demographics of experimental animals used for this study

Animal	Date of birth	Age at euthanasia (months)	Gender
1	20/04/2013	71	female
2	23/05/2011	94	female
3	17/05/2007	142	female
4	10/06/2008	129	female
5	28/05/2013	70	female
6	15/05/2012	82	female
7	01/04/2014	59	female
8	01/02/2005	169	female

The ponies arrived at the animal facility 4 weeks before starting the procedure to get acclimatized and were housed as a group at pasture. Prior to surgery they were moved to individual boxes and were fed a standard diet of concentrates with hay *ad libitum* with free access to fresh water.

For surgery, ponies were premedicated with detomidine (intravenous (IV), 10 $\mu\text{g}\cdot\text{kg}^{-1}$) and morphine (IV, 0.1 $\text{mg}\cdot\text{kg}^{-1}$) and anesthesia was induced with midazolam (IV, 0.06 $\text{mg}\cdot\text{kg}^{-1}$) and ketamine (IV, 2.2 $\text{mg}\cdot\text{kg}^{-1}$). Anesthesia was maintained with isoflurane in oxygen together with continuous rate infusion of detomidine (IV, 10 $\mu\text{g}\cdot\text{kg}^{-1}/\text{h}$) and ketamine (IV, 0.5 $\text{mg}\cdot\text{kg}^{-1}/\text{h}$). Meloxicam (IV, 0.6 $\text{mg}\cdot\text{kg}^{-1}$), morphine (Epidural injection, 0.1 – 0.2 $\text{mg}\cdot\text{kg}^{-1}$) and ampicillin (IV, 10 – 15 $\text{mg}\cdot\text{kg}^{-1}$) were administered pre-operatively as analgesic medication and antibacterial preventative therapy, respectively.

The medial femoral ridge of the stifle joint was exposed by arthrotomy and an osteochondral lesion (diameter = 6 mm, depth = 6 mm) was surgically created using a power drill. The surgical area was flushed by saline for cooling and removal of debris. Cell-laden constructs were implanted press-fit in a randomly chosen hind limb, with the cell-free control being implanted in the contralateral limb. After closing the arthrotomy wound in 3 layers in routine fashion, procaine penicillin was administered (Procopen, intramuscular (IM), 20 $\text{mg}\cdot\text{kg}^{-1}$). Post-operatively, nonsteroidal anti-inflammatory medication (metacam, per os (PO), SID, 0.6 $\text{mg}\cdot\text{kg}^{-1}$) was administered for 5 days and opioids (tramadol, PO, BID, 5 $\text{mg}\cdot\text{kg}^{-1}$) were administered for 2 days.

Post-operatively, the animals were kept stabled for 6 weeks with daily monitoring of vital signs, lameness checks at walk and examination of the operated joints for swelling or other signs of inflammation. In weeks 5 and 6, they were hand-walked for 10 minutes twice daily and from week 7 they were kept at pasture. Quantitative gait analysis and radiographic exams were performed at 3 weeks, 3 months and 6 months post-operatively. After 6 months,

the animals were humanely euthanized by intravenous injection of an overdose of pentobarbital, following sedation and induction. All procedures had been approved by the ethical and animal welfare body of the Utrecht University (Approval nr. AVD108002015307 WP23).

Gait analysis during *in vivo* testing period

During the acclimatization period, the ponies were trained on a treadmill (Mustang, Fahrwangen, Switzerland) using a standard protocol for treadmill habituation. Twenty-eight spherical reflective markers (diameter = 24 mm (topline) and 19 mm (elsewhere)) were attached with double-sided tape and second glue to anatomical landmarks (**Supplementary Figure 1**). Kinematic data were collected at trot using six infrared optical motion capture cameras (ProReflex, Qualisys, Gothenburg, Sweden) recording for 30 seconds (frame rate = 200 Hz) at each session to obtain a sufficient number of strides.

To process the data, the reconstruction of three-dimensional coordinates of each marker was automatically calculated by Q-Track software (Qtrack, Qualisys, Gothenburg, Sweden). Each marker was identified and labelled using an automated model (AIM model) and manual tracking and raw data were exported to Matlab (version 2018a, Niantics, California) for further analysis. Using custom written scripts, two symmetry parameters were calculated using the vertical displacement of the head and pelvis (tubera sacrale) markers, for each stride. Additionally, the differences between the two vertical displacement minima of the head ($\text{MinDiff}_{\text{head}}$) and pelvis ($\text{MinDiff}_{\text{pelvis}}$) were calculated. Using the markers, limb-segments were formed and angles between these limb-segments were calculated. The difference between the maximal and minimal angle was defined as the range of motion (ROM) of a joint. For each timepoint, the mean value of all strides for each parameter was calculated.

Evaluation of *in vivo* neo bone tissue formation (UCT)

Microcomputed tomography (μ -CT) was employed for the quantitative analysis of the bone compartments from the harvested osteochondral lesions (N=8 for cell-laden constructs, N=8 for cell-free constructs). Six freshly made osteochondral grafts were scanned in a μ -CT scanner (Quantum FX-Perkin Elmer) to quantify the initial volume of pCaP material, pre-operatively. The post-mortem harvested tissue containing the defect area and the surrounding native tissue were similarly scanned (voltage = 90 kV, current = 200 μ A, voxel size = 30 μm^3 and total scanning time = 3 minutes). Subsequently, the 3D-reconstructed images were processed and analyzed using image J³⁷ and Bone J³⁸ software. Two-dimensional regions of interest (ROIs) were selected in an axial plane at the boundary between the defect and the surrounding native tissue and interpolated to form 3D-volumes of interest (VOI). Thresholding was performed to separately selected area of ceramics and newly formed bone for further calculation. Then, the percentages of mineralized newly formed bone, of non-

mineralized tissue and of remaining ceramics, including the percentage of ceramics volume loss, were quantified.

Evaluation of *in vivo* cartilage formation

After explantation, the implants were macroscopically evaluated and pictures were taken with a stereomicroscope (Olympus stereomicroscope (Olympus Soft Imaging Solutions GmbH, The Netherlands). Biopsies (diameter = 1 mm) of the newly formed tissue and adjacent native tissue were taken for biochemistry. The rest of the explant was further processed for immuno(histological) evaluation.

Statistics

Data is presented as mean \pm standard deviation, unless otherwise specified. All *in vitro* studies were performed in triplicate, and mechanical analysis was performed with $n = 5$. To test the differences between groups, either an unpaired t-test, or a one-way ANOVA with post hoc Bonferroni test was performed. Difference between groups was considered statistically significant if $p < 0.05$. For the *in vivo* study, randomization was done to decide which construct (cell-seeded or not) was implanted in which stifle joint and post-explantation evaluation was performed blindly by making use of a key.

RESULTS

Multi-scale 3D biofabrication of the osteochondral implant

Hierarchy in fibre orientation and cell density was successfully achieved after optimization of MEW printing parameters (**Figure 2**). An increase in voltage resulted in a decrease in measured line spacing between the fibres deposited on top of the bone phase of the OC implant (**Figure 2A**).

A voltage of 7 kV and a relative collector distance of 5 mm resulted in the most accurate line spacing ($409.11 \pm 48.96 \mu\text{m}$) as compared to the programmed value ($400 \mu\text{m}$). A further increase in relative collector distance resulted in a decrease in the measured line spacing (**Figure 2B**). A voltage of 7 kV and relative collector distance of 5 mm led to the most homogeneous fibre deposition, featuring a difference between the line spacing on top of the OC plug and outside of the plug of only $25 \mu\text{m}$ (**Figures 2C, D**). Similar trends were observed with silicon as a surrounding material, yet the voltage used was higher (10 – 16 kV) as compared to when aluminium was used as a surrounding material (data not shown). Using a voltage of 7 kV and a relative collector distance of 5 mm, with aluminium as surrounding material, a bi-layered cartilage phase (**Figure 2E**) with a clearly distinct pattern in the layer representing the deep and middle zones compared to the layer representing the superficial zone was obtained. The deep and middle zone demonstrated a wood-piled structure and z-

directional stacking (**Figure 2F**), whereas the superficial zone featured primarily horizontally aligned fibres with little z-directional stacking (**Figure 2G**). Line spacings of 100 μm , 200 μm , and 400 μm corresponded with pore sizes of $49.21 \pm 6.17 \mu\text{m}$, $110.11 \pm 17.38 \mu\text{m}$ and $359.22 \pm 29.56 \mu\text{m}$, respectively (**Supplementary Figures 2A, B**). Cells were able to pass through all meshes, irrespective of pore size (**Supplementary Figure 2C**); however, most cells were caught by the mesh that was fabricated with a line spacing of 100 μm (**Supplementary Figure 2D**). Therefore, 100 μm line spacing, which was the smallest that resulted in the creation of a smooth surface with consistently accurate fibre stacking, was selected for the superficial zone of the OC implants.

***In vitro* evaluation of OC implants**

Mechanical characterization of bi-layered reinforcement:

Prior to *in vitro* culture, the compressive Young's modulus of the cell-laden hydrogel was $13.9 \pm 0.2 \text{ kPa}$. When reinforced with a boxed fibre structure it increased to $192.3 \pm 54.6 \text{ kPa}$ and when combined with the bi-layered fibre reinforcement the modulus further increased to $222.6 \pm 30.7 \text{ kPa}$ (**Figure 3A**). Over the culture period of 28 days, an increase in the compressive Young's modulus was observed for all groups, which was associated with the increase of deposited cartilage-like tissue matrix (**Figure 3B**). Although an increase was observed for all groups, the compressive Young's modulus of the bi-layered reinforced constructs was higher ($603.2 \pm 205.4 \text{ kPa}$) than those of the boxed-reinforced ($294.2 \pm 147.5 \text{ kPa}$) and cell-laden hydrogel constructs ($19.63 \pm 5.82 \text{ kPa}$). In addition, the inclusion of the bi-layered reinforcing structure also resulted in a higher complex shear modulus ($87.8 \pm 21.7 \text{ kPa}$) after 28 days of culture compared to the cell-laden hydrogel ($10.3 \pm 3.0 \text{ kPa}$) and the boxed-reinforced constructs ($30.5 \pm 11.8 \text{ kPa}$).

Formation of cartilage-like tissue components:

To allow for the deposition of cartilage-like tissue matrix components, the OC implants were cultured for 28 days *in vitro* prior to implantation. This resulted in an overall GAGs content of $27.2 \pm 9.8 \mu\text{gGAG} \cdot \mu\text{gDNA}^{-1}$ (**Figure 3C**), which was, together with type II collagen, homogeneously distributed in the deep and middle, and the superficial zones of the cartilage component of the implant (**Figure 3D**). Further, the reinforcing MEW fibres, which appeared in the stained histological sections as white, were oriented in line with the outcomes of the initial SEM imaging (**Figure 2**).

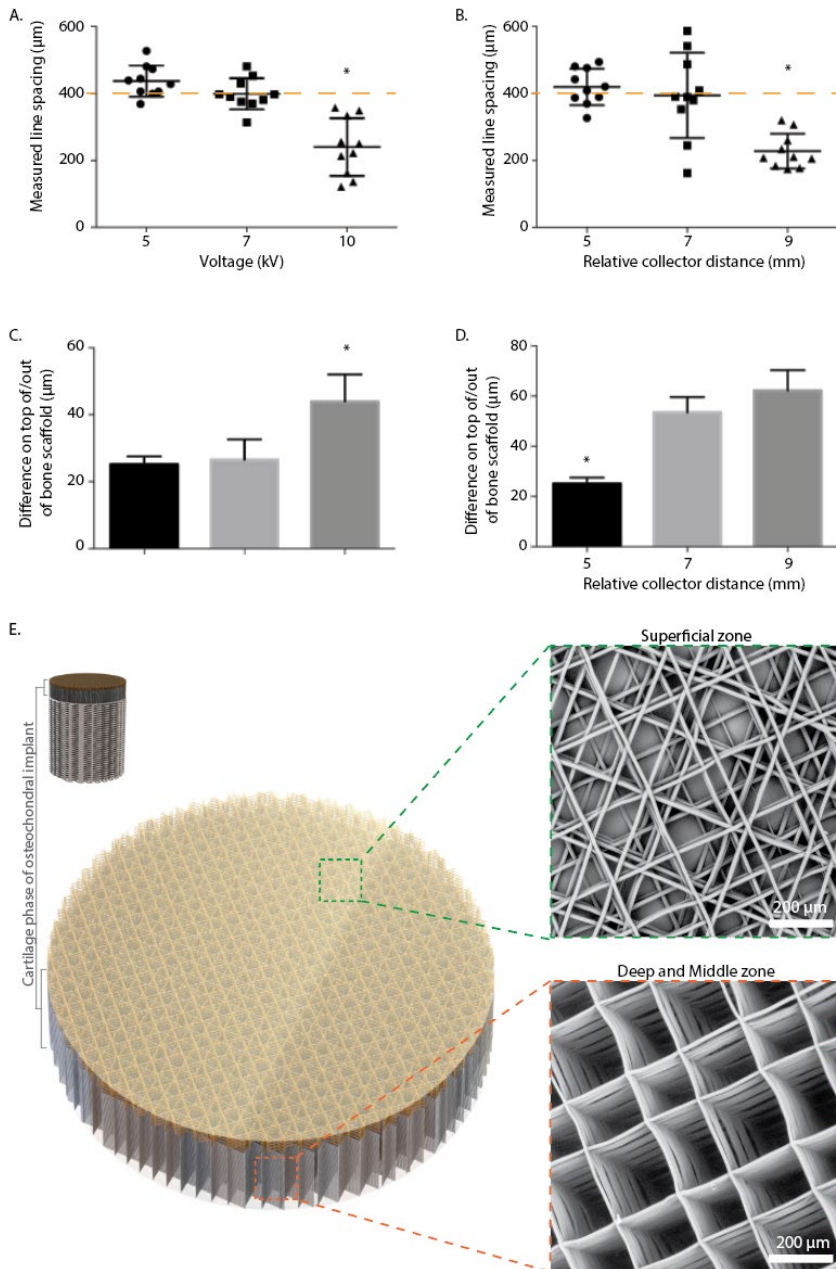


Figure 2. Optimization of process parameters for MEW on top of the pCaP implant using aluminium as a surrounding material. A, B) Voltage and relative collector distance both affect measured line spacing. C, D) Difference of line spacing on top of the implant as compared to outside of the implant is affected by voltage and relative collector distance. E). Illustration of bi-layered cartilage phase. SEM images of fibrous component of the deep and middle, and superficial zone. * = Statistically different from all other groups ($p < 0.05$).

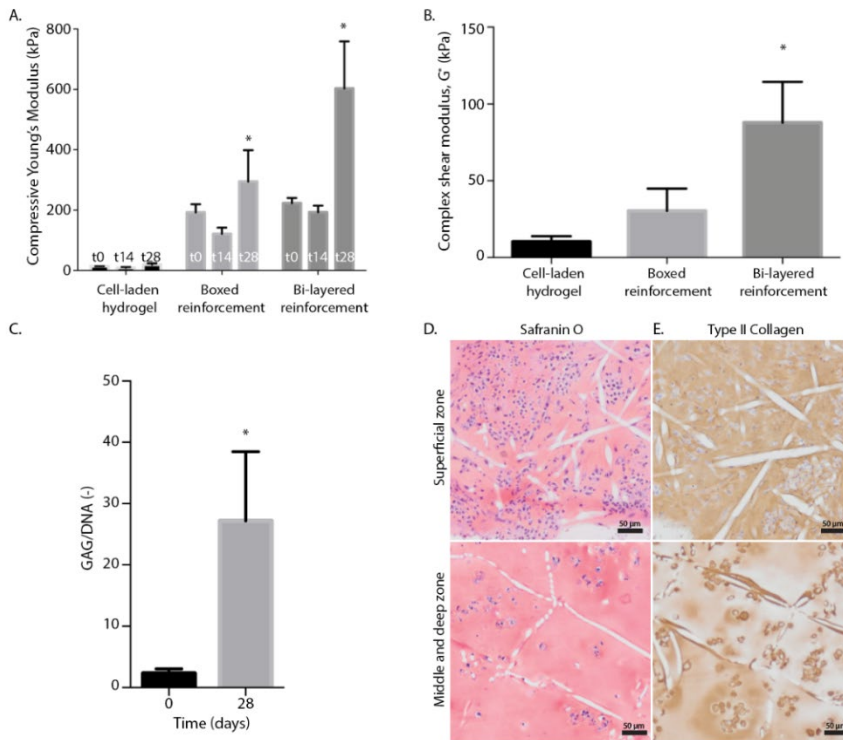


Figure 3. Mechanical analysis and *In vitro* cartilage-like tissue formation of the osteochondral implants. A) Compressive Young's modulus measured 0, 14 and 28 days of culture. B) Complex shear modulus measured 28 days of culture. C) Quantitative GAGs deposition normalized per DNA. D) (Immuno-) histological staining for safranin-O and type II collagen of the superficial and middle/deep zone after 28 days of culture (empty white spaces between the stained matrix reflect the location of the MEW fibres). * = $p < 0.05$, one-way ANOVA, post hoc Bonferroni (A, B), unpaired t-test (C).

In vivo evaluation

Radiographic examination (X-rays) confirmed the correct implant orientation of the implants after 3 and 6 months of implantation (**Supplementary Figure 3**).

Gait analysis:

Symmetry parameters were not affected by the type of implant. No difference was found between the cell-laden and cell-free group at any time point (**Figure 4**). Symmetry parameters (MinDiff Head and MinDiff Pelvis) show a slight change after 3 months of implantation, yet these values were back to base level after 6 months of implantation (**Figure 4A, B**). Limb parameters were not affected by the type of implant. No difference was found in fetlock extension, limb height, protraction, and retraction between the cell-laden and cell-free groups (**Figure 4F-I**).

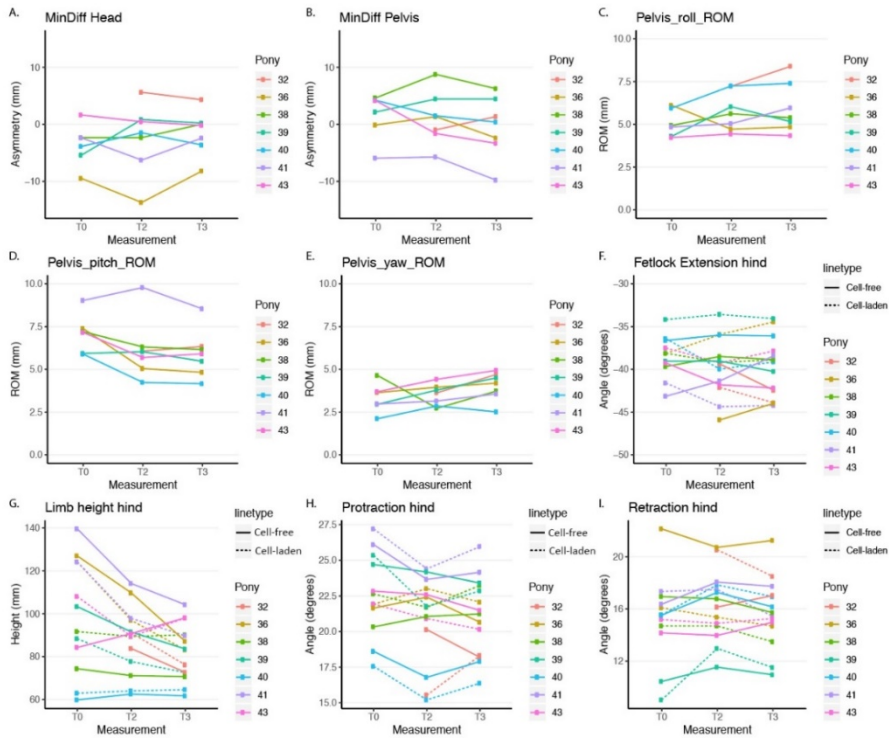


Figure 4. Gait analysis after 0, 3, and 6 months. A, B) Symmetry data of the head and pelvis. C) Pelvis roll range of motion. D) Pelvis pitch range of motion. E) Pelvis Yaw range of motion. F) Fetlock extension hind. G) Limb height hind. H) Protraction hind. I) Retraction hind. T0 = Prior to implantation. T2 = After 3 months of implantation. T3 = After 6 months of implantation.

Post-mortem evaluation

Cross-sections of the implants, stained with Haematoxylin & Eosin (H&E), revealed the lateral bone ingrowth in the osteal anchor of the implant (**Figure 5A**). Additionally, these tissue sections confirmed that the cartilage compartments of the implants still remained intact and provided a good filling of the original defect after 6 months of implantation (**Figure 5A**). Moreover, the reinforcing MEW fibres (“F” in **Figure 5B**) remained visible throughout the entire cartilage compartment of the implant. Quantitatively, no significant difference in compressive Young’s modulus was found ($p = 0.073$) between the cell-free (0.47 ± 0.15 MPa) and cell-laden implants (0.55 ± 0.06 MPa) (**Figure 5D**). Mechanical properties of the cell-laden implants were conserved and no significant decrease in compressive Young’s modulus was found after 6 months implantation. Importantly, at that time point, the cell-free implants had gained significant additional mechanical resilience, and an internal control analysis revealed that there was no significant difference with the compressive Young’s modulus of the cell-laden implants ($\text{difference}_{(\text{Cell-laden})-(\text{Cell-free})} = 99.3 \pm 138.4$ KPa) (**Figure 5C**).

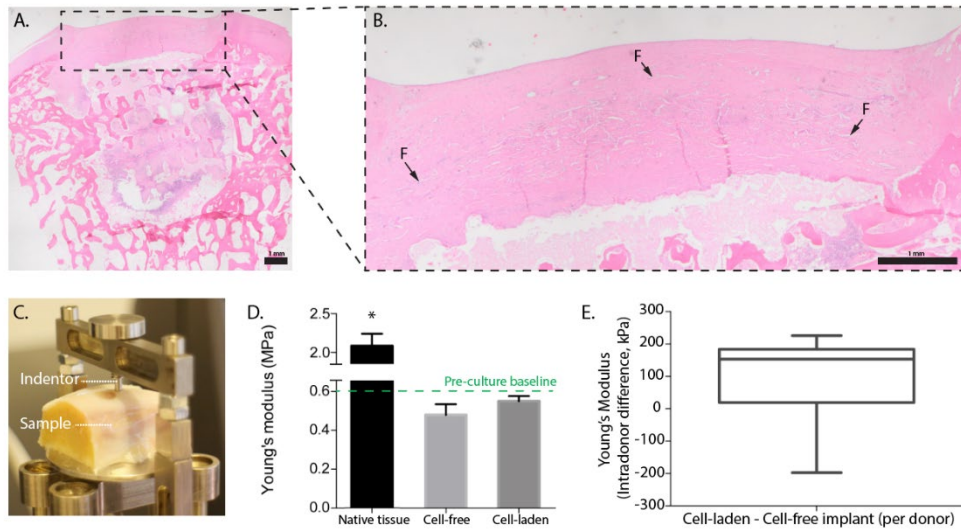


Figure 5. Structural and mechanical evaluation of the implants. A, B) H&E staining of implant, highlighting the presence of the reinforcing fibres throughout the cartilage phase (F = MEW fibre). C) Compressive mechanical testing of the implants and native tissue after explantation. D) Compressive Young's modulus of the implants and native tissue after explantation. E) Internal difference per animal between the cell-laden and cell-free implants. * = $p < 0.05$, one-way ANOVA, post hoc Bonferroni.

Macroscopic evaluation of the implants at surgery and after 6 months of implantation:

Pre-cultured OC constructs were implanted in the trochlea of stifle joint, slightly below the articulating surface (0.49 ± 0.36 mm). After 6 months, within the majority of the implants repair tissue was observed macroscopically (**Figure 6**). At most of the sites that had received a cell-free implant the defect was partially filled with repair tissue with a transparent to whitish colour (**Figure 6B**). In one of them, there was surface penetration of the pCaP scaffold with little to no repair tissue formation (**Figure 6C**) and a kissing lesion at the opposing patella was found. The repair tissue in the defects treated with cell-laden implants had a more whitish and less transparent character (**Figure 6E**). One of these implants featured a reddish-brown well below the level of the surrounding native tissue, indicating that little to no repair tissue was formed in this defect (**Figure 6F**).

Neo-bone tissue formation:

Micro-CT imaging revealed degradation of the pCaP bone anchor (**Figure 7A**). The pCaP volume decreased significantly from 129.2 ± 8.5 mm³ to 31.7 ± 14.2 mm³ and 31.6 ± 21.5 mm³ for the cell-free and cell-laden implants, respectively (**Figure 7B**). No significant difference in percentage of pCaP degradation was found between the cell-free (75.5 ± 11.0 %) and cell-laden (75.6 ± 16.6 %) groups (**Figure 7C**). Some of the implants showed bone

infiltration into the pCaP part, while other implants showed bone resorption around the pCaP part. There was no significant difference in neo-bone tissue formation between the cell-free ($28.3 \pm 30.8 \text{ mm}^3$ or $15.9 \pm 16.3 \%$) and cell-laden ($21.48 \pm 19.5 \text{ mm}^3$ or $12.2 \pm 12.4 \%$) implants (**Figures 7D, E**). Furthermore, no significant difference was found for non-mineralized tissue and void volume/percentage between the cell-free ($123.4 \pm 30.0 \text{ mm}^3$ or $72.2 \pm 12.7 \%$) and cell-laden ($137.1 \pm 35.2 \text{ mm}^3$ or $67.1 \pm 11.9 \%$) implants (**Figure 7F, G**).

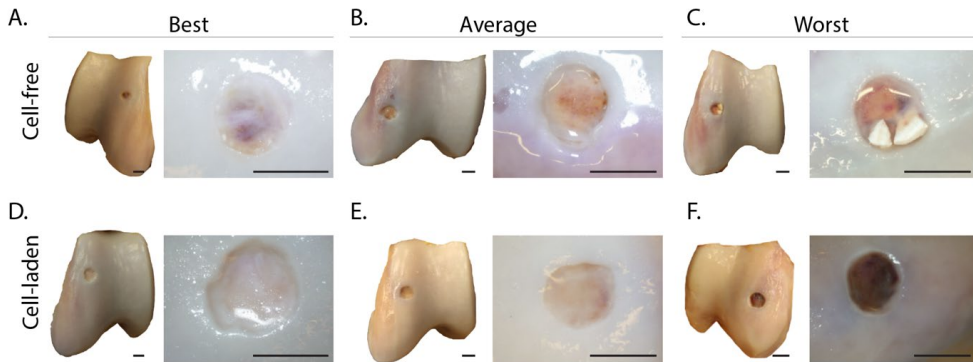


Figure 6. Macroscopic evaluation of the explants showing the best, average, and worst looking samples. A-C) Cell-free implants. D-F) Cell-laden implants. Scale bar = 6 mm.

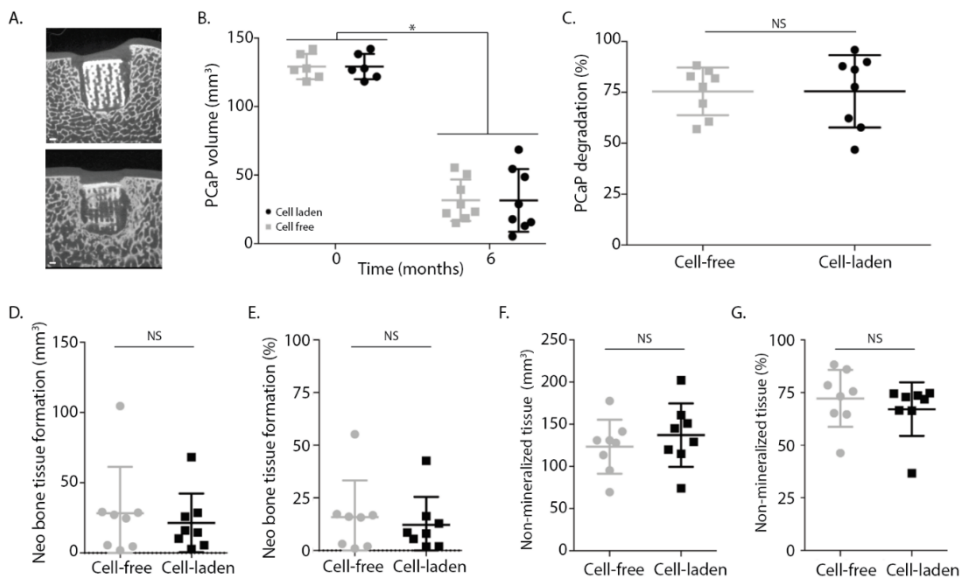


Figure 7. Micro-CT data after 6 months of implantation. A) Representative visualization of implants in the defect. B) Total volume of pCaP over 6 months. C) pCaP degradation over 6 months in percentages. D, E) Neo-bone tissue formation in volume and percentages. F, G) Non-mineralized tissue in volume and percentages. * = $p < 0.05$, unpaired t-test.

Neo-cartilage tissue formation:*Cellular infiltration and cell morphology*

Haematoxylin and eosin staining of tissue sections also showed abundant infiltration of cells in the cartilage compartment of the cell-free implants (**Figure 8A**). Furthermore, the bone compartment of all implants showed considerable cell infiltration, whereas some implants additionally showed neo-bone tissue formation (**Figure 8B**). Cells in the cartilage compartment of both the initially cell-free and cell-laden implants showed a mixed morphology of fibrous/spindle-shaped and rounded cells (**Figure 8C**).

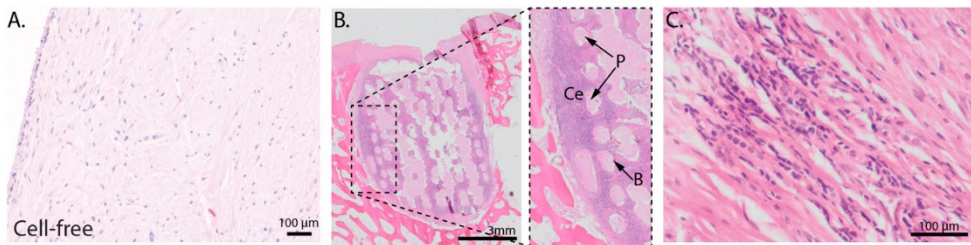


Figure 8. Haematoxylin and eosin staining, cell infiltration and cell morphology. A) Cell infiltration in cartilage part of cell-free implants. B) Cell infiltration in bone part of the implant. (P = pCaP voids, Ce = cells, B = neo-bone tissue formation). C) Cells show a mixture of spindle/fibrous and rounded chondrogenic morphology.

Biochemical evaluation of the cartilage compartment

The implants showed increased GAG/DNA after 6 months of implantation compared to the pre-culture (t28) timepoint (**Figure 9A**). However, no significant difference in GAG/DNA was found ($p = 0.1813$) between the initially GAGs deprived cell-free implants ($41.49 \pm 9.03 \mu\text{g} \cdot \mu\text{g}^{-1}$) and the cell-laden implants ($45.44 \pm 16.25 \mu\text{g} \cdot \mu\text{g}^{-1}$) (**Figure 9A**). However, both the cell-free and cell-laden implants showed significantly less GAG/DNA content in comparison to the native tissue ($117.45 \pm 74.37 \mu\text{g} \cdot \mu\text{g}^{-1}$). A similar trend was observed for the overall GAGs content normalized per dry weight and no significant differences were found between the cell-free ($8.67 \pm 4.24 \mu\text{g} \cdot \text{mg}^{-1}$) and cell-laden implants ($8.81 \pm 6.75 \mu\text{g} \cdot \text{mg}^{-1}$) (**Figure 9B**). However, the implants showed a 10-fold lower level of GAGs as compared to native tissue with average of $83.30 \pm 55.37 \mu\text{g GAG} \cdot \text{mg sample}^{-1}$. Additionally, no difference in DNA content, normalized per dry weight, was found between the cell-free ($176.07 \pm 104.47 \mu\text{g} \cdot \text{mg}^{-1}$) and cell-laden implants ($202.53 \pm 127.93 \mu\text{g} \cdot \text{mg}^{-1}$) (**Figure 9C**). The implants showed a 3 to 4-fold lower DNA content as compared to native tissue ($694.38 \pm 117.57 \mu\text{g DNA} \cdot \text{mg sample}^{-1}$).

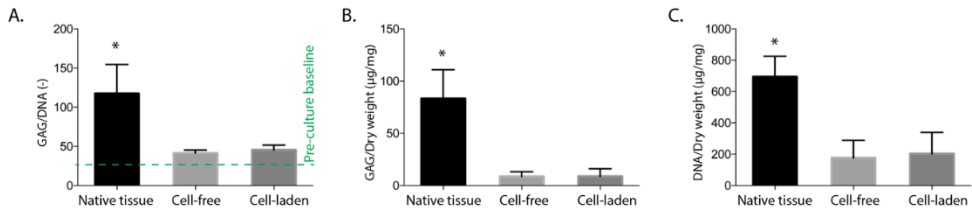


Figure 9. Quantitative biochemistry. A) Average GAG/DNA compared with native tissue. Green dotted line represents the level of GAG/DNA prior to implantation. B) Average GAG/Dry weight compared with native tissue. C) Average DNA/Dry weight compared with native tissue. * = $p < 0.05$, one-way ANOVA, post hoc Bonferroni.

Histological evaluation of formed repair tissue in the cartilage compartment:

Histological overview images of the cell-free and cell-laden implants showed limited staining for type II collagen (**Figure 10A**). However, some type II collagen positive patches were found within both the cell-free and cell-laden implants. Both the cell-free and cell-laden implants stained slightly positive for type VI collagen (**Figure 10B**). Furthermore, the cartilage compartments of the cell-free and cell-laden implants stained negative for type X collagen (**Figure 10C**) and type I collagen (**Figure 10D**). An overview of all (immuno-) histological stainings on all implants can be found in Supplementary **Figures 4-8**.

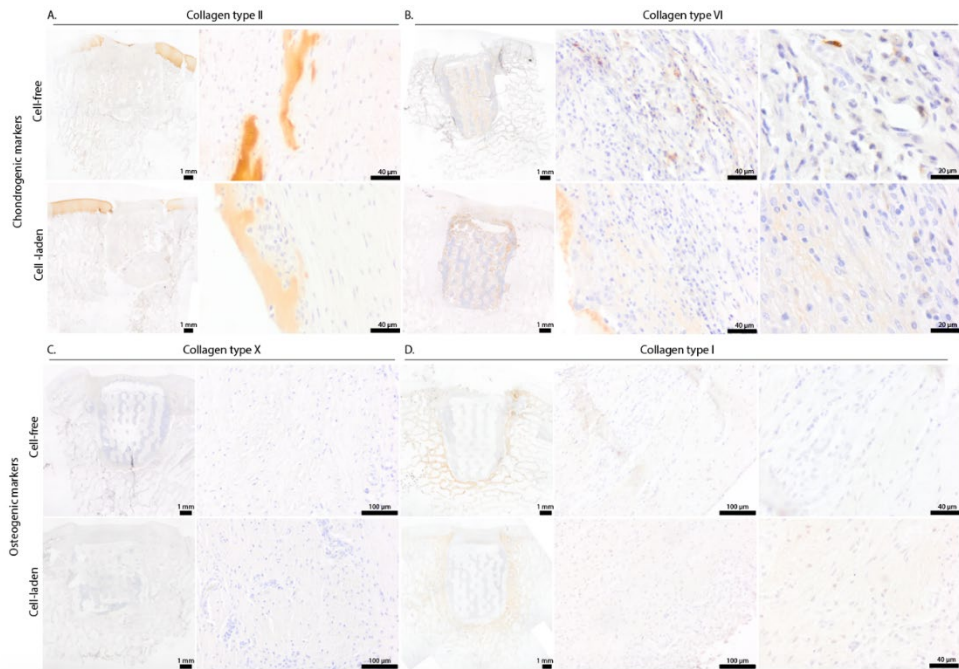


Figure 10. Immunohistochemistry of implants. A) Type II collagen staining. B) Type VI collagen staining. C) Type X collagen staining. D) Type I collagen staining. Brown color depicts the stained protein in all figures. Haematoxylin counterstaining for cell nucleus.

DISCUSSION

This study is the first in its kind to show successful long-term implantation of a 3D-biofabricated durable osteochondral implant for cartilage repair that is based on converging multiple additive manufacturing technologies in the challenging equine model. The high potential of biofabrication technologies for the generation of regenerative and patient-specific implants has been postulated for over a decade.³⁹ However, up until now, long-term success has not yet been reported for large animal models. Many promising cartilage regenerative *in vitro* results have been shown employing a variety of biofabrication techniques³⁹, but the combination of enabling tissue-specific matrix deposition while providing sufficient mechanical stability that will stand the harsh intra-articular environment, still remains a significant challenge. In this study, control was obtained over fibre architecture on a multi-scale level and this was successfully combined with the control over the deposition of the cells by using a combination of converging biofabrication technologies.

Our mechanically stable design is inspired by the architecture of native osteochondral tissue and based on the integration of a technique to reinforce the cartilage phase by the inclusion of hierarchically oriented fibres⁴⁰ and of a novel strategy to integrate the cartilage reinforcement with a bone anchor.²⁵ Moreover, the implants were generated through an integrated approach that also allowed for the simultaneous printing of the fine polymer fibres and deposition of cell-laden bioinks.²⁶ Inspired by the zonal variation of cell density in native articular cartilage, the superficial layer included a higher density of cells than the middle and deep zones. Furthermore, inclusion of hierarchy in the fibre orientation by adding a superficial layer increased both the compressive and shear properties of the implant. The increase in compressive properties can likely be attributed to the Poisson-factor in combination with an improved load distribution thanks to the addition of the fibre-dense superficial layer.^{24, 40} The observed increase in shear modulus could be explained by the increase in fibre density, or again by a more equal load distribution. The design of the constructs is obviously still far off the native Benninghoff arcades⁴¹ and could still be further improved to better capture the unique architecture, and function, of the fibrous part of the cartilage matrix. The fibre diameters obtained with the MEW process are already one to two orders of magnitude smaller than those obtained with conventional extrusion-based techniques. Nevertheless, they are still much thicker than the native collagen fibres, which function as the reinforcing fibrous component of articular cartilage and also play a role in the entrapment of deposited GAGs.⁴² We recently postulated that better understanding of the mechanisms of collagen structure development combined with evolving (bio)fabrication and printing approaches would lead to further functional mimicking of articular cartilage tissue¹², but the exact degree of tissue-mimicry required is still topic of debate. The work reported here, is the first to underscore that hypothesis in a representative large animal model and further stresses that a solution for further tissue-mimicry potentially lies in the convergence of additive manufacturing technologies.⁴³

While the feasibility of converging MEW and bioprinting has been shown, MEW on top of existing structures remains a challenge. Once an element is introduced between the spinneret and the collector plate during the MEW process, this element alters the electrical field, which subsequently affects MEW fibre deposition accuracy [data not shown]. As a result of inaccurate fibre deposition, fibres will pile up at the edges of an existing structure when attempting to deposit fibres onto this structure. Obviously, this needs to be avoided as for cartilage implants a smooth surface is required for proper *in vivo* performance. In this study, an approach is described to overcome this challenge of by using surrounding materials with conductive (aluminium) or isolating (silicon) properties. Even though silicon was more easy to handle in combination with the brittle pCaP, aluminium was chosen as the surrounding material as this allowed MEW at lower voltages, which allows for the printing on top of higher existing structures and yields more homogeneous fibre deposition, as well as higher reproducibility. This underscores that process parameters, such as applied voltage and relative collector distance, which are known to be important regulators for the accurate deposition of fibres on conventional flat collector plates,^{18, 22} are also key parameters when printing on top of existing structures, such as the pCaP bone phase.

When the constructs were cultured *in vitro* for 4 weeks, an increase in GAGs content and associated mechanical properties was found, consistent with previous studies where ACPCs were encapsulated in gelMA hydrogels.^{34, 44} The hydrogel composition used in this study resulted in GAG/DNA values that are similar to the ones reported in previous studies performed with gelMA encapsulated ACPCs.³⁴

After optimization of fabrication, 4 weeks of *in vitro* culture, and biological and mechanical characterization, the implants were orthotopically implanted *in vivo* in the equine model. The equine model has shown to be a good, yet challenging, model for orthotopic *in vivo* studies as equine joints are roughly similar in size when ponies are concerned, have comparable cartilage thickness and biochemical composition of the cartilage.⁴⁵ Moreover, (degenerative) joint disease is as prevalent in horses as it is in humans and, given the use of the species, signifies a comparable unmet clinical need.⁴⁶ Previous studies showed that the fixation of chondral implants is challenging in large animal models^{33, 47}, and press-fit surgical fixation of osteochondral constructs has been suggested as the current best solution.³³ For this reason for this study an osteochondral approach was chosen. The fixation of the cartilage part to the bone component was addressed by the stable integration with an osteoinductive pCaP anchor, inspired by the native bone cartilage interface.²⁵

However, the pCaP is known to be a rather brittle material, which means that the slightest deviation in diameter of the extruded pCaP implants can cause damage to the implants upon press-fit implantation, potentially resulting in micro-movements of the implant which can hamper bone-tissue ingrowth or lead to bone resorption around the implant. However, placement of the samples in the aluminium surrounding during fabrication aided to avoid the formation of these irregularities. The biodegradable nature of pCaP allows for increased neo-bone tissue formation. However, it remains important to consider potential implant-shifting upon loading, when applying degradable materials. This, however, was not

a major issue in the current study as the cartilage layer remained stable, despite the degradation of the pCaP component.

In vivo monitoring by means of gait analysis and X-ray imaging confirmed the correct placement of the implants and revealed no lameness, discomfort or abnormalities in ranges of motion of various kinematical parameters, indicating no functional impairment. However, it should be noted that the animals were operated bilaterally, and that bilateral lameness is harder to detect than unilateral.

After 6 months of implantation, macroscopically all implants showed formation of repair tissue, yet the defects were not always completely filled. Recently, it has been proposed that the critical size defect for equine articular cartilage is 4 mm in diameter for osteochondral defects and 2 mm for chondral defects⁴⁸, highlighting the fact that equine articular cartilage has a similarly limited capacity for spontaneous healing as human articular cartilage and indicating that spontaneous healing of the 6 mm diameter defects created in this study would be highly unlikely.

Interestingly, biochemical assessment of the post-mortem retrieved implants showed a further increase in $\text{GAG} \cdot \text{DNA}^{-1}$ for the cell-laden implants ($45.4 \mu\text{g} \cdot \mu\text{g}^{-1}$ of $\text{GAG} \cdot \text{DNA}^{-1}$) compared to the pre-implantation timepoint ($28.0 \mu\text{g} \cdot \mu\text{g}^{-1}$ of $\text{GAG} \cdot \text{DNA}^{-1}$). This observation provides the quantitative evidence that additional ECM production occurred during the implantation. The fact that qualitative, subjective assessment of the degree of safranin-O staining could not be performed, can be attributed to the prolonged decalcification protocol (**Supplementary figure 8**). The increase in $\text{GAG} \cdot \text{DNA}^{-1}$ during implantation is a very encouraging finding showing that the implants used in this study performed considerably better than those in earlier studies in which GAG content decreased and where they were hypothesised to leach out of the precultured implants, probably due to loading exposure.^{33, 49} The addition of the fibre-dense and cell-dense superficial layer in this study might have contributed in limiting GAG leakage.

An important finding is that the gel-fibre combination used as the cartilage phase of the implants showed the ability to attract chondrogenic ECM producing cells in the *in vivo* situation and $\text{GAG} \cdot \text{DNA}^{-1}$ content of the neo-tissue for these cell-free scaffolds was equal to the level observed for the cell-laden, pre-cultured implants. This suggests that it is the restoration and maintenance of the mechanical environment, rather than the transplantation of the chondrogenic cells that is the underlying cause for the cartilage-like tissue formation.

Although native levels of GAGs were still not reached, the knowledge that ECM can actually be formed *in vivo*, implies that future research should focus generating the right environment for regeneration and retainment of ECM components. Further mimicking the native articular cartilage superficial layer by an increase in fibre-density, decrease in fibre diameter, or surface treatment of the fibres in this superficial layer, might allow for even more GAGs deposition and prevention of leakage and eventually lead to regenerative osteochondral implants that show the production of ECM with similar specifications as those of native tissue.

The GAG-induced swelling pressure combined with the tension of the collagen network is the key mechanism for the mechanical resilience of articular cartilage and mimicking this phenomenon appears a valid approach for the engineering of functional articular cartilage. Despite the fact that multiple approaches to improve the mechanical properties of cartilage implants with 3D biofabrication have been proposed^{40, 50, 51}, none of the resulting implants have thus far demonstrated long-term functionality in a large animal model. This study shows, however, that multi-scale fabrication via converging of (bio)printing technologies can result in mechanically stable implants that can survive the challenging *in vivo* environment for a prolonged period and even apparently can offer an environment in which cells can thrive and can produce ECM components. These results strongly support the hypothesis that, if we can further mimic the cartilage architecture *in vitro*, we will be able to create implants that are functional *in vivo*.

Importantly, this study showed that even without the presence of transplanted regenerative cells, a mechanically stable environment is generated that induces the deposition of a GAG-rich matrix with homogeneous type II collagen staining over the 6 months of implantation. The exposure to loading may have further stimulated the induction of cartilage matrix formation and tissue organization as has also been shown in mechanically stimulating bioreactor systems⁵². For example, Daly *et al.* used cellular aggregates to resurface the tibia plateau and stimulated these scaffolds mechanically for 10 weeks.⁵² They showed that this dynamic culture outperformed the static cultures and could induce some type II collagen alignment. Interestingly, after 10 weeks of dynamic *in vitro* culture, the cartilage-like tissue overgrew the already stiff fused deposition modelling (FDM) PCL fibres, and the alignment of this overgrown tissue had improved mechanical properties compared to scaffolds cultured for 4 weeks. Despite the fact that equal tissue formation was observed in both groups in the current study, the use of similar culture and loading pre-culture protocols would be an interesting avenue to explore for the improvement of the performance of the cell-laden constructs. Nevertheless, to further understand the intricate relation between tissue maturation, reorganization, and *in vivo* outcomes, additional research is needed on the effect of these pre-culture times and protocols on the level of maturation prior to implantation and subsequent *in vivo* performance.

CONCLUSION

This study demonstrates that implants with a defined hierarchy in the cartilage compartment that are made using a combination of different sophisticated (bio-)printing technologies are able to withstand the challenging *in vivo* situation in a large animal model for a prolonged period. Converging biofabrication technologies allowed for multi-scale implant fabrication with bi-layered reinforcement in the chondral compartment, which improved both the compressive and shear properties of the implant. Importantly, implants that contained pre-cultured regenerative cells and abundant cartilage-like matrix at the time of implantation, did not outperform cell-free implants with the same biomaterial architecture, strongly suggesting

that the mechanical environment is more determining for success of the implant than the presence of cells, which observation is of great translational importance.

ACKNOWLEDGEMENT

The primary antibodies against collagen type II (II-II6B3) developed by T. F. Linsenmayer and E. S. Engvall, respectively, were obtained from the DSHB developed under the auspices of the NICHD and maintained by the University of Iowa, Department of Biology, Iowa City, IA, USA. Support with SEM imaging was kindly provided by Marco Viveen. This work was financially supported by the European Research Council under grant agreement 647426 (3D-JOINT), EU funded E11312 BioArchitect project and by Reuma Nederland (grants CO-14-1-001, LLP-12 and LLP-22).

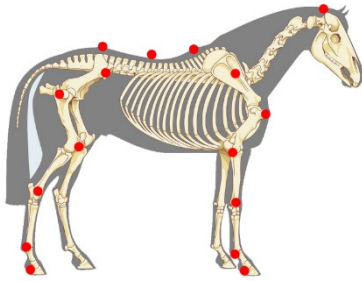
REFERENCES

1. Buckwalter, J. A., Articular cartilage: injuries and potential for healing. *J Orthop Sports Phys Ther* **1998**, 28 (4), 192-202.
2. Buckwalter, J. A.; Mankin, H. J., Articular cartilage: degeneration and osteoarthritis, repair, regeneration, and transplantation. *Instr Course Lect* **1998**, 47, 487-504.
3. Hunter, D. J.; Bierma-Zeinstra, S., Osteoarthritis. *Lancet* **2019**, 393 (10182), 1745-1759.
4. Muthuri, S. G.; Hui, M.; Doherty, M.; Zhang, W., What if we prevent obesity? Risk reduction in knee osteoarthritis estimated through a meta-analysis of observational studies. *Arthritis Care & Research* **2011**, 63 (7), 982-990.
5. Brittberg, M.; Lindahl, A.; Nilsson, A.; Ohlsson, C.; Isaksson, O.; Peterson, L., Treatment of deep cartilage defects in the knee with autologous chondrocyte transplantation. *N Engl J Med* **1994**, 331 (14), 889-95.
6. Hunter, W., Of the structure and disease of articulating cartilages. 1743. (0009-921X (Print)).
7. Pisanu, G.; Cottino, U.; Rosso, F.; Blonna, D.; Marmotti, A. G.; Bertolo, C.; Rossi, R.; Bonasia, D. E., Large Osteochondral Allografts of the Knee: Surgical Technique and Indications. *Joints* **2018**, 6 (1), 42-53.
8. Groll, J.; Boland, T.; Blunk, T.; Burdick, J. A.; Cho, D. W.; Dalton, P. D.; Derby, B.; Forgacs, G.; Li, Q.; Mironov, V. A.; Moroni, L.; Nakamura, M.; Shu, W.; Takeuchi, S.; Vozzi, G.; Woodfield, T. B.; Xu, T.; Yoo, J. J.; Malda, J., Biofabrication: reappraising the definition of an evolving field. *Biofabrication* **2016**, 8 (1), 013001.
9. Klein, T. J.; Malda, J.; Sah, R. L.; Hutmacher, D. W., Tissue engineering of articular cartilage with biomimetic zones. *Tissue Eng Part B Rev* **2009**, 15 (2), 143-57.
10. Poole, A.; Robin PhD, D.; Kojima, T.; Md, P.; Yasuda, T.; Md, P.; Mwale, F.; Kobayashi, M.; Md, P.; Laverty, S.; Mvb, D., Composition and Structure of Articular Cartilage: A Template for Tissue Repair. *Clin Orthop* **2001**, 391, S26-S33.
11. Mac, C. M., The movements of bones and joints; the mechanical structure of articulating cartilage. (0301-620X (Print)).
12. Malda, J.; Groll, J.; van Weeren, P. R., Rethinking articular cartilage regeneration based on a 250-year-old statement. *Nat Rev Rheumatol* **2019**, 15 (10), 571-572.
13. Prielipp, H.; Knechtel, M.; Claussen, N.; Streiffner, S. K.; Müllejjans, H.; Rühle, M.; Rödel, J., Strength and fracture toughness of aluminum/alumina composites with interpenetrating networks. *Materials Science and Engineering: A* **1995**, 197 (1), 19-30.
14. Shin, S. R.; Bae, H.; Cha, J. M.; Mun, J. Y.; Chen, Y.-C.; Tekin, H.; Shin, H.; Farshchi, S.; Dokmeci, M. R.; Tang, S.; Khademhosseini, A., Carbon Nanotube Reinforced Hybrid Microgels as Scaffold Materials for Cell Encapsulation. *ACS Nano* **2012**, 6 (1), 362-372.
15. Coburn, J.; Gibson, M.; Bandalini, P. A.; Laird, C.; Mao, H. Q.; Moroni, L.; Seliktar, D.; Elisseeff, J., Biomimetics of the Extracellular Matrix: An Integrated Three-Dimensional Fiber-Hydrogel Composite for Cartilage Tissue Engineering. *Smart Struct Syst* **2011**, 7 (3), 213-222.
16. Brown, T. D.; Dalton, P. D.; Hutmacher, D. W., Melt electrospinning today: An opportune time for an emerging polymer process. *Progress in Polymer Science* **2016**, 56, 116-166.
17. Dalton, P. D., Melt electrowriting with additive manufacturing principles. *Current Opinion in Biomedical Engineering* **2017**, 2, 49-57.
18. Robinson, T. M.; Hutmacher, D. W.; Dalton, P. D., The Next Frontier in Melt Electrospinning: Taming the Jet. *Advanced Functional Materials* **2019**, 29 (44), 1904664.
19. Bas, O.; De-Juan-Pardo, E. M.; Meinert, C.; D'Angella, D.; Baldwin, J. G.; Bray, L. J.; Wellard, R. M.; Kollmannsberger, S.; Rank, E.; Werner, C.; Klein, T. J.; Catelas, I.; Hutmacher, D. W., Biofabricated soft network composites for cartilage tissue engineering. *Biofabrication* **2017**, 9 (2), 025014.
20. Brown, T. D.; Dalton, P. D.; Hutmacher, D. W., Direct Writing By Way of Melt Electrospinning. *Advanced Materials* **2011**, 23 (47), 5651-5657.
21. de Ruijter, M.; Hrynevich, A.; Haigh, J. N.; Hochleitner, G.; Castilho, M.; Groll, J.; Malda, J.; Dalton, P. D., Out-of-Plane 3D-Printed Microfibers Improve the Shear Properties of Hydrogel Composites. *Small* **2018**, 14 (8), 1702773.

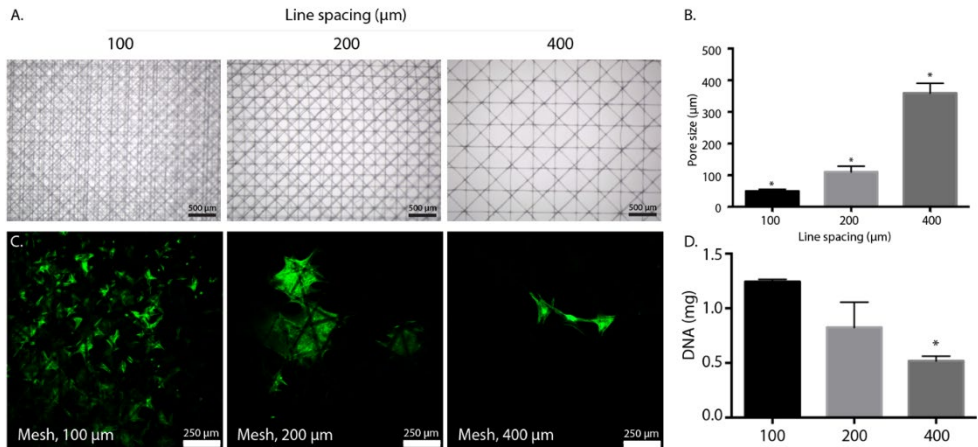
22. Hochleitner, G.; Youssef, A.; Hrynevich, A.; Haigh Jodie, N.; Jungst, T.; Groll, J.; Dalton Paul, D., Fibre pulsing during melt electrospinning writing. In *BioNanoMaterials*, 2016; Vol. 17, p 159.
23. Visser, J.; Melchels, F. P. W.; Jeon, J. E.; van Bussel, E. M.; Kimpton, L. S.; Byrne, H. M.; Dhert, W. J. A.; Dalton, P. D.; Hutmacher, D. W.; Malda, J., Reinforcement of hydrogels using three-dimensionally printed microfibrils. *Nature Communications* **2015**, *6* (1), 6933.
24. Castilho, M.; Hochleitner, G.; Wilson, W.; van Rietbergen, B.; Dalton, P. D.; Groll, J.; Malda, J.; Ito, K., Mechanical behavior of a soft hydrogel reinforced with three-dimensional printed microfibre scaffolds. *Scientific Reports* **2018**, *8* (1), 1245.
25. Diloksumpan, P.; de Ruijter, M.; Castilho, M.; Gbureck, U.; Vermonden, T.; van Weeren, P. R.; Malda, J.; Levato, R., Combining multi-scale 3D printing technologies to engineer reinforced hydrogel-ceramic interfaces. *Biofabrication* **2020**, *12* (2), 025014.
26. de Ruijter, M.; Ribeiro, A.; Dokter, I.; Castilho, M.; Malda, J., Simultaneous Micropatterning of Fibrous Meshes and Bioinks for the Fabrication of Living Tissue Constructs. *Adv Healthc Mater* **2019**, *8* (7), e1800418.
27. Apelgren, P.; Amoroso, M.; Lindahl, A.; Brantsing, C.; Rotter, N.; Gatenholm, P.; Kolby, L., Chondrocytes and stem cells in 3D-bioprinted structures create human cartilage *in vivo*. *PLoS One* **2017**, *12* (12), e0189428.
28. Apelgren, P.; Karabulut, E.; Amoroso, M.; Mantas, A.; Martínez Ávila, H.; Kólby, L.; Kondo, T.; Toriz, G.; Gatenholm, P., *In Vivo* Human Cartilage Formation in Three-Dimensional Bioprinted Constructs with a Novel Bacterial Nanocellulose Bioink. *ACS Biomaterials Science & Engineering* **2019**, *5* (5), 2482-2490.
29. Kunisch, E.; Knauf, A. K.; Hesse, E.; Freudenberg, U.; Werner, C.; Bothe, F.; Diederichs, S.; Richter, W., StarPEG/heparin-hydrogel based *in vivo* engineering of stable bizonal cartilage with a calcified bottom layer. *Biofabrication* **2018**, *11* (1), 015001.
30. Xu, T.; Binder, K. W.; Albanna, M. Z.; Dice, D.; Zhao, W.; Yoo, J. J.; Atala, A., Hybrid printing of mechanically and biologically improved constructs for cartilage tissue engineering applications. *Biofabrication* **2013**, *5* (1), 015001.
31. You, F.; Chen, X.; Cooper, D. M. L.; Chang, T.; Eames, B. F., Homogeneous hydroxyapatite/alginate composite hydrogel promotes calcified cartilage matrix deposition with potential for three-dimensional bioprinting. *Biofabrication* **2018**, *11* (1), 015015.
32. Hutmacher, D. W., Scaffolds in tissue engineering bone and cartilage. *Biomaterials* **2000**, *21* (24), 2529-2543.
33. Mancini, I. A. D.; Vindas Bolanos, R. A.; Brommer, H.; Castilho, M.; Ribeiro, A.; van Loon, J.; Mensinga, A.; van Rijen, M. H. P.; Malda, J.; van Weeren, R., Fixation of Hydrogel Constructs for Cartilage Repair in the Equine Model: A Challenging Issue. *Tissue Eng Part C Methods* **2017**, *23* (11), 804-814.
34. Levato, R.; Webb, W. R.; Otto, I. A.; Mensinga, A.; Zhang, Y.; van Rijen, M.; van Weeren, R.; Khan, I. M.; Malda, J., The bio in the ink: cartilage regeneration with bioprintable hydrogels and articular cartilage-derived progenitor cells. *Acta Biomaterialia* **2017**, *61*, 41-53.
35. Williams, R.; Khan, I. M.; Richardson, K.; Nelson, L.; McCarthy, H. E.; Anabelsi, T.; Singhrao, S. K.; Dowthwaite, G. P.; Jones, R. E.; Baird, D. M.; Lewis, H.; Roberts, S.; Shaw, H. M.; Dudhia, J.; Fairclough, J.; Briggs, T.; Archer, C. W., Identification and clonal characterisation of a progenitor cell sub-population in normal human articular cartilage. *PLoS One* **2010**, *5* (10), e13246.
36. Melchels, F. P. W.; Dhert, W. J. A.; Hutmacher, D. W.; Malda, J., Development and characterisation of a new bioink for additive tissue manufacturing. *Journal of Materials Chemistry B* **2014**, *2* (16), 2282-2289.
37. Schindelin, J.; Arganda-Carreras, I.; Frise, E.; Kaynig, V.; Longair, M.; Pietzsch, T.; Preibisch, S.; Rueden, C.; Saalfeld, S.; Schmid, B.; Tinevez, J. Y.; White, D. J.; Hartenstein, V.; Eliceiri, K.; Tomancak, P.; Cardona, A., Fiji: an open-source platform for biological-image analysis. *Nat Methods* **2012**, *9* (7), 676-82.
38. Doube, M.; Klosowski, M. M.; Arganda-Carreras, I.; Cordelieres, F. P.; Dougherty, R. P.; Jackson, J. S.; Schmid, B.; Hutchinson, J. R.; Shefelbine, S. J., BoneJ: Free and extensible bone image analysis in ImageJ. *Bone* **2010**, *47* (6), 1076-9.
39. Mouser, V. H. M.; Levato, R.; Bonassar, L. J.; D'Lima, D. D.; Grande, D. A.; Klein, T. J.; Saris, D. B. F.; Zenobi-Wong, M.; Gawlitta, D.; Malda, J., Three-Dimensional Bioprinting and Its Potential in the Field of Articular Cartilage Regeneration. *Cartilage* **2017**, *8* (4), 327-340.

40. Castilho, M.; Mouser, V.; Chen, M.; Malda, J.; Ito, K., Bi-layered micro-fibre reinforced hydrogels for articular cartilage regeneration. *Acta Biomater* **2019**, *95*, 297-306.
41. Benninghoff, A., Form und Bau der Gelenkknorpel in ihren Beziehungen zur Funktion. *Zeitschrift für Zellforschung und Mikroskopische Anatomie* **1925**, *2* (5), 783-862.
42. Maroudas, A., Balance between swelling pressure and collagen tension in normal and degenerate cartilage. *Nature* **1976**, *260* (5554), 808-809.
43. Levato, R.; Jungst, T.; Scheuring, R. G.; Blunk, T.; Groll, J.; Malda, J., From Shape to Function: The Next Step in Bioprinting. *Adv Mater* **2020**, e1906423.
44. Mouser, V. H. M.; Levato, R.; Mensinga, A.; Dhert, W. J. A.; Gawlitta, D.; Malda, J., Bio-ink development for three-dimensional bioprinting of hetero-cellular cartilage constructs. *Connect Tissue Res* **2020**, *61* (2), 137-151.
45. Malda, J.; Benders, K. E.; Klein, T. J.; de Grauw, J. C.; Kik, M. J.; Hutmacher, D. W.; Saris, D. B.; van Weeren, P. R.; Dhert, W. J., Comparative study of depth-dependent characteristics of equine and human osteochondral tissue from the medial and lateral femoral condyles. *Osteoarthritis Cartilage* **2012**, *20* (10), 1147-51.
46. Wineland, Nora., Lameness and Laminitis in U.S. Horses. USDA:APHIS:VS, CEAH, National Animal Health Monitoring System. Fort Collins, CO., **2000** #N318.0400.
47. Bothe, F.; Deubel, A. K.; Hesse, E.; Lotz, B.; Groll, J.; Werner, C.; Richter, W.; Hagmann, S., Treatment of Focal Cartilage Defects in Minipigs with Zonal Chondrocyte/Mesenchymal Progenitor Cell Constructs. *Int J Mol Sci* **2019**, *20* (3).
48. Salonijs, E.; Rieppo, L.; Nissi, M. J.; Pulkkinen, H. J.; Brommer, H.; Brünott, A.; Silvast, T. S.; Van Weeren, P. R.; Muhonen, V.; Brama, P. A. J.; Kiviranta, I., Critical-sized cartilage defects in the equine carpus. *Connective Tissue Research* **2019**, *60* (2), 95-106.
49. Vindas Bolaños, R. A.; Cokelaere, S. M.; Estrada McDermott, J. M.; Benders, K. E. M.; Gbureck, U.; Plomp, S. G. M.; Weinans, H.; Groll, J.; van Weeren, P. R.; Malda, J., The use of a cartilage decellularized matrix scaffold for the repair of osteochondral defects: the importance of long-term studies in a large animal model. *Osteoarthritis and Cartilage* **2017**, *25* (3), 413-420.
50. Daly, A. C.; Freeman, F. E.; Gonzalez-Fernandez, T.; Critchley, S. E.; Nulty, J.; Kelly, D. J., 3D Bioprinting for Cartilage and Osteochondral Tissue Engineering. *Adv Healthc Mater* **2017**, *6* (22).
51. Groen, W. M.; Diloksumpan, P.; van Weeren, P. R.; Levato, R.; Malda, J., From intricate to integrated: Biofabrication of articulating joints. *J Orthop Res* **2017**, *35* (10), 2089-2097.
52. Daly, A. C.; Kelly, D. J., Biofabrication of spatially organised tissues by directing the growth of cellular spheroids within 3D printed polymeric microchambers. *Biomaterials* **2019**, *197*, 194-206.

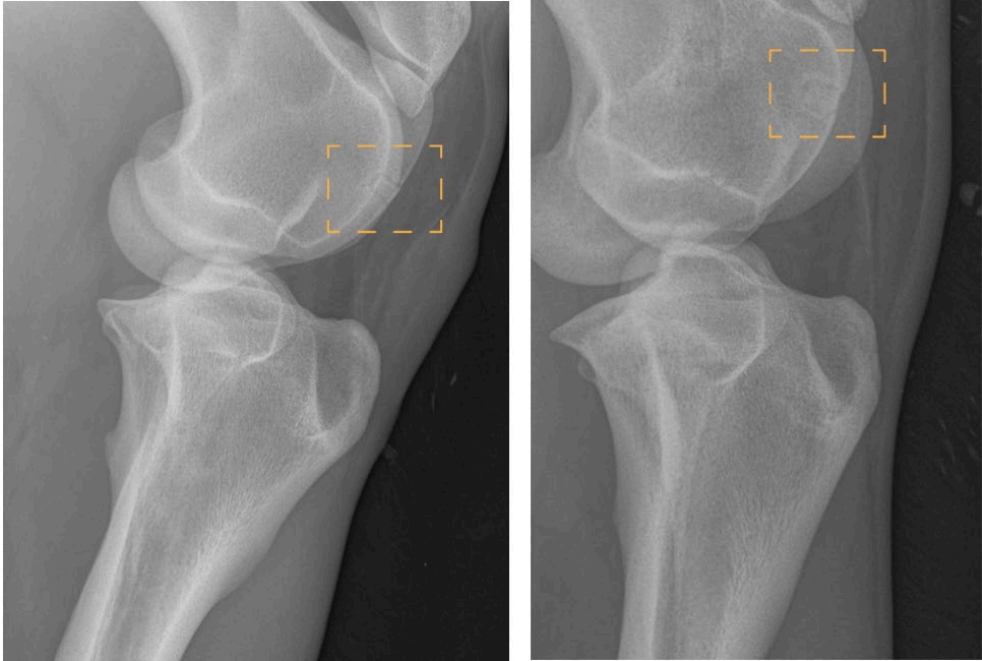
SUPPLEMENTARY INFORMATION



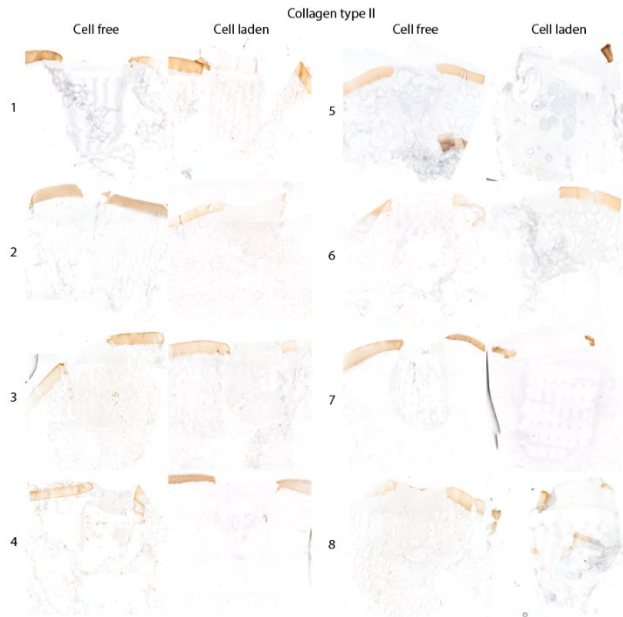
Supplementary figure 1. Schematic picture representing marker location based on anatomical landmarks for gait analysis.



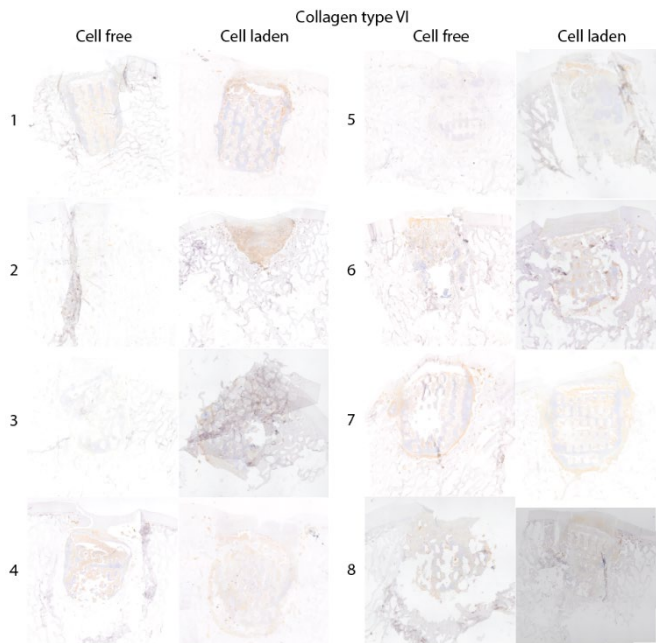
Supplementary figure 2. Optimization of the superficial layer for cell infiltration. A) Top view images of superficial layers with differently programmed line spacings. B) Quantification of actual average pore size as a result of programmed line spacing. C) Fluorescently labelled ACPCs entrapped in meshes with different line spacings. (LIVE/DEAD staining) D) Quantification of DNA in the superficial layers with different line spacings. * = $p < 0.05$, one-way ANOVA, post hoc Bonferroni.



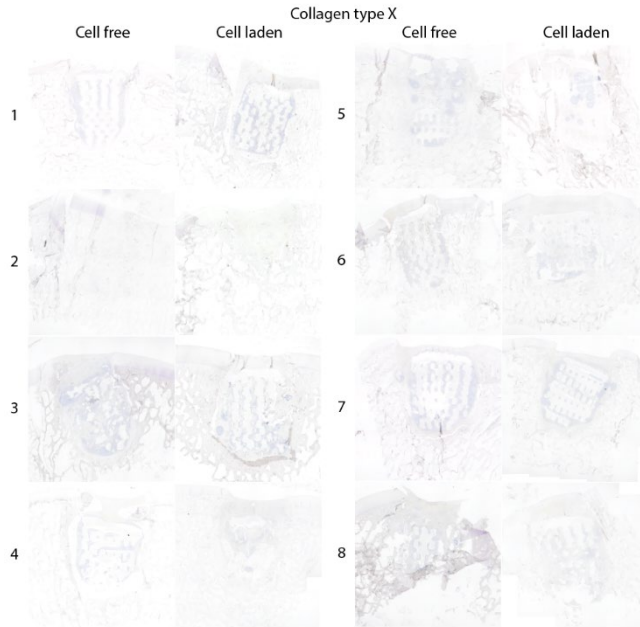
Supplementary figure 3. Representative X-rays during the implantation period.



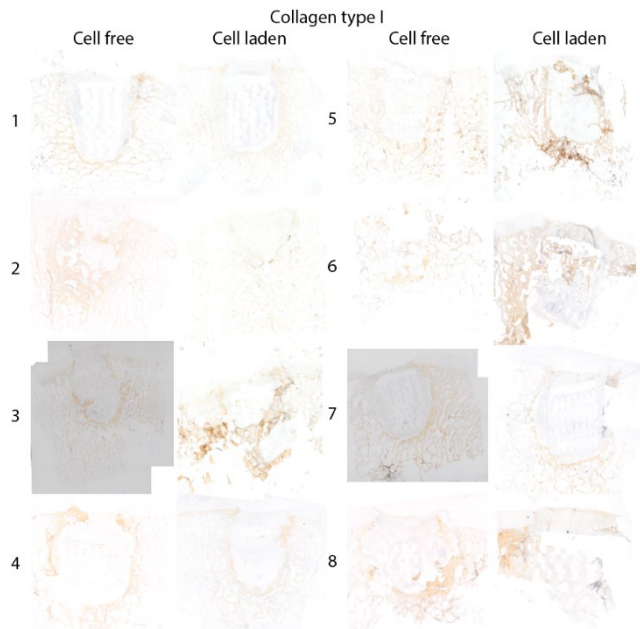
Supplementary figure 4. Overview of the collagen type II immuno-histological staining for all implants. Brown staining represents collagen type II.



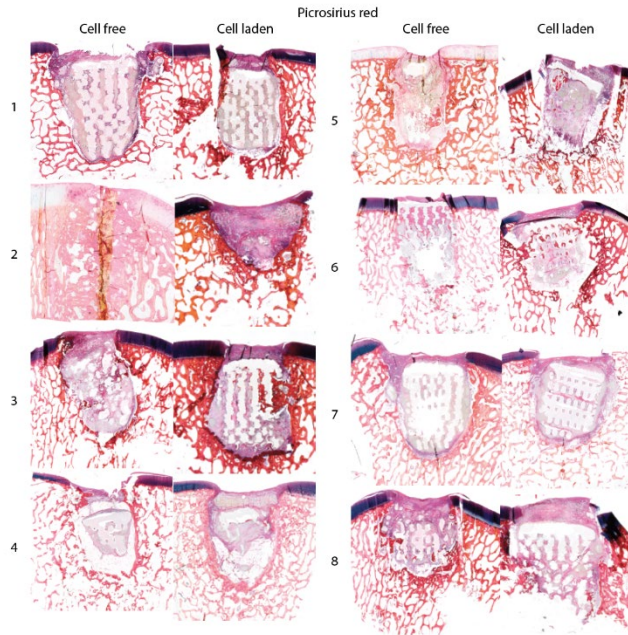
Supplementary figure 5. Overview of the collagen type VI immuno-histological staining for all implants. Brown staining represents collagen type VI.



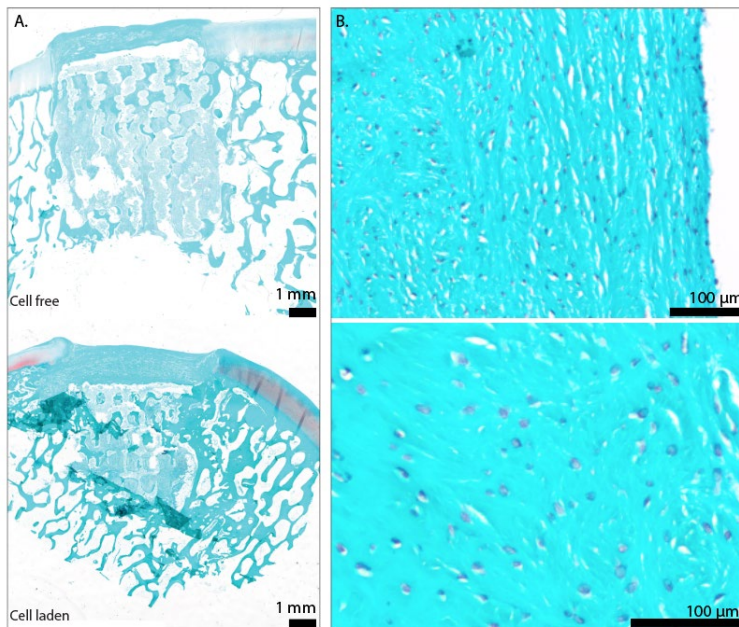
Supplementary figure 6. Overview of the collagen type X immuno-histological staining for all implants. All samples stained negative for collagen type X.



Supplementary figure 7. Overview of the collagen type I immuno-histological staining for all implants. Brown staining represents collagen type I.



Supplementary figure 8. Overview of the picrosirius red histological staining for all implants.



Supplementary figure 9. Safranin O staining after a prolonged decalcification protocol. A) Overview image of cell free and cell laden implants. B) Detailed image of the cell-laden implants.



CHAPTER 7

General Discussion

The statement that “*an ulcerated cartilage is universally allowed to be a very troublesome disease; that it admits of a cure with more difficulty than a carious bone; and that, when destroyed it is never recovered*” (Hunter 1743) is (unfortunately) one of the few, if not the only, medical axioms dating back to the 18th century that still stands. The quest for techniques that will allow the regeneration, or at least the fully functional repair, of articular cartilage is still ongoing and this thesis presents an effort to contribute to this daunting task. In particular, it focusses on the use of various novel biofabrication techniques and the careful combination of those.

The concept

The conceptual hypothesis of this thesis was that the use of a converged biofabrication approach would permit the creation of more functional osteochondral constructs. Biofabrication technologies share the common aspect of enabling the automated 3D spatial patterning of different cells and materials, to construct complex, tissue mimetic architecture. However, each of these technologies can target specific ranges of resolution and process certain families of materials. Hence, a single technique alone is insufficient to fully capture the complex, hierarchical composition of living tissues within the joint. Converging biofabrication techniques into a single, integrated process holds high promises to address such challenge. Specifically, the convergence refers to the combination of multiple printing technologies, which allows to create structures with intricate architectures across different dimensional scales. In this thesis, this strategy was implemented to achieve the functional integration of engineered bone and cartilage phases that finally compose functional osteochondral implants. Such constructs hence would come closer to the “recovery” of the “ulcerated” cartilage than either natural healing or existing therapeutic approaches.

To achieve this, several obstacles have to be cleared. Two of these were addressed in this thesis: 1) how to integrate the osteal and the cartilage phase of the implant and 2) how to optimize the osteal anchor of the construct. These questions were addressed from the design and the *in vitro* evaluation point of view, and up to the long-term *in vivo* testing in a large animal model.

The integrating interface

In the native joint, the hyaline cartilage and the subchondral bone display large differences in biochemical composition and biomechanical characteristics. Yet, both are strongly interconnected and the interface between the two tissues is formed by the calcified cartilage layer that serves both to provide a gradual transition in physical and biochemical tissue characteristics from one tissue to the other and as a diffusional barrier modulating the exchange of solutes and bioactive signals to and from the cartilage layer, which communication is crucial for maintaining joint homeostasis.

In the engineering of osteochondral constructs, the two tissue types are usually mimicked through the use of different approaches and materials (*e.g.*, hydrogels for the cartilage phase and a variety of ceramic bone scaffolds for the osteal part). Hydrogel-based materials have been extensively used as cell carriers for cartilage repair since they display partly comparable properties to native tissues and they provide a favorable environment for cell viability and functionality.¹ At the same time, several bone scaffolds have been developed and employed as an osteal anchor for tissue-engineered osteochondral grafts.^{2, 3} Among several options, calcium phosphate-based materials are attractive candidates due to their similar composition to the inorganic part of the native bone, their biocompatibility, and their biodegradability.⁴ This thesis focused on establishing a durable integration of a hydrogel-based structure with a calcium phosphate bone anchor, as well as the integration of the anchor with the native subchondral bone to provide stability to the implant.

To achieve this, we hypothesized that converging biofabrication techniques, specifically MEW and extrusion-based printing, could enable the creation of an integrated interphase between the bone and cartilage parts of the osteochondral constructs. Recently, it was shown that polycaprolactone (PCL) microfiber scaffolds produced with MEW can reinforce cell-laden hydrogel structures, resulting in compressive mechanical properties comparable to native cartilage.⁵ This strategy was used as starting point to develop a stable tissue-engineered cartilage phase for the osteochondral constructs. To integrate this microfiber-reinforced hydrogel of the chondral compartment with a calcium phosphate based bone anchor, low-temperature setting calcium phosphates were studied to permit co-printing with the PCL framework of the cartilage region, without damaging the structural stability of this low-melting point thermoplastic polymer. Alpha-tricalcium phosphate (α -TCP) was the main powder constituent for developing such printable-low-temperature setting calcium phosphate based paste, as it allows self-setting at room temperature into a calcium deficient hydroxyapatite (CDHA) cement.^{6, 7} To make it printable, the powder was mixed with poloxamer (40% w·v⁻¹), which forms shear thinning and thermoreversible hydrogels, and that thus improves injectability and cohesion of the calcium phosphate based composite.⁸⁻¹⁰ Similar constituents were investigated previously for the development of a self-hardening injectable bone paste for application in minimally invasive surgery, which demonstrated the advantage of using poloxamer as a liquid constituent, although a different powder-to-liquid ratio (P/L ratio) and concentration of poloxamer was used.¹¹ However, because poloxamer is typically non-biodegradable, we used a custom synthesized hydrolytically degradable poloxamer, following a synthetic route previously developed in our laboratory.¹² Overall, this formulation could be extruded and continuously printed at ambient temperature without adding extra rheological modifiers or support materials. Therefore, by directly depositing this paste on the melt electrowritten PCL microfiber structures, an integration between this reinforcing microfiber mesh of the chondral compartment and the calcium phosphate-based bone anchor was realized. During these efforts, we identified two major factors influencing the success of the interlocking between the PCL and the ceramic: the physicochemical properties of printable calcium phosphate paste (pCaP) and the parameters for extrusion

printing of the material. Regarding the pCaP paste, viscosity, mechanical properties, and consistency are important and are correlated with each other. The viscosity of the developed pCaP paste was high enough so that the paste remains trapped within the PCL layers where it is extruded, rather than freely flowing, and completely filling the pores within the PCL mesh, when deposited without sacrificial support underneath. Additionally, this viscosity allowed fiber formation after extrusion. Both poloxamer concentration and the powder to liquid ratio of the paste determine initial viscosity of the paste, which in our studies was characterized by rheometry, as detailed in **Chapter 3**. It was shown previously that higher viscosity could be achieved when depositing this poloxamer-containing paste at ambient temperature (20-25°C), thanks to overcoming the gelling temperature of the thermo-reversible hydrogel in the liquid constituent of this pCaP paste. Additionally, the setting reaction of α -TCP might also contribute to this viscosity. In fact, the reaction of the ceramic particles can start during the residence time of the materials in the printer, as the material hydrolysis is initiated in the water-rich environment of the paste, and the setting kinetics are accelerated by increasing the environmental temperature. When aiming to print large constructs, which require long printing times, it is thus important to stabilize the paste to ensure a constant and optimal viscosity during printing. Therefore, for the work in this thesis, the temperature of the printing environment was controlled at 20 – 25 °C. This compromise permits the gelation of the poloxamer component, while minimizing the effect on the rate of α -TCP hydrolysis.⁷ In addition, the thermal gelation of poloxamer is also fundamental to prevent sedimentation and phase separation of the powder component within the paste^{8, 9}, thus allowing the production of filaments and structures with a homogenous composition and thus equal mechanical properties.¹¹ Overall, this structural stability of the paste allowed for continuous printing and to form an osteal compartment with the capability to support weight from the upper consecutive layers without deformation. Indeed, even cm-scale constructs could be readily obtained. Correct deposition parameters while printing using an extrusion-based printer, are also essential to ensure an integration between the two materials. These parameters include extrusion pressure, deposition velocity, nozzle geometry, and distance between the tip of the nozzle and the depositing surface. In this thesis, a 250 μm diameter conical nozzle was employed, as it was the lowest diameter that the paste could be extruded through and therefore a main factor in determining the resolution of each printed filament. Therefore, the other parameters were optimized for using with this nozzle dimension. It was found that a combination of low extrusion pressure (0.2 MPa) with a low depositional speed (2 $\text{mm}\cdot\text{s}^{-1}$), and keeping an optimal distance between nozzle and mesh surface (80% of mesh thickness) may contribute to the success of secured integration (**Chapter 3**). A homogeneous distribution of the paste on the mesh surface was observed when printing with a low extrusion pressure (0.2 MPa), with correlated speed (2 $\text{mm}\cdot\text{s}^{-1}$). Potentially, this secure integration could be affected by a homogeneous adhesion between the two materials. The nozzle distance is important for preserving the structural integrity of the PCL mesh, while simultaneously ensuring ceramic-polymer integration. From the printing tests, we identified an optimal distance (80% of mesh thickness). Smaller distances will result in the nozzle and extruded

material damaging the PCL mesh structure, while higher distances will result in insufficient integration between the chondral and osteal scaffolds.

Using this strategy, secure anchoring of the PCL microfiber-reinforced hydrogel within the ceramics bone-mimetic scaffold could be realized, resulting in improved resistance against shear forces compared to the non-anchored hydrogel-ceramic structure. For the integration of a hydrogel-based chondral compartment with a stiff bone graft, thus far two methods had been described in literature. In the first method a stiff bone graft is inserted into to cartilage part in its pre-gel phase¹³, in the second a low viscosity pre-gel is poured onto the stiff bone graft.¹⁴ However, in both methods the strength of the integration is solely based on the intrinsic physical gelation or on additional chemical crosslinks. Using our novel converged printing approach, osteochondral constructs with a higher interfacial strength could be obtained, though the strength was still inferior to that of native osteochondral units¹⁵. A potential drawback of the solution presented in our study is that it still lacks a gradual transition from the bony phase to the cartilage phase because of the absence of a calcified cartilage layer. Future studies should hence address the possibility to introduce such a layer, either via printing of a specialized bioink, or via establishing new protocols to locally differentiate cells into hypertrophic chondrocytes only in the proximity of the bony template. Likewise, besides the mechanical aspect, a thorough optimization of the diffusional and barrier properties of the engineered interfaces would be useful, for reasons indicated above.

Importantly, the interfacial strength that was achieved with our approach proved to be sufficient to allow easy surgical handling of the osteochondral grafts, as well as to ensure the long-term survival of the biofabricated structure in the challenging *in vivo* environment of the equine knee joint. Yet, the interfacial shear stress at the interface of the microfiber-reinforced hydrogel with the ceramic phase of the constructs was still 300-fold lower than in native tissue.¹⁵ This suggests that, at least for focal defects, less than native strength may be sufficient. In this context, it will be interesting to investigate cell behavior at the interface and to assess the ability of the repair tissue to restore native strength. However, the strength achieved in our study may not be sufficient for larger constructs that will be necessary to produce partial or total knee replacements, which cannot rely on the neighboring native tissue to share the mechanical loads. Therefore, research to further improve the mechanical properties at the engineered osteochondral boundary is indicated. This could be done by testing different architectures and laydown patterns for the printed fibers¹⁶, tuning the bone and cartilage material composition¹⁷, or, as already mentioned, through the engineering of a calcified cartilage-mimetic layer^{15, 18}, or a combination of these approaches.

The design of the printed architecture at the bone-cartilage interface in our study (one spacing of the micro-fiber mesh, deposited with a 0-90°C laydown pattern) was based on earlier studies that aimed at improving the mechanical properties of the cartilage compartment in our lab.⁵ It has further been shown previously that modifying the microstructure at the interface, for instance by mimicking an interdigitating pattern, the interfacial shear strength can be improved.¹⁹ Mechanical reinforcement can also be realized by incorporating cells and stimulating biological factors that, thus mimicking the gradient

from calcified cartilage to bone.^{18, 20} Cell incorporation in the chondral compartment was effectuated in our study through *in vitro* pre-culture and the zonal organization of cartilage was addressed in **Chapter 6**. However, this only to create a distinction between the superficial and deeper zones of the cartilage, not to address the calcified zone at the osteochondral boundary. The *in vitro* studies gave evidence that our calcium phosphate cement did not hamper neo-hyaline cartilage matrix synthesis by adjacent cells in the chondral hydrogel, but did not address specifically how to guide the production of calcified matrix.

The strength of the integration of the two layers was tested by applying unidirectional shear force until failure. Shear stress at the interface had been suggested as an important mechanical characterization for cartilage repair, but without guidelines how to realize this.^{21, 22} It is clear that, when in the future more challenging larger and geometrically complex constructs that mimic patient-specific anatomical features will have to be evaluated, more complex mechanical tests that address the anisotropic and inhomogeneous load distribution in the joint will be needed. *Ad hoc* developed bioreactors mimicking the mechanics of human locomotion may need to be fabricated and used to test the constructs that can be later translated towards (human and veterinary) clinical practice. An interesting aspect of such class of bioreactor would be the possibility to investigate the role of loading and hydraulic flow across the cartilage and bone components in promoting diffusion of nutrients and bioactive signals in these engineered grafts.

The osteal anchor

Any construct meant to be implanted in the biomechanically demanding high-load articular environment is doomed to fail if proper fixation cannot be guaranteed. Several techniques have been tried to fixate cartilage phase-only constructs, but largely in vain. The use of osteochondral implants that can be placed surgically press-fit is seen as the best way to ensure that the implants stay in place.² Therefore, an ideal osteal scaffold should be able to facilitate progressive formation of the new bone structure, while degrading at an equal rate. In fact, low-temperature setting calcium phosphate (CaP)-based materials have such properties, in contrast to sintered CaP-based materials, polymers, and metals.

To use the developed pCaP formulation for the production of the bone anchor structures, several factors need to be considered. These include the material composition, the way these custom-structures should be produced in order to perfectly match the size and shape of the defect, as well as their internal architecture.

Regarding the material composition, low-temperature setting CaP-based material, with α -TCP as the main powder component, can convert to form calcium-deficient hydroxy apatite (CDHA) through hydrolysis. It has been shown that the crystal structure of CDHA is comparable with the inorganic constituent of the native bone. As, such the scaffolds made of these materials have been considered biomimetic.²³ In our study the CDHA was obtained in line with previous studies described in literature that showed that poloxamer, the liquid

constituent of the paste, could not hamper the hydrolysis conversion of α -TCP.¹¹ Additionally, nano-hydroxyapatite (nano-HA) was also added in order to ensure the induction of bone formation by the formulation with a lower degradation rate compared to CDHA. Limited toxicity of the formulation developed in **Chapter 3** was observed. Also, during osteogenic differentiation *in vitro* no release of harmful components from the material was observed. Therefore, we were confident to evaluate this formulation in a realistic *in vivo* environment.

To ensure high-quality fixation allowing an integration between the native bone and the-implant, the fabricated constructs should perfectly match the dimensions and shape of the defect site. High fidelity of the final construct does depend on the precision of the printing process and the ability of shape maintenance of the printed material over time.²⁴ Therefore, this sets important requirements for the material properties, printing parameters, and post-processing methods of potential materials applied for the generation of the bone anchors.²⁵ In our case, the powder-to-liquid ratio (P/L ratio) of the pCaP formulation was rather high. This provided us with the ability to retain the shape of the structures while ensuring adequate mechanical strength to support the weight of the consecutively printed layers. However, the high particle content can influence the extrudability of this self-setting CaP-based ink over time due to the effect of the setting reaction.^{26,27} We therefore used highly viscous poloxamer (40% w·v⁻¹), as a liquid constituent, to improve injectability and to reduce the phase separation in the pCaP paste. Clearly, this is a delicate balance and increasing this liquid component will affect the duration of the setting time²⁷, while it may also compromise mechanical strength of the ink. There is further room for improvement here. For the printing of the structures in this thesis, atmospheric temperature was controlled and limited amounts of pCaP paste were printed in a limited time frame. However, the controlled atmospheric temperature (between 20-25°C) may partially affect the setting reaction by maintaining viscosity of poloxamer²⁸ and delaying setting of α -TCP^{7, 11}. Although the temperature was controlled, variations in the diameter of the printed filaments were observed when printing pCaP from the same cartridge for a longer period. Therefore, to prevent problems during the printing process, limited amounts of pCaP were placed in the cartridge, so the material could be printed within 30 minutes, in line with previous observations of Maazouz et al., who used an α -TCP/gelatin composite for robocasting at room temperature (approximately 22.5 °C). They recommended to print the α -TCP/gelatin composite within 15 – 30 minutes post-mixing when the required extrusion force was still low and rather stable based on their extrusion force study.²⁶ Although the P/L ratio and liquid constituent in our study were different, this same limited time frame was assumed to be appropriate as well for our α -TCP/poloxamer composite and was effectuated by letting the paste in the printer-chamber environment for 5 minutes after taking it out from the ice. With respect to the printing parameters, all pCaP constructs were made with help of an extrusion printer with limited resolution (minimum size 200 – 100 μ m).²⁹ When using this type of printer, several factors need to be considered, like layer height, extrusion pressure, and deposition speed. For our pCaP formulation, the layer

height was selected based on the obtained average diameter of a printed strand that could ensure good adhesion between each layer and this was the height that did not prevent flow of extruded paste. The interplay between extrusion pressure, deposition speed and the distance between the tip of the nozzle and the substrate influences the quality of printed filaments when using this type of printer.³⁰ For printing of the structures described in this thesis, low extrusion pressure (0.2 MPa) together with low deposition speed ($2 \text{ mm}\cdot\text{s}^{-1}$) were selected to obtain the highest filament quality in terms of material cohesion and accuracy and precision of deposition of the highly viscous paste. The printing path and more specifically the angles or corners, can also affect the fidelity of printed structures.^{30, 31} Most structures that were printed in this thesis were of cylindrical shape, filled in with a meander pattern inside. Therefore, deposition of material at the concave sides of the meander pattern within this circular shape may affect the fidelity of the construct. This indeed resulted in an irregular perimeter when printed filaments at the concave areas collapsed due to gravitation and lack of support underneath. Further, even with controlled atmospheric temperature and amount of pCaP paste, slightly inconstant extrudability of pCaP paste could be observed. This required intermittent manual adjustment of the printing pressure during the process, which, in itself, also could affect the fidelity of the printed structure. For post-processing, the printed structures were set at physiological temperature through hydrolysis without sintering and hence without the need for high temperature treatment. For this reason, no obvious shrinkage was observed for any of the printed structures in this thesis.

The internal architecture of scaffolds is another important parameter that influences performance for bone regeneration. Therefore, in **Chapter 4** two main architectures were compared: constant, and gradient porosity. Generally, recommended pore size for optimal bone ingrowth is larger than $300 \mu\text{m}$.^{32, 33} The pore size of the constant porosity structure was $500 \mu\text{m}$ with one layer of non-porous material. In the gradient structure, porosity ranged from $500 \mu\text{m}$ to non-porous. In this study the aim was to observe the performance of these architectures when implanted in large bone defects at an orthotopic and non-load bearing site. To better evaluate the capacity of the constructs to facilitate bone ingrowth, the scaffolds were encased in a non-porous cylindrical PCL chamber that only permitted bone ingrowth from the bottom. Unintentionally, these PCL chambers also made the somewhat irregular perimeter of the CDHA scaffolds (which was due to the printing process, as explained above), smoother and therefore better fitting in the defect. This experiment gave evidence for two main properties of the newly developed material needed for bone regeneration: osteointegration and osteoconduction. As the implantation site was orthotopic, no conclusion was possible about osteoinductive properties.³⁴ However, earlier work has shown that by tuning the pore architecture of nanostructured CDHA the material can be made osteoinductive.³⁵ Our study showed that there was more ingrowth of new bone into the constant pore architecture than into the gradient architecture after implantation for 7 months.

Mechanical strength is another parameter that is of great importance for materials used in bone regeneration. Calcium phosphate-based materials are known to have low fracture resistance, which typically limits the application of these materials to non-load

bearing areas.³⁶ In our case, the situation was worse, as the CDHA obtained from hydrolysis at low temperature is apatite that has lower mechanical properties compared to sintered apatite. Indeed, the compressive modulus and ultimate strength of the printed porous structures were within the lower range of human cancellous bone. This still allows for testing the material at non-load bearing sites but may restrict use at load-bearing areas.

The calcium phosphate-based paste that was used in this thesis offers several advantages and possibilities that could be used for forming the innovative integration between the low-melting temperature polymer and the biomimetic bone graft, however, there are still several aspects that could be improved. First, a construct for press-fit implantation needs to have perfect size and shape, which allows for a smooth implantation and perfect fit in the defect site and should also have adequate mechanical properties. The compressive modulus and ultimate strength of the non-porous structure with and without poloxamer were similar, suggesting no clear influence of the incorporated poloxamer on the mechanical properties of this α -TCP formulation. Several other strategies can be applied for manipulating the mechanical properties of bone grafts through modifying material composition, such as the use of a polymeric additive, to achieve the properties that are suitable for the intended application.³⁷⁻³⁹ Silk is a natural material that possesses excellent elastic mechanical properties, biocompatibility, biodegradability and has been explored for several biomedical applications including for bone regeneration.⁴⁰ Additionally, it has been developed also for using with several 3D printing techniques⁴¹; therefore, this material might be a possible option for developing new compositions for future bone grafts. Secondly, precision and accuracy of the printed structure could possibly be improved by developing a material formulation that could be used for printing with higher resolution technology and hence will produce smaller printing errors.

The proof of the pudding

Tissue engineering is a research field in which the distribution of research papers over the line from bench to bedside is extremely skewed with the vast majority of papers reporting on *in vitro* data and much less on *in vivo* results or clinical studies.⁴² Many promising techniques in the lab do not stand the real-life challenges of the harsh articular environment.⁴³ Testing *in vivo* is therefore a *condicio sine qua non*, even if outcome is more often than not disappointing. For the constructs developed in this thesis we opted for the equine large animal model.

To introduce new therapeutic approaches into the clinics, it is essential to perform a preclinical evaluation in the most relevant models that closely imitate the common human clinical scenario.⁴⁴ In this thesis, horses were chosen as experimental animals, as the equine model is well accepted in translational regenerative orthopedics, among other things because of the high loads they experience in their musculoskeletal system.^{44, 45} The equine model offers several advantages for the translation of potential treatments for cartilage damage to humans. First, horses are generally kept because of their locomotor performance, either for

leisure or as equine athletes (*e.g.* racehorses and show jumpers) and are therefore, like humans, vulnerable for disorders of the musculoskeletal system, sharing to a large extent the same pathologies. In addition, horses display a similarly low intrinsic healing capacity and similar anatomy (thickness) and biochemical composition of the articular cartilage of the knee joint as humans.⁴⁶ Not unimportantly, the horse is a companion animal that can be trained to perform specific exercises, such as running on a treadmill, which facilitates the quantitative assessment of key gait parameters, which provide insight in the functional response to implants in the joint. There are also some disadvantages due to size of the animal, which need to be kept in mind. Horses are large animals with weight ranging roughly between 100 – 1000 Kg; therefore, they need special clinical facilities and have specific husbandry requirements, causing higher expenses and the need for specialized personnel. Further, it is important to realize that horses cannot unload limbs for any prolonged period, like humans or smaller animal species can, which means that any construct will have to be able to stand immediate load bearing after implantation.

Several analytical methods are available to monitor the clinical output of joint repair strategies when using the equine model. Invasive monitoring, for instance through arthroscopy with or without the use of advanced intra-articular imaging techniques such as optical coherence tomography⁴⁷ or near infrared spectroscopy⁴⁸, is in contrast to the more common smaller experimental animals, well possible in this species. However, it requires an, albeit minimally invasive, surgical intervention with related costs and anesthetic risk. Non-invasive monitoring through medical imaging and objective, quantitative gait analysis are valid alternative options. With respect to medical imaging, radiography and ultrasonography are routinely used in horses. Magnetic resonance imaging (MRI) and Computed Tomography, with or without the use of contrast agents, are options as well, although in large horses bore size of the available equipment may still make imaging of the equine stifle (knee) joint difficult. Additionally, quantitative objective gait analysis, which is actually going through a phase of very rapid development⁴⁹⁻⁵¹ is another excellent option that can be used to quantify gait as a functional outcome over time and which is certainly an asset of the equine model.

To investigate the performance of the newly developed microfiber-reinforced hydrogel-ceramic osteochondral graft produced in this thesis, we performed *in vivo* studies upon implantation in experimentally created osteochondral defects in the stifle joint of Shetland ponies. In the work described in **Chapters 5 and 6**, the osteal anchor of the construct and the interface and cartilage reinforcement components were the same, while the engineered cartilage region was different. In the experiment described in **Chapter 5** the chondral component embedded within the reinforcing PCL mesh was constituted by neo-matrix entirely produced by cultured cells. In that experiment, two groups were tested: i) a cell-free control, and ii) a cell seeded group in which a high density of ACPCs was present and was stimulated with growth differentiation factor 2 prior to implantation. Unfortunately, it was not possible to draw conclusions from this study concerning the designed research question as the grafts failed in the bone region, due to failed integration with the native bone,

even though the osteoconductive properties of the scaffold had been clearly demonstrated in earlier studies. The surgical implantation proved to be particularly difficult, due to geometrical imperfections in the 3D printed anchors, which resulted in sub-optimal placement of the graft, partial fragmentation upon implantation and ultimately mechanical failure under load. Consequently, bone loss surrounding the osteal anchors was observed in all samples. Stabilization of the immature chondral graft is a critical issue for the induction cartilage regeneration and hence for the restoration of cartilage damage, which was underlined by these events. Although the printed CDHA scaffolds showed strongly positive osteogenic performance when implanted in the equine tuber coxae (**Chapter 4**), a weakly loaded area, the same performance was not observed in this study. A major difference between the two studies was that in the second study the implants were not enclosed within a PCL chamber, which is a deformable polymer that enabled better press-fit implantation than the more rigid and brittle CDHA material alone without such outer shell, where implantation led to fragmentation of the ceramic that caused micro-movements at the bone-scaffold interface, eventually causing bone resorption and failure of the bone anchor. Micro-movement is a well-known cause of osteolysis around implants and later failure.⁵² It was concluded that the balance is delicate and that the unintentional change of structure from one study to the other led to completely different outcomes.

A totally different outcome was seen when using the same microfiber-reinforced hydrogel-ceramic osteochondral graft for cartilage repair in the experiment described in **Chapter 6**. In this study, the variable part was again the chondral hydrogel, which was either cell-free or loaded with zonally distributed ACPCs. However, in this case, the imperfections at the borders of the 3D printed bone implant were trimmed to ensure a smooth fitting into the surgically imparted defect. Consequently, press-fit surgical placement was much easier and the integration into the surrounding native bone was much better with limited misalignment of the implants and substantially less extensive osteolysis surrounding the implant with some variation in osteointegration due to inter-donor variability. In this study, the chondral compartment of the tissue-engineered osteochondral graft had been prepared by simultaneously printing the MEW-PCL microfibers and the cell-encapsulating hydrogel in the chondral compartment after integrating the microfibers within the ceramics-based bone anchor. This procedure required perfect stabilization during the printing process. Therefore, the osteal anchor was perfectly fit within a custom-made metal fixation that facilitated deposition of the hydrogel and microfibers. The inner dimension of custom-made fixation was designed to be identical to the defect in which the construct would be implanted. It was this procedure that resulted in a much less irregular perimeter of the CDHA osteal anchor and hence a better fit of the scaffold to the defect site with no formation of fragments during surgical implantation, preventing failure due to collapse of the bone anchor, as seen in the study described in **Chapter 5**.

Overall, the anchoring strategy developed in this thesis was proven successful at preserving the mechanical integrity of the osteochondral implant over the course of 6 months, a condition that was paramount to enable cartilage repair. At the same time, using such brittle

material for the bone anchor was proven to greatly limit the flexibility and error margins of the surgical procedure. Scaffolds with minimal tolerance over the printed sizes and geometries are necessary to permit ease of implantation and satisfactory clinical outcome. Consequently, application of our osteochondral integration multi-scale printing approach to new osteal materials, that overcome the brittleness of the CDHA employed herein, is recommended.

Conclusion and avenues for further research

The osteochondral unit is a highly complicated functional unit in an extremely demanding environment. The reconstitution of this unit is still the proverbial mythical *Holy Grail* that is so hard to find. The current study made steps in the right direction by adding complexity through the convergence of two state-of-the-art biofabrication technologies. While it may still take a while until Hunter's age-old axiom will finally fall and possibly much more complexity needs to be added, it is felt that it is through the convergence of these novel technologies, *i.e.* the conceptual basis of this thesis, that clinically very relevant breakthroughs may be realized.

To concretize this, additional improvements and optimization will, however, be needed. This is true for the osteal anchor and the integrating interface as outlined above, but also for the cartilage phase that was not the main subject of this thesis, but is crucial for the osteochondral implant as it is the layer that is directly loaded and that will not repair in the natural situation. Therefore, sufficient mechanical resistance of this compartment since implantation until having enough tissue formation is also important.

Even if we would be able to design the ideal implant, there will remain challenges to overcome; these include the integration of the implant in the native tissue and the prevention of abrupt transitions in tissue properties, as well as creating the right environment in terms of joint homeostasis. It all seems much and indeed Hunter cannot be supposed to surrender quickly and easily, but modern technology is closing in on him.

REFERENCES

1. Spiller, K. L.; Maher, S. A.; Lowman, A. M., Hydrogels for the repair of articular cartilage defects. *Tissue Eng Part B Rev* **2011**, *17* (4), 281-99.
2. Mancini, I. A. D.; Vindas Bolaños, R. A.; Brommer, H.; Castilho, M.; Ribeiro, A.; van Loon, J. P. A. M.; Mensinga, A.; van Rijen, M. H. P.; Malda, J.; van Weeren, R., Fixation of Hydrogel Constructs for Cartilage Repair in the Equine Model: A Challenging Issue. *Tissue Engineering Part C: Methods* **2017**, *23* (11), 804-814.
3. Oryan, A.; Alidadi, S.; Moshiri, A.; Maffulli, N., Bone regenerative medicine: classic options, novel strategies, and future directions. *J Orthop Surg Res* **2014**, *9* (1), 18.
4. Habraken, W.; Habibovic, P.; Epple, M.; Bohner, M., Calcium phosphates in biomedical applications: materials for the future? *Materials Today* **2016**, *19* (2), 69-87.
5. Visser, J.; Melchels, F. P. W.; Jeon, J. E.; van Bussel, E. M.; Kimpton, L. S.; Byrne, H. M.; Dhert, W. J. A.; Dalton, P. D.; Huttmacher, D. W.; Malda, J., Reinforcement of hydrogels using three-dimensionally printed microfibrils. *Nature Communications* **2015**, *6* (1), 6933.
6. Ginebra, M. P.; Fernández, E.; De Maeyer, E. A. P.; Verbeeck, R. M. H.; Boltong, M. G.; Ginebra, J.; Driessens, F. C. M.; Planell, J. A., Setting Reaction and Hardening of an Apatitic Calcium Phosphate Cement. *Journal of Dental Research* **1997**, *76* (4), 905-912.
7. TenHuisen, K. S.; Brown, P. W., Formation of calcium-deficient hydroxyapatite from alpha-tricalcium phosphate. *Biomaterials* **1998**, *19* (23), 2209-17.
8. Franco, J.; Hunger, P.; Launey, M. E.; Tomsia, A. P.; Saiz, E., Direct write assembly of calcium phosphate scaffolds using a water-based hydrogel. *Acta Biomaterialia* **2010**, *6* (1), 218-228.
9. O'Neill, R.; McCarthy, H. O.; Montufar, E. B.; Ginebra, M. P.; Wilson, D. I.; Lennon, A.; Dunne, N., Critical review: Injectability of calcium phosphate pastes and cements. *Acta Biomaterialia* **2017**, *50*, 1-19.
10. Perez, R. A.; Kim, H.-W.; Ginebra, M.-P., Polymeric additives to enhance the functional properties of calcium phosphate cements. *Journal of Tissue Engineering* **2012**, *3* (1), 2041731412439555.
11. Maazouz, Y.; Montufar, E. B.; Malbert, J.; Espanol, M.; Ginebra, M.-P., Self-hardening and thermoresponsive alpha tricalcium phosphate/pluronic pastes. *Acta Biomaterialia* **2017**, *49*, 563-574.
12. Melchels, F. P. W.; Blokzijl, M. M.; Levato, R.; Peiffer, Q. C.; de Ruijter, M.; Hennink, W. E.; Vermonden, T.; Malda, J., Hydrogel-based reinforcement of 3D bioprinted constructs. *Biofabrication* **2016**, *8* (3), 035004.
13. Bal, B. S.; Rahaman, M. N.; Jayabalan, P.; Kuroki, K.; Cockrell, M. K.; Yao, J. Q.; Cook, J. L., *In vivo* outcomes of tissue-engineered osteochondral grafts. *J Biomed Mater Res B Appl Biomater* **2010**, *93* (1), 164-74.
14. Hung, C. T.; Lima, E. G.; Mauck, R. L.; Taki, E.; LeRoux, M. A.; Lu, H. H.; Stark, R. G.; Guo, X. E.; Ateshian, G. A., Anatomically shaped osteochondral constructs for articular cartilage repair. *Journal of Biomechanics* **2003**, *36* (12), 1853-1864.
15. St-Pierre, J.-P.; Gan, L.; Wang, J.; Pilliar, R. M.; Grynblas, M. D.; Kandel, R. A., The incorporation of a zone of calcified cartilage improves the interfacial shear strength between *in vitro*-formed cartilage and the underlying substrate. *Acta Biomaterialia* **2012**, *8* (4), 1603-1615.
16. Holmes, B.; Zhu, W.; Li, J.; Lee, J. D.; Zhang, L. G., Development of novel three-dimensional printed scaffolds for osteochondral regeneration. *Tissue Eng Part A* **2015**, *21* (1-2), 403-15.
17. Erisken, C.; Kalyon, D. M.; Wang, H.; Örnek-Ballanco, C.; Xu, J., Osteochondral Tissue Formation Through Adipose-Derived Stromal Cell Differentiation on Biomimetic Polycaprolactone Nanofibrous Scaffolds with Graded Insulin and Beta-Glycerophosphate Concentrations. *Tissue Engineering Part A* **2010**, *17* (9-10), 1239-1252.
18. Lee, W. D.; Gawri, R.; Pilliar, R. M.; Stanford, W. L.; Kandel, R. A., Sol gel-derived hydroxyapatite films over porous calcium polyphosphate substrates for improved tissue engineering of osteochondral-like constructs. *Acta Biomaterialia* **2017**, *62*, 352-361.
19. Zhang, W.; Lian, Q.; Li, D.; Wang, K.; Hao, D.; Bian, W.; Jin, Z., The effect of interface microstructure on interfacial shear strength for osteochondral scaffolds based on biomimetic design and 3D printing. *Materials Science and Engineering: C* **2015**, *46*, 10-15.

20. Mohan, N.; Wilson, J.; Joseph, D.; Vaikkath, D.; Nair, P. D., Biomimetic fiber assembled gradient hydrogel to engineer glycosaminoglycan enriched and mineralized cartilage: An *in vitro* study. *Journal of Biomedical Materials Research Part A* **2015**, *103* (12), 3896-3906.
21. Marchiori, G.; Berni, M.; Boi, M.; Filardo, G., Cartilage mechanical tests: Evolution of current standards for cartilage repair and tissue engineering. A literature review. *Clinical Biomechanics* **2019**, *68*, 58-72.
22. Patel, J. M.; Wise, B. C.; Bonnevie, E. D.; Mauck, R. L., A Systematic Review and Guide to Mechanical Testing for Articular Cartilage Tissue Engineering. *Tissue Eng Part C Methods* **2019**, *25* (10), 593-608.
23. Sadowska, J. M.; Guillem-Marti, J.; Montufar, E. B.; Espanol, M.; Ginebra, M. P., (*) Biomimetic Versus Sintered Calcium Phosphates: The *In Vitro* Behavior of Osteoblasts and Mesenchymal Stem Cells. *Tissue Eng Part A* **2017**, *23* (23-24), 1297-1309.
24. Kyle, S.; Jessop, Z. M.; Al-Sabah, A.; Whitaker, I. S., 'Printability' of Candidate Biomaterials for Extrusion Based 3D Printing: State-of-the-Art. *Adv Healthc Mater* **2017**, *6* (16).
25. Liu, Z.; Zhang, M.; Bhandari, B.; Wang, Y., 3D printing: Printing precision and application in food sector. *Trends in Food Science & Technology* **2017**, *69*, 83-94.
26. Maazouz, Y.; Montufar, E. B.; Guillem-Marti, J.; Fleps, I.; Öhman, C.; Persson, C.; Ginebra, M. P., Robocasting of biomimetic hydroxyapatite scaffolds using self-setting inks. *Journal of Materials Chemistry B* **2014**, *2* (33), 5378-5386.
27. Montufar, E. B.; Maazouz, Y.; Ginebra, M. P., Relevance of the setting reaction to the injectability of tricalcium phosphate pastes. *Acta Biomaterialia* **2013**, *9* (4), 6188-6198.
28. Attwood, D.; Collett, J. H.; Tait, C. J., The micellar properties of the poly(oxyethylene) - poly(oxypropylene) copolymer Pluronic F127 in water and electrolyte solution. *International Journal of Pharmaceutics* **1985**, *26* (1), 25-33.
29. Ozbolat, I. T.; Hospodiuk, M., Current advances and future perspectives in extrusion-based bioprinting. *Biomaterials* **2016**, *76*, 321-43.
30. He, Y.; Yang, F.; Zhao, H.; Gao, Q.; Xia, B.; Fu, J., Research on the printability of hydrogels in 3D bioprinting. *Sci Rep* **2016**, *6*, 29977.
31. Darhuber, A. A.; Troian, S. M.; Wagner, S., Physical mechanisms governing pattern fidelity in microscale offset printing. *Journal of Applied Physics* **2001**, *90* (7), 3602-3609.
32. Karageorgiou, V.; Kaplan, D., Porosity of 3D biomaterial scaffolds and osteogenesis. *Biomaterials* **2005**, *26* (27), 5474-91.
33. Loh, Q. L.; Choong, C., Three-dimensional scaffolds for tissue engineering applications: role of porosity and pore size. *Tissue Eng Part B Rev* **2013**, *19* (6), 485-502.
34. Habibovic, P.; de Groot, K., Osteoinductive biomaterials--properties and relevance in bone repair. *J Tissue Eng Regen Med* **2007**, *1* (1), 25-32.
35. Barba, A.; Maazouz, Y.; Diez-Escudero, A.; Rappe, K.; Espanol, M.; Montufar, E. B.; Öhman-Mägi, C.; Persson, C.; Fontecha, P.; Manzanera, M.-C.; Franch, J.; Ginebra, M.-P., Osteogenesis by foamed and 3D-printed nanostructured calcium phosphate scaffolds: Effect of pore architecture. *Acta Biomaterialia* **2018**, *79*, 135-147.
36. Bohner, M.; Gbureck, U.; Barralet, J. E., Technological issues for the development of more efficient calcium phosphate bone cements: a critical assessment. *Biomaterials* **2005**, *26* (33), 6423-9.
37. Jakus, A. E.; Rutz, A. L.; Jordan, S. W.; Kannan, A.; Mitchell, S. M.; Yun, C.; Koube, K. D.; Yoo, S. C.; Whiteley, H. E.; Richter, C.-P.; Galiano, R. D.; Hsu, W. K.; Stock, S. R.; Hsu, E. L.; Shah, R. N., Hyperelastic "bone": A highly versatile, growth factor-free, osteoregenerative, scalable, and surgically friendly biomaterial. *Science Translational Medicine* **2016**, *8* (358), 358ra127.
38. Wagoner Johnson, A. J.; Herschler, B. A., A review of the mechanical behavior of CaP and CaP/polymer composites for applications in bone replacement and repair. *Acta Biomater* **2011**, *7* (1), 16-30.
39. Perez, R. A.; Kim, H. W.; Ginebra, M. P., Polymeric additives to enhance the functional properties of calcium phosphate cements. *J Tissue Eng* **2012**, *3* (1), 2041731412439555.
40. Melke, J.; Midha, S.; Ghosh, S.; Ito, K.; Hofmann, S., Silk fibroin as biomaterial for bone tissue engineering. *Acta Biomaterialia* **2016**, *31*, 1-16.
41. Wang, Q.; Han, G.; Yan, S.; Zhang, Q., 3D Printing of Silk Fibroin for Biomedical Applications. *Materials (Basel)* **2019**, *12* (3).

42. Armiento, A. R.; Stoddart, M. J.; Alini, M.; Eglin, D., Biomaterials for articular cartilage tissue engineering: Learning from biology. *Acta Biomater* **2018**, *65*, 1-20.
43. Vindas Bolaños, R. A.; Cokelaere, S. M.; Estrada McDermott, J. M.; Benders, K. E. M.; Gbureck, U.; Plomp, S. G. M.; Weinans, H.; Groll, J.; van Weeren, P. R.; Malda, J., The use of a cartilage decellularized matrix scaffold for the repair of osteochondral defects: the importance of long-term studies in a large animal model. *Osteoarthritis and Cartilage* **2017**, *25* (3), 413-420.
44. Chu, C. R.; Szczodry, M.; Bruno, S., Animal models for cartilage regeneration and repair. *Tissue Eng Part B Rev* **2010**, *16* (1), 105-15.
45. Ahern, B. J.; Parvizi, J.; Boston, R.; Schaer, T. P., Preclinical animal models in single site cartilage defect testing: a systematic review. *Osteoarthritis Cartilage* **2009**, *17* (6), 705-13.
46. Malda, J.; de Grauw, J. C.; Benders, K. E. M.; Kik, M. J. L.; van de Lest, C. H. A.; Creemers, L. B.; Dhert, W. J. A.; van Weeren, P. R., Of Mice, Men and Elephants: The Relation between Articular Cartilage Thickness and Body Mass. *PLOS ONE* **2013**, *8* (2), e57683.
47. te Moller, N. C. R.; Brommer, H.; Liukkonen, J.; Virén, T.; Timonen, M.; Puhakka, P. H.; Jurvelin, J. S.; van Weeren, P. R.; Töyräs, J., Arthroscopic optical coherence tomography provides detailed information on articular cartilage lesions in horses. *The Veterinary Journal* **2013**, *197* (3), 589-595.
48. Sarin, J. K.; te Moller, N. C. R.; Mancini, I. A. D.; Brommer, H.; Visser, J.; Malda, J.; van Weeren, P. R.; Afara, I. O.; Töyräs, J., Arthroscopic near infrared spectroscopy enables simultaneous quantitative evaluation of articular cartilage and subchondral bone *in vivo*. *Scientific Reports* **2018**, *8* (1), 13409.
49. Serra Bragança, F. M.; Rhodin, M.; van Weeren, P. R., On the brink of daily clinical application of objective gait analysis: What evidence do we have so far from studies using an induced lameness model? *The Veterinary Journal* **2018**, *234*, 11-23.
50. Serra Bragança, F. M.; Roepstorff, C.; Rhodin, M.; Pfau, T.; van Weeren, P. R.; Roepstorff, L., Quantitative lameness assessment in the horse based on upper body movement symmetry: The effect of different filtering techniques on the quantification of motion symmetry. *Biomedical Signal Processing and Control* **2020**, *57*, 101674.
51. van Weeren, P. R.; Gómez Álvarez, C. B., Equine gait analysis: The slow start, the recent breakthroughs and the sky as the limit? *Equine Veterinary Journal* **2019**, *51* (6), 809-810.
52. Albrektsson, T.; Becker, W.; Coli, P.; Jemt, T.; Mölne, J.; Sennerby, L., Bone loss around oral and orthopedic implants: An immunologically based condition. *Clinical Implant Dentistry and Related Research* **2019**, *21* (4), 786-795.



ANNEX I

**Addressing the brittleness of printable
calcium phosphate (pCaP) cements via
supplementation with
resilient silk fibroin**

INTRODUCTION

Mechanical stability and correct surgical implantation of osteal scaffolds are fundamental to achieve successful osteointegration, a key step towards the functional repair of osteochondral defects, as clearly illustrated in Chapters 5 and 6 of this thesis. In particular, materials that are compliant with common surgical procedures and can be inserted into defects with minimal effort by the surgeon, may prove advantageous. The bone substitute and osteal anchor used in this Thesis required the printing of pre-designed parts that had to fit perfectly in the defects that had been created surgically in the equine knee joints. However, a non-perfect fit, possibly caused by minimal geometrical and size variations of the brittle ceramic scaffold, was shown to have a detrimental effect and to lead to the misalignment of the regenerative prosthesis, the inability to sufficiently withstand mechanical loads, the release of ceramic wear particles in the joint space, and eventually to the failure of the entire implant (see Chapter 5).

Where theoretically this undesired outcome can be overcome by optimizing the geometrical features of the scaffold and by taking extreme care with the surgical implantation, such a scenario is complicated and not ideal. Addressing the brittleness of the bioceramic material would be a better option, but it remains a major challenge. As already discussed in this thesis, bioceramic materials based on calcium phosphate (CaP) have gained extensive attention as substitute biomaterials to guide new bone regeneration, due to the fact that their composition closely mimics that of the inorganic phase of the native bone.¹ Moreover, these materials can also be processed into patient-specific devices by means of 3D-printing.² Although convincing proof-of-concept studies have been reported, two main hurdles for the clinical translation of such patient-specific scaffolds remain. First, the CaP cements are brittle and fracture easily when solidified, limiting their use for load bearing applications. In addition, the use of harsh setting/sintering methods does not allow incorporation of reinforcing polymers or bioactive drugs that could enhance the mechanical and biological properties of the ceramic-based materials. Recently, the brittleness of ceramic materials has been elegantly addressed via the extrusion printing of ceramic particles within a low concentration polymer solution, giving rise to a ceramic-polymer composite defined as “hyperelastic bone”.³ Such composites show remarkable deformability, which is ideal for surgical implantation, yet they still require the use of toxic organic solvents during the fabrication and printing process, which strongly contrasts with the bio-friendly fabrication process described in this thesis.

We, therefore, aimed at investigating new bioceramic formulations that would still permit printing and processing under ambient and physiological conditions, while at the same time generating highly resilient structures, able to address the mechanical challenges experienced during surgery, as well as after the implantation within the subchondral bone. In order to achieve this, the brittle ceramic paste was reinforced with resilient biodegradable polymer hydrogelators, specifically silk fibroin, a material well known for its outstanding

mechanical properties.⁴ In addition, the mechanical properties of the printed scaffolds were modulated through a more accurate design of the inner architecture. While extrusion printing relies on the use of fibers, deposited in a layer-by-layer fashion, as building blocks, lithography-based techniques, (*i.e.* stereolithography or digital light projection (DLP) printing), allow for the solid free-form fabrication of virtually any geometry, with a resolution superior to that of other printing techniques⁵. This increases the range of geometries that can be obtained and thus allows for enhanced control of scaffold mechanics. The explorative studies performed in this annex also aim to assess the feasibility of developing a silk-based ceramic inks compatible with 3D lithographic printing, in which photocrosslinking of the ceramic precursor is facilitated through the presence of visible-light responsive functional groups from the silk protein.⁶ This will provide an additional possibility to increase the complexity of the generated scaffolds, and potentially can complement the array of structures processable by extrusion printing.

MATERIALS AND METHODS

Materials and ink preparation

Silk fibroin was extracted from cocoons of *Bombyx Mori*, via degumming in boiling Na₂CO₃ in order to remove sericins, followed by drying, and solubilization in 9.3 M LiBr⁷. The obtained polymer was purified via dialysis (3.5 kDa MWCO), and dialyzed silk fibroin solutions displaying different polymer concentrations (7, 14 and 21 %w/v) were stored at 4°C until further use.

Forty mg of nano-hydroxyapatite (nano-HA, particle size <200 nm, Ca₅(OH)(PO₄)₃, Sigma Aldrich) and 360 mg of milled alpha-tricalcium phosphate microparticles (α -TCP, average size 3.83 μ m, Cambioceramics, Leiden, the Netherlands) were mixed with silk fibroin solutions. Photocrosslinking was performed by mixing into the aqueous phase of the ink 2 mM Tris(2,2'-bipyridyl)ruthenium(II) chloride and 20 mM sodium persulfate (Ru/SPS, Sigma Aldrich), which together form a biocompatible visible light responsive photoinitiator ($\lambda_{\text{excitation}} = 400\text{-}450$ nm).⁵ This photoinitiator system has been previously optimized for high resolution DLP printing⁵ and can induce the formation of silk hydrogels by forming di-phenol bonds through oxidizing the native tyrosine residues within the silk backbone.⁶ Photocrosslinking of the silk component within the ink was achieved via exposure to a wide spectrum LED light for 5 minutes/side. Subsequently, silk-calcium phosphate composites were set under relative saturate humidity. A particle concentration of 40% was selected based on tests performed for printing with the DLP printer, being the maximum concentration at which the ink shows a viscosity that is low enough to still permit mixing by the movable platform of the printer.

Mechanical testing

Dumbbell-shaped test samples (cross-sectional dimension = 0.5 cm x 0.3 cm and length = 3 cm) were produced using custom-made molds. Different ink formulations, as detailed in Table 1, were cast into the molds, allowed to set and photocrosslinked as described in the previous section. In addition, the formulations were either used as obtained after photocrosslinking, or were further treated with methanol (absolute methanol for 1 hour, followed by 3 times washing with ultrapure water), to induce β -sheet formation of the silk fibroin chains, which are known to greatly improve the stiffness and mechanical strength of the polymer⁸. Samples were loaded onto a tensile testing machine (Zwick/Roell Z010 tensile tester 2) and subjected to a displacement ramp of 1 mm/minute. Elastic modulus was calculated from slope at linear elastic region of stress-strain-curve. Energy to failure was calculated from area under stress-strain curve. Ultimate stress was a maximum stress. Finally, ultimate strain was strain at failure point.

Table 1: Ceramic-silk composite formulations for the tensile tests

Formulation	Particle phase	Liquid phase	Photocrosslinking agents	Methanol treated
1	40% w/w alpha TCP+nano HaP	water	No	No
2	Without Particle	7% w/v silk fibroin in water	Yes	No
3	Without Particle	7% w/v silk fibroin in water	Yes	Yes
4	40% w/w alpha TCP+nano HaP	7% w/v silk fibroin in water	Yes	No
5	40% w/w alpha TCP+nano HaP	7% w/v silk fibroin in water	Yes	Yes
6	Without Particle	14% w/v silk fibroin in water	Yes	No
7	Without Particle	14% w/v silk fibroin in water	Yes	Yes
8	40% w/w alpha TCP+nano HaP	14% w/v silk fibroin in water	Yes	No
9	40% w/w alpha TCP+nano HaP	14% w/v silk fibroin in water	Yes	Yes
10	Without Particle	21% w/v silk fibroin in water	Yes	No
11	Without Particle	21% w/v silk fibroin in water	Yes	Yes
12	40% w/w alpha TCP+nano HaP	21% w/v silk fibroin in water	Yes	No
13	40% w/w alpha TCP+nano HaP	21% w/v silk fibroin in water	Yes	Yes

DLP working curve

To identify the minimum layer thickness that could be printed by processing the silk-calcium phosphate composite using the DLP technique (Atum 3D DLP station), ink formulations with of different silk fibroin concentrations and different particle concentrations were prepared, as detailed in Table 2. Each formulation was exposed to 100% light intensity ($15 \text{ mW}\cdot\text{cm}^{-2}$) for 1, 2.5, 5 and 10 seconds. Then, thickness in the z-axis was measured from stereo-microscopical images using ImageJ software.⁹

Table 2: Ceramic-silk composite formulations for DLP printing optimization

Formulation	Liquid phase	Particle phase
1	14% w/v silk fibroin in water	30% w/w alpha TCP+nano HaP
2	14% w/v silk fibroin in water	40% w/w alpha TCP+nano HaP
3	14% w/v silk fibroin in water	50% w/w alpha TCP+nano HaP
4	21% w/v silk fibroin in water	30% w/w alpha TCP+nano HaP
5	21% w/v silk fibroin in water	40% w/w alpha TCP+nano HaP
6	21% w/v silk fibroin in water	50% w/w alpha TCP+nano HaP

RESULTS

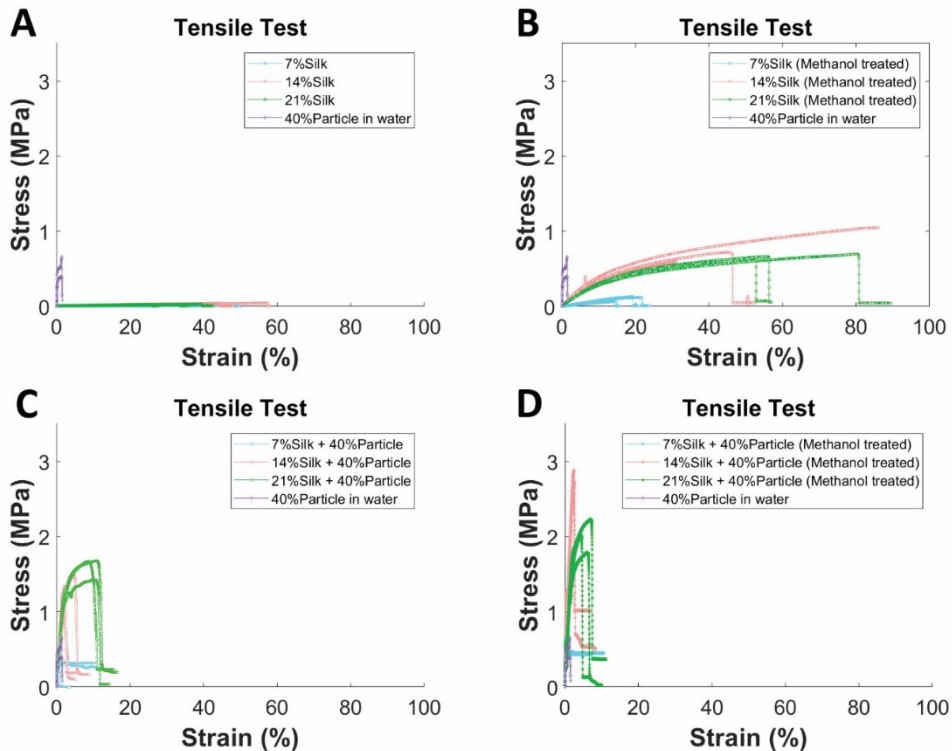


Figure 1. Tensile stress-strain curves representing A) pristine and B) methanol-treated silk hydrogels compared to silk-free CDHA; and C) unmodified and D) methanol treated silk-ceramic samples.

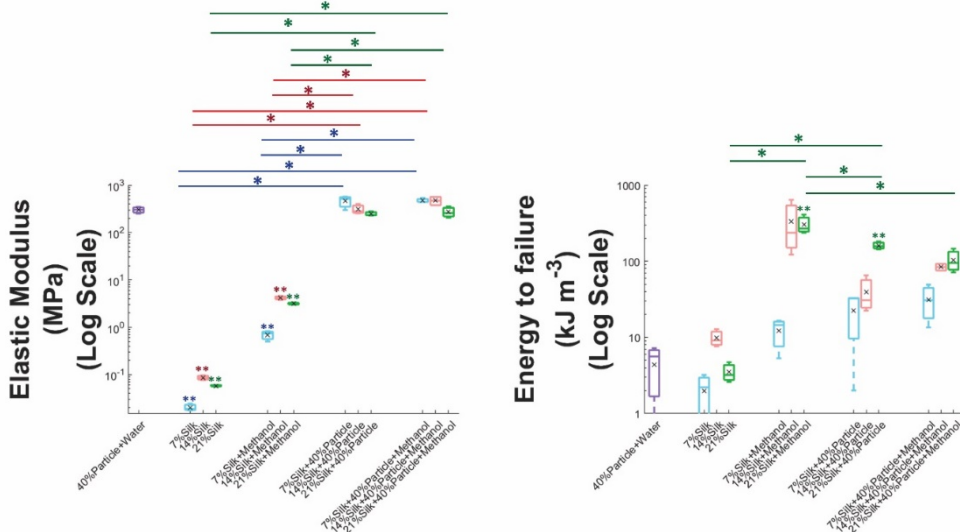


Figure 2. A) Elastic modulus and B) Tensile toughness of the silk-ceramic composites showing how the addition of silk can improve the tensile toughness of the CDHA cement up to 1.5 orders of magnitude compared to the silk-free ceramic formulation, without major impact on the overall tensile stiffness of the material. A one-way ANOVA with post hoc Bonferroni was performed to test differences between groups of the same silk concentration (** indicate significant different to silk- free composition (control) ($p < 0.05$)).

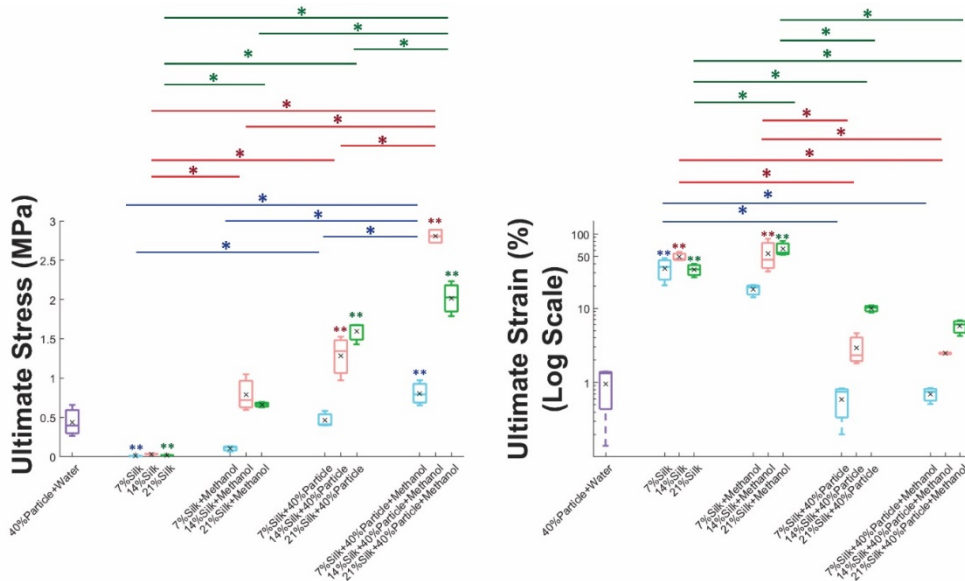


Figure 3. Ultimate A) stress and B) strain increase up to 6-fold and 10-fold respectively in CDHA formulations loaded with silk. A one-way ANOVA with post hoc Bonferroni was performed to test differences between groups of the same silk concentration (** indicate significant different to silk-free composition (control) ($p < 0.05$)).

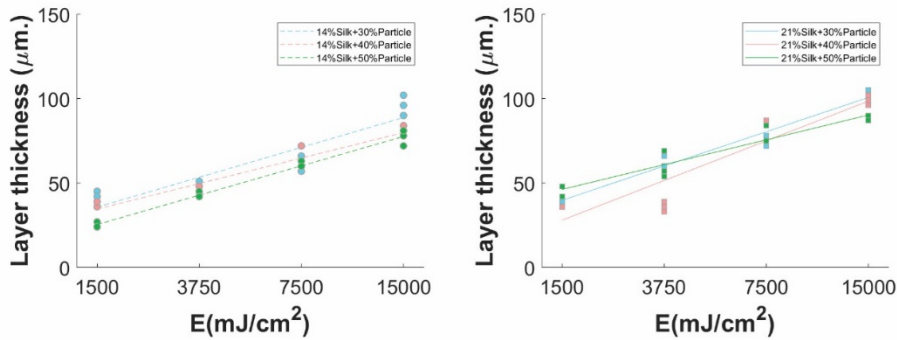


Figure 4. Working curve constructed for 14% and 21% of silk fibroin + 2mM Ruthenium/20 mM SPS with different calcium phosphate particle (α -TCP + nano HaP) concentrations.

CONCLUSIONS

The results from these experiments indicate that the incorporation of silk fibroin at a concentration equal or above 14% $w \cdot v^{-1}$, with and without induction of β -sheet formation by methanol treatment, can successfully improve the toughness of the bioceramic biomaterial ink, and can result in structures with improved ultimate stress at failure, showing up to a 6-fold increment and also a 6-fold higher deformation at breaking compared to the pristine, silk-free calcium phosphate material. Likewise, the toughness of the material, as measured by the energy necessary to provoke failure of the sample could be improved up to 20 – 25 - fold, compared with the silk-free calcium phosphate structure. Overall, treatments with methanol improved the mechanical strength of the materials, although they generally decrease deformability and ultimate strain. These promising results show increased toughness under tensile stresses, to which ceramic materials typically display low resistance, underscoring that the supplementation with silk fibroin may be an advantageous approach to address the brittleness of pCaP cements. Further tests on selected unmodified and methanol-treated silk-laden composites (14 and 21% silk) under cyclic compression and bending will be undertaken to select the optimal composition to enhance the performance under loading of these materials as bone substitutes.

Proof-of-concept studies have indicated that the materials can be photocrosslinked using a DLP printer, and a minimum resolution in the z-layer of approximately 30 μm can be reached with both the 14 and 21% w/v silk formulation. Future endeavors will focus on creating bone scaffolds with tunable architecture to introduce control over porosity and further refine the mechanical behavior. Moreover, although the processability with DLP imposed an upper limit to 40% w/v for the ceramic content in the ink paste, additional studies can be envisioned testing the mechanical properties at higher ceramic contents, in a setting in which extrusion printing is used as described in this thesis.

REFERENCES

1. Dorozhkin, S. V., Bioceramics of calcium orthophosphates. *Biomaterials* **2010**, *31* (7), 1465-1485.
2. Trombetta, R.; Inzana, J. A.; Schwarz, E. M.; Kates, S. L.; Awad, H. A., 3D Printing of Calcium Phosphate Ceramics for Bone Tissue Engineering and Drug Delivery. *Annals of Biomedical Engineering* **2017**, *45* (1), 23-44.
3. Jakus, A. E.; Rutz, A. L.; Jordan, S. W.; Kannan, A.; Mitchell, S. M.; Yun, C.; Koube, K. D.; Yoo, S. C.; Whiteley, H. E.; Richter, C.-P.; Galiano, R. D.; Hsu, W. K.; Stock, S. R.; Hsu, E. L.; Shah, R. N., Hyperelastic “bone”: A highly versatile, growth factor-free, osteoregenerative, scalable, and surgically friendly biomaterial. *Science Translational Medicine* **2016**, *8* (358), 358ra127.
4. Ma, D.; Wang, Y.; Dai, W., Silk fibroin-based biomaterials for musculoskeletal tissue engineering. *Materials Science and Engineering: C* **2018**, *89*, 456-469.
5. Lim, K. S.; Levato, R.; Costa, P. F.; Castilho, M. D.; Alcalá-Orozco, C. R.; van Dorenmalen, K. M. A.; Melchels, F. P. W.; Gawlitta, D.; Hooper, G. J.; Malda, J.; Woodfield, T. B. F., Bio-resin for high resolution lithography-based biofabrication of complex cell-laden constructs. *Biofabrication* **2018**, *10* (3), 034101.
6. Cui, X.; Soliman, B. G.; Alcalá-Orozco, C. R.; Li, J.; Vis, M. A. M.; Santos, M.; Wise, S. G.; Levato, R.; Malda, J.; Woodfield, T. B. F.; Rnjak-Kovacina, J.; Lim, K. S., Rapid Photocrosslinking of Silk Hydrogels with High Cell Density and Enhanced Shape Fidelity. *Advanced Healthcare Materials* **2020**, *9* (4), 1901667.
7. Rockwood, D. N.; Preda, R. C.; Yücel, T.; Wang, X.; Lovett, M. L.; Kaplan, D. L., Materials fabrication from Bombyx mori silk fibroin. *Nature Protocols* **2011**, *6* (10), 1612-1631.
8. Wu, X.; Wu, X.; Yang, B.; Shao, M.; Feng, G., Methanol–Water-Dependent Structural Changes of Regenerated Silk Fibroin Probed Using Terahertz Spectroscopy. *Applied Spectroscopy* **2017**, *71* (8), 1785-1794.
9. Schindelin, J.; Arganda-Carreras, I.; Frise, E.; Kaynig, V.; Longair, M.; Pietzsch, T.; Preibisch, S.; Rueden, C.; Saalfeld, S.; Schmid, B.; Tinevez, J. Y.; White, D. J.; Hartenstein, V.; Eliceiri, K.; Tomancak, P.; Cardona, A., Fiji: an open-source platform for biological-image analysis. *Nat Methods* **2012**, *9* (7), 676-82.



Appendices

Nederlandse samenvatting

Summary in English

List of Abbreviations

Acknowledgements

List of publications

Curriculum vitae

Nederlandse samenvatting

De moderne drie-dimensionale (3D) bioprinttechnieken bieden verschillende mogelijkheden voor de productie van op maat gemaakte chondrale of osteochondrale implantaten, maar het met behulp van deze technieken integreren van materialen met (zeer) uiteenlopende mechanische eigenschappen is nog steeds een forse uitdaging binnen de regeneratieve geneeskunde. In dit proefschrift wordt via een tweetal wegen geprobeerd een antwoord op deze uitdaging te vinden. Deze twee benaderingen zijn: 1) de ontwikkeling van printbare materialen voor de productie van de botcomponent van het implantaat met dusdanige fysische en chemische eigenschappen dat die materialen tegelijkertijd geprint kunnen worden met de hydrogelen die gebruikt worden voor het kraakbeengedeelte van het implantaat; en 2) de ontwikkeling van een proces waarbij op meerdere schaalniveaus geprint kan worden om de bot- en kraakbeencompartimenten te kunnen integreren. Via deze routes wordt in dit proefschrift een veelbelovende strategie ontwikkeld waarbij verschillende 3D (bio-)printtechnieken gecombineerd worden om een geïntegreerd osteochondraal implantaat te produceren dat bestaat uit een kraakbeendeel dat gebaseerd is op hydrogelen die met microvezels versterkt zijn en een botcompartiment op basis van een calciumfosfaat product.

Recent is aangetoond dat de drukbestendigheid van gelatine methacrylaat (gelMA) hydrogelen verbeterd kan worden, tot waarden die vergelijkbaar zijn met die van natuurlijk kraakbeen, door gegoten gelen te verstevigen met fijne polycaprolactone (PCL) netwerken die geproduceerd zijn door middel van melt electrowriting (MEW), een 3D printtechniek op microschaal waarbij vezelstructuren gemaakt worden uit polymeersmeltingen.

Deze versterkte, kraakbeenvervangende structuren moeten dan nog stevig verankerd worden in de onderliggende botcomponent om zo samen een optimaal functioneel osteochondraal implantaat te vormen.

In dit proefschrift wordt een methode beschreven om dit te realiseren (**Hoofdstuk 3**). Er wordt aangetoond dat ingewikkelde structuren die geproduceerd zijn met MEW en opgebouwd zijn uit vezels van PCL, een materiaal dat al bij een relatief lage (60°) temperatuur smelt, hun karakteristieke architectuur (samen met de hydrogelen bepalend voor de mechanische eigenschappen) behouden wanneer ze gecombineerd worden met een keramische botcomponent die uithardt bij lage temperatuur. Voor die botcomponent werd, uitgaande van alfa-tricalciumfosfaat (α -TCP), een materiaal ontwikkeld dat uithardt bij fysiologische temperaturen. Dat materiaal werd gecombineerd met een specifiek ontwikkelde thermoreversibele drager voor hydrogelen. Een dergelijke samengestelde keramische component kan dan uitharden op lage temperatuur waarbij calciumdeficiënt hydroxyapatiet (CDHA) gevormd wordt waardoor het mogelijk wordt labiele materialen zoals PCL hierin integraal op te nemen. Het mengsel van α -TCP met de thermoreversibele hydrogel geeft het materiaal shear-thinning eigenschappen die het mogelijk maken het materiaal te gebruiken als bio-inkt voor extrusie-printen bij omgevingstemperatuur. Dat maakt het produceren van een verbindende structuur tussen de kraakbeen- en botfase van het implantaat, vergelijkbaar

met de subchondrale botplaat in de natuurlijke situatie, mogelijk. De geïntegreerde PCL-CDHA structuren werden verkregen na het uitharden van de direct op het PCL microvezel versterkingsnetwerk geprinte calciumfosfaat composiet (pCaP). Op deze manier werd de resistentie tegen afschuifkrachten van de verbinding tussen kraakbeen- en botcomponent van het implantaat aanzienlijk verhoogd. Dat maakte het mogelijk de chondrale regio met hydrogel te combineren met de botcomponent en maakte het implantaat tevens bestand tegen de manipulatie bij de implantatie in het defect, zowel in de *ex vivo* als in de *in vivo* situatie.

Voorafgaand aan de translatie naar *in vivo* van deze samengestelde biomaterialen zijn de mechanische en biologische eigenschappen ervan uitgebreid onderzocht met als specifiek aandachtspunt het botvormende vermogen van het botanker. Dat is uiteraard van groot belang voor implantaten die bedoeld zijn voor het genezen van osteochondrale defecten.

Het bleek dat bij een porositeit tussen de 20 en 60% de geprinte CDHA structuur vergelijkbare belastbaarheid op druk had als menselijk subchondraal bot. Ook bleek dat uit het beenmerg afkomstige mesenchymale stromale cellen niet alleen konden groeien in medium met CDHA en op het geprinte CDHA zelf, maar zich ook konden ontwikkelen als botvormende cellen indien ze voorzien werden van specifieke factoren die de botvorming stimuleren. Deze positieve bevindingen vormden de basis voor een *in vivo* studie naar het effect van twee vormen van porositeit op het botvormend vermogen van cilindervormige CDHA structuren; een constante porositeit werd hierbij vergeleken met een van boven naar beneden toenemende porositeit (zoals ook het geval is in natuurlijk subchondraal bot) (**Hoofdstuk 4**). Deze studie werd gedaan bij paarden waarbij een groot defect gecreëerd werd in bot op een niet op druk belaste locatie en waarbij botingroei slechts van onderop kon plaatsvinden. Uit de studie bleek dat de verhouding tussen resorptie van de CDHA-structuur en botnieuwvorming beter was bij de structuur met de constante porositeit en ook was bij die structuren de botnieuwvorming meer homogeen verdeeld. Op basis van deze bevindingen werd de keuze gemaakt voor deze CDHA architectuur voor de verdere ontwikkeling van het osteochondrale implantaat.

Het uiteindelijke implantaat werd getest in een tweetal *in vivo* studies in het kniegewricht van ponies. Bij deze studies zat het verschil in het kraakbeendeel van het osteochondrale implantaat; het botdeel en de overgang van bot naar kraakbeen bestonden in beide gevallen uit de bovenbeschreven calciumfosfaat composiet waarin de MEW microvezels waren verankerd.

In de eerste studie werd in het kraakbeendeel gelMA, met daarin kraakbeenstamcellen (ACPCs) en met toevoeging van de groeifactor GDF-2 (growth differentiation factor 2), gegoten in het netwerk van PCL vezels wat resulteerde in de vorming van een kraakbeenachtige schijf die omgeven werd door de PCL vezels na een voorkweek van een maand (**Hoofdstuk 5**). In de tweede studie werd de gel met daarin de kraakbeenstamcellen samen geprint met het PCL netwerk en werd het geheel eveneens gedurende een maand gekweekt in een chondrogeen medium (**Hoofdstuk 6**). Voor beide studies werden celvrije implantaten als controles gebruikt. In beide gevallen deden de ACPCs

het goed in de voorkweek en werd er een kraakbeenachtige extracellulaire matrix gevormd met glycosaminoglycanen (GAGs) en collageen type II. Na 6 maanden *in vivo* waren de resultaten echter sterk verschillend, hetgeen herleid kon worden tot het (dis)functioneren van het botdeel van het implantaat.

Bij de GDF-2 studie was er sprake van een sterke afname van het GAG-gehalte en van de biomechanische eigenschappen. In het botgedeelte was er maar een minimale hoeveelheid bot gevormd en ook waren er aanwijzingen voor een redelijk ernstige ontsteking, zowel in de groep met als in die zonder cellen. Verder was het duidelijk dat vele implantaten niet (meer) juist in de osteochondrale defecten zaten, maar verzakt waren of anderszins van positie veranderd. Geconcludeerd moest worden dat de combinatie van een suboptimale pasvorm van het botdeel van de implantaten met een grote brosheid van de keramische component geleid had tot het ontstaan van schade bij de chirurgische procedure die uiteindelijk geresulteerd heeft in fragmentvorming en verlies van voldoende stevigheid om de belasting te kunnen verdragen met als gevolg het inzakken van het hele implantaat.

Bij de andere studie waren de resultaten veel beter. De iets andere fabricagetechniek had bij dat experiment tot een veel beter passen van het implantaat gezorgd, waardoor de bovengenoemde problemen niet speelden en het implantaat bijna geheel gevrijwaard bleef van structurele schade. Bij dit experiment bleek het GAG-gehalte over de implantatieperiode niet afgenomen, maar juist (licht) gestegen. Dat gold ook voor de mechanische eigenschappen. In de botcomponent van het implantaat was er goede botnieuwvorming. Een bijzondere bevinding was dat deze gunstige resultaten voor zowel de implantaten met als zonder cellen golden.

Al met al laten beide studies de beperkingen van de gebruikte calciumfosfaat composiet zien, maar ook de veelbelovendheid van het type osteochondraal implantaat zoals dat ontwikkeld is in dit proefschrift. Ook is duidelijk geworden dat het paardenmodel weliswaar uitdagend is, maar tegelijkertijd ook zeer relevant, zowel als translationeel model als voor klinische toepassingen bij de diersoort zelf, waar sprake is van een duidelijke klinische vraag.

Samenvattend kan gesteld worden, dat dit proefschrift laat zien hoe er door het uitgekende gebruik van verschillende 3D printtechnieken om componenten met heel verschillende mechanische eigenschappen integraal te verbinden, belangrijke voortgang is geboekt bij de ontwikkeling van regeneratieve osteochondrale implantaten die voldoende mechanische kwaliteiten hebben. Natuurlijk moeten er nog wel enige stappen gezet worden voordat er sprake is van een product dat toepasbaar is in de kliniek, met name op het gebied van vermindering van de brosheid van het botgedeelte. Verder zal er ook nog gekeken moeten worden naar de verbinding van de kraakbeen- en botdelen, met name op het vlak van de permeabiliteit en de optimale opvang en verdeling van de belasting. De natuurlijke situatie kan daarbij als voorbeeld dienen.

English Summary

Three-dimensional (3D) printing technologies offer multiple possibilities for the custom-tailored fabrication of either cartilage or bone grafts. However, employing this technology for the integration of different materials that possess mechanically distinct properties, is still a major challenge in tissue engineering and regenerative medicine. To address this challenge, two main approaches were developed in this thesis: 1) the development of printable materials for use as a bone scaffold with physical and chemical properties that permit their patterning in direct contact with the microfiber-reinforced hydrogels that are used as chondral substitutes, and 2) the development of a multi-scale printing process for integrating such bone and cartilage compartments. Therefore, this thesis presents a promising strategy for combining different 3D printing technologies to integrate microfiber-reinforced, hydrogel-based chondral constructs and calcium phosphate-based subchondral bone compartments, in order to establish and engineer a functional osteochondral interface.

Recently, the compressive properties of gelatin methacrylate hydrogels (gelMA) were increased to values comparable to those of native cartilage, by reinforcing cast gels with polycaprolactone (PCL) microfiber meshes that were produced by melt electrowriting (MEW), a microscale 3D printing technology. To further improve such composite structures and enable their application in large osteochondral defects, the anchoring of such reinforced structures on osteal scaffolds in a way that mimics the natural subchondral bone, was addressed in this thesis (**Chapter 3**). Highly organized microfiber lattices produced by MEW using PCL, a thermoplastic synthetic polymer susceptible to melt at relatively low temperatures (approximately 60°C), were shown to preserve their unique architecture (responsible for the mechanical reinforcement that is observed in combination with infused hydrogels), when combined with low-temperature setting ceramics.

For this purpose, a calcium phosphate-based material that could set at physiological temperature, with alpha-tricalcium phosphate (α -TCP) as main ceramic component, was developed and combined with a custom-synthesized thermo-reversible hydrogel carrier. Such composite bioceramics can be solidified at low temperature, forming calcium-deficient hydroxyapatite (CDHA). This process is compatible with the inclusion of labile materials like PCL. The mixture of α -TCP with the thermo-reversible hydrogel endowed the system with shear-thinning properties that allowed the use of the composite as bio-ink for printing with an extrusion-based printer at ambient temperature, hence facilitating the fabrication of a subchondral bone plate-mimicking interface and a cancellous bone-mimicking structure underneath. These integrated PCL-CDHA structures were obtained after solidification of directly dispensed printable calcium phosphate-based composite (pCaP) onto the PCL microfiber reinforcing framework of the chondral compartment. The adequate and secure integration permitted to greatly increase the shear strength of the engineered bone-to-cartilage boundary, which permitted additional manipulation of the construct, such as

hydrogel infusion in the chondral region and implantation in surgically produced osteochondral defects *ex vivo* and *in vivo*.

Prior to the *in vivo* translation of these composite biomaterials, this thesis extensively investigated the mechanical and biological performance *in vitro* of the constructs, thereby focusing on unravelling the bone-forming potential of the osteal anchor, a necessary step for functional healing of osteochondral defects. The porous CDHA structures produced by 3D printing appeared to exhibit compressive properties within the range of human cancellous bone when porosity ranged between 20% and 60%. Additionally, bone-marrow derived mesenchymal stromal cells were shown to proliferate both within CDHA-incubated medium and on the printed CDHA itself, and to differentiate toward the osteogenic lineage when supplemented with osteogenic induction factors. These positive findings justified proceeding with *in vivo* evaluations. For that purpose, cylindrical, 3D printed bony scaffolds displaying different pore distributions, with either a constant porosity throughout the scaffold or a decreasing gradient of porosity along the axial direction of the cylinder (as in natural subchondral bone), were tested in a large (cm-scale) critical size bone defect in a non-load-bearing orthotopic location in an equine model (**Chapter 4**). A PCL case around the cylinder permitted invasion of the newly-formed bone only from the bottom. Results demonstrated better scaffold resorption, paired with more and more homogeneous bone regeneration in the implants with constant porosity. Given this superior performance, the constant porosity architecture was chosen for the further development of the osteochondral construct for cartilage repair at a load-bearing site.

The final concepts of the osteochondral graft were tested in two *in vivo* studies in ponies in which the chondral compartments had a different composition and architecture. In both implants the bone phase and interphase between the bone and the cartilage phase were similar consisting of the pCaP composite with anchored MEW fibers as osteal anchor and subchondral bone phase of the graft. In the first study, the chondral phase was composed by articular cartilage derived progenitor cells (ACPCs) seeded within the PCL mesh, and stimulated during pre-culture *in vitro* with growth differentiation factor-2 (GDF-2), resulting in the formation of a cartilaginous disc entangled within the polymeric microfibers (**Chapter 5**). In the second study, ACPC-laden gelMA was co-printed with the PCL meshwork and the constructs were cultured for a month with chondrogenic differentiation media (**Chapter 6**). Cell-free controls were used in both studies. In all cases, regardless of the configuration of the implant, the scaffolds permitted ACPCs to proliferate and produce cartilage-related extracellular matrix molecules, such as glycosaminoglycans (GAGs) and type II collagen during the 4-week culture prior to implantation. After an implantation for 6 months, the results were totally different for the two studies, which seemed to be due to striking differences in the performance of the bony phases.

In the GDF-2 study, at 6 months after implantation the GAG-content of the cell-laden structure had substantially decreased compared to the level after pre-culture. There was also a minimal volume of newly-formed bone, and a rather heavy inflammatory reaction was

observed after implantation for 6 months, both in the cell-laden group and in the cell-free control. Additionally, misalignment and misposition of the grafts was clearly visible.

In the other group, pre-culture GAG content had slightly increased from the time of implantation until 6 months after implantation in the study. Interestingly, a similar GAG content was observed in cell-free controls. The volume of newly-formed bone in the subchondral bone compartment was higher compared with the GDF-2 study and there was much less misalignment.

It was hypothesized that the imperfect geometry of the printed subchondral bone compartment in the GDF-2 study, combined with the brittleness of the ceramic material might have led to structural damage of the implants during surgical implantation, fragilizing the structure and eventually leading to its collapse when subjected to loading, and overall implant failure. This had not happened in the other study thanks to the use of a mold in that study when producing the bone phase, which led to better shape fidelity post-printing and thus better geometrical fitting in the defects. These studies, while showing the appropriateness of the concept and the feasibility of the proposed approach, also clearly demonstrated the limitations of the current, brittle, pCaP composite for application at load-bearing sites. Finally, the equine model showed to be a challenging, but relevant model as a translational model preparing for clinical use in human and animal patient populations.

It can be concluded that the work in this thesis has produced substantial progress towards the final goal of clinical translation of fully mechanically competent and regenerative osteochondral grafts by the clever use of various 3D-printing technologies to integrate two mechanically distinct materials together to form an entire osteochondral graft. Nevertheless, there are several challenges that still need to be explored further, especially regarding the development of alternative materials with higher fracture toughness for the bone compartment. Additionally, improvements can be made to the interface itself as well. For instance, with respect to permeability and its role in load distribution and dissipation. Better recapitulation of the natural situation may be the way to go here.

List of Abbreviations

2D	two-dimensional
3D	three-dimensional
ACPCs	articular cartilage-derived progenitor cells
ALP	alkaline phosphate
AM	additive manufacturing
APS	ammonium persulphate
ASAP	L-ascorbic acid 2-phosphate
α -MEM	minimum essential medium alpha
α -TCP	alpha-tricalcium phosphate
bFGF	basic fibroblast growth factor
BID	twice a day
BMP-7	bone morphogenetic factor-7
β -GP	beta-glycerophosphate
C	crosslinkable
CAD	computer aided design
CaP	calcium phosphate
CBC	complete blood count
CDHA	calcium deficient hydroxyapatite
C-pCaP	crosslinkable printable calcium phosphate
CR	ceramic remnant
DAB	3, 3-diaminobenzidine-horseradish peroxidase
DLP	digital light projection
DMA	dynamic mechanical analyzer
DMMB	dimethylmethylene blue
ECM	extracellular matrix
FCS	fetal calf serum
FDM	fused deposition modelling
GAGs	glycosaminoglycans
GDF-2	growth differentiation factor-2
gelMA	methacryloyl-modified gelatin
GRF	ground reaction force
HEPES	N-2-hydroxyethylpiperazine-N-2-ethane sulfonic acid
H&E	hematoxylin and eosin
IGF-1	insulin-like growth factor-1
IM	intramuscular
IV	intravenous
LDH	lactate dehydrogenase
LVR	linear viscoelastic range

MEW	melt electrowriting
MMA	methyl methacrylate
MRI	magnetic resonance imaging
MSCs	mesenchymal stem cells, mesenchymal stromal cells
μ -CT	micro-computed tomography
NaOH	sodium hydroxide
Nano-HA	nano-hydroxyapatite
NB	new bone ingrowth
NC	non-crosslinkable
NC-pCaP	non-crosslinkable printable calcium phosphate
OC	osteocondral
PCL	polycaprolactone
PDMS	polydimethylsiloxane
PLA	polylactic aci
PO	oral administration
ROI	region of interest
ROM	range of motion
SD	standard deviation
SEM	scanning electron microscopy
SID	once a day
TEMED	tetramethylethylenediamine
TGF- β 3	transforming growth factor beta 3
TRAP	tartrate-resistant acid phosphatase
VOI	volume of interest
XRD	x-ray diffraction pattern

Acknowledgements

I am extremely grateful to the numerous people who have cultivated my experiences and reshape my perspective during this chapter of my life while studying the doctoral degree in the Netherlands. Additionally, the completion of this thesis would not have been possible without the support and nurturing of supervisors, colleagues, friends, and family.

First of all, my deepest gratitude goes to Royal Thai Government scholarship awards (for the Science and Technology section) for providing me the financial support during studying in the Netherlands. This scholarship allowed me an opportunity for having experiences in doing research with specialists and expertise within an international environment to further applying knowledge for developing my home country.

I would like to extend my sincere gratitude to Prof. Dr. Jos Malda and Prof. Dr. Paul René van Weeren for your kindness in accepting me as a Ph.D. student to work within your groups. I would like to thank you for all supports that allowed me: to learn and to have experiences in the biomedical additive manufacturing field; to perform experiments; to have a chance to work with other colleagues in your groups; and to meet other scientists in several conferences. I would also like to thank you for your invaluable time, and your patience in answering my questions; giving me suggestions and guidance; encouragement during critical steps.

I would like to extend my deepest appreciation to Asst. Prof. Dr. Riccardo Levato for your kindness in accepting me as one of your Ph.D. students. I would like to thank you for all your help, support, empathy, and patience since I started working in the lab. Under your supervision, you always dedicate your time to answer my questions, giving me guidance for both conducting scientific research and presenting scientific content including encouraging me along the way during studying. All constructive advice helps me to reframe my perspective toward working in scientific research which motivates me to put more effort to improve quality and to overcome obstacles. Thank you very much!

I would like to express my sincere thanks to Asst. Prof. Dr. Miguel Castilho for all help, support, and practical suggestions especially on the mechanical aspect of my research work.

I would like to also express my deepest appreciation to Prof. Dr. Harold Brommer for all help and helpful suggestions on horse-related research including all help and support from the anesthesia team and surgical assistance team in the Equine clinic.

I would like to extend my sincere thanks to Asst. Prof. Dr. scient. med. Phornphop Naiyanetr, the first person who introduced me to know more about the world of biomedical engineering which eventually inspired me to pursue the doctoral degree for working in research and development in the biomedical engineering field. Additionally, I would like to also extend my sincere thanks to Prof. Dr. Mongkol Techakumphu, Assoc. Prof. Dr. Wichai Tantasuparuk and Asst. Prof. Dr. Theerawat Tharasanit, who let me have had some

experiences in the Veterinary research field which eventually inspired me to work in the research field.

It would be long to list all individuals, however, I would also like to extend my gratitude to colleagues, technicians, animal caretaker, and friends from Biofabrication group; Centaur group; Regenerative Medicine program; (former) Department of Equine Sciences, Faculty of Veterinary medicine (UU); Department of Orthopedics (UMC, Utrecht), Department of Oral and Maxillofacial Surgery & Special dental care (UMC, Utrecht); Department of Pharmaceutics, Utrecht Institute for Pharmaceutical Sciences (UIPS), Faculty of Science (UU) for hospitality, thoughts, help, support, and unforgettable friendship along the way during working and studying in the Netherlands.

I am also grateful to administrators at the Bureau of International Contacts (BIC), Faculty of Veterinary Medicine (UU, NL); Marloes Verboven; Brenda Roosendaal; administrators at the Office of the Civil Service Commission (OCSC, TH); administrators at the student & educational affairs, the Royal Thai embassy (The Hague); administrators at the National Science and Technology Development Agency (NSTDA, TH); administrators at the National Metal and Materials Technology Center (MTEC, TH) and whom I may have missed for all support in arrangement and process of necessary documents for studying and staying in the Netherlands.

Finally, I would like to also thank Thai friends in the Netherlands for all memorable friendship, and, last but not least, my family for support and encouragement during working in the Netherlands.

List of publications

Groen, W.M., **Diloksumpan, P.**, van Weeren, P.R., Levato, R. and Malda, J. (2017), From intricate to integrated: Biofabrication of articulating joints. *J. Orthop. Res.*, 35: 2089-2097. <https://doi:10.1002/jor.23602>

Diloksumpan, P., de Ruijter, M., Castilho, M., Gbureck, U., Vermonden, T., van Weeren, P. R., Malda, J., Levato, R. (2020). Combining multi-scale 3D printing technologies to engineer reinforced hydrogel-ceramic interfaces. *Biofabrication*. <https://doi.org/10.1088/1758-5090/ab69d9>

Diloksumpan, P., Bolaños, R.V., Cokelaere, S., Pouran, B., de Grauw, J., van Rijen, M., van Weeren, R., Levato, R. and Malda, J. (2020), Orthotopic Bone Regeneration within 3D Printed Bioceramic Scaffolds with Region-Dependent Porosity Gradients in an Equine Model. *Adv. Healthcare Mater.*. <https://doi:10.1002/adhm.201901807>

Diloksumpan, P., Abinzano, F., de Ruijter, M., Mensinga, A., Plomp, S., Khan, I., Brommer, H., Smit, I., Castilho, M., van Weeren, R., Malda, J., and Levato, R., The Complexity of Joint Regeneration: How an Advanced Implant could Fail by Its *In Vivo* Proven Bone Component, Submitted

Curriculum vitae

Paweena Diloksumpan was born on July 28th 1983 in Bangkok, Thailand. After finishing high school from Satriwithaya school, she started to study Veterinary medicine in 2003 at the Faculty of Veterinary Sciences, Chulalongkorn University and graduated in 2009. After that, she worked as a livestock veterinarian for 2 years at the research and technology transfer station, center for learning and academic service, the network of Chulalongkorn university, Nan province. To pursue her interest in engineering, she decided to study master's degree in biomedical engineering at the Faculty of Engineering, Mahidol university, Thailand and earned the degree in 2013. In 2014, she was awarded the scholarship from Royal Thai government scholarship program (for science and technology section) for studying doctoral degree, abroad. From September 2015 – July 2020, she worked as a PhD student in regenerative medicine program at the Department of Equine Sciences, Faculty of Veterinary Medicine, Utrecht university under supervision of Prof. dr. Jos Malda, Prof. dr. René van Weeren and Asst. Prof. dr. Riccardo Levato. From September 2020, Paweena will continue her career as a researcher at the National Metal and Materials Technology Center (MTEC), Thailand.

